HAL
open science

Investigation of new multiferroic materials with coexistence of several ferroic and structural instabilities

Hongbo Liu

To cite this version:

Hongbo Liu. Investigation of new multiferroic materials with coexistence of several ferroic and structural instabilities. Other. Ecole Centrale Paris, 2011. English. NNT : 2011ECAP0047 . tel-00711475

HAL Id: tel-00711475

https://theses.hal.science/tel-00711475v1

Submitted on 4 Jul 2014

HAL is a multi-disciplinary open access archive for the deposit and dissemination of scientific research documents, whether they are published or not. The documents may come from teaching and research institutions in France or abroad, or from public or private research centers.

L'archive ouverte pluridisciplinaire **HAL**, est destinée au dépôt et à la diffusion de documents scientifiques de niveau recherche, publiés ou non, émanant des établissements d'enseignement et de recherche français ou étrangers, des laboratoires publics ou privés.

ÉCOLE CENTRALE DES ARTS ET MANUFACTURES
— ÉCOLE CENTRALE PARIS —

THÈSE
présentée par

LIU Hongbo

en vue de l'obtention du

Grade de Docteur de l'École Centrale Paris

Spécialité: Science des matériaux
Laboratoire d'accueil: Structures, Propriétés et Modélisation des Solides
Sujet :

INVESTIGATION OF NEW MULTIFERROIC MATERIALS WITH COEXISTENCE OF SEVERAL FERROIC AND STRUCTURAL INSTABILITIES

Soutenance prévue le 4 Novembre 2011 devant un jury composé de:

Kornev, Igor	Professeur à l'École Centrale Paris	Directeur de thèse
Kreisel, Jens	Directeur de Recherche à CNRS-Grenoble INP	Rapporteur
Defay, Emmanuel	Ingénieur à CEA-Grenoble	Rapporteur
Le Marrec, Françoise	Maître de Conférences à Université de Picardie Jules Verne	Membre du jury
Dkhil, Brahim	Maître de Conférences à l'École Centrale Paris	Membre du jury
Kiat, Jean-Michel	Directeur de Recherche à l'École Centrale Paris	Membre du jury

École Centrale Paris
Grande Voie des Vignes
92295 CHATENAY-MALABRY

Résumé

L'étude des matériaux multiferroiques est sans doute un des domaines de recherche actuelle les plus actifs et prolifiques de la matière condensée. Dans ces matériaux, coexistent polarisation, aimantation et élasticité. On comprend bien que cette coexistence permet une multifonctionnalité très attrayante pour un grand nombre d'applications mais aussi fournit un vivier extraordinaire pour étudier les interactions entre ces grandeurs ainsi que les mécanismes microscopiques sous-jacents. Cet attrait s'en trouve d'autant plus renforcé du fait des phénomènes de couplage entre ces grandeurs physiques autorisant des fonctionnalités nouvelles comme par exemple le renversement d'une aimantation avec un champ électrique au lieu d'un champ magnétique classiquement. Cependant, ces matériaux multiferroiques sont d'une part en petit nombre et d'autre part, exploitent pour beaucoup d'entre eux, la polarisation d'un ferroélectrique et l'aimantation d'un antiferromagnétique. Ceci étant, il existe d'autres types d'arrangements polaires et magnétiques encore non-exploités, c'est dans ce cadre que s'inscrit ce travail de thèse.

L'objectif de la thèse était de synthétiser de nouveaux multiferroiques présentant des arrangements polaires et magnétiques originaux et d'en caractériser les propriétés. Nous nous sommes tout particulièrement intéressés aux oxydes $PbFe_{2/3}W_{1/3}O_3$ (PFW) et $PbZrO_3$ (PZO). PFW présente des ordres polaires et magnétiques à longue et à courte portée : ferroélectrique-relaxeur et antiferromagnétique-verre de spin (ou ferromagnétisme faible). PZO est quant à lui antiferroélectrique avec antiferrodistorsivité (rotation des octaèdres d'oxygène) et présence d'instabilité ferroélectrique. Nous avons d'une part combiné ces deux matériaux pour former une solution solide et d'autre part réalisé un dopage de PZO avec des ions magnétiques. Après avoir synthétisé ces matériaux, nous les avons caractérisés électriquement (constante diélectrique, phénomène de relaxation, polarisation, température de Curie), magnétiquement (susceptibilité magnétique, aimantation) et structuralement (transition de phase). Ainsi, nous avons montré qu'il était possible d'obtenir un matériau multiferroique (50%PFW-50%PZO) présentant l'ensemble des instabilités ferroiques et structurales. Ces nouveaux matériaux ouvrent ainsi de nouvelles perspectives d'étude dans ce riche domaine en particulier en utilisant des antiferroélectriques.

Abstract

Multiferroics are currently intensely investigated because the coexistence and coupling of ferroic arrangements brings about new physical effects and, for the few room-temperature examples, interesting prospects for applications in various fields. This interest is illustrated by the recent publication of several articles on multiferroics in high impact reviews over the last five years. The main goal of the thesis was to look for new multiferroics by exploiting overlooked and original polar and magnetic arrangements. We more precisely investigated compounds based on lead iron tungsten $PbFe_{2/3}W_{1/3}O_3$ (PFW) and lead zirconate $PbZrO_3$ (PZO) oxides. PFW displays long- and short-range both polar and magnetic orders (ferroelectric-relaxor and antiferromagnetic-spin-glass) while PZO is antiferroelectric with antiferrodistorsivity (oxygen tilts) and existence of ferroelectric instabilities. Combining various techniques from synthesis to electric, magnetic and structural characterizations, we demonstrated that it is possible to get a multiferroic compound (50%PFW-50%PZO) with coexistence of multiple ferroic and structural arrangements with room temperature properties of practical interest. This work opens new prospects in this rich field of multiferroics in peculiar by using antiferroelectrics.

Contents

Résumé **i**

Abstract **iii**

1 Introduction **1**
1.1 Perovskite . . . 1
1.1.1 The prototype perovskite . . . 1
1.1.2 The deformation perovskite . . . 2
1.2 Ferroelectricity . . . 4
1.2.1 Broken symmetry . . . 4
1.2.2 Second-order Jahn-Teller Effect . . . 5
1.2.3 Landau theory of phase transitions . . . 5
1.2.4 Soft mode theory . . . 8
1.2.5 Curie-Weiss law . . . 8
1.3 Relaxor . . . 8
1.3.1 Diffuse phase transitions . . . 8
1.3.2 Vogel-Fulcher relationship . . . 9
1.3.3 Local and long range polar order . . . 9
1.4 Magnetism . . . 10
1.4.1 Magnetic moment . . . 10
1.4.2 Exchange interaction . . . 11
1.4.3 Double exchange interaction . . . 11
1.4.4 Superexchange interaction . . . 12
1.4.5 Jahn-Teller effect . . . 12
1.4.6 Curie Law . . . 14
1.5 Spin Glass . . . 14
1.6 Multiferroics . . . 15
1.6.1 Definition . . . 15
1.6.2 Recent progress of multiferroics . . . 15
1.6.3 Two approaches . . . 15
1.6.4 Magnetoelectric couping . . . 16
1.7 Workplan of the thesis . . . 17

2 Structure, Electric and Magnetic Characterization **19**
2.1 Crystal structure and diffraction . . . 19
2.1.1 Diffraction geometry . . . 19
2.1.2 Diffraction theory . . . 20
2.1.3 Neutron diffraction . . . 21
2.1.4 Rietveld refinement . . . 21

2.2 Electric characterization . . . 23
2.2.1 Dielectric permittivity . . . 23
2.2.2 Piezoelectric measurement . . . 24
2.2.3 Pyroelectric current . . . 24
2.2.4 Ferroelectric hysteresis loop . . . 25
2.2.5 Electric modulus and complex conductivity . . . 25
2.2.6 Dielectric relaxation . . . 26
2.3 Magnetic characterization . . . 28
2.4 A paradox . . . 28

3 Intrinsic Properties of Lead Iron Tungsten and Lead Zirconate 29
3.1 Literature review on the multiferroic lead iron tungsten . . . 29
3.2 Reexamination of the properties of lead iron tungsten . . . 30
3.2.1 Structural aspects . . . 30
3.2.2 Polar order . . . 33
3.2.3 Magnetic order in PFW . . . 40
3.3 Literature review on the antiferroelectric lead zirconate PZO . . . 42
3.4 Reexamination of lead zirconate properties . . . 44
3.4.1 The stability of AFE . . . 44
3.4.2 Existence of a FE intermediate phase . . . 44
3.5 Conclusion . . . 59

4 Lead Iron Tungsten - Lead Zirconate Solid Solution System 61
4.1 Literature review on lead iron tungsten based solid solution systems . . . 61
4.1.1 PFW-PTO . . . 61
4.1.2 PFW-PZT . . . 61
4.1.3 Antiferromagnetic phase transition . . . 62
4.2 PFW-PZO solid solution . . . 63
4.3 Crystal structures of PFW-PZO . . . 63
4.4 Phase transitions and polar properties of PFW-PZO . . . 70
4.4.1 (100-x) PFW - x PZO: $0 < x \leq 40$ . . . 70
4.4.2 (100-x)PFW - x PZO: $50 \leq x \leq 80$ . . . 76
4.4.3 90PZO . . . 82
4.4.4 95PZO . . . 85
4.5 PFW-PZO under electric field . . . 88
4.6 Polar phase diagram of PFW-PZO . . . 90
4.7 Magnetic properties of PFW-PZO . . . 91
4.7.1 Magnetic susceptibility . . . 91
4.7.2 Magnetic hysteresis loop . . . 91
4.8 Conclusion . . . 97

5 Magnetic Ions Doped Lead Zirconate 99
5.1 Limitation of doping . . . 99
5.2 Doping effects . . . 100
5.2.1 Stability of AFE . . . 100
5.2.2 Instability of octahedron . . . 101
5.2.3 Existence of a ferroelectric intermediate phase . . . 102
5.2.4 Magnetic properties . . . 103
5.3 Dielectric relaxation . . . 107
5.4 Conclusion . . . 110

6 Conclusions and Perspectives **111**
6.1 Conclusions 111
6.2 Perspectives 111

Bibliography **127**

Acknowledge **129**

Chapter 1

Introduction

Multifunctional materials that combine multiple physical properties have always generating a strong interest. Among them, multiferroic materials, that exhibit at least magnetic and polar orders cause an increasing research activity over the last few years due to both their diverse properties and their potential use in new type of magnetoelectric device applications (new high-density magnetic memories, spintronics, ...). Indeed, multiferroics are at the intersection of magnetic materials (with the possibility to have colossal magnetoresistance, magnetocapacitance, superconductivity effect, ...) and polar materials (with the possibility to have giant piezoelectricity, huge dielectric constant, ...).

Nevertheless, nowadays only a limited number of multiferroic materials have been discovered although all the possibilities offered. Indeed, the main inverstigations are done on the prototype multiferroic $BiFeO_3$ compound that crystallizes in the perovskite ABO_3 structure. It is worth noting that this perovskite structure is of huge interest in the context as one may choose different A and B cations in order to combine magnetic and polar properties. Therefore by playing on A/B i. e. magnetic / polar components, it is possible to modify the global physical properties of the multiferroic and thus to acquire a better understanding of the magnetic / polar coupling which in turn will guide synthesis of novel and greatly improved materials.

In this Chapter, the related concepts are introduced and the relationship between structure and property is highly emphasized.

1.1 Perovskite

The mineral perovskite ($CaTiO_3$) was firstly discovered and named by Gustav Rose in 1839. Now, many compounds of ABO_3 composition are named perovskite. A / B represents a cation or mixture with different cations or/and vacancies, O represents O^{2-}. The function properties of perovskite oxides vary depending on composition and structure.

1.1.1 The prototype perovskite

In the opinion of symmetry, the cubic $Pm\overline{3}m$ space group is the highest symmetry of perovskite. The cations occupy 1a or 1b positions and the oxygens occupy 3c or 3d positions, the two possibilities of occupation come from two different views of the unit cell by shifting origin to $(\frac{1}{2}\frac{1}{2}\frac{1}{2})$ (see fig. 1.1). The first view (fig.1.1(a)) is preferred because it highlights octahedron. We also use such kind of describing. The structure is always taken as a reference to understand structural deformation related properties. The cubic prototype structure is always expected at high temperature for all perovskites, the cubic similar structure is expected at high pressure. In fact, incipient ferroelectric $SrTiO_3$ is a cubic prototype at room temperature.

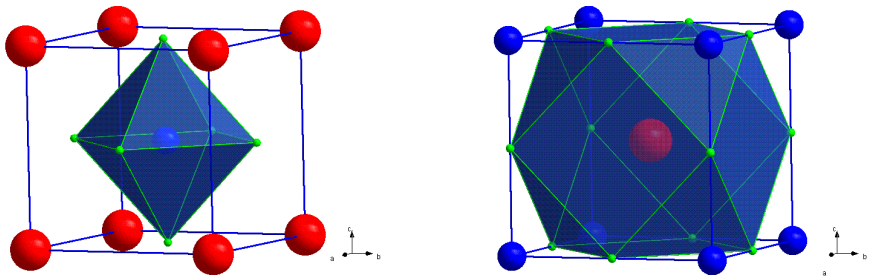

(a) BO_6 octahedral (b) AO_{12} tetrakaidecahedron

Figure 1.1 *Two different views of the unit cell of the ABO_3 cubic perovskite structure: (a) The B ion (blue) is at the center with 6 oxygen (green) first neighbors. (b) The A ion (red) is at the center with 12 oxygen first neighbors*

1.1.2 The deformation perovskite

Many function properties are directly related to deformation of perovskite. The deformation was first studied by H. D. Megaw [1] [2], A. M. Glazer [3] [4] and else. It can be classified into three types:

1. Cation Displacement,
2. Octahedron Distortion,
3. Anion Octahedron Tilt.

Cation displacement is found in many compounds, especially in ferroelectric materials. Octahedron distortion occurs in magnetic perovskites. The octahedrons of prototype perovskite are regularly arranged as shown in fig. 1.2. Tilt is a more complex deformation which reflects the rotation of neighbouring octahedrons.

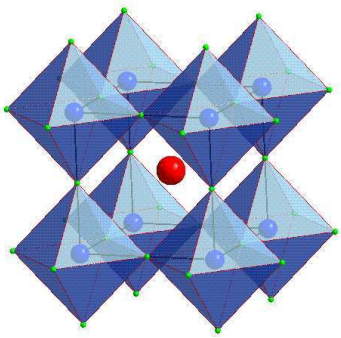

Figure 1.2 *Octahedral framework of cubic perovskite*

A standard notation was developed by Glazer to describe octahedral tilt in perovskite [3]. The notation describes a tilt system by rotations of BO6 octahedron about any of three orthogonal cartesian axes, which are coincident with the three axes of the aristotype cubic unit cell. The notation specifies the magnitude and phase of the octahedral rotations. The letters in Glazer notation indicate the magnitude of the rotation about a given axis, e.g., the letters a, b, and c imply unequal tilts about the x, y, and z axes. A superscript is used to denote the phase of the octahedral tilting in neighboring layers. A positive superscript would denote the neighboring octahedral tilt in the same direction (in-phase) and a negative superscript implies the tilts of neighboring octahedral tilt in the opposite direction (out of phase). A superscript of 0 signifies no tilt about that axis. The tilt of octahedron reduces the symmetry of prototype perovskite.

Glazer derived 23 different tilt systems, which lead to 15 different space groups. There are 15 tilt systems that occur in real crystals, each with a different space group. The tilt can be modeled by software Megaw[1] and even can be predicted by software SPuDS [5].

The classic formula describing the deformation of perovskite was proposed by Goldschmidt [6]:

$$t = \frac{r_A + r_O}{(r_B + r_O)\sqrt{2}} \tag{1.1}$$

Here, r_A, r_B and r_O are the radii of A, B and O ions which were summarized by Shannon [7]. Considering the ionic radii change in different chemical environments, the revised formula is:

$$t = \frac{d_{A_O}}{(d_{B_O})\sqrt{2}} \tag{1.2}$$

Here, d_{A_O} and d_{B_O} are the distances between cations (A or B) and anion (O). The distance can be predicted by Bond Valence Wizard [8] or structure refinement which will be discussed in next chapter. t factor equals to 1 for ideal perovskite structure. It is a sign of crystal lattice types. According to H. L. Yakel [9], 0.8 < t < 0.9 is orthorhombic, 0.9 < t < 0.97 is cubic, 0.97 < t < 1.02 is tetragonal. However, according to Y. Tokura [10], t < 0.96 is orthorhombic, 0.96 < t < 1 is rhombohedral.

Many ferroelectric compounds crystallizes in a rhombohedral structure. In some publications, the names of hexagonal, trigonal and rhombohedral are misused. In fact, the hexagonal, trigonal and rhombohedral are careful defined in INTERNATIONAL TABLES FOR CRYSTALLOGRAPHY [11]. Hexagonal crystal family is separated into trigonal and hexagonal crystal system. Seven space groups (R$\bar{3}$, R32, R3m, R3c, R$\bar{3}$m and R$\bar{3}$c)in trigonal have two different coordinate systems: 1. a=b=c and $\alpha = \beta = \gamma$ (rhombohedral axes, primitive cell); 2. $a = b, \alpha = \beta = 90^\circ, \gamma = 120^\circ$ (hexagonal axes, triple obverse cell). This kind of cells are called rhombohedral. The polar R3m and R3c are two model ferroelectric structures. In R3m, cation shifts along [111] direction of cubic prototype cell. R$\bar{3}$c combines cations shifting along [111] direction and octahedral rotations along [111] direction ($a^-a^-a^-$ tilts). For R3m, the primitive cell has one formula unit ($a \cong a_{p.c.}$) but conventional hexagonal cell has three formula units ($a \cong \sqrt{2}a_{p.c.}, b \cong \sqrt{2}a_{p.c.}, c \cong \sqrt{3}a_{p.c.}$). For R3c, the primitive cell has two formula units ($a \cong \sqrt{2}a_{p.c.}, \alpha_{rh} \cong 60^\circ$) but conventional hexagonal ($a \cong \sqrt{2}a_{p.c.}, b \cong \sqrt{2}a_{p.c.}, c \cong 2\sqrt{3}a_{p.c.}$) has six formula units. Here $a_{p.c.}$ is pseudo-cubic (p.c.) lattice parameter.

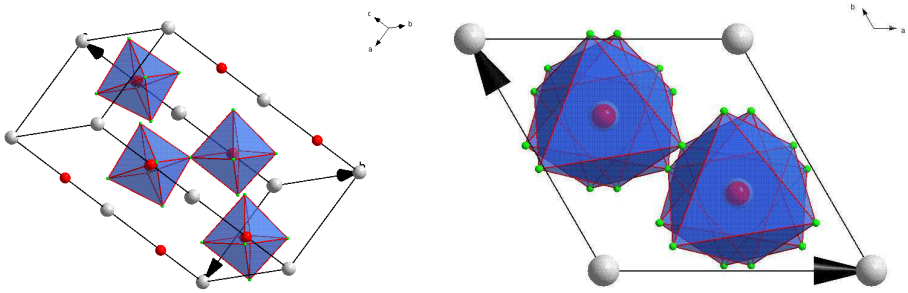

(a) p.c.100 (b) h.001

Figure 1.3 *Projections of R$\bar{3}$c space group along pseudo-cubic [100] and hexagonal [001] direction. White, red and green balls represent A, B and O ions*

Many magnetic perovskites crystallize in an orthorhombic structure (Pbnm, space group #62) which is also named $GdFeO_3$-type structure. It is a $a^-a^-c^+$ tilts structure which is favored for small tolerance factor (t < 0.975). It maximizes coulombic attractions and minimizes repulsive ion-ion interactions [12]. The tilts can be clear seen along [110] direction (fig. 1.4).

[1] http://www.amg122.com/programs/megaw.htm

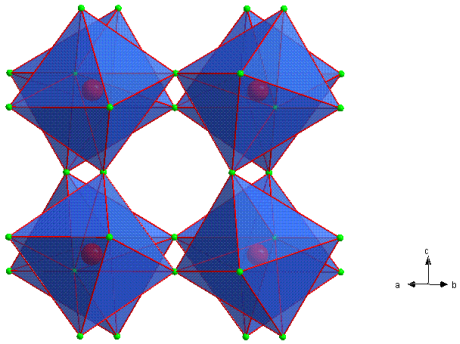

Figure 1.4 *Projection of $GdFeO_3$ type tilts along [110] direction*

1.2 Ferroelectricity

Ferroelectricity is a property of certain materials in which they possess a spontaneous electric polarization that can be reversed by the application of an external electric field. At null electric field, the material process two or more discrete stable or metastable states with different nonzero electric polarization, but any two of states are identical in crystal structure. With the electric field, the polarization must be possible to switch between these states [13] [14]. The ferroelectricity is a subgroup of piezoelectricity which is a subgroup pyroelectricity. Thus, ferroelectric (FE) material has both pyroelectric and piezoelectric properties. The FE can be directly proved by FE hysteresis loop. The normal dielectric or the paraelectric (PE) state of FE has linear relationship between polarization and electric field (fig. 1.5(a)) but the FE state has nonlinear hysteresis behavior (fig. 1.5(b)). Importantly, the polarization (so-called spontaneous polarization) is not zero in the absent of an electric field and there are two polarization states.

In contrast to FE, AFE are those in which some ferroic entities are spontaneously polarized along one direction while the adjacent ferroic groups are polarized in the opposite direction. Therefore, there is no net spontaneous polarization contrary to FE [15].

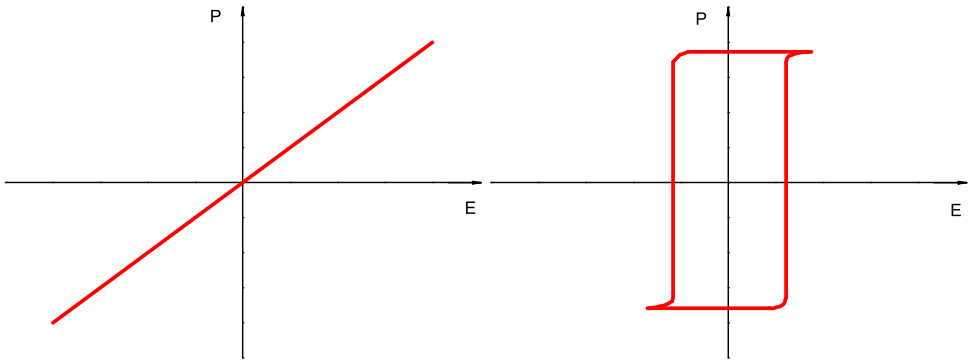

(a) PE state (b) FE state

Figure 1.5 *P-E relationships*

1.2.1 Broken symmetry

The symmetry broken is required for all FE whatever classic FE, relaxor or geometrically driven FE. For example, the stucture of classic FE $BaTiO_3$ [16] [17] [18] [19] is centosymmetric $Pm\overline{3}m$ above ∼393K, it transforms to tetrogonal P4mm, orthorhombic Amm2 and rhombohedral R3m with Ti^{4+} shifting along <001>, <110> and <111> direction below ∼393K, ∼273K and ∼173K correspondingly.

The centrosymmetry is broken accompanying phase transition.

1.2.2 Second-order Jahn-Teller Effect

In ionic crystal, long-range Coulomb forces favor FE state but short-range repulsions prefer nonpolar state [20]. The centrosymmetry broken of FE was explained by second-order Jahn-Teller (J-T) effect in coordination chemistry [21]. In the theory, ground energy of electronic was expanded until second order of distortion. Under two conditions: (1) There exist hight occupied (ground state, like $2p$) and lowest unoccupied (excited state, like d^0) molecular orbitals, energy difference between two is very small, (2) Comparing ground state, excited state has a different centrosymmetric, the distortion occurs. For example in $BaTiO_3$, the centrosymmetry octahedron d^0 B cation may displace tetragonally along C_4 axis, orthorhombically along C_2 axis and rhombohedrally along C_3 axis, mixing with oxygen p orbitals, the prerequisite condition of FE is satisfied (fig.1.6). The theory was firstly proposed for B site driving FE. In fact, A site driving FE which is also called the lone pair (ns^2) FE, i.e. $PbTiO_3$, is also driven by second order J-T effect.

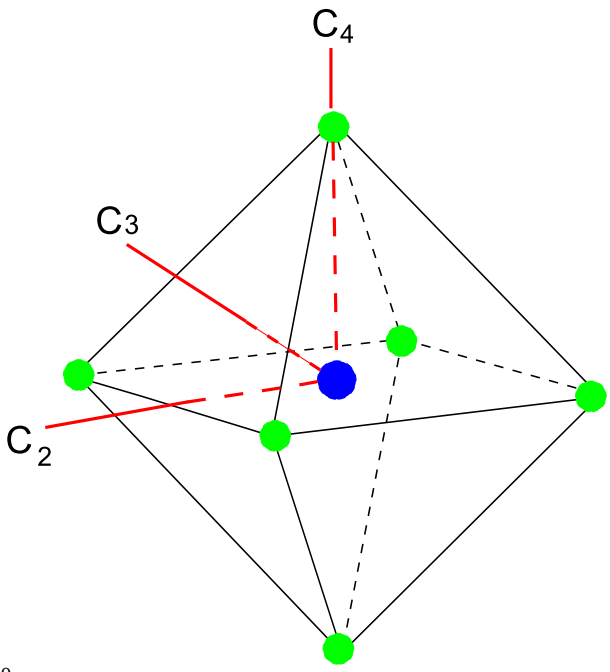

Figure 1.6 *d^0 B site ion (blue) shifts in a octahedron along different directions*

1.2.3 Landau theory of phase transitions

Stability of FE is explained by Second-order J-T effect. Phase transition of FE is explained by phenomenal landau phase transition theory. In the theory, free energy is written as a function of polarization:

$$F = \frac{1}{2}aP^2 + \frac{1}{4}bP^4 + \frac{1}{6}cP^6 - EP \tag{1.3}$$

The equilibrium configuration is determined by finding the minima of F:

$$\frac{\partial F}{\partial P} = 0 \tag{1.4}$$

so:

$$E = aP + bP^3 + cP^5 \tag{1.5}$$

Considering the PE state equilibrium conditions ($\frac{\partial F}{\partial E}$ = 0, P = 0), the parameter a is directly related to dielectric susceptibility:

$$\chi = \frac{\partial P}{\partial E} = \frac{1}{a} \tag{1.6}$$

In fact, a is the function of temperature by a = a_0 (T - T_0). This is assumption of Landau-Devonshire theory, also, it is Curie-Weiss law which is observed in FE material.

Including the linear temperature dependence of a, the free energy is re-expressed by:

$$F = \frac{1}{2}a_0(T - T_0)P^2 + \frac{1}{4}bP^4 + \frac{1}{6}cP^6 - EP \tag{1.7}$$

If b > 0, retaining the lowest-order terms in the formula 1.5 and E = 0, the polarization is a function of temperature:

$$P = [\frac{a_0}{b}(T_0 - T)]^{\frac{1}{2}} \tag{1.8}$$

The polarization as a function of temperature is plotted in fig.1.8(a). The spontaneous polarization will continue to increase if temperature decreases from T_0. This is second order (continuous) phase transition which was was discussed by C. Haas [22]. The free energy as a function of temperature is plotted in fig.1.7:

1. T $\geq$ T_0, P = 0 is stable state.
2. T < T_0, P = $\pm$ P_s are stable states.

T_0 is the phase transition temperature.

If b < 0, the high-order polarization in formula 1.5 should not be neglected. By adding new condition F = 0, the critical temperature T_c is found :

$$T_c = T_0 + \frac{3b^2}{16a_0c} \tag{1.9}$$

with polarization P = $\sqrt{\frac{3|b|}{4c}}$ and three local energy minima (-P_S, 0 P_S) coexist at T_c. In fact, three energy minima can exist between T_0 and T_1 = T_0 + $\frac{b^2}{4a_0c}$:

1. T > T_1, P = 0 is stable state.
2. T $\in$ [T_c, T_1], P = 0 is stable state, but P = $\pm$ P_s can exist.
3. T = T_C, P = 0 and P = $\pm$ P_s both are stable state.
4. T $\in$ [T_0, T_c], P = $\pm$ P_s is stable state, but P = P_0 can exist.
5. T < T_0, P = P_s is stable state.

The squared polarization is expressed by:

$$P^2 = \frac{|b|}{2c}[1 + \sqrt{1 - \frac{4a_0c(T - T_0)}{b^2}}] \tag{1.10}$$

The polarization as a function of temperature is plotted in fig.1.8(b). The polarization jumps at T_0, phase transition is discontinuous and thermal hysteresis is obvious for first order phase transition.

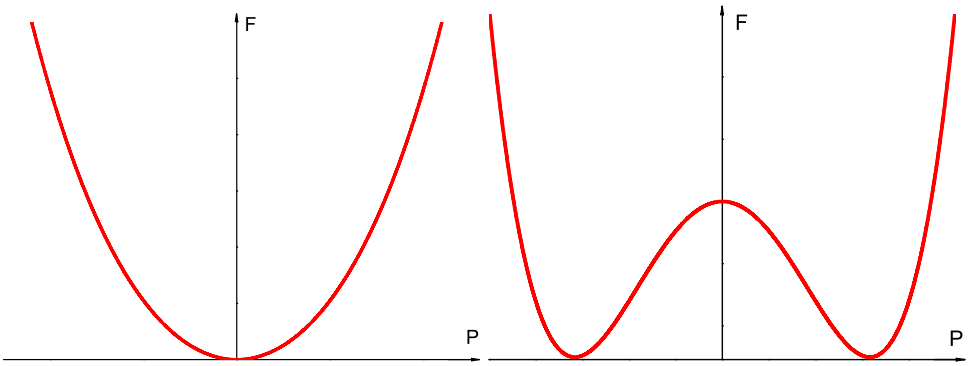

(a) PE state (b) FE state

Figure 1.7 *Free energy versus polarization*

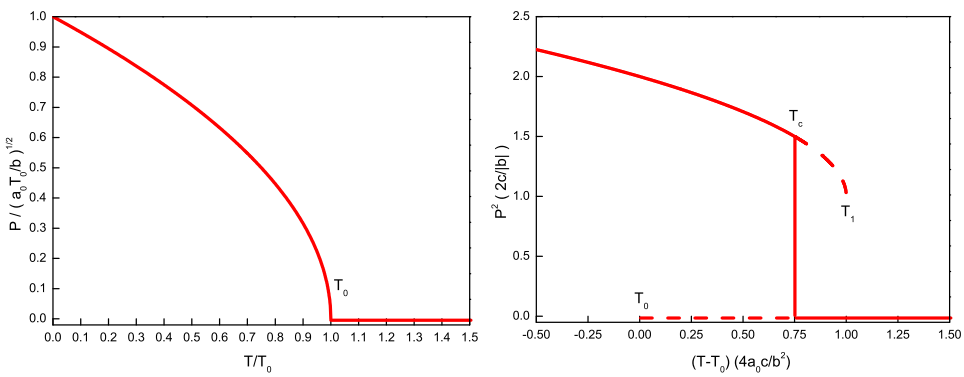

(a) Second order phase transition (b) First order phase transition

Figure 1.8 *Polarization versus temperature*

1.2.4 Soft mode theory

Soft mode theory was developed by lattice dynamic study on FE [23] [24] [25]. The lowest-frequency polar-phonon mode becomes softer during cooling, finally goes to zero frequency at T_C. The dielectric permittivity peak is successful explained by soft mode theory. After R. A. Cowley [26], BSW notation [27] is prevalent used in describing dynamic properties of perovskite structure. The dynamic matrix calculation [26], various experiment methods (neutron scattering, infrared and Raman spectroscopy ...) [28] and first principle calculation [29] [30] are used to study the instability of FE. FE related Γ point instability appears in FE $BaTiO_3$ and $PbTiO_3$. It is primarily B-ion character in $BaTiO_3$ but A-ion character in $PbTiO_3$. The R point instability appears in $PbZrO_3$ which is antiferroelectric (AFE) with oxygen octahedron rotation.

1.2.5 Curie-Weiss law

Curie-Weiss law is one of classic behavior of FE. The dielectric permittivity will divergence at T_0 for second order phase transition and jump for first order phase transition at T_C. At PE phase, the dielectric permittivity obeys C-W law:

$$\varepsilon' = \frac{C}{T - T_0} \tag{1.11}$$

Here, C and T_0 are the Curie constant and the Curie temperature respectively. For second order phase transition, $T_0 = T_C$, for first order phase transition, $T_0 < T_C$. As we already described, this is also the assumption of Landu-Devonshire theory.

1.3 Relaxor

The study of relaxor is strongly related to FE. Different with FE, relaxor displays [31] [32]:

1. a strong frequency dependence of the dielectric permittivity,
2. a broad dielectric anomaly around the temperature of the maximum dielectric permittivity, T_m, for a given frequency,
3. no structural macroscopic phase transition across T_m.

It is generally accepted that the strong dielectric relaxation around T_m needs two crucial ingredients [32]. The first one concerns the quenched random electric [33] and strain fields (RFs) arising from chemical disorder and the difference in ionic charges and radii between the different kinds of B cations (in fact, the cations on the B site of the perovskite structure typically deviate from a perfectly random distribution by possessing a short range order at a nanoscale through chemically ordered regions). The second ingredient concerns the dynamical polar nanoregions (PNRs), which nucleate several hundred degrees above T_m at the Burns temperature, T_B [34].

1.3.1 Diffuse phase transitions

In relaxor, C-W law was observed only at temperature much higher than T_m, typical near T_B in $PbMg_{1/3}Nb_{2/3}O_3$ [35].

For describing the diffuse phase transition (DFT) character in relaxor, Smolenskii [36] hypothesized the composition fluctuation model. The total number of relaxators which contribute to the dielectric response in the vicinity of the permittivity peak is temperature dependent and the temperature

distribution of this number is given by a Gaussian function with a mean value T_0 and a standard deviation δ:

$$\frac{\varepsilon - \varepsilon_\infty}{\varepsilon_0} = exp[-\frac{(T - T_0)^2}{2\delta^2}] \tag{1.12}$$

Here, ε_∞ is the electronic and ionic permittivity. Neglecting the value of ε_∞ and assuming $T_0 = T_m$:

$$\varepsilon = \frac{\varepsilon_m}{1 + \frac{(T - T_m)^2}{2\delta^2}} \tag{1.13}$$

This quadratic law is valid at T > T_m for complete DFT materials. More general formula describing DFT follows powder law [37] [38]:

$$\frac{\varepsilon_m}{\varepsilon} = 1 + \frac{(T - T_m)^\gamma}{2\delta_m^2} \qquad (1 \leq \gamma \leq 2) \tag{1.14}$$

Here, γ corresponds to degree of relaxation, in a normal FE γ =1, in a typical relaxor γ = 2. δ_m is the broadening parameter. ε_m is the dielectric permittivity maximum at temperature T_m.

Considering the reasonable unit of σ and dielectric permittivity around T_m , the powder law can also be expressed as [39] [40]:

$$\frac{\varepsilon_m}{\varepsilon} = 1 + (\frac{(T - T_m)}{\Delta})^\xi \tag{1.15}$$

Here, Δ is similar with σ and ξ is similar with γ. According the study of later [41] [42], the formula 1.14 and 1.15 have the same fitting results.

1.3.2 Vogel-Fulcher relationship

Empirically, Vogel-Fulcher (V-F) relation is used to describe dynamic behavior of relaxor [43] [44]:

$$f = f_0 exp[-\frac{E_a}{k_B(T_m - T_f)}] \tag{1.16}$$

Here, f is the experiment frequency. T_m is the temperature of maximum dielectric permittivity. E_a is the polarization fluctuation activation energy of an isolated cluster. k_B is the Boltzmann constant. T_f is the freezing temperature at which the dynamic of PNRs slow down and freezing out. By defining the relaxation time τ = 1/ω =1/2πf, it is obvious that the characteristic relaxation time diverges at the freezing temperature T_f as f→0.

Recently, another character temperature named T* was found in lead-based relaxor FE [32] which corresponds to a nanoscale phase transition associated with random fields.

The relation between also these character temperatures is $T_B > T* > T_m > T_f > 0$. During cooling, the dynamic PNRs nucleate at the Burns temperature T_B, the static PNRs appear at the temperature T*, slow down and freeze out at the freezing temperature T_f.

1.3.3 Local and long range polar order

In perovskite relaxor, one of common character is that the same symmetry position is occupied by disorder non-isovalent ions, no long range order is observed. One of fantastic properties of relaxor perovskite is quite different structure phase transitions. For example, PMN ($PbMg_{1/3}Nb_{2/3}O_3$) remains the average cubic symmetry whatever the temperature, however, PZN ($PbZn_{1/3}Nb_{2/3}O_3$) displays rhombohedral symmetry below 390K (T_m =405K).

The origin of polar in relaxor was revealed after the study on $PbMg_{0.3}Nb_{0.6}Ti_{0.1}O_3$ [45]. The polar comes from Pb^{2+} in a sophisticated method. The composition of cooperative shifting along the [111]

polar direction plus Pb^{2+} short-range shifting along [$\bar{1}$ $\bar{1}$2] direction gives the local position of Pb^{2+}: slight shifting deviating one of <100> direction about 13° (see fig.1.9).

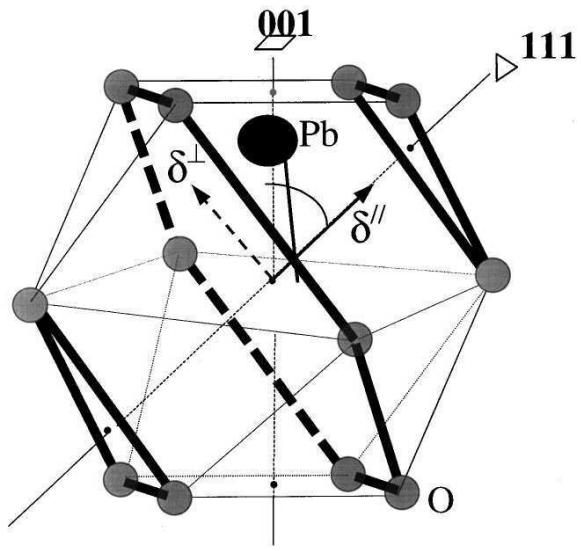

Figure 1.9 *Pb^{2+} shifts in an oxygen cuboctahedron [45]*

1.4 Magnetism

The physical quantities describing magnetic materials are comparable with FE materials. Magnetization ($\vec{M}$) is the net magnetic moments in unit volume. Magnetic induction ($\vec{B}$) is given by:

$$\vec{B} = \mu_0(\vec{H} + \vec{M}) = \mu_0[\vec{H} + (\mu_r - 1)\vec{H}] = \mu_0\mu_r\vec{H} \tag{1.17}$$

Here, $\vec{H}$ is the magnetic field, $\mu_r - 1$ is the magnetic susceptibility (χ_m).

Similar to FE, ferromagnetic (FM) is a material has a spontaneous magnetic moment (parallel each other) even in zero applied magnetic field.

1.4.1 Magnetic moment

The magnetic property of an atom is decided by the electron configuration. The magnetic moments of an electron is separated into orbital angular momentum magnetic moment:

$$\vec{m}_z = -\mu_B l_z \tag{1.18}$$

and spin magnetic moment:

$$\vec{m}_{s_z} = -g_e\mu_B s_z \tag{1.19}$$

Here, $\mu_B = e\hbar/2m_e$, is Bohr magneton, $g_e = 2(1 + e^2/4\pi\varepsilon_0 hc) = 2.0023$, l_z is the magnetic quantum number, $s_z = \pm\frac{1}{2}$ is spin quantum number.

The total magnetic moment is related to the total angular momentum quantum number (**J**):

$$\vec{m}_z = -g\mu_B J_z \tag{1.20}$$

Here, g is called the landé splitting factor which is given by

$$g = \frac{3}{2} + \frac{S(S+1) - L(L+1)}{2J(J+1)} \tag{1.21}$$

J is decided by the couplings of orbit-orbit, orbit-spin and spin-spin. For light atoms, as the orbit-spin interaction is weak, the coupling is simple to Russell-Saunders coupling and is specified by Hund's rules. Thus, it is possible to compare the magnetic moments of ions between experiment and calculated values (the magnitude of total magnetic moment is m = $g\mu_B\sqrt{J(J+1)}$).

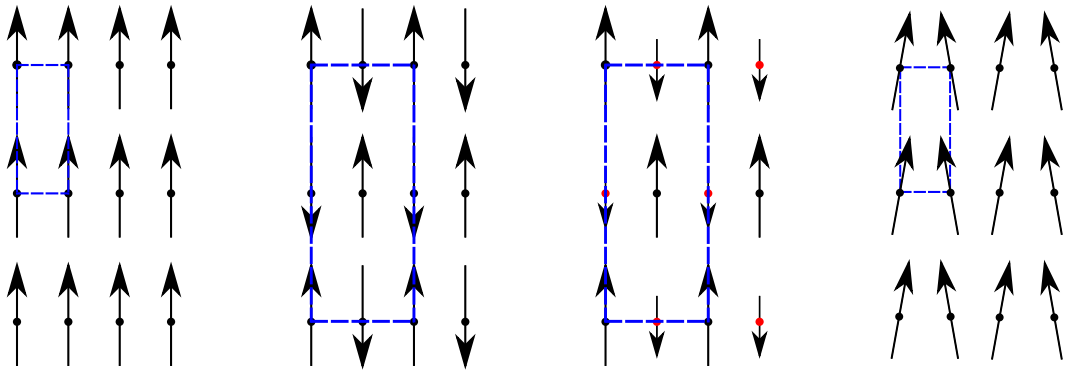

(a) FM (b) AFM (c) FIM (d) Canted

Figure 1.10 *Some simple magnetic orders*

If **J** equals zero, the material displays diamagnetic behavior which is explained by classic electromagnetic theory. If **J** is not zero, ferromagnetic (FM), antiferromagnetic (AFM), ferrimagnet (FIM) and more complicated magnetic order structures like helical, canted, spiral, umbrella and etc. can exist in solid. The simple magnetic orders are shown in fig 1.10.

All these magnetic structures are instable at high temperature because of thermal agitation effect. The material shows paramagnetic(PM) behavior at high temperature. The stability of magnetic structure is related to exchange interaction.

1.4.2 Exchange interaction

According Pauli Exclusion Principle, there is zero probability of finding two electrons of the same spins at the same point in space, but opposite spins can be find at the same point. So the average separation of electrons r will be larger for parallel spins than anti-parallel spins. The inter-electron coulomb repulsion energy ($e^2/4\pi\varepsilon_0 r$) is smaller for parallel than anti-parallel spins. This effect is referred to as the exchange interaction. For the whole solid, the exchange energy is expressed as:

$$H = \sum_i \sum_{i \neq j} J_{ij} \cdot \vec{S}_i \cdot \vec{S}_j \tag{1.22}$$

The coupling constant J signs magnetic order: positive J is FM, negative J is AFM. Very short distance supports AFM, then FM, the long distance supports PM because the exchange interaction is a short-range interaction.

1.4.3 Double exchange interaction

The metallic FM order can be explained by double exchange interaction [46] [47], i.e. in manganites. Because of the existence disordered mixture of Mn^{3+} and Mn^{4+}, the electron hops from Mn^{3+} to O^{2-}, from O^{2-} to Mn^{4+} depending on the alignment of local spins of Mn^{3+} and Mn^{4+}. If the spins of Mn^{3+} and Mn^{4+} are parallel, e_g electron of Mn^{3+} hops to the vacated spin site of the oxygen which was leaved

by electron hoping to Mn^{4+}. If the spins of Mn^{3+} and Mn^{4+} are anti-parallel, the e_g spin electron can not hop to the oxygen because its spin is parallel to the spin remained in the oxygen. According this mechanism, the compound of FM has itinerant electron and behaves like conductor.

1.4.4 Superexchange interaction

Superexchange was proposed by Hendrik Kramers in 1934 [48] and developed by Phillip Anderson [49] [50], John Bannister Goodenough [51] and Junjiro Kanamori [52] in 1950's-1960's. The insulator FM and AFM orders are explained by superexchange depending on orbital configurations. Two magnetic ions (B with part occupied e_g orbitals or B' with empty e_g orbitals) couple through an intermediary non-magnetic ion (e. g. O^{2-}). Depending on magnetic ions (B or B') and orbital couping orientations (parallel or orthogonal), there are 5 cases in superexchange interaction (fig. 1.11): (a) strong AFM, (b) weak AFM, (c) weak FM, (d) FM, (e) AFM.

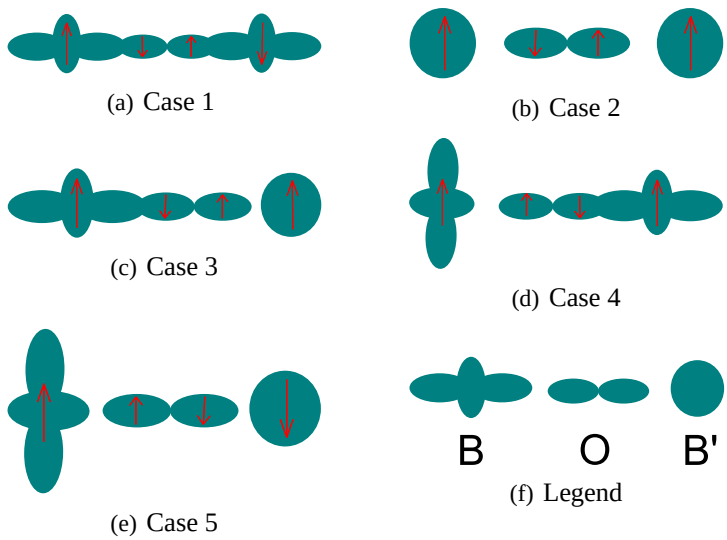

(a) Case 1 (b) Case 2 (c) Case 3 (d) Case 4 (e) Case 5 (f) Legend

Figure 1.11 *Different magnetic orders because of superexchange interaction [53] [54]*

Superexchange effect is successful in explaining the AFM order in many insulator perovskites. Similar to AFE, the magnetic moments exist in AFM but the net magnetic moment in one magnetic cell is zero because every magnetic moment has a anti-parallel magnetic moment neighbor. In perovskite compounds, different AFM orders below magnetic phase transition temperature T_N were named after E. O. Wollan and W. C. Koehler who studied perovskite magnetic orders by neutron diffraction [55] (see fig.1.12).

In simple perovskite $BiFeO_3$(BFO), disordered complex perovskite $PbFe_{1/2}Nb_{1/2}O_3$ (PFN), $PbFe_{1/2}Ta_{1/2}O_3$ (PFT) and $PbFe_{2/3}W_{1/3}O_3$ (PFW), G-type AFM order is related to Fe-O-Fe superexchange effect [56] [57] [58] [59] [60]. The AFM phase transition point (T_N) may relate to the quantity of Fe^{3+} in the compound. T_N of PFN, PFT, PFW and BFO are 143K [61], 133K-180K [62], 350K [63], and 643K respectively. Recently, the Fe-Pb-Fe also is expected to explain the enhanced Néel temperature [64] [65].

1.4.5 Jahn-Teller effect

As we already described, except cation displacement and tile, distortion is a another type deformation in perovskite, especially in magnetic perovskite materials.

If odd number of electrons occupy the e_g orbitals (i.e. d^9, low-spin d^7 and high-spin d^4) in octahedron center position, the pronounced J-T distortion occurs. According crystal field theory, in octahedral environment, the five d orbits split into lower energy t_{2g} states (d_{yz}, d_{xz}, d_{xy}) which point

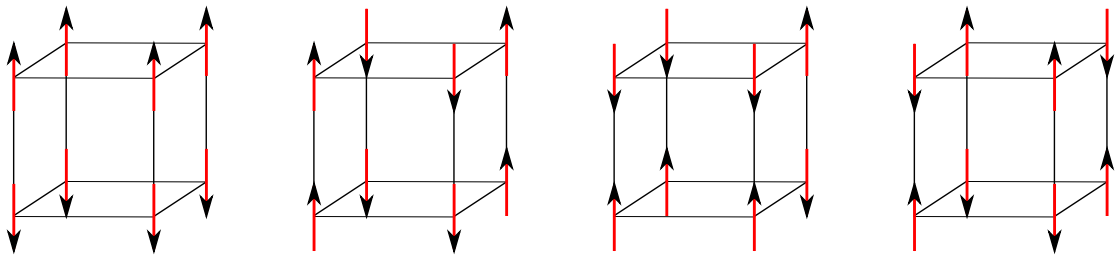

(a) A (b) C (c) E (d) G

Figure 1.12 *Different AFM orders in perovskite [55]*

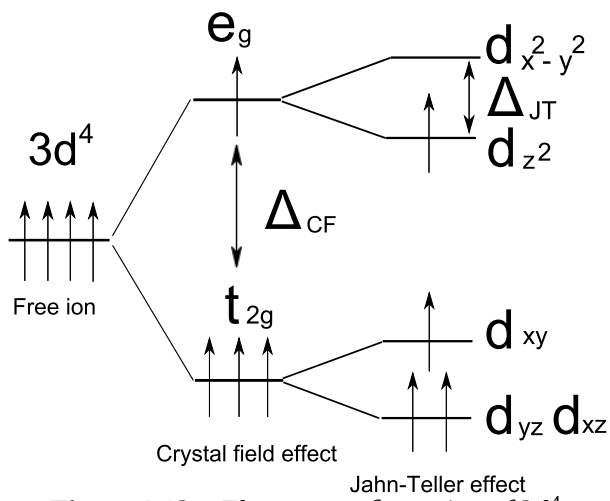

Figure 1.13 *Electron configuration of* $3d^4$

between oxygen ions and higher energy e_g states (d_{z^2}, $d_{x^2-y^2}$) which point toward six oxygen ions. Using group theory, H. A. Jahn and E. Teller proved that these degenerate electronic ground states are instable [66]. Considering the e_g state, if octahedron is elongated along the z-axis, the d_{z^2} is less overlapped with apical oxygen orbitals, so d_{z^2} becomes a lower energy level than $d_{x^2-y^2}$.

J-T effect in $3d^4$ configuration is shown in fig 1.13. There are two type of distortions [52](fig.1.14): the orthorhombic normal mode Q_2 (the normal coordination equals $1/\sqrt{2}(x_1 - x_4 - y_2 + y_5)$) shortens two 180° M-O bonds elongates another two M-O bonds in the same plane, the tetragonal normal mode Q_3 (the normal coordination equals $1/\sqrt{6}(2z_3 - 2z_6 - x_1 + x_4 - y_2 + y_5)$) shortens all the M-O bonds in the same plane but elongates two perpendicular M-O bonds. As the undistorted structure is centrosymmetric, the inversion center is preserved after distortions.

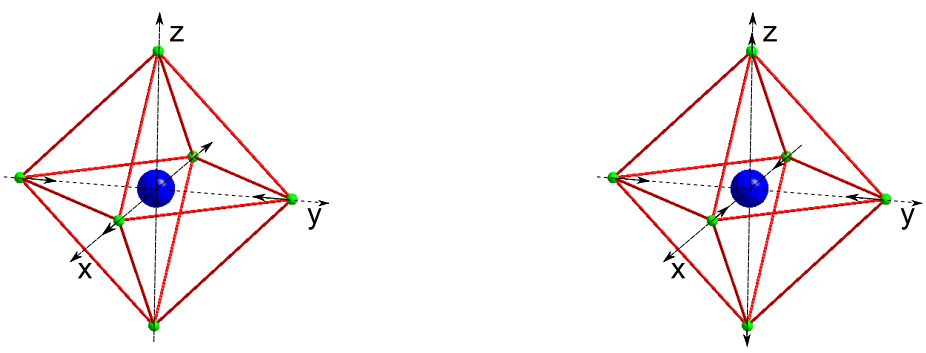

(a) Q_2 (b) Q_3

Figure 1.14 *Two different J-T distortions: normal mode* Q_2 *and* Q_3 *[52]*

1.4.6 Curie Law

In Langevin paramagnetic theory, the magnetization of a material is the competition result of magnetic field and thermal agitation:

$$M = NmL(\frac{\mu_0 mH}{k_B T}) = Nm[coth(\frac{\mu_0 mH}{k_B T}) - \frac{k_B T}{\mu_0 mH}] \tag{1.23}$$

Under huge magnetic field (μ_0 m H » k_B T), M = Nm; under high temperature (μ_0 m H « k_B T), M = $\frac{\mu_0 N m^2 H}{3k_B T}$. When spatial quantization is considered, Langevin function L ($\frac{\mu_0 mH}{k_B T}$) is replaced by Brillouin function $B_J(\frac{Jg\mu_B H}{k_B T})$:

$$M = NgJu_B B_J(\frac{Jg\mu_B H}{k_B T}) = NgJu_B[\frac{2J+1}{2J}coth(\frac{2J+1}{2J}\frac{Jg\mu_B H}{k_B T}) - \frac{1}{2J}coth(\frac{1}{2J}\frac{Jg\mu_B H}{k_B T})] \tag{1.24}$$

The susceptibility becomes:

$$\chi_{PM} = \frac{M}{H} = \mu_0 \frac{Ng^2 J(J+1)\mu_B^2}{3k_B T} = \frac{C}{T} \tag{1.25}$$

This is Curie law for PM, N is the number of atoms per unit volume, k_B is the Boltzmann constant. Curie-Weiss Law for FM is expressed by:

$$\chi_{FM} = \frac{C}{T - T_C} \tag{1.26}$$

Here, $T_C = \gamma\mu_0 \frac{Ng^2 J(J+1)\mu_B^2}{3k_B}$, γ is called the "molecular field" constant. Weiss derived the formula by just adding "molecular field" ($\vec{H}_W = \gamma \vec{M}$) in the formula 1.25. The origin of "molecular field" is the quantum exchange effect.

The similar behavior in AFM and ferrimagnetic was studied by Néel and was called Curie-Neel Law:

$$\chi_{AFM} = \frac{C}{T + T_N} \tag{1.27}$$

$$\frac{1}{\chi_{FI}} = \frac{T + C/\chi_0}{C} - \frac{b}{T - \theta} \tag{1.28}$$

1.5 Spin Glass

Similar to the relationship between FE and relaxor, spin glass is a concept which corresponds to classic magnetic behavior. Spin glass is a magnetic system exhibiting both quenched disorder and frustration. Recently, spin glass behavior was found in many perovskite compounds.

In PFN, glasslike state freezes at 27.6K [67] and is proved by muon spin rotation and neutron scattering [68]. In PFT, magnetic phase transition point was found about 55K which could be related to spin glass behavior [69]. In BFO, spin glass behavior was found in single-crystal [70] and thin film [71]. The phase transition temperature $T_{s.g.}$ is about 30K and weak FM was found below 10K [70]. The magnetic hysteresis loop was found at 2K for PFN [67], below 10K for BFO [70], even room temperature for PFT [69]. All these results seems imply that spin glass state is quite normal for Fe based perovskites. In fact, in PFW-PZT, low temperature magnetic relaxor was also found this year [72].

The weak FM below 9K for PFN and PFT [73], below 20K for PFW [63] was explained by weak long-range superexchange interaction between Fe-O-X-O-Fe (X is related no magnetic ion in the compounds). This is a short-range order at B site. which is similar to spin glass order.

1.6 Multiferroics

1.6.1 Definition

Multiferroics have been formally defined as materials that exhibit more than one primary ferroic order parameter simultaneously. The four basic primary ferroic order parameters are ferromagnetism, ferroelectricity, ferroelasticity [73] and ferrotoroidicity [74]. The definition of schmid emphasizes "the same phase". In fact, the definition can be expanded to include non-primary order parameters, such as antiferromagnetism, ferrimagnetism and antiferroelectricity. If the coupling between electric and magnetic order parameters exists, a multiferroic material becomes a magnetoelectric material. But a magnetoelectric (or a multiferroic) material does not necessary to be a multiferroic (or a magnetoelectric) material [75] (see fig.1.15).

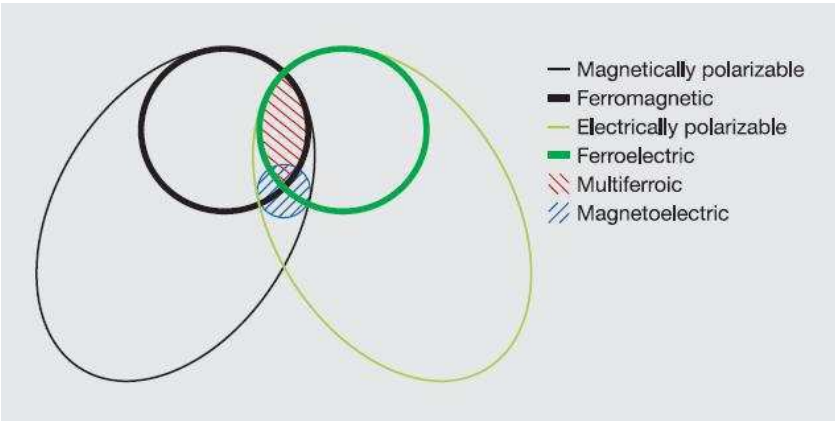

Figure 1.15 *Relationship between multiferroic and magnetoelectric materials [75]*

1.6.2 Recent progress of multiferroics

The history of magnetoelectric multiferroics can be traced back to the 1960s [76]. In the most general sense the field of multiferroics was born from studies of magnetoelectric systems. In recent 10 years, there is a great revival in multiferroics. In 2000, Nicola A. Hill gave an answer about scarcity of ferromagnetic ferroelectric coexistence [77]. In 2003 the large ferroelectric polarization was discovered in epitaxially grown thin films of $BiFeO_3$ [78]. The same year, the strong magnetic and electric coupling was found in orthorhombic $TbMnO_3$ [79] and $TbMn_2O_5$ [80].

The recent studies of multiferroics clearly show the important of collaboration between experiment technology and modeling design. There are many classic review articles discussing the interesting multiferroics [81] [75] [82] [83] [84].

1.6.3 Two approaches

We have already see that J-T effect keeps centrosymmetry of octahedron but second order J-T effect breaks centrosymmetry of octahedron, it becomes difficult to design a B site driven multiferroic. There are two type of methods to avoid the incompatibility in ABO_3 perovskite:

1. A-site participates in electric (or magnetic order) while B-site brings magnetic order (or electric order), i.e. A-site is occupied by the stereochemical activity lone pair cation which provides the ferroelectric but B-site cation carries magnetic moment.

2. Fabrication double perovskite, one of sublattices consists of d^n magnetic cation while the other consists of d^0 ferroelectric cation.

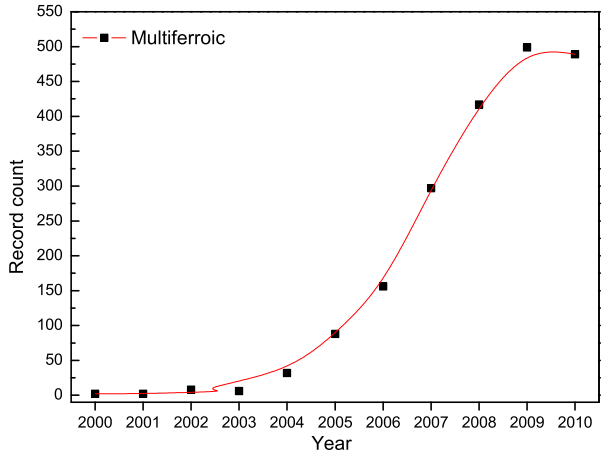

Figure 1.16 *Publications on the topic of multiferroics: data come from ISI web database*

There are also some challenges from technical side. For example, the direct FE proving method needs good insulation property of material, however, magnetic transition metal ions accommodating different valence states can lead to oxygen nonstoichiometry and hopping conductivity.

1.6.4 Magnetoelectric couping

Magnetoelectric (ME) couping describes the influence of a magnetic (electric) field in the polarization (magnetization) of a material. ME effect can be obtained by expanding the free energy in terms of the electric field $\vec{E}$ and magnetic field $\vec{H}$ [81]:

$$F(\vec{E},\vec{H}) = F_0 - P_i^S E_i + M_i^S H_i - \frac{1}{2}\varepsilon_0\varepsilon_{ij}E_iE_j - \frac{1}{2}\mu_0\mu_{ij}H_iH_j - \alpha_{ij}E_iH_j - \frac{1}{2}\beta_{ijk}E_iH_jH_k - \frac{1}{2}\gamma_{ijk}H_iE_jE_k - \cdots \tag{1.29}$$

Here, i, j and k are directions, P^S and M^s are the spontaneous polarization and magnetization, ε and μ are the electric permittivity and magnetic permeability. α expresses the linear magnetoelectric couping, induces polarization (magnetization) by an electric (magnetic) field. β and γ express bilinear magnetoelectric couping. Polarization and magnetization can be gotten by differentiation the equation:

$$P_i(\vec{E},\vec{H}) = -\frac{\partial F}{\partial E_i} = P_i^S + \varepsilon_0\varepsilon_{ij}E_j + \alpha_{ij}H_j + \frac{1}{2}\beta_{ijk}H_jH_k + \cdots \tag{1.30}$$

$$M_i(\vec{E},\vec{H}) = -\frac{\partial F}{\partial H_i} = M_i^S + \mu_0\mu_{ij}H_j + \alpha_{ij}E_i + \frac{1}{2}\gamma_{ijk}E_jE_k + \cdots \tag{1.31}$$

in formula 1.30, setting $P_i^S = 0, E_i = 0$, one obtains

$$P_i(\vec{H}) = \alpha_{ij}H_j + \frac{1}{2}\beta_{ijk}H_jH_k + \cdots \tag{1.32}$$

in formula 1.31, setting $M_i^S = 0, H_i = 0$, one obtains

$$M_i(\vec{E}) = \alpha_{ij}E_i + \frac{1}{2}\gamma_{ijk}E_jE_k + \cdots \tag{1.33}$$

Equations 1.32 and 1.33 express the magnetic (electric) induced polarization (magnetization). The boundary condition of linear ME couping was discussed by W. F. Brown [85]. The couping coefficient was expressed by:

$$\alpha_{ij} < \sqrt{\varepsilon_0\mu_0\varepsilon_{ii}\mu_{jj}} = \frac{\sqrt{\varepsilon_{ii}\mu_{jj}}}{c_0} \tag{1.34}$$

Here, $\mu_0 = 4\pi \times 10^{-7} \frac{V \cdot s}{A \cdot m}$, $\varepsilon_0 = \frac{1}{36\pi \times 10^9} \frac{A \cdot s}{V \cdot m}$, $c_0 = 3 \times 10^8 \frac{m}{s}$.

The formula highlights that large linear ME couping can be gotten by large electric permittivity and magnetic permeability even without ferroic orders.

In multiferroic, magnetoelectric coupling may through directly couping or indirectly couping by strain. The strain effect does not discussed in the free energy equation. In fact, strong coupling is expected if strain is induced. The idea pushes us using antiferroelectric $PbZrO_3$ design novel multiferroic system.

The typical behavior of AFE is electric induced phase transition (see fig.1.17). In a multiferroic system, if the direct magnetoelectric coupling exists, under electric field, a big change of the magnetoelectric coupling is expected because of the rearrangement of polarization (see fig.1.18(a)). If polarization and magnetization are coupled through strain (indirect coupling), because of the induced strain (in the case of $PbZrO_3$, the change of volume is 0.74%) it is also expected a big change of the magnetoelectric coupling (see fig.1.18(b)).

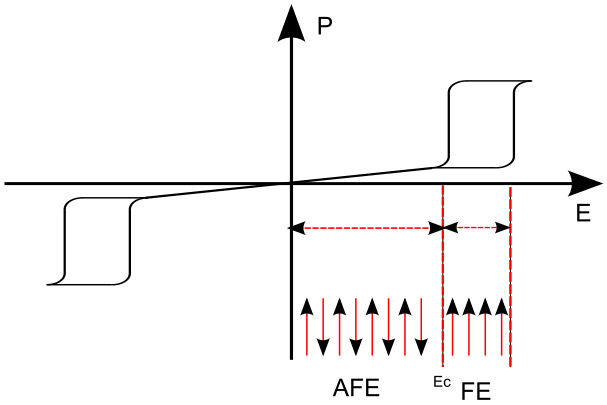

Figure 1.17 *Electric field induced phase transition in AFE*

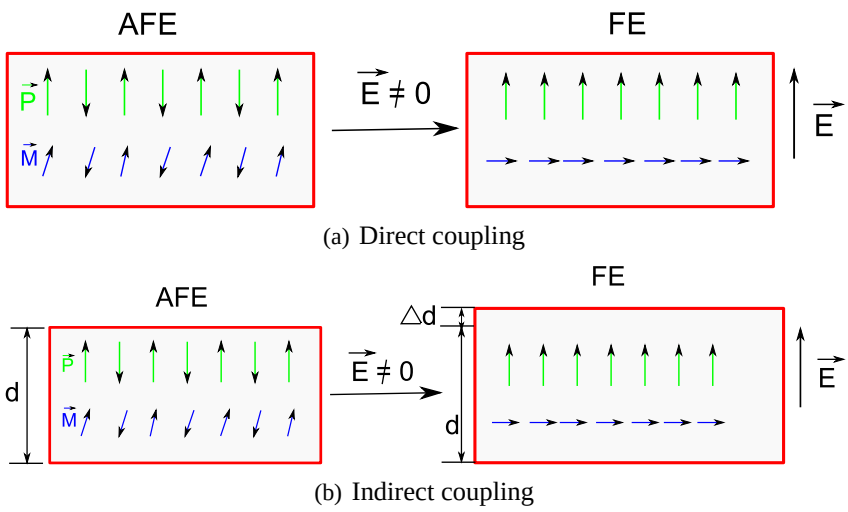

(a) Direct coupling

(b) Indirect coupling

Figure 1.18 *Possibilities of magnetoelectric coupling based on AFE*

1.7 Workplan of the thesis

Voluntarily, we do not dedicated a chapter on the synthesis in order to lighten the manuscript and to go directly to the main goal i.e. the investigation of new solid solutions with coexistence of various

structural, polar and magnetic instabilities. Nevertheless, it is worth mentioning here that the fabrication of homogeneous powders and good quality ceramics is not an easy task especially when dealing with lead and iron compounds at high temperature. It has taken a lot of time with several attempts to get good samples free of any parasitic phase at least using the “eyes” of lab x-ray diffraction technique.

Moreover, in order to simplify the presentation of the thesis work, a short but complete state-of-the-art is made when appropriated.

After this first chapter reminding the main structural and physical properties needed for the understanding of this manuscript, Chapter 2 presents the experimental techniques we used during the thesis work for the measurements of the properties of our materials. A peculiar attention is done for describing the dielectric relaxation and complex conductivity because the compounds under investigation display coexistence of polar states and electronic conduction. Chapter 3 will allow to re-examine the properties of both $PbFe_{2/3}W_{1/3}O_3$, (PFW) and lead zirconate $PbZrO_3$, (PZO) compounds for which a lot of questions are still open. The goal here is to show that these compounds have a lot of instabilities (polar, magnetic and structural). In Chapter 4 the solid solution between PFW and PZO will be investigated in order to look for a material having multiferroic properties close to room temperature. Finally Chapter 5 is an alternative solution in which PZO is doped with magnetic ions. The goal is to create an antiferroelectric with magnetic properties.

Chapter 2

Structure, Electric and Magnetic Characterization

2.1 Crystal structure and diffraction

2.1.1 Diffraction geometry

A crystal or crystalline is a material whose constituent atoms, molecules or ions are periodical repeat in space (1D, 2D, 3D or 3+nD). The periodical structure in 3D is named space group which have 230 types possibilities. The diffraction methods are the main technique to study crystal structure. Neutron diffraction bringing magnetic moment is unique in determination magnetic structure.

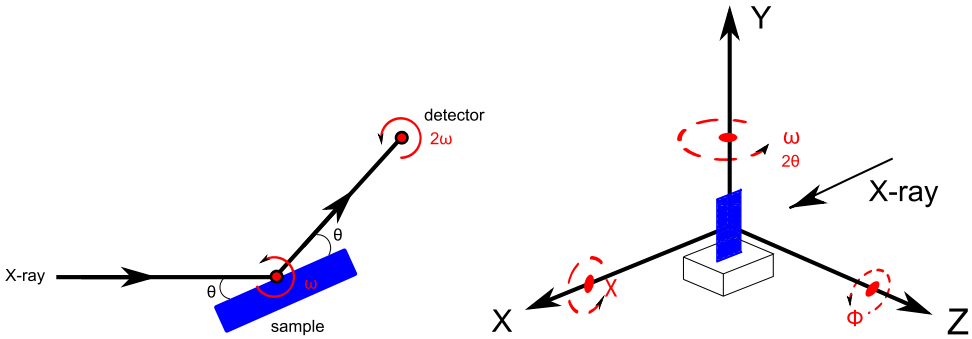

(a) Bragg-brentano geometry

(b) Translation and rotation of diffraction plane sample

Figure 2.1 *Diffraction geometry and adjustment of diffraction plane in SPMS*

The diffraction obeys Bragg's law:

$$n\lambda = 2d_{hkl}sin\theta_{bragg} \tag{2.1}$$

λ is the wavelegth, θ_{bragg} is the diffraction angle, d_{hkl} is the interplanar distance of neighbouring net planes (hkl). For triclinic lattice (lengths of basis vectors a, b and c; interaxial angles α, β and γ respect to $\mathbf{b} \wedge \mathbf{c}, \mathbf{c} \wedge \mathbf{a}$ and $\mathbf{a} \wedge \mathbf{b}$),

d_{hkl} =

$$\sqrt{\frac{(1-cos^2\alpha-cos^2\beta-cos^2\gamma+2cos\alpha cos\beta cos\gamma)}{\frac{h^2}{a^2}sin^2\alpha+\frac{k^2}{b^2}sin^2\beta+\frac{l^2}{c^2}sin^2\gamma+2\frac{hl}{ac}(cos\alpha cos\gamma-cos\beta)+2\frac{hk}{ab}(cos\alpha cos\beta-cos\gamma)+2\frac{kl}{bc}(cos\beta cos\gamma-cos\alpha)}} \tag{2.2}$$

Equation 2.2 is the most normal condition so it can been used for all the lattice by symmetry restrictions.

In bragg-brentano geometry (2.1(a)) (sample moving θ - detector moving 2θ) diffractometer, a diffraction peak will induced if the equation is satisfied except when extinction happens.

In SPMS[1], diffraction plane can been precisely adjusted by translation (X, Y and Z, up to 0.001mm) and rotation (ω, ϕ and χ, up to 0.0001°) sample (2.1(b)) by newport MM4006 motion controller, the same time, large temperature range and strong electric filed environment of sample can be gotten by combining with cryostat (80K - 480K) or four (300K - 800K) and Keithley 50-5000V high voltage supply. The C-like syntax software SPEC [2] is used to control all the system. The software intensité was compiled by GUIBLIN Nicolas for visualization the data. Two type wavelengths, K_α(mixed λ $K_{\alpha 1}$ = 1.5405Å or λ $K_{\alpha 2}$ = 1.5443Å), K_β = 1.3922Å can facile be switched which are generated by Rigaku 18 kW X-ray generator with Cu as anode material.

2.1.2 Diffraction theory

Diffraction is waves elastic diffusion by matter. With the concept of reciprocal lattice, the generalization Bragg's law is expressed as:

$$\vec{K_d} - \vec{K_i} = \vec{H} \tag{2.3}$$

$\vec{K_d}$ $(\frac{1}{\lambda})$ is diffraction vector, $\vec{K_i}$ $(\frac{1}{\lambda})$ is incident vector, $\vec{H}$ $(h\vec{a}* + k\vec{b}* + l\vec{c}*)$ is a reciprocal vector.

The diffraction intensity of X-ray by N unit cells is expressed as:

$$I = N^2 I_0 \frac{e^4}{r^2 m^2 c^4} (\frac{1+cos^2 2\theta}{2}) |F_{hkl}|^2 \tag{2.4}$$

$I_0 \frac{e^4}{r^2 m^2 c^4} (\frac{1+cos^2 2\theta}{2})$ is single electron diffraction intensity (The formula itself proves the diffraction of nucleus is negligible). F_{hkl} is structure factor:

$$F_{hkl} = \sum_{j=1}^{N} f_j exp[2\pi i(hx_j + ky_j + lz_j)] \tag{2.5}$$

N is the atom number in the unit cell; f_j is the scattering factor of atom j; x_j, y_j and z_j are the coordinates of atom j. The dynamic behavior of atoms can be summarized in Debye-Waller factor (B / u factor or the temperature factor). Basically, the structure factor is expressed as:

$$F_{hkl} = \sum_{j=1}^{N} f_j exp[2\pi i(hx_j + ky_j + lz_j) - B\frac{sin^2\theta}{\lambda^2}] \tag{2.6}$$

The temperature factor can be expressed as the function of atom displacement parameter (ADP) by relationship:

$$F_{hkl} = \sum_{j=1}^{N} f_j exp[2\pi i(hx_j + ky_j + lz_j) - 8\pi^2 U_j \frac{sin^2\theta}{\lambda^2}] \tag{2.7}$$

or:

$$F_{hkl} = \sum_{j=1}^{N} f_j exp[2\pi i(hx_j + ky_j + lz_j) - 2\pi^2 (U_{11}^* x^{*2} + U_{22}^* y^{*2} + U_{33}^* z^{*2} + 2U_{12}^* x^* y^* + 2U_{13}^* x^* z^* + 2U_{23}^* y^* z^*)] \tag{2.8}$$

[1] http://www.spms.ecp.fr/equipements.html

[2] http://www.certif.com/

for anisotropic atom displacement.

In fact, many factors influence the intensity of x-ray, like Lorentz polarization($\frac{1}{sin2\theta}$), absorption (I = $I_0 e^{-\mu x}$)...

2.1.3 Neutron diffraction

Neutron is produced as a result of nuclear reaction which is also be used as diffraction source. The special characteristics of neutron diffraction are:

1. Neutron is scattered by nuclear force (X-ray is scattered by electron)
2. The nuclear scattering does not depend on scattering angle, no polarization factor($\frac{1+cos^2 2\theta}{2}$) as in X-ray.
3. Neutron with spin ($\frac{1}{2}$) interacts with magnetic moment, additional diffraction peaks could be induced for magnetic materials.

Neutron is important in magnetic structure decision. In nuclear unit cell, magnetic moment is described by summation of basis vector:

$$S^{\vec{k}} = \sum_{v} C_v \varphi_v \tag{2.9}$$

plus a propagation vector ($\vec{k}$). The basis vector can be gotten by group theory. Softwares like Sarah [86] or Moody [87] can do such kind of calculation. The coefficient can be gotten by magnetic structure refinement. Then magnetic moments can be expanded as a Fourier series:

$$m_j = \sum_{\vec{k}} S_j^{\vec{k}} e^{-2\pi i \vec{k}\vec{t}} \tag{2.10}$$

The $\vec{t}$ is translation($\vec{t} = t_1\vec{a} + t_2\vec{b} + t_3\vec{c}$) vector. The magnetic scattering vector is the summation of the reciprocal lattice vector $\vec{H}$ and the magnetic moment propagation vector $\vec{k}$ ($\vec{h} = \vec{H} + \vec{k}$), magnetic structure factor is given by:

$$\vec{F}_m(\vec{H}+\vec{k}) = p \sum_{j=1}^{n_c} f_j(\vec{H}+\vec{k}) S_{\vec{k}j} exp 2\pi i (\vec{H}+\vec{k}) r_j \tag{2.11}$$

$p = \frac{r_e \gamma}{2} = \frac{e^2 \gamma}{mc^2} = 0.2695$, is used to convert magnetic moments from Bohr magneton μ_B to scattering lengths units $10^{-12} cm$.

2.1.4 Rietveld refinement

The splitting of Bragg diffraction peaks gives the information about lattice type. The splitting regulation of some typical p.c. Bragg peaks are summarized in table 2.1 for perovskite.

Table 2.1 *Splitting p.c. Bragg peaks (200), (220) and (222) for different symmetries*

Lattice type	(200)	(220)	(222)
Cubic	1	1	1
Tetragonal	2	2	1
Rhombohedral	1	2	2
Orthorhombic	3	3	1

Unit cell can be indexed by Crysfire suite [88] which includes many indexing softwares. Many methods were developed to deal with diffraction data. Lebail fitting [89] is a powerful profile matching method. Structure information can be gotten by charge flipping method based software like superflip [90]. The precise crystal structure can be obtained by Rietveld refinement which is first devised by Hugo rietveld [91]. The Rietveld method uses a least squares approach to refine a theoretical profile until it matches with the measured profile. There are many softwares can do such kind of work, like XND [92], Fullprof [93] and Jana2006 [94]. The international union of crystallography commission on powder diffraction has published a Rietveld refinement guidelines [95]. Basically, structure refinement is not structure determination, also, there are many intrinsic (Lorentz polarization ...) and material (preferred orientation, absorption, grain size ...) factors which influence refinement results.

The basic assumption of powder refinement is that the step-scanning peak profile intensity can described by a function. Different peak-shape functions were used [96]. Two important functions are:

$$G(2\theta) = \frac{2}{FWHM}\sqrt{\frac{ln2}{\pi}}exp[-\frac{4ln2}{FHMW^2}(2\theta - 2\theta_{bragg})] \tag{2.12}$$

and

$$L(2\theta) = \frac{\frac{2}{\pi FWHM}}{1+\frac{4}{FWHM^2}(2\theta - 2\theta_{bragg})^2} \tag{2.13}$$

The former (formula 2.12) is Gaussian function which is predominant in neutron diffraction, the later (formula 2.13) is Lorentzian function which is predominant in X-ray diffraction. In practical profile, Pseudo-voigt (P-V) function is used:

$$PV(2\theta) = \eta L(2\theta) + (1-\eta)G(2\theta) \tag{2.14}$$

it gives best fitting results [97]. The different between Gaussian and Lorentzian function is shown in fig 2.2 by setting diffraction Bragg angle to 20°, changing FWHM (Full Width at Half Maximum) from 0.001 to 1, normalized peaks intensity to 1. Obviously, Lorentzian function is better to fit broadening peak.

Agreement factors of profile are calculated by:

$$R = 100\frac{\sum|y_i - y_c|}{\sum y_i} \quad R_w = 100\left[\frac{w_i\sum|y_i - y_c|^2}{w_i\sum y_i^2}\right]^{1/2} \tag{2.15}$$

Agreement factors of refinement are calculated by:

$$R_F = 100\frac{\sum|F_{obs} - F_{calc}|}{\sum|F_{obs}|} \quad R_{Fw} = 100\left[\frac{w_{obs}\sum|F_{obs} - F_{calc}|^2}{w_{obs}\sum|F_{obs}|^2}\right]^{1/2} \tag{2.16}$$

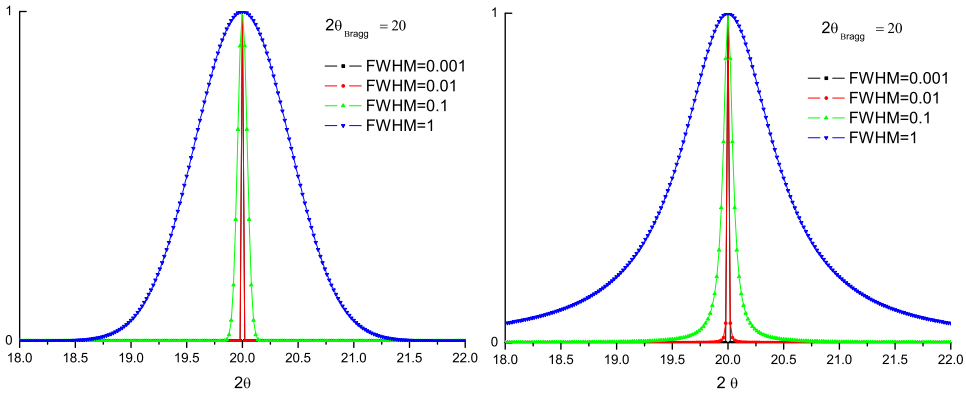

(a) $G(2\theta)$ (b) $L(2\theta)$

Figure 2.2 *Normalized peak shapes of $G(2\theta)$ and $L(2\theta)$ with different FWHM, the Bragg angle is set to 20°*

2.2 Electric characterization

Under electric field, both displacement current and polarization current are induced in materials. Dielectrics refers to materials which have larger polarization current than displacement current under electric filed. Generally, dielectrics is an insulator. The polarization current is positive and negative charges (+q and -q) shifting each other with limited distance ($\vec{d}$), this coupling is named dipole and moment (electric dipole moment) is given by:

$$\vec{p} = q\vec{d} \tag{2.17}$$

The density of the electric dipole moment is polarization ($\vec{P}$). Polarization is a important parameter for multiferroics. Here, Polarization related electric properties and measurements will be introduced.

2.2.1 Dielectric permittivity

In a dielectric material, the electric displace field ($\vec{D}$) is defined as:

$$\vec{D} = \varepsilon_0\vec{E} + \vec{P} = \varepsilon_0(1+\chi_e)\vec{E} = \varepsilon_r\varepsilon_0\vec{E} \tag{2.18}$$

ε_r is relative permittivity, more normally is named dielectric permittivity or dielectric constant. At zero frequency, it is named static dielectric permittivity. Generally, it is a complex but the real part is still named dielectric permittivity. χ_e is electric susceptibility.

The capacitance is defined as:

$$C = \varepsilon_r\varepsilon_0\frac{S}{d} \tag{2.19}$$

This is also the basic relationship for dielectric permittivity measurement. In SPMS, two impedance analyzers, HP 4192 (5Hz - 13MHz) and Agilent 4294A (40Hz - 100MHz) are used in combination with cryostat (80K - 500K) or four (300K - 1000K) achieving large temperature range dielectric characterization.

For most insulator, the basic electric circuit can modeled as parallel or series of capacitor and resistor. In our case, the parallel model was used (fig.2.3) and initial measured parameter was complex admittance (Y = G + jB). The temperature of sample was detected by KEITHLEY 195 Digital Multimeter. The measurement was controlled under LabVIEW based softwares, basic dielectric parameters was calculated by the formulas:

$$\varepsilon' = k\frac{B}{f} \tag{2.20}$$

$$\varepsilon'' = k\frac{G}{f} \tag{2.21}$$

$$tan\delta = \frac{G}{B} \tag{2.22}$$

k ($\frac{72t\times10^9}{\pi d^2}$) is geometric parameter related with thickness t (mm) and diameter d (mm). f is frequency (Hz). Other electric parameters, like impedance, conductivity or electric modulus can also be calculated and more complex electric circuit can be modeled to calculate electric parameters.

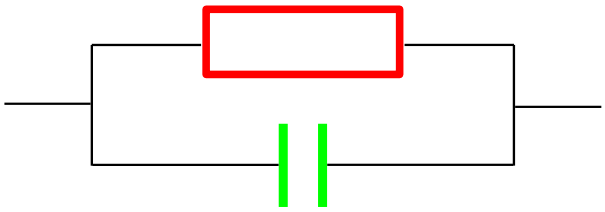

Figure 2.3 *Equivalent electric circuit of a dielectric material.*

2.2.2 Piezoelectric measurement

Piezoelectricity is the charge that accumulates in a material in response to applied mechanical stress. It is a subgroup of dielectricity. The IEEE recommended piezoelectric measurement is complex impedance method (fig 2.4). This method is based on mechanical resonance of samples excited by a low voltage oscillation. Near the vibration frequency, the behavior is modeled by Mason circuit (fig. 2.4). The resonance and antiresonance angular frequencies are:

$$\omega_r = \frac{1}{\sqrt{L_1C_1}} \qquad \omega_a = \sqrt{\frac{C_0+C_1}{L_1C_0C_1}} \tag{2.23}$$

These frequencies are identified by extrema in the impedance spectrum. The electric-mechanical coefficients can be calculated by formulas depending on specific vibration modes.

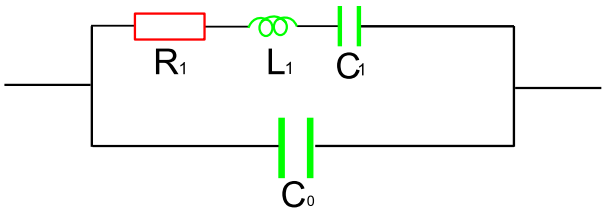

Figure 2.4 *Resonant equivalent circuit of piezoelectric measurement*

2.2.3 Pyroelectric current

Pyroelectricity is the ability of a material to generate a temporary current when it is heated or cooled. It is a subgroup of piezoelectricity. Under electric field, the current (I) passing through a materials can be separated as conduction current (I_C) and displacement current (I_D):

$$I = I_C + I_D \tag{2.24}$$

Displacement current is defined as:

$$I_D = S\frac{\partial\vec{D}}{\partial t} = S\frac{\partial\varepsilon_0\vec{E}+\vec{P}}{\partial t} = S\frac{\partial\vec{P}}{\partial t} = S\frac{\partial\vec{P}}{\partial T}\frac{\partial\vec{T}}{\partial t} \tag{2.25}$$

During heating or cooling a material by a velocity $\frac{\partial \vec{T}}{\partial t}$, the change of polarization will induce polarization current.

The pyroelectric current measurement in SPMS is realized by Keithley 617 programmable electometer collaborating with cryostat for heating or cooling. The pyroelectric coefficient is calculated by:

$$p_i = \frac{I}{vS} \tag{2.26}$$

v is the speed of heating or cooling, S is the surface of sample.

2.2.4 Ferroelectric hysteresis loop

Ferroelectricity is the subgroup of pyroelectricity. FE hysteresis loop is the direct proving of ferroelectricity. Classic electric circuit for FE hysteresis loop measurement is named Sawyer-Tower electric circuit [98]. The measurement circuit can be simplified like fig. 2.5. C_x is the capacitance of a FE meterial, C_y is the capacitance of a constant capacitor. The polarization (P) is the function of voltage of the constant capacitor (V_y).

$$P = \frac{V_y C_y}{S} - \varepsilon_0 E \tag{2.27}$$

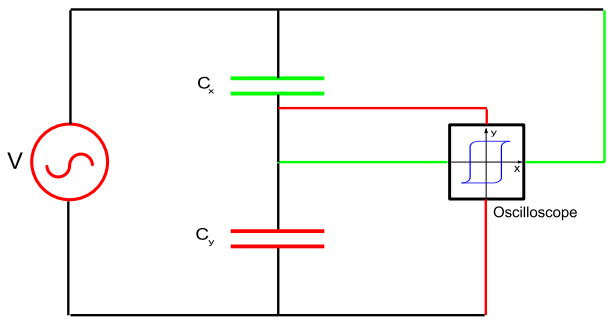

Figure 2.5 *Sawyer-Tower electric circuit for ferroelectric hysteresis loop measurement*

In SPMS, we used sin function as signal source which was amplified by high tension circuit, the frequency was 50Hz. The hysteresis behavior is directly shown on a Tektronix TDS 320 Digitizing Oscilloscope and the data was recorded by LabVIEW based software.

2.2.5 Electric modulus and complex conductivity

In many cases, a material is not a ideal insulator. If a material exhibits a large leakage current, electric modulus and complex conductivity are used to analyze polarization behavior.

Electric modulus

The electric modulus is the reciprocal of dielectric permittivity, it is defined as:

$$M^*(\omega) = \frac{1}{\varepsilon^*} = M' + iM'' = \frac{\varepsilon'(\omega)}{\varepsilon'(\omega)^2 + \varepsilon''(\omega)^2} + i\frac{\varepsilon''(\omega)}{\varepsilon'(\omega)^2 + \varepsilon''(\omega)^2} \tag{2.28}$$

Electric modulus corresponds to the relaxation of electric field in a material when electric displacement remains constant. It is more sensitive to conductivity relaxation behavior and high capacitance effect can be avoided [99]. The conductivity can aslo be suppressed when the data are presented in the

modulus representation($M = i\omega C_0(Z + \frac{1}{i\omega C_s}) = (M' + \frac{C_0}{C_s}) + iM''$). Considering electrical heterogeneity effect, imaginary part of impedance is sensitive to big resistance but the imaginary part of electric modulus is more sensitive to small capacitance.

Complex conductivity

Complex conductivity is defined as:

$$\sigma = \sigma^{'} + \sigma_0 + i\sigma^{''} = i\omega\varepsilon_0\varepsilon \tag{2.29}$$

Here, σ_0 is the direct current(DC) conductivity, $\sigma^{'}$ is the alternating current (AC) conductivity. The existence of σ_0 in the formula is a open question. The relationship between two can be looked as:

$$\sigma_0 = lim\sigma^{'} \quad as \quad \omega \to 0 \tag{2.30}$$

In the thesis, AC conductivity was calculated by:

$$\sigma_{AC} = \varepsilon_0\varepsilon^{''}\omega \tag{2.31}$$

For many dielectrics, the frequency dependent AC conductivity satisfies universal dielectric response (UDR) [100]:

$$\sigma_{AC} = A\omega^n \tag{2.32}$$

or nearly constant loss (NCL):

$$\sigma_{AC} = A\omega \tag{2.33}$$

UDR is understood as ion hopping effect [101] [102]. But, electric heterogeneity can also induce this behavior at high frequency [103]. NCL happens at sufficiently low temperature or high frequency [101], the origin was understood as vibration relaxation [101] or off-center relaxations swear out into a broad distribution [102]. More general AC conductivity can be formulated by:

$$\sigma_{AC} = \sigma_0[1 + (\frac{\omega}{\omega_H})^n] \tag{2.34}$$

Different from AC conductivity, DC conductivity does not change with frequency. However, DC conductivity is related with hopping transition and it is strong temperature dependent:

$$\sigma_{DC}T = \sigma_0 exp(\frac{-E}{k_B T}) \tag{2.35}$$

The fitted thermal activity energy give a information about current carriers.

2.2.6 Dielectric relaxation

Debye relaxation

The polarization momentary delays to electric sign is named relaxation. Classic Debye relaxation is expressed as:

$$\varepsilon = \varepsilon_\infty + \frac{\varepsilon_0 - \varepsilon_\infty}{1 + i\omega\tau} \tag{2.36}$$

Here ε_0 and ε_∞ are the static and high frequency limit dielectric permittivity respectively. τ is the character relaxation time which is the function of temperature:

$$\tau = \tau_0 e^{E/kT} \tag{2.37}$$

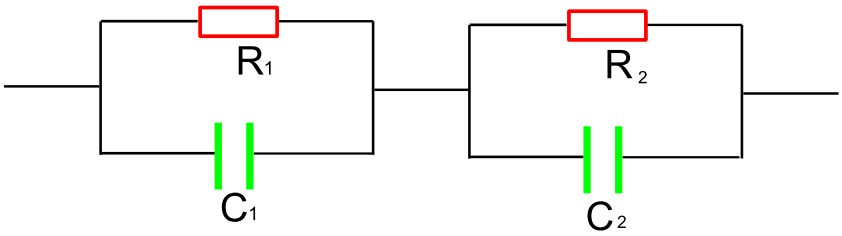

Figure 2.6 *Two-layer electric circuit model of M-W relaxation*

Maxwell-Wagner relaxation

Ideal Debye relaxation seldom happens in a solid material. Normally, electrical heterogeneity can induce Maxwell-Wagner (M-W) relaxation [104] [105]. Two-layer model of M-W is shown in fig. 2.6.
The dielectric permittivity is expressed as:

$$\varepsilon = \varepsilon_\infty + \frac{\varepsilon_0 - \varepsilon_\infty}{1 + i\omega\tau} - i\frac{\sigma}{\omega} \tag{2.38}$$

All the parameters are directly related with circuit elements:

$$\varepsilon_\infty = \frac{1}{C_0}\frac{1}{\frac{1}{C_1} + \frac{1}{C_2}} \tag{2.39}$$

$$\varepsilon_0 = \frac{R_1^2 C_1 + R_2^2 C_2}{C_0 (R_1 + R_2)^2} \tag{2.40}$$

$$\sigma = \frac{1}{C_0 (R_1 + R_2)} \tag{2.41}$$

$$\tau = \frac{R_1 R_2 (C_1 + C_2)}{R_1 + R_2} \tag{2.42}$$

$$C_0 = \varepsilon_0 S/d \tag{2.43}$$

The obvious relaxation would be observed when there are a big difference between two resistances. The temperature character of the relaxation is directly related with the temperature character of the small resistance. The impedance of the circuit can be expressed as:

$$Z' = \frac{R_1}{1 + (\omega R_1 C_1)^2} + \frac{R_2}{1 + (\omega R_2 C_2)^2} \tag{2.44}$$

$$Z'' = R_1 [\frac{\omega R_1 C_1}{1 + (\omega R_1 C_1)^2}] + R_2 [\frac{\omega R_2 C_2}{1 + (\omega R_2 C_2)^2}] \tag{2.45}$$

The impedance normalization highlights small resistance relaxation. The electric modulus of the circuit can be expressed as:

$$M' = \frac{C_0}{C_1}[\frac{(\omega R_1 C_1)^2}{1 + (\omega R_1 C_1)^2}] + \frac{C_0}{C_2}[\frac{(\omega R_2 C_2)^2}{1 + (\omega R_2 C_2)^2}] \tag{2.46}$$

$$M'' = \frac{C_0}{C_1}[\frac{\omega R_1 C_1}{1 + (\omega R_1 C_1)^2}] + \frac{C_0}{C_2}[\frac{\omega R_2 C_2}{1 + (\omega R_2 C_2)^2}] \tag{2.47}$$

The electric modulus normalization highlights small capacitance relaxation. Considering the specific values of resistance and capacitance in ceramic materials, relaxation is more easier noticed by electric modulus normanization.

2.3 Magnetic characterization

The magnetization can be measured by superconducting quantum interference device magnetometer (SQUID) after the discovery of Josephson effect. The magnetic behavior of our materials were measured by Quantum Design MPMS-5 (0 - 5.5T, 1.7 - 800K). The raw data are magnetic moment (m) in electomagnetic units (1 emu = 10^{-3} A·m^2 = 10^{-3} J/T) and magnetic moment in unit mass (m_m, $emu \cdot g^{-1}$). Two conventional measurement procedures were used during experiments: zero field cool (ZFC) and field cool (FC). In ZFC, the sample was measured by heating accompanying magnetic field after a first cooling without magnetic field. In FC, the sample was measured by cooling accompanying magnetic field. The magnetization (M) was calculated by:

$$M = m_m \rho \tag{2.48}$$

Here, ρ is the density of sample. Hypothesis magnetization just coming from the spin (this is the case for the first-raw transition metals [106]), the spin quantum number of atoms can be calculated by formula:

$$s_c = m_m \frac{M}{N_A \cdot N \cdot g_0 \cdot \mu_B} \tag{2.49}$$

μ_B = 9.27400915(23)$\times$ 10^{-24} A $\cdot$ m^2, N$_A$ = 6.02214179(30)$\times$ 10^{23} mol^{-1}, g$_0$ = 2, M is the molar mass, N is the number of magnetic atoms.

In published results, different authors may used different units for magnetization and magnetic susceptibility. We summarized a conversion table of different units (tab. 2.2), where M$_{mol}$ and ρ are the mole mass (g/mol) and the density (g/cm^3) of a material.

Table 2.2 *Magnetization and magnetic susceptibility units conversion*

Quantity	Unit			
M	emu $\cdot$ g^{-1}	μ_B per f.u.	emu / cc	A$\cdot$ m ^{2} / kg
factor	1	$\times$ M$_{mol}$/5585	$\times\rho$	1
χ	emu $\cdot$ g$^{-1} \cdot Oe^{-1}$	μ_B per f.u. $\cdot$ Oe^{-1}	cm$^3\cdot$ g^{-1}	m$^3\cdot$kg^{-1}
factor	1	$\times$ M$_{mol}$/5585	4π	$4\pi\cdot$ 10^{-3}

2.4 A paradox

There are many similar behaviors between FE and FM, for example, both polarization and magnetization follow C-W law, both of them have hysteresis loops. However, there is a obvious contradiction: the conductivity of a material can totally erase FE behavior [107] [108] but many magnetic materials are good conductor because of exchange interaction. The precise characterization small FE polarization is still a problem.

Chapter 3

Intrinsic Properties of Lead Iron Tungsten and Lead Zirconate

Our aim being the investigation of the solid solution between lead iron tungsten $PbFe_{2/3}W_{1/3}O_3$, (PFW) and lead zirconate $PbZrO_3$, (PZO), we first re-examined the properties of both PFW and PZO which are our reference compounds. As already stressed, PFW is already a multiferroic system having relaxor ferroelectric character and antiferromagnetic features. The role of PZO in our solid solution is to introduce, in addition to PFW ferroic orders, antiferroelectric (and antiferrodistorsive) instabilities. While these two compounds are rather well known at a first glance, it appears from the literature that there remain several not yet understood experimental observations leading to a situation that needs to be clarified. This chapter, in which PFW is first presented followed by PZO, will give us a basic background to understand the richness to combine both compounds.

3.1 Literature review on the multiferroic lead iron tungsten

PFW was first studied by smolenskii's group [109] and displays both FE and AFM features. PFW is also a so-called relaxor FE with T_m, the temperature associated to the maximum dielectric constant near 180K. The ralaxor behavior in PFW is of course related to short range local order [110].

Fig. 3.1 illustrates the electric and magnetic orders in PFW.

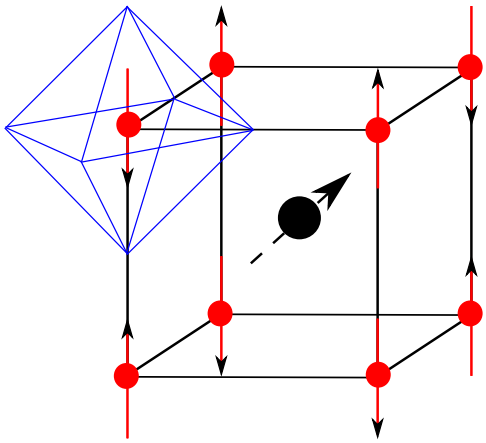

Figure 3.1 *Electric and magnetic orders in PFW [60],the red and black bowls represent Fe ions and Pb ions respectively, here the oxygen ions are omitted. The dashed black line represents the possible polar component through Pb^{2+} displacements along <111> direction [60]. The red arrows represent the magnetic moment direction alternatively distributed up and down along <100> directions.*

As in the model PMN relaxor, the structure of PFW remains cubic with $Pm\overline{3}m$ space group down to 10K [60]. As a result, no macroscopic polarization was observed in PFW without application of external electric field [111] [112]. However, at a short-range scale some structural deviations from the ideal cubic perovskite were reported. Indeed, the atoms are not located onto their ideal cubic positions [63] and more precisely Pb^{2+} shifts along <111> directions [60] were reported suggesting the existence of rhombohedral nanopolar clusters [110]. In addition chemical ordering at nanoscale giving rise to doubling of the perovskite structure were also reported [113] [114]. These features are typical of lead-based relaxors.

While lead ions are responsible of the polar properties , the iron ions are associated to the magnetic features in PFW. Indeed, 2/3 of the perovskite B-site in PFW is occupied by Fe^{3+} bringing $5.92\mu_B$ spin ($3d^5$ electron configuration) net magnetic moment. The arrangment of these magnetic moments gives rise to a G-type AFM ordering [60]. The AFM phase transition point i.e. T_N was reported to be 383K [109], 370K [115] or 350K [63] using magnetic measurements, and 343K by neutron diffraction [60] technique. Interestingly, at the same time at low temperatures, a weak FM was also found below 20K [63] or 9K [115]. This magnetic character is similar to that observed in low temperature spin glass states reported in many Fe-based perovskites as $PbFe_{1/2}Nb_{1/2}O_3$ (PFN) [67] [68], $PbFe_{1/2}Ta_{1/2}O_3$ (PFT) [69] or $BiFeO_3$ (BFO) [70] [71] [70].

Moreover, we believe that the discrepencies bewteen the values of the critical temperatures is sample-dependent. Indeed, it is obvious that the magnetism arises from the iron ions. However these ions are not distributed in a same way from one sample to another one as they correspond to 2/3 of the B-site and are randomly distributed. Therefore the magnetic exchange interactions should be slightly different from one sample to another one, which may explain the different critical temperatures reported.

3.2 Reexamination of the properties of lead iron tungsten

3.2.1 Structural aspects

Fig. 3.2 shows some characteristic Bragg peak reflections at 100K, 180K, 250K and 390K. All the peaks remains single whatever the temperature attesting of the cubic symmetry of PFW.

For illustration, we show the Room Temperature (RT) Rietveld refinement results. The experimental diffraction pattern and the calculated one are plotted in fig. 3.3 and the refined parameters are listed in table 3.1.

Table 3.1 *Refined structural parameters and agreement factors for PFW at room temperature*

a = 3.98Å				
	Coordinates			
Atom	x	y	z	U
Pb	0	0	0	0.024
Fe	0.5	0.5	0.5	0.002
W	0.5	0.5	0.5	0.002
O1	0.5	0.5	0	0.002
R = 12.18%,		R_w = 15.28%		
R_F = 6.37%,		R_{Fw} = 7.44%		

It is obvious that the cubic model allows a rather good matching between the observed and calculated diffraction patterns. However, as shown in the inset of figure 3.3 the high angle diffraction pattern shows some discrepencies and in addition, the thermal agitation parameter of Pb-ions is abnormally

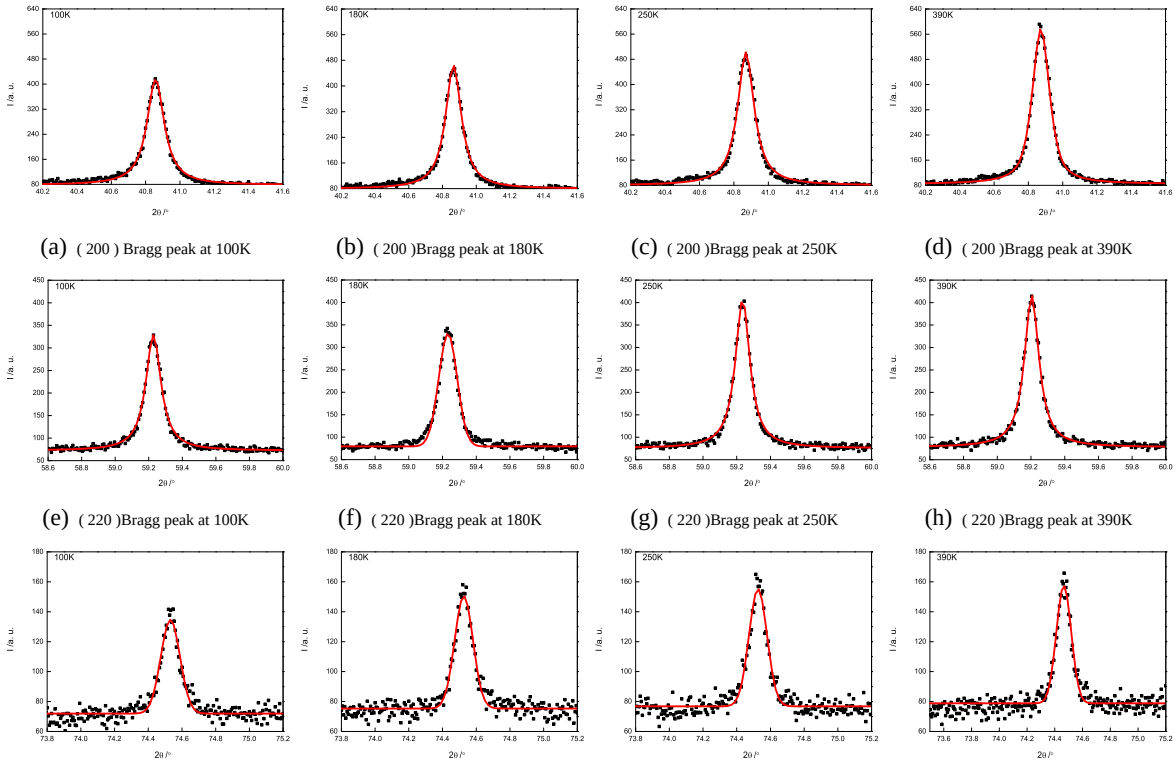

(a) (200) Bragg peak at 100K (b) (200)Bragg peak at 180K (c) (200)Bragg peak at 250K (d) (200)Bragg peak at 390K

(e) (220)Bragg peak at 100K (f) (220)Bragg peak at 180K (g) (220)Bragg peak at 250K (h) (220)Bragg peak at 390K

(i) (222)Bragg peak at 100K (j) (222)Bragg peak at 180K (k) (222)Bragg peak at 250K (l) (222)Bragg peak at 390K

Figure 3.2 *Main Bragg diffraction peaks (200), (220) and (222) of PFW at different temperatures*

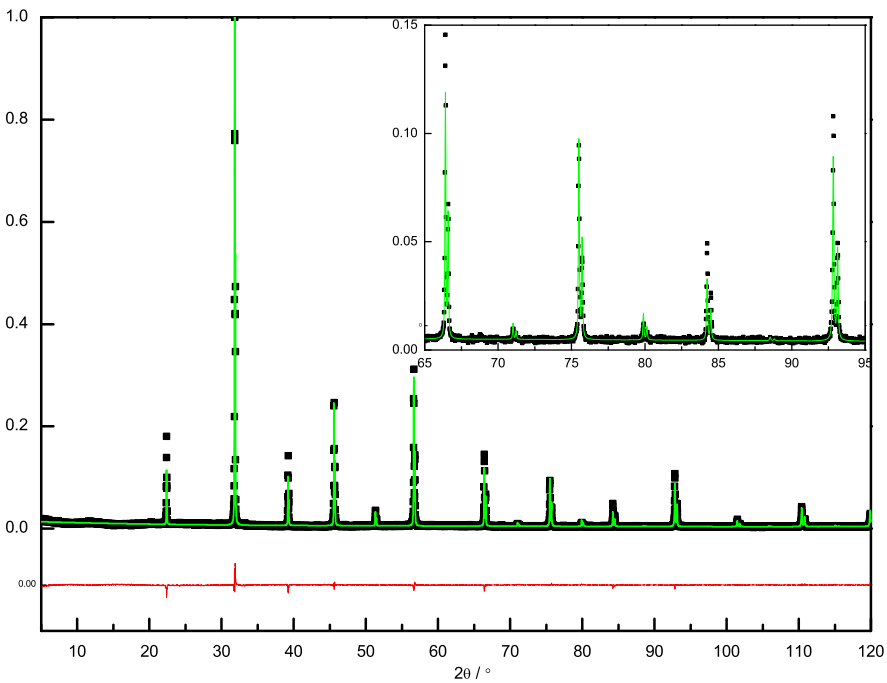

Figure 3.3 *Diffractogram of PFW with Rietveld refinement*

strong. These observations which affect the Bragg peak intensities reflect local disorder which probably comes from ion displacements. Indeed, in lead-based relaxors Pb atom is supposed to be localed in a multiwelled potential around its special Wyckoff position [45]. To check this, we used a common procedure [45] which has already proved its efficiency. During this refinement procedure, only thermal u factor of Pb atom, the whole scale factor are free while all the other parameters are kept fix. Pb atom is then smoothly moved along different directions i.e. <100>, <110>, <111> and <123> corresponding, respectively to 6, 8, 12 and 48 equivalent directions in the cubic symmetry. This approach allows the agreement factors to decrease attesting a better matching between the observed and calculated diffraction pattern. The agreement R factor R_F is plotted as a function of Pb atom shift in fig. 3.4.

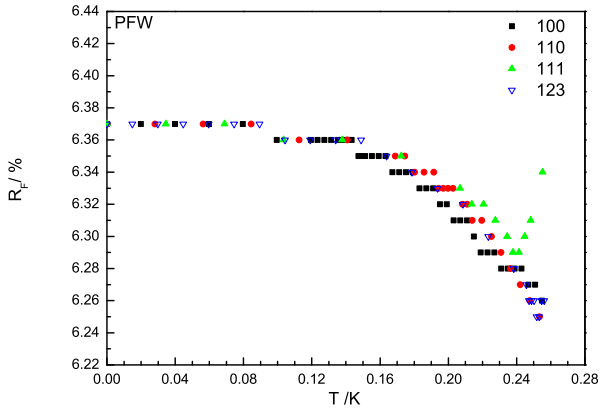

Figure 3.4 *R_F as a function of Pb shift in different directions at 300K. (sin θ /λ up to 0.56Å^{-1})*

A minimum is obtained at 0.238Å, for <111> direction, and at 0.252Åfor all the other directions. Thus as already observed in many other Pb-based relaxors, there is a strong polar displacement of Pb ions. However, we can not say how this ionic shifts arrange themselves, if they are randomly distributed or correlated to form the so-called polar nanoregions (PNRs). It is intersting to remark that in case of the antiferroelectric PZO, the antiparallel shift of Pb atoms is about 0.24Å, a value very close to that we determined for PFW.

In order to get more insights into the possible correlation of Pb ions, we carefully analyzed the Bragg peaks as a function of temperature. The (200), (220) and (222) Bragg diffraction peaks depicted in fig. 3.2 show already indication of such correlations. Indeed, the first indication comes from the temperature evolution of the intensity of the Bragg peaks. In fig. 3.2, the data are plotted at the same scale. It is clear that the maximum of the intensity of each Bragg peak is decreasing with temperature decreasing. However, in a standard situation one would expect an increase of the intensity with temperature decreasing. Indeed when the temperature decreases, the contribution to the thermal diffuse scattering (TDS) decreases too. As a consequence, if no structural modifications occur, the maximum of the Bragg peak intensity should increases when the temperature diminishes as the TDS also decreases; in other words the TDS goes from the backgroud into the main Bragg peak when the temperature decreases. Our data rather show that the intensity is going somewhere else when the temperature decreases. Contrary to single crystals in which the diffuse scattering can be accessed, it is difficult to reach it in powder samples. Nevertheless, the presence of polar shift correlations should affect the width of the Bragg peak and even its position.

The Full-Width-at-Half-Maximum (FWHM) for the (200), (220) and (222) peaks are plotted in fig.3.5(a).

At a first glance, it appears in fig.3.5(a) that the FWHM remains constant whatever the temperature as one would expect for a cubic phase. However a careful look to the FWHM of (200) Bragg peak (fig. 3.5(b)) allows to evidence a weak enhancement of the width below 160-170K. It is worth recalling that usually the so-called butterfly diffuse scattering observed in Pb-based relaxors which is associated to

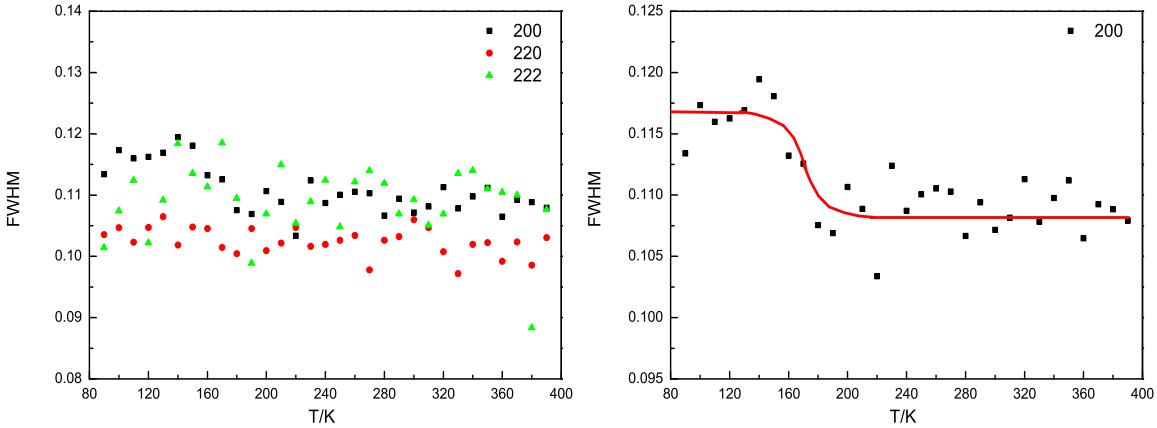

(a) (b)

Figure 3.5 *FWHM of Bragg (200), (220) and (222) peaks of PFW*

the PNRs is more pronounced around h00-type Bragg reflections. It can then explain why the FWHM broadens in case of (200) and not (or at least, less) for (220) and (222)peaks. The structural anomaly at 160-170K is better seen in the pseudo-cubic lattice parameter extracted from the Bragg peak positions versus temperature in fig.3.6.

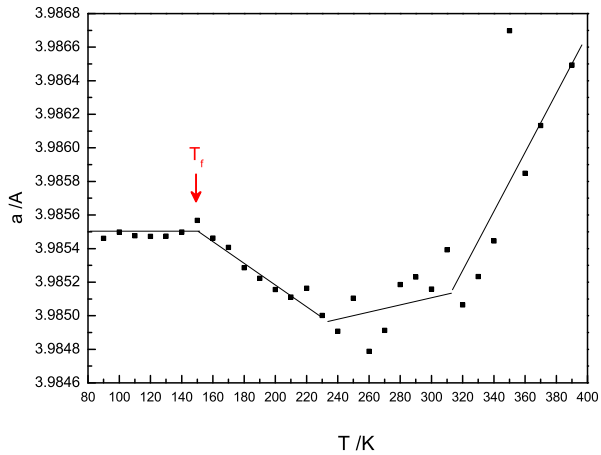

Figure 3.6 *Temperature dependence of the pseudo-cubic lattice parameter in PFW*

Indeed, below 160K-170K a plateau is obviously evidenced. Such plateau has been also reported in other systems like the model relaxor PMN. In addition to the 160-170K anomaly, other structural anomalies can be observed in fig.3.6. Indeed starting from high temperature, there is a deviation of the linear evolution at about 300K below which the pseudocubic lattice parameter becomes soft (almost constant with temperature) before increasing below 240K. And finally the plateau occurs below 160-170K. It appears then that something in the structure is occuring between 240K and 300K. The increasing of the volume on cooling below 240K might be a signature of a phase transition. However, as no splitting or additional Bragg peaks is evidenced if such phase transition occurs, it would be at a local scale.

3.2.2 Polar order

The real part of the dielectric permittivity and the dielectric losses of PFW are shown in fig 3.7 between 100K and 300K for a frequency ranging from 1kHz to 1MHz. As expected for a relaxor compound, there is a strong dielectric relaxation below 210K for this frequency range. It is worth mentioning that

in addition to this relaxor behavior a high temperature dielectric dispersion can be evidenced. Such frequency dispersion is related to conduction and will be discussed latter in this paragraph.

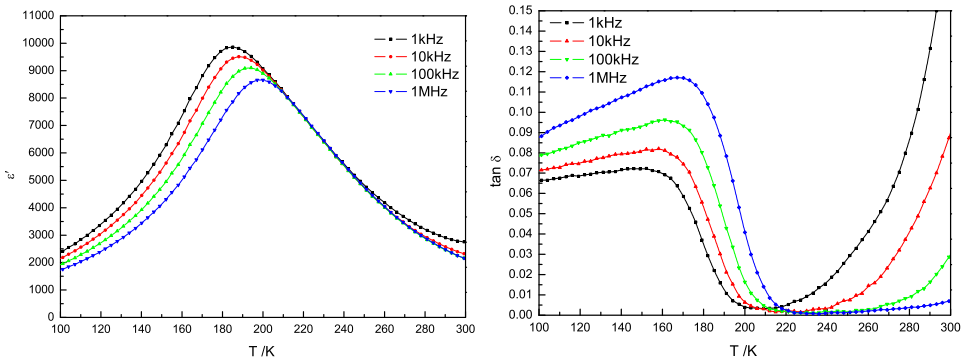

(a) Dielectric permittivity (b) Dielectric loss tangent

Figure 3.7 *Temperature dependent dielectric permittivity and dielectric loss tangent of PFW*

The temperature T_m associated to the maximum of the dielectric permittivity increases with frequency increasing: 185K at 1kHz, 188K at 10kHz, 194K at 100kHz and 200K at 1MHz. The dielectric losses show similar behavior.

The dielectric relaxation of relaxors can be treated using the so-called Vogel-Fulcher (V-F) relation in order to extract dynamic properties related to PNRs and the freezing temperature T_f. In the fig. 3.8, the V-F relation (solid line) fits rather well with the experimental points.

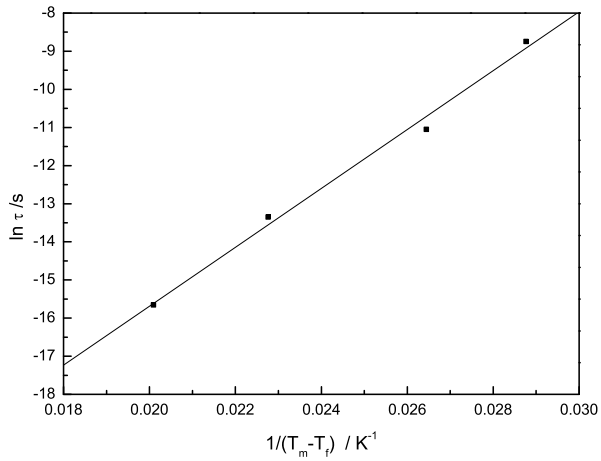

Figure 3.8 *Vogel-Fulcher freezing in PFW*

The fitting data gives T_f = 150.2K, f_0 = 5.30*10^{12}, E_a = 0.067 eV, $\Delta[T_m(1\text{MHz})-T_f]$ = 49.8K. These results are in good agreement with previous report giving T_f = 153K, f_0 = 6.19*10^9, E_a = 0.0396 eV [116]. Besides, the activation energy E_a and the characteristic relaxation time f_0 values are also close to those found in other relaxors, for example, in PMN-10PT [43], f_0 = 1.03*10^{12}, E_a = 0.0407 eV. It is remarkable that the freezing temperature T_f 150K found using the V-F relationship is close to the temperature associated to the appearance of the plateau in the diffraction data (fig.3.6) and the broadening of the (200) Bragg peak (fig.3.5(a)).

We also used power law formula to model the dielectric response around T_m. Both experimental data and the fitted power law of dielectric permittivity are plotted in fig. 3.9.

As expected the power law describes rather well the dielectric response around and above T_m but does not match the low temperature dielectric response because of the slowing down of the PNRs. The fitted parameters are listed in table 3.2, γ is 1 for normal FE while it becomes equal to 2 for ideal relaxor.

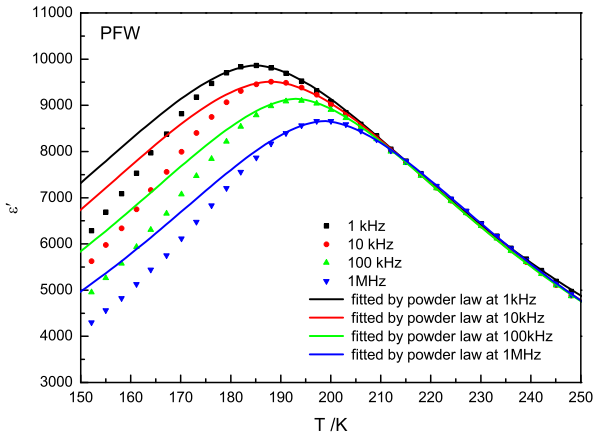

Figure 3.9 *Dielectric permittivity of PFW fitted by powder law*

Here in case of PFW, γ value is about 1.75 attesting the relaxor-like shape of the dielectric response around T_m.

Table 3.2 *Powder law parameters for PFW at different frequencies*

f	ε_m	T_m	γ	δ_m
1kHZ	9864	185	1.74	26.34
10kHZ	9512	188	1.80	28.92
100kHZ	9142	193	1.73	24.37
1MHZ	8659	199	1.75	24.45

However far above T_m, the power law is no more valid and instead of a Curie-Weiss (C-W) law is much more adapted to describe the high temperature dielectric response. As illustration, the reciprocal dielectric permittivity at 1MHz and the fits using both the power law and C-W relationship are plotted in the same figure (fig. 3.10); note that T_f is also marked.

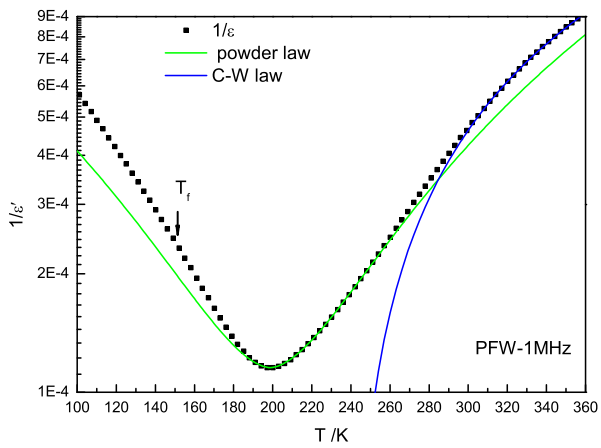

Figure 3.10 *Modeling dielectric permittivity of PFW*

Interestingly, the C-W law gives parameters which are T_0 = 239K and C = 1.3*10^5 and deviates below roughly 300K. These two peculiar temperatures i.e. 240K and 300K determined by dielectric analysis, are quit close to those already evidenced using X-ray diffraction (see fig.3.6). Besides it is also worth mentioning that the power law deviates at around 240K, showing that indeed this temperature is specific to PFW. Combining both dielectric constant and structure data, it may be suggested that a local phase transition occurs indeed at T_0 240K. One may also speculate that the anomaly observed

at 300K in both dielectric and XRD measurements might correspond to the 'beginning' of the local phase transition assuming a first order-like transition i.e. in between T_0 and 300K there is a phase coexistence.

Let us now come back to the high-temperature-like dielectric dispersion evidenced in fig 3.7. Such dispersion can be more easily evidenced by dielectric loss tangent data (fig.3.11(a)) which display a series of relaxations.

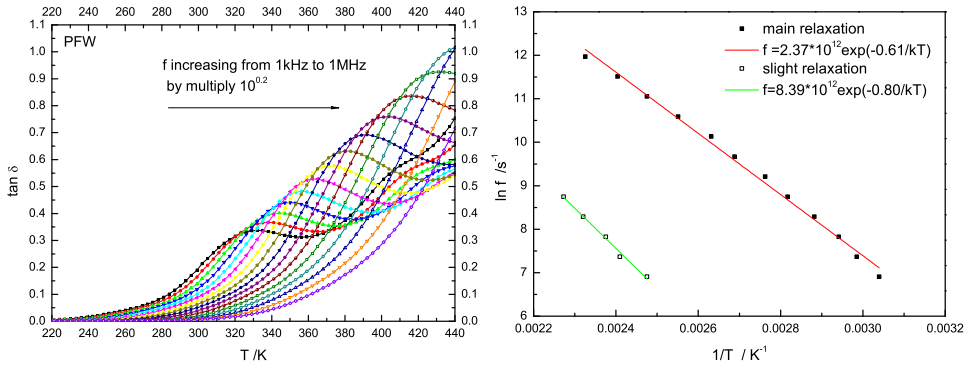

(a) Dielectric loss tangent (b) Arrhenius fitting tangent

Figure 3.11 *Non conventional dielectric relaxation in PFW*

For example for a frequency of 1kHz, the dielectric losses show two obvious maxima at 320K and 410K and suggest further at least a third one above 440K. The first 320K relaxation is prominent with a broad temperature peak shift over the frequency range which we name a main relaxation for convenient discussion. The second relaxation is weaker as it spreads over a narrower temperature scale into the temperature-frequency range we selected, therefore it is named slight relaxation. These both relaxations/dispersions follow a classical Arrhenius law as shown in fig.3.11(b). The black solid square points correspond to the main relaxation experiment while the open square points correspond to the slight relaxation experiment. The straight lines are the fits using Arrhenius law. For the main relaxation and slight relaxation, the thermal activation energy obtained are 0.61eV and 0.80eV respectively while the pre-exponential factors are $2.37*10^{12}$ and $8.39*10^{12}$ respectively.

These parameters are typical for relaxations related to defects as it was already obseved in pure PFW [116] [117], La-doped PFW [118], PFW-PTO [119] [120] or Mn- and Co-doped PFW [117].

According to the thermal activation energy value, a first feeling is to attribute these relaxations to oxygen vacancy defects which are usual in perovskite oxides [121] [122] [123] [124] [125] [126]. However, we rather assume that here they are much more related to Pb vacancies as was also recently suggested [116] [117]. Indeed, two key features supporting such assumption have been reported. Indeed, the relaxations can be eliminated by annealing in nitrogen atmosphere [119] which is a typical reducing environment and thus can not be explained oxygen vacancies. Moreover, it was also shown using hall effect measurement [118] that in PFW there exist hole carriers which is in agreement with existence of Pb defects.

Let us now come back to the polar aspect of PFW. In this goal, the polarization of PFW was measured directly through FE hysteresis loop as a function of temperature (fig. 3.12) obtained using Sawer-Tawer electrical circuit.

As one may see while the macroscopic symmetry remains cubic thus centrosymmetric, a rather soft hysteresis loop can be measured. The loop is soft meaning that the polarization vs electric field has a "'S"' shape rather than a rectangular one as expected for a normal FE. The hysteresis loop becomes bigger on cooling indicating continuous growth of the polarization in PFW. The polarization reaches a maximum value of about 14 μC·cm^{-2} and gets a remanent value of 7 μC·cm^{-2} . This is in agreement with previous report [111]. The polarization can be fitted in the mean field theory based on the following

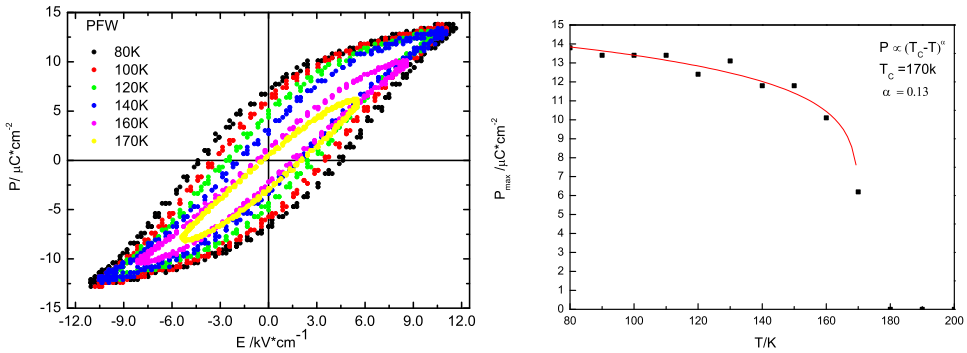

(a) FE hysteresis loops at some character temperatures

(b) Polarization as a function of temperature. Points are experimental data; curve are the fit by mean field theory

Figure 3.12 *Ferroelectric properties of PFW*

formula:

$$P \propto (T_C - T)^{\beta} \tag{3.1}$$

which gives T_C = 170K and β = 0.13. The obtained critical temperature is 20K higher than the freezing temperature T_f and very comparable to the temperature associated to the appearance of a plateau in the diffraction data (see fig.3.6). Moreover, the value of the critical exponent β is far from mean field theory (β = 0.50). It is rather closer to 1/8 which corresponds to a description of the polarization within an Ising model into 2-dimension. It is worth mentioning that close values have been already observed in other perovskites like $NaNbO_3$ (β = 0.17) et $RbCaF_3$ (β = 0.18) and have been explained [127] because of the presence of asymmetric defects that broken the local symmetry (β= 0.125 for a 3D system). This last explanation is better appropriate in our case as indeed both either chemical inhomogeneities and/or PNRs can be responsible of such lowering of the local symmetry.

It is now of interest to investigate how the polar state can be affected using an external dc-electric field. In this goal we especially investigated the dielectric constant vs temperature in two different electric field regimes i.e. Field-Cooling (FC) and Zero-Field-Heating-after-Field-Cooling (ZFHaFC). During the FC regime, an electric field value between 1kV/cm to 6kV/cm is applied at 450K and the dielectric constnat is recorded on cooling keeping the electric field constant. Then at 100K, the electric field is switched off and a short-circuit is realized in order to discharge the capacitor from any parasitic electron-hole carriers. Finally the dielectric constant is recorded on heating (ZFHaFC) till 450K. Figure 3.13 shows the dielectric constant and losses in both regimes at a frequency of 1MHz.

As one may see there is no drastic change of the permittivity until an electric field value of 6kV/cm. Both the maximum of the dielectric constant and T_m are decreasing with increasing of the strenght of electric field as shown in fig. 3.14.

Moreover, a small and sharp signal is evidenced at 210K under FC and 220K under ZFHaFC (see arrow on fig 3.13). This additional dielectric signal is much more enhanced at a frequency close to 500kHz (see fig.3.15).

This behavior is explained by a piezoelectric resonance and is associated to an electric-field-induced phase transition. Note that the critical temperature is the same whatever the electric field value meaning that in contrast to the maximum of the dielectric constant this dielectric signal corresponds to a 'normal' ferroelectric phase transition. This transition is also of a first order as it takes place at different temperature on cooling and heating. Interestingly a FE phase transition can be also induced by an electric field in case of PMN the model relaxor. However, while in case of PMN such phase is induced at a temperature below T_m, in case of PFW it occurs above T_m.

To confirm the piezoelectric resonance, the modulus and phase of the impedance as a function of frequency is measured at different temperature (fig.3.16).

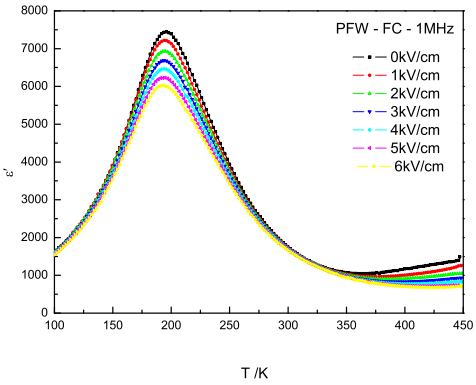

(a) Dielectric permittivity for FC

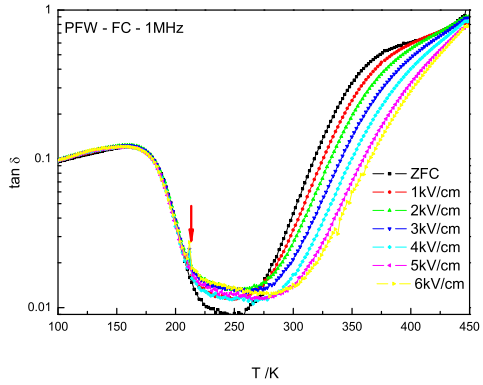

(b) Dielectric loss tangent for FC

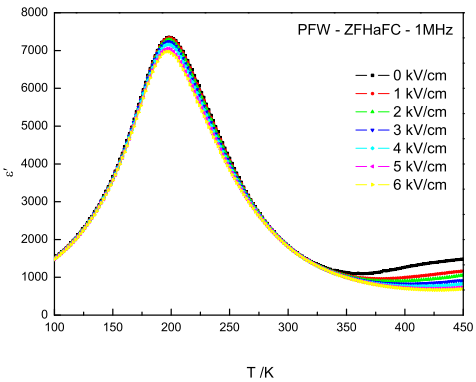

(c) Dielectric permittivity for ZFHaFC

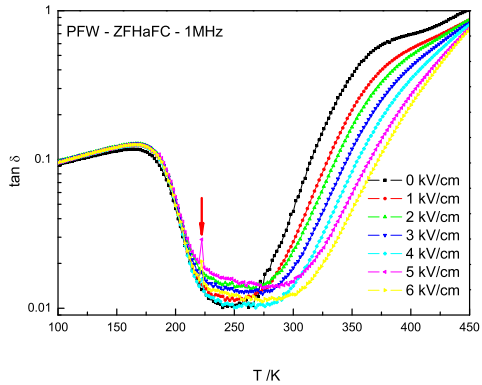

(d) Dielectric loss tangent for ZFHaFC

Figure 3.13 *Dielectric permittivity and dielectric loss tangent of PFW at 1MHz for FC and ZFHaFC*

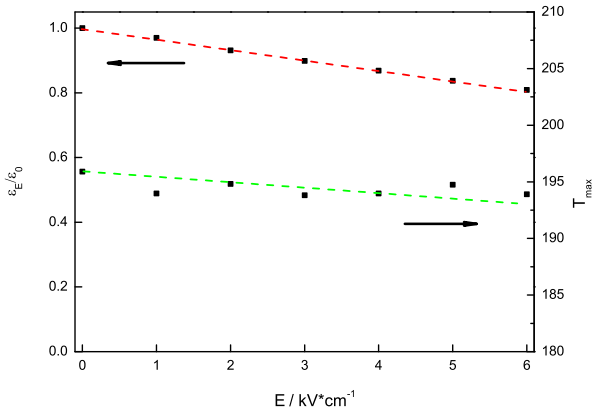

Figure 3.14 $\frac{\varepsilon_E}{\varepsilon_0}$, *and* T_m *vs E on FC regime.*

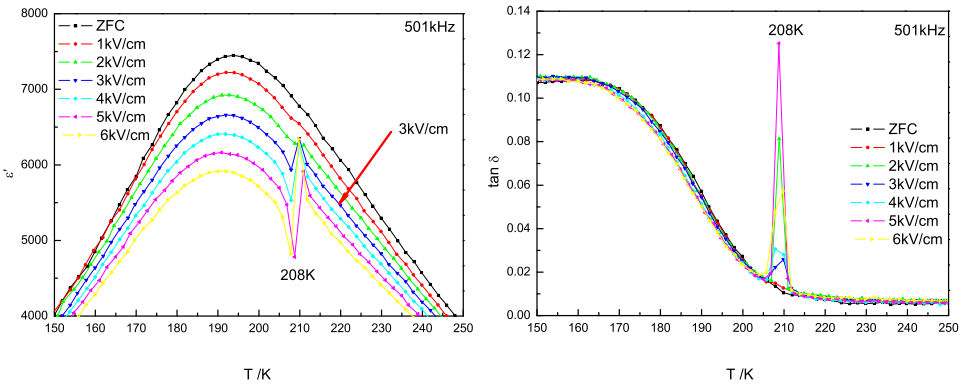

(a) Dielectric constant for FC at 501kHz (b) Dielectric losses for FC at 501kHz

Figure 3.15 *Dielectric constant and losses at 501kHz for FC*

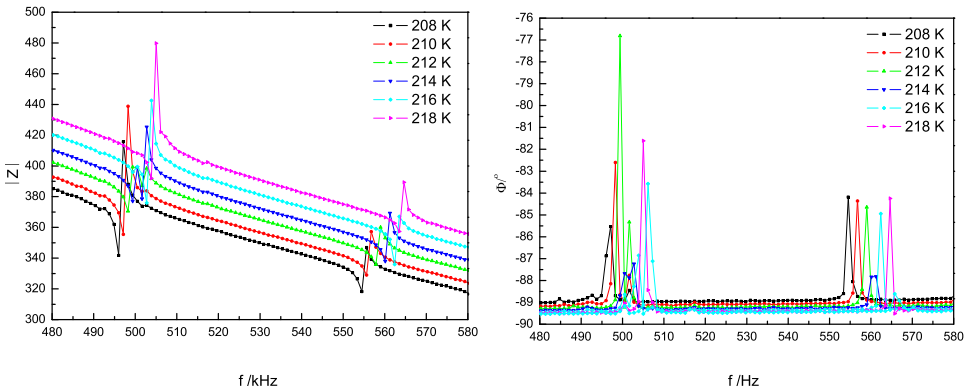

(a) Z (b) Φ

Figure 3.16 *Impedance and phase angle vs frequency for different temperatures*

As shown in fig.3.16 several resonances (associated to the dimensions of the pellet used for the measurement) are obtained for frequencies around 500kHz. Using such data, it is possible to extract electromechanical properties of PFW ceramics. The effective transverse k_{31} coefficient is close to 6.6% and the mechanical factor of quality Q_m is 235 which rather small values.

In order to determine the 'true' critical temperature of this induced phase transition, the amplitude of the resonance signal ($\frac{(Z_{max}-Z_{min})}{Z_{min}}$) versus temperature is plotted in fig 3.17. While the maximum is observed at 210-220K, the signal still exists until 240K which can be then considered as the "'true"' T_C. This temperature of the induced-phase transition in PFW is then close to the 240K anomaly evidenced by Curie-Weiss analysis and diffraction results.

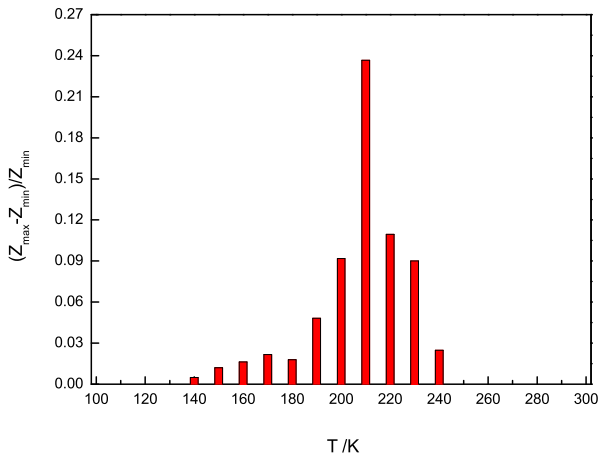

Figure 3.17 *Amplitudes of resonance signal*

3.2.3 Magnetic order in PFW

Beyond its original polar properties, PFW exhibits also magnetic properties. Fig. 3.18 shows the magnetic susceptibility of PFW as a function of temperature measured by SQUID on Zero-Field-Cooling (ZFC). In low temperature range(2K - 300K) the Field Cooling (FC) susceptibility (with a magnetic field fixed at 100 Oe) is also measured in addition to ZFC regime.

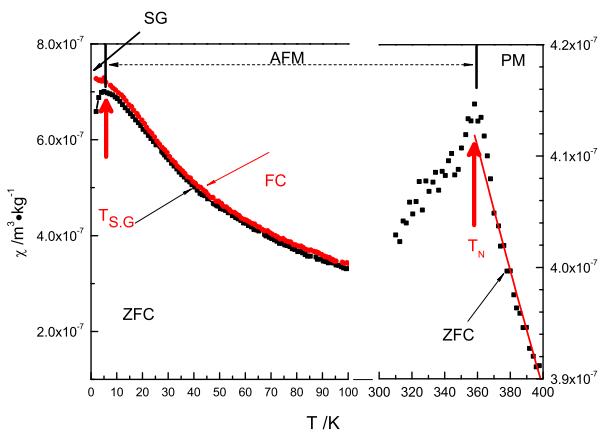

Figure 3.18 *Magnetic susceptibility of PFW*

At high temperature, a sharp peak at 358K (marked by an arrow) corresponds to T_N the temperature associated to the ParaMagnetic (PM) to AntiFerroMagnetic (AFM) phase transition. The straight line in figure 3.18 corresponds to the fit using Curie-Neel law which gives Curie constant $2.95\times10^{-4}\ m^3 \cdot kg^{-1}$

$\cdot$ K^{-1}. As one may see, the transition occurs in a very small magnitude of the susceptibility making its detection rather difficult. This can explain why T_N is slightly higher than that obtained by neutron powder diffraction [60] and similar to that determined by magnetic measurement [63]. To confirm the long-range AFM character, figure 3.19 shows the room temperature neutron diffraction data. The data have been recorded at Institute Laue Langevin (Grenoble, France) in D2B beamline.

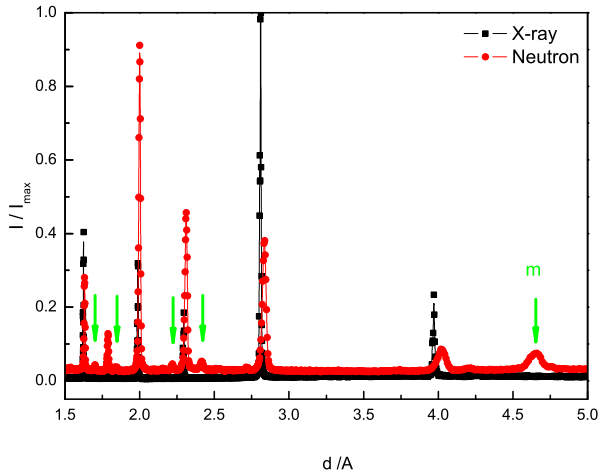

Figure 3.19 *Comparison of x-ray and neutron diffraction patterns at room temperature*

Comparing x-ray diffraction, the neutron diffraction pattern exhibits extra-peaks of $\left\{\frac{1}{2},\frac{1}{2},\frac{1}{2}\right\}$-type associated to the magnetic ordering. As expected at 300K, the magnetization versus the applied magnetic field (M-H) remains linear up to 5000 Oe with a slope of χ= 9.8$\times$10^{-5} μ_B/Oe (fig.3.20).

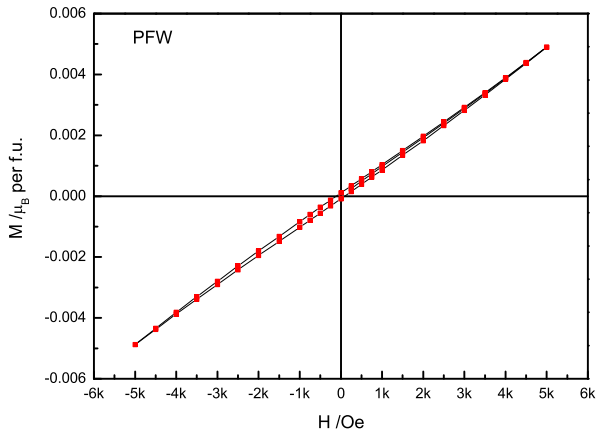

Figure 3.20 *Magnetization-magnetic field loop of PFW at room temperature*

Assuming the molecular field approximation, the 0K perpendicular AFM susceptibility is given by $\chi_\perp$ = M_0/ H_E, where M_0 is the magnetization of one sublattice and H_E is the first neighbor exchange field. Besides, H_E is linked to the Néel temperature by k_BT_N = (1/3)M_0H_E. In case of powder, the susceptibility is written as χ_{AFM} = (2/3)$\chi_\perp$ [128]. Using T_N =358K and M_0 = (2/3)$\times$5.92μ_B, we obtain χ_{AFM} = 6.5 $\times$10^{-5} μ_B, which is very close to the measured slope (χ= 9.8$\times$10^{-5} μ_B/Oe).

However in addition to this long-range AFM order, a short-range one exists. Indeed at low temperature, ZFC-FC has a cusp (see arrow in fig. 3.18) at 5K ($T_{S.G.}$) which is typical of spin-glass-like behavior. Note that a weak FM was also reported at 1.9K [115] in PFW meaning that indeed at a short scale, some magnetic arrangments coexists within the long-range AFM one.

Moreover, having a look at the room temperature M-H curve (fig.3.20) , the magnetic moment is not zero at zero magnetic field and is roughly equal to 1$\times$10^{-4} μ_B. This weak magnetization can be

explained either by some magnetic impurities or by a canting of the AFM spin giving rise to a magnetic order with a non zero value. This situation might be similar to the well-known BFO multiferroic [129] with its net magnetization of $0.021\mu_B$. Here PFW displays a net magnetic moment of 0.067 μ_B which indeed can suggest a canted magnetic order in PFW.

Finally as for the polar features, PFW displays both long-range and short-range magnetic orders. Typically, the AFM order can be related to Fe^{3+}-O- Fe^{3+} superexchange mechanism through Fe/W disordered regions and the weak FM may come from Fe^{3+}-O-W-O-Fe^{3+} superexchange through Fe/W chemically ordered regions [63]. Indeed, nanoscale ordered domains of 2-5 nm size were found on PFW because of alternating 1:1 Fe^{3+} and W^{6+} chemical order along the <111> direction [113]. Besides, the competitions between weak FM clusters within an AFM matrix can give rise to a spin glass (or frustrated) behavior at low temperature.

3.3 Literature review on the antiferroelectric lead zirconate PZO

Lead zirconate ($PbZrO_3$, PZO) was the first compound identified as an AntiFerroElectric (AFE). In its low-temperature phase (T < T_c ~505K) PZO crystallizes in an orthorhombic symmetry allowing 60°, 90° and 180° domain structures [130] [131] [132] to satisfy the AFE character and the head-to-tail arrangement of the polarization. The unit cell contains eight formula units (f.u.) and is derived from the single-perovskite cubic structure ($a_c \sim 4.16$ Å). The unit-cell parameters are a = $\sqrt{2}a_c$ = 5.89 Å, b = $2\sqrt{2}a_c$ = 11.76 Å, and c =$2a_c$ = 8.22 Å. The orthorhombic phase of PZO is strongly AFE in the plane perpendicular to the c-axis [133] [134]. Indeed, the AFE character is defined by the Σ_3 normal-mode displacement corresponding to antiparallel shifts of the lead ions along one of the [110]-cubic like directions (see fig. 3.21).

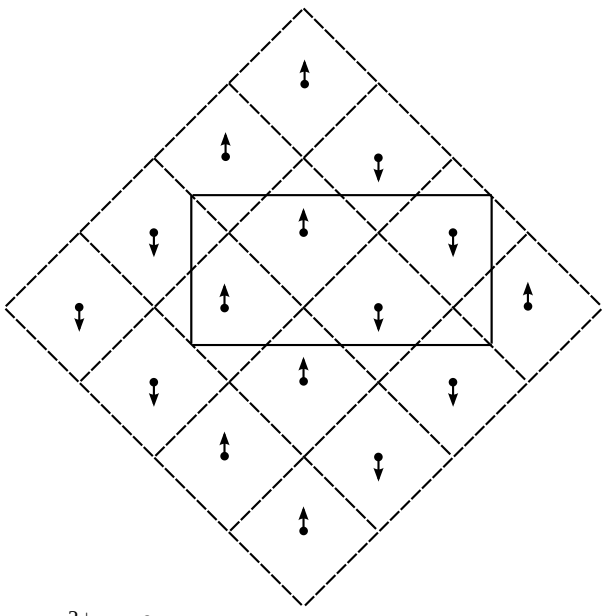

Figure 3.21 *Pb^{2+} shifts along [110] direction within (001) plane of PZO*

In addition to this vibration mode, two other phonons associated to the oxygen octahedra exist i.e. the zone-boundary R_{25} and M_5 modes [13] which correspond to opposite octahedral rotations in successive layers and rotations in the same direction in all layers along the [001]-axis, respectively. As a consequence, such displacements make the [001]-axis polar and thus a zone-centre polar mode Γ_{15} similar to that observed in normal FE like $BaTiO_3$ is also instable and make PZO not a strict antiferroelectric according to Kittel's theory [15] and might explain the weak piezoelectric effect ($\sim 10^{-13}$ C/F

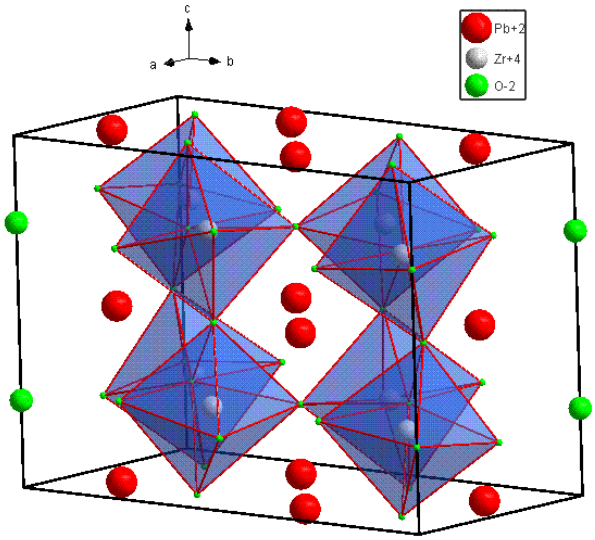

Figure 3.22 *Oxygen octahedra tilts in the unit cell of PZO*

) [135] and the ferroelectric hysteresis loop obtained by Dai [136] at room temperature. The existence of weak ferroelectric behavior is also supported by structural analysis as the noncentrosymmetric Pba2 space group was reported [135] [136] [137] [138]. However, structural refinements with oxygen tilts is not an easy task and moreover it is well known that hysteresis loop measurements have to be considered with care because of parasitic free charges that can results in wrong hysteresis loop. Note that it was reported that there is no geometric similarity between the displacements of the lead ions and the dipole moments responsible for the antiferroelectricity, a two-layer model of the dipole ordering of PZO was proposed [139]. Therefore, the FE behavior at room temperature of PZO remains doubtful and despite many published conflicting studies about the symmetry, a centrosymmetric Pbam space group [140] [141] [142] is now more frequently considered for the structure of PZO description. At high temperature, PZO displays the prototype PE Pm$\bar{3}$m cubic perovskite structure whereas existence of polar clusters [143] [144] associated to anharmonic lead-ions hopping was reported. By decreasing the temperature a pronounced dielectric anomaly [133] [134] [145] is observed at T_C ~505K with a dielectric permittivity value of several thousands similar to first-order like phase transition occurring in classical ferroelectric materials. Based on infrared reflectivity measurements, it was proposed that an overdamped low-frequency mode the so-called central mode dominates in the PE phase and is responsible for most of the strong dielectric anomaly near the phase transition [146]. The phase transition of PZO was investigated by several techniques including X-ray, neutron and electron diffraction [141] [142] [147] [148] [149] [150], Raman spectroscopy [138] [143], electrical conductivity [151], etc. In between the orthorhombic AFE and cubic PE structure, an intermediate FE phase of rhombohedral symmetry was reported [138] [143] [149] [150] [151] in a narrow temperature interval (~10 K) and might present oxygen octahedra rotation mode [150]. However no real consensus exists yet concerning its existence as it seems to be related to the defect concentration and stoichiometry [152]. Moreover, first-principles calculations confirm that it exists a small energy difference between AFE and FE states [153] [154]. Despite still some unclear features, some basic conclusions can be made:

1. There exists a competition between FE (polar) and AFE (antipolar) orders in PZO.

2. Extrinsic factors (temperature, electric field, strain/pressure, defects, doping,...) can easily affect the properties of PZO.

3.4 Reexamination of lead zirconate properties

3.4.1 The stability of AFE

PZO at ambient condition

In general, the anti-parallel displacements of Pb^{2+} along p.c. (110)-direction are associated to the AFE state of PZO. Besides, oxygen tilts are always present when AFE order. To investigate oxygen tilts usually is better to consider neutron diffraction technique. Indeed in X-ray diffraction, light elements have small contribution to the intensity compared to heavy ones. Nevertheless, we performed a RT Rietveld refinement using X-ray data. For this purpose we consider the admitted Pbam space group (note that it is difficult, even impossible to distinguish this space group from the other one proposed i.e. Pba2). to illustrate the role of oxygen tilts, we consider modeling by considering either ideal oxygen octahedra or free to rotate oxygen octahedra. The refinement results are listed in table 3.3 and table 3.4.

Table 3.3 *Refined structural parameters and agreement factors for PZO at room temperature. The coordinates of O were fixed.*

a = 5.88Å	b = 11.77Å	c = 8.22Å		
	Coordinates			
Atom	x	y	z	U
Pb1	0.705	0.130	0	0.0100
Pb2	0.711	0.123	0.5	0.0140
Zr1	0.242	0.124	0.248	0.0013
O1	0.250	0.125	0	0.001
O2	0.250	0.125	0.500	0.001
O3	0.000	0.250	0.250	0.001
O4	0	0.500	0.250	0.001
O5	0	0	0.250	0.001
R = 10.46%,		R_w = 16.05%		
R_F = 5.46%,		$R_F w$ = 6.68%		

There are no significant differences on Pb and Zr coordinates (note that Pb are shifted anti-parallel), but the R factors are obvious larger in no tilts structure model attesting that indeed the ($a^-a^-c^0$) tilt system has to be taken into account. The diffraction patterns of both experimental and calculated structure are shown in fig.3.23.

3.4.2 Existence of a FE intermediate phase or how single-crystal and powder samples are different

The existence or not of an intermediate phase is still debated. Even when it is observed, its polar nature (FE or rather AFE) or its symmetry (rhombohedral) are not clear. Here, we study both ceramic and crystal of PZO using dielectric, pyroelectric, hysteresis loop and XRD measurements.

Dielectric permittivity of PZO as a function of temperature is plotted in Fig.3.24. While for ceramic, an obvious difference between heating and cooling scans over 30K (470K∼500K) can be clearly evidenced, only a sharp dielectric peak which is around 506K is observed in crystal whatever heating or cooling process.

Note that in contrast to our findings, there are some reports showing the existence of an intermediate region even in single crystal [155] [152] [156]. Moreover, in our single-crystal, the similar curve on

Table 3.4 *Refined structural parameters and agreement factors for PZO at room temperature. The coordinates of O were refined.*

a = 5.88Å b = 11.77Å c = 8.22Å				
	Coordinates			
Atom	x	y	z	U
Pb1	0.705	0.129	0	0.0122
Pb2	0.711	0.124	0.5	0.0125
Zr1	0.241	0.124	0.252	0.0013
O1	0.285	0.106	0	0.001
O2	0.266	0.165	0.500	0.001
O3	0.031	0.262	0.242	0.001
O4	0	0.500	0.304	0.001
O5	0	0	0.279	0.001
R = 9.08%, R_w = 14.61%				
R_F = 3.02%, $R_F w$ = 3.50%				

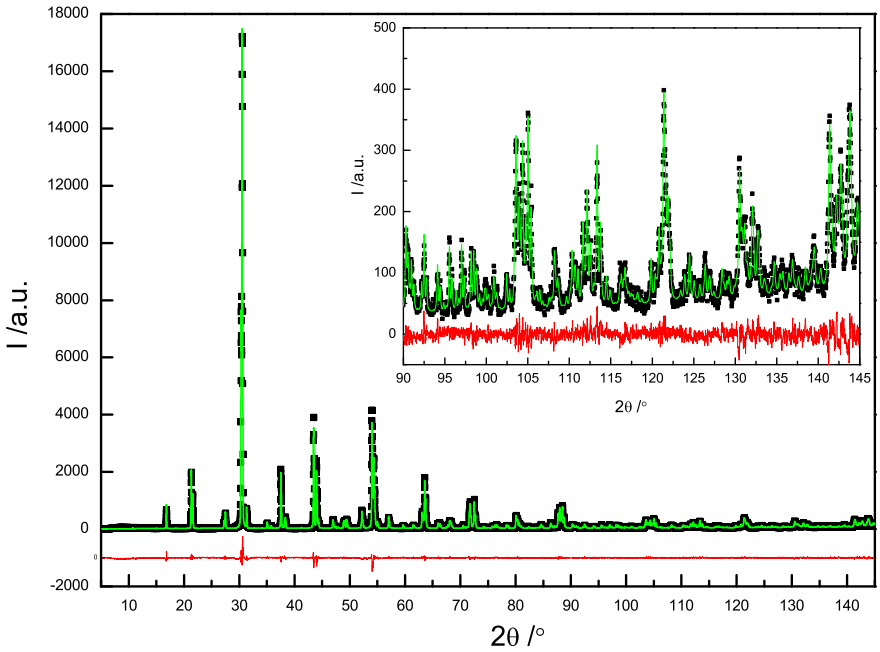

Figure 3.23 *Diffractogram of PZO with Rietveld refinement*

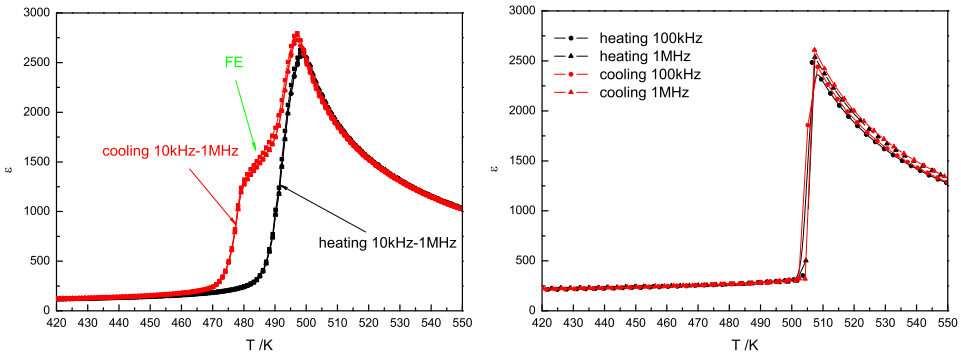

(a) Ceramic (b) Crystal

Figure 3.24 *Dielectric permittivity versus temperature of PZO*

heating and cooling (no hysteresis loop) suggests a second order phase transition despite the discontinuous jump of the dielectric constant. Let us first investigate the intermediate state observed in ceramic sample. To determine the possible polar character of the intermediate phase, pyroelectric current and FE hysteresis loop measurements were performed. It is worth mentioning that the intermediate phase was observed in several studies [151] [155] [138] [152] [143] [141] [142] [148]. Some of them support a FE phase [151] [155] [138] [152] [143] while others support rather a AFE phase [141] [142] [148]. Here, the pyroelectric current is measured on heating and cooling the ceramic sample around the phase transition region. On heating, a current peak at 500K is observed with a shoulder at 504K while on cooling two well separated peaks at 484K and at 505K are evidenced (fig. 3.25(a)). These peaks confirms the existence of two phase transitions.

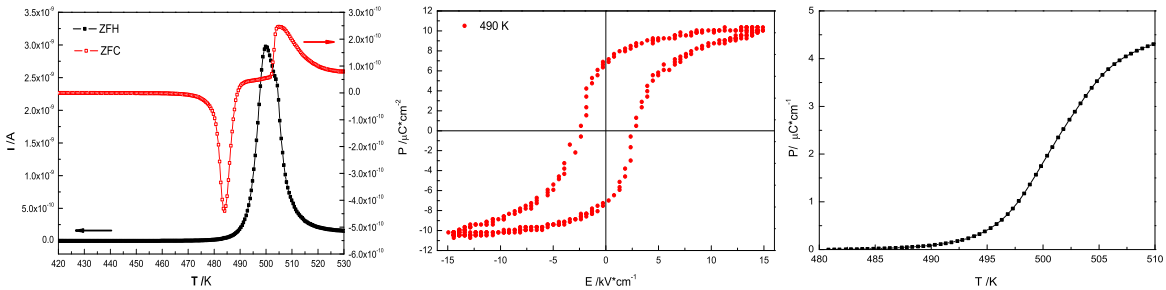

(a) (b) (c) Polarization by pyroelectric measurement

Figure 3.25 *Ferroelectric properties of PZO. (a) shows pyroelectric current on heating and cooling. (b) shows a ferroelectric hysteresis loop at 490K. (c) shows calculated polarization by pyroelectric current data*

In the intermediate region i.e. from 490K to 505K on heating and from 475K to 500K on cooling, it is possible to measure a FE hysteresis loop. Fig. 3.25(b) shows the hysteresis loop at 490K which is typical of a FE behavior and thus confirms the FE nature of the intermediate phase. The remanent polarization P_r of PZO at 490K is around 7 μ C/cm^{-2}. Using the pyroelectric current, the polarization can be also calculated through $P = \int \frac{I}{S*v} dT$, where v is the rate of heating, S is the area of the disk sample, T is the temperature. The as-determined polarization on heating is plotted in fig. 3.25(c). It gives a polarization value of 4.6 μ C/cm^{-2} which is very close to that determined from hysteresis loop.

The phase transitions can also be investigated using x-ray diffraction measurements. For the single crystal which is oriented along [00l] direction, the p.c. (400) is recorded from 300K to 600K by heating sample. In case of the ceramic, p.c. (111), (200), (220), (222) Bragg peaks are measured from 300K to 800K on heating. Some Bragg peaks at different temperatures are plotted in 3.26 for illustration.

It is clear that the strong shift of the (400) peak for the crystal and the splitting of the Bragg peaks in the ceramic indicate the phase transitions. Using a Pseudo-voigt shape to fit these data from 300K to

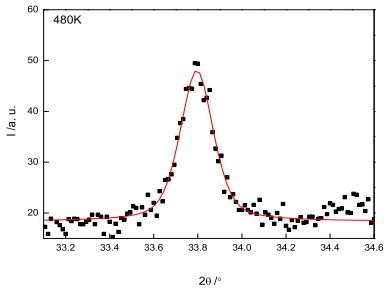

(a) p.c. peak (111) at 480K for ceramic sample

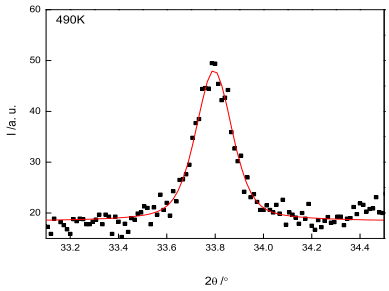

(b) p.c. peak (111) at 490K for ceramic sample

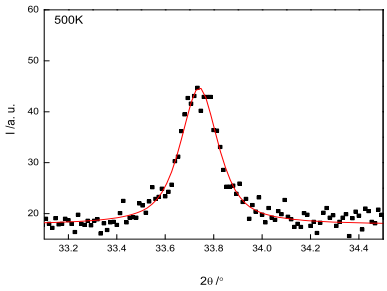

(c) p.c. peak (111) at 500K for ceramic sample

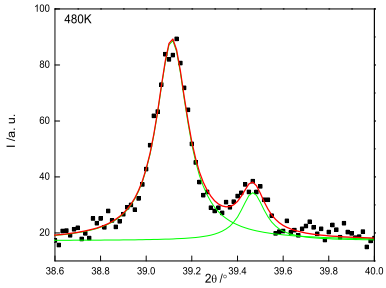

(d) p.c. peak (200) at 480K for ceramic sample

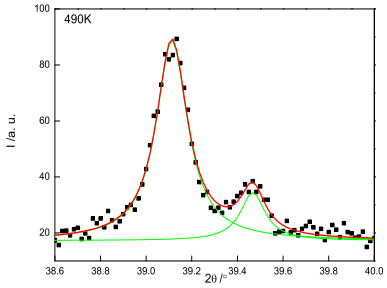

(e) p.c. peak (200) at 490K for ceramic sample

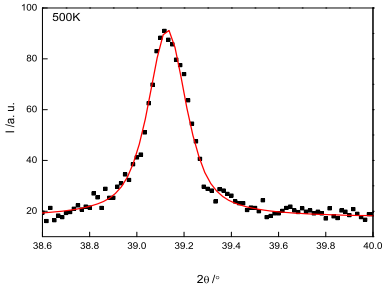

(f) p.c. peak (200) at 500K for ceramic sample

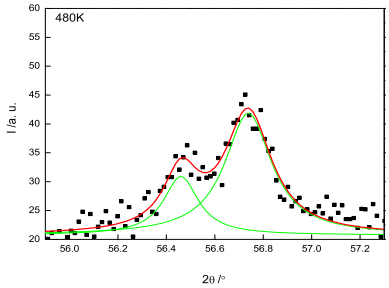

(g) p.c. peak (220) at 480K for ceramic sample

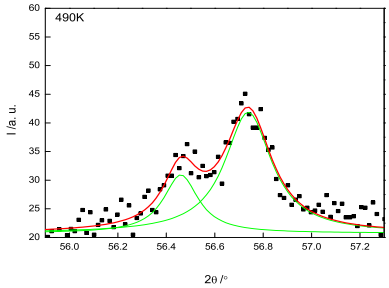

(h) p.c. peak (220) at 490K for ceramic sample

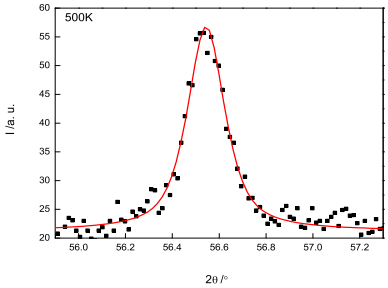

(i) p.c. peak (220) at 500K for ceramic sample

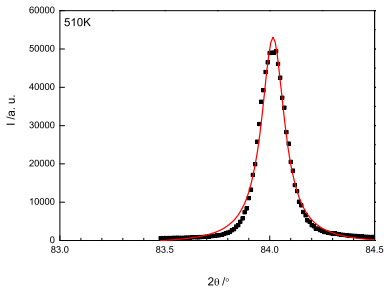

(j) p.c. peak (004) at 510K for crystal sample

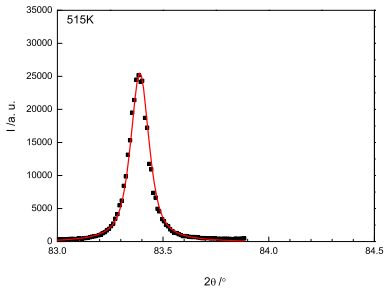

(k) p.c. peak(004) at 515K for crystal sample

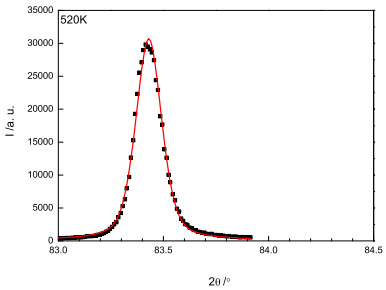

(l) p.c. peak(004) at 520K for crystal sample

Figure 3.26 *Some p.c. Bragg diffraction peaks of PZO at different temperatures*

600K , the lattice parameters normalized for comparison between crystal and ceramic are shown in fig. 3.27(a).

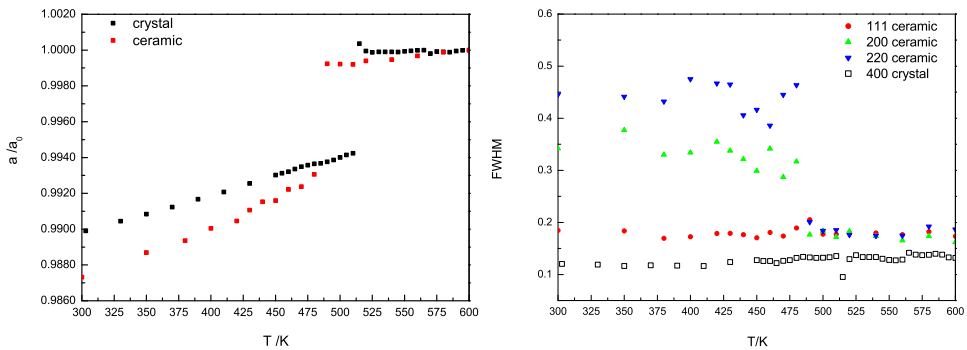

(a) Normalized lattice parameters (b) FWHM

Figure 3.27 *Normalized lattice parameters (a) and FWHM (b) as a function of temperature for PZO.*

For the ceramic, the structural phase transition occurs at 490K while for crystal the phase transition occurs at higher temperature i.e. at 515K. For both the phase transition is accompanied by a strong volume change of 0.6%. For both samples the phase transition, according to the jump in the volume of the unit cell, is of first order. This suggests then that even for the single crystal, the dielectric constant (see fig 3.24(b)) should display at least a weak hysteresis through heating and cooling. The Note that for the ceramic, it is difficult to extract properly the lattice parameters within the intermediate region, it is why it does not appear in fig. 3.27(a). To exctract much more information on this intermediate FE phase, the FWHM is also plotted (3.27(b)) in addition to the data (peak position and width) of p.c. (222) diffraction peak measured on heating and cooling around the phase transition(see fig. 3.28).

Having a look to fig. 3.28(c) and 3.28(d) a clear hysteresis on cooling and heating is observed. It is worth noting that on heating the change through the intermediate phase is soft compared to that on cooling. It is clear that the intermediate phase is FE and thus it is excluded that this temperature region can be explained by a phase coexistence of AFE orthorhombic low temperature phase and PE cubic high temperature phase. Rather one has to imagine another phase phase which is FE and should have a non-centrosymmetric structure. Some authors have suggested a rhombohedral FE phase. However, this solution can be safely excluded because while (222) peak indeed broadens in the intermediate phase, the (200) peak broadens too which is not compatible with a rhombohedral symmetry. Assumming a first-order phase transition towards a FE phase which can not be neither rhombohedral nor tetragonal ((222) peak is splitted) and because of group-sub-group relationship, it is possible to suggest an orthorhombic phase with a Amm2 space group. Indeed such phase corresponds to the FE orthorhombic phase of $BaTiO_3$ and satisfy all above requirements. We did some Rietveld refinements to check this possibility. It is clear that the Amm2 phase gives a better agreement factors and better matching between experimental-calculated diffraction patterns than a cubic or rhombohedral phase (R_F are 4.39%, 4.50% and 5.25% for Amm2, R3m and $Pm\bar{3}m$ respectively).

PZO under electric field

It was not possible to induce at RT, the FE state from the AFE state by applying an external electric field. The reason is that the voltage to be applied is very strong i.e. roughly 22 MV/m and thus the breakdown occurs before (10MV/m). To induce such transition using such high electric field, the idea is to go towards thin film. Here we rather decided to investigate the effect of the electric field in the FC regime as we did for pure PFW in the previous section. Fig 3.29 shows the dielectric constant on FC regime for electric field values from 0kV/cm to 7kV/cm.

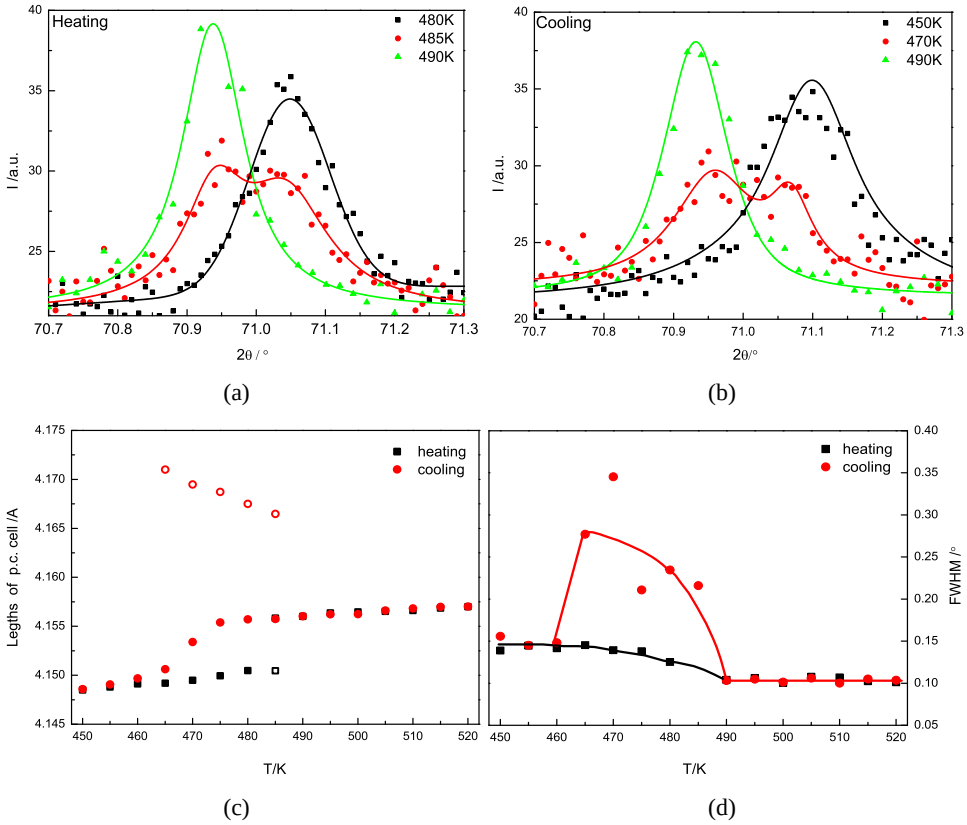

Figure 3.28 *A intermediate phase is proved by X-ray diffraction of P.c. (222) peak. (a) P.c. Bragg peak (222) at selected temperatures on heating. (b) P.c. Bragg peak (222) at selected temperatures on cooling. (c) calculated lattice parameters (d) FWHM.*

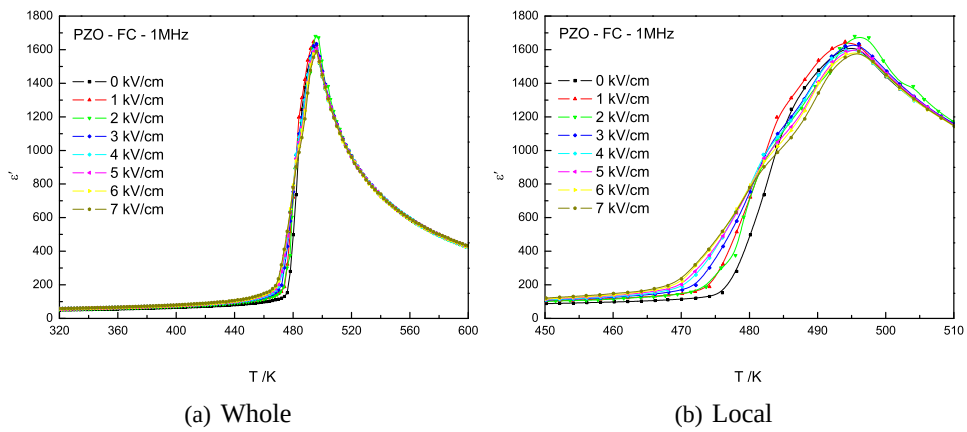

Figure 3.29 *Dielectric permittivity of PZO for different electric field strengths on FC regime*

As one may see no significative change is observed. Having a careful look (see fig. 3.29(b)) around the phase transition one can see that the electric field affects the slop of the discontinuity (the region where the intermediate FE phase is observed for ceramics). The slope is decreasing with the electric field or in other words the phase transition is broad. This tendency vanishes in the ZFHaFC regime (see fig 3.30).

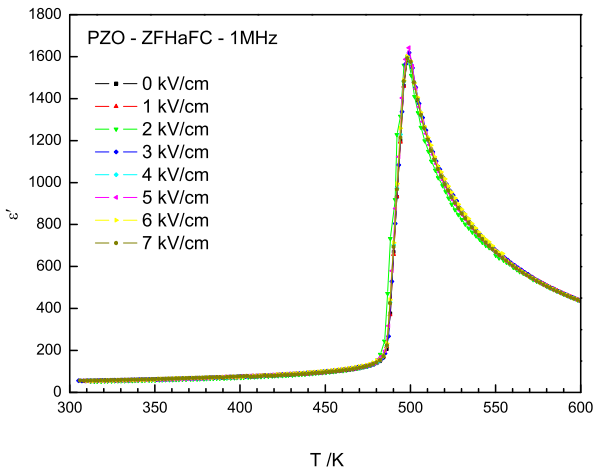

Figure 3.30 *Dielectric permittivity versus temperature on ZFHaFC regime*

It appears that the electric field does not affect efficiently the properties of PZO. This can be explained by the rather weak electric field applied and thus push further research towards thin films where much higher electric field values can be reached.

PZO under pressure

As mentioned before in order to improve the efficiency of the electric field, one has to decrease the thickness of the sample and thus to go towards thin films. It is well-known that one of the main effect of such size reduction is the stress/strain coming from the clamping onto the substrate. It is not our goal here to study thin films but rather to bring some understanding elements on the effect of stress on the structure. Therefore in this paragraph we investigate the effect of hydrostatic pressure in order to highlight what would be the consequences on the structure of PZO.

At RT, the AFE configuration in PZO is stabilized. However, a FE phase can be induced under strong enough electric field (2.2×10^7 V/m) [157] [158]. The polarization in AFE state comes from Pb^{2+} shifts along pseudo cubic $[\bar{1}10]$ or $[1\bar{1}0]$ direction. The electric field will rotate all the polar vectors of 90° but still remaining within the (001) plane.

Such instability can also be produced by external stress. Generally, the stability of the structure is balanced between the long-range coulomb forces and short-range electronic repulsions. The pressure has been revealed as a powerful tool to influence interatomic distance and thus is widely used to investigate structure (in-)stability of ferroelectrics for a long time [159] and multiferroics more recently [160] [161].

The high pressure behavior of PZO was studied by DTA [162], dielectric measurements [163] [164], Raman spectroscopy [165] [166] and ab initio method [167] [168]. The first studies have found triple phase points around 0.64 GPa [162] or 0.5 GPa [163]. Most recent studies have been rather performed at room temperature and used higher pressure value for the investigation. As a matter of fact, several phase changes have been evidenced. For instance, there are obvious color changes on PZO at 19 GPa and 37 GPa [164]. Using Raman spectroscopy phase transitions were found near 2.3 and 17.5 GPa [165] [166]. A broad dielectric peak at ∼3 and a sharp one at 19 GPa have evidenced by dielectric measurements [164]. Ab initio method have demonstrated the occurence of a phase transition at 4 GPa which is related

with M_3 mode [168]. Moreover, while X-ray diffraction measurements have showed that orthorhombic phases are stabilized under high pressure, it was proposed that PZO structure becomes monoclinic at 39.9 GPa and changes to another monoclinic phase at 75.9 GPa [164]

High pressure synchrotron x-ray diffraction experiments of PZO were performed at the European Synchrotron Radiation Facility (ESRF) on the ID27 beamline up to 60.79 GPa in collaboration with P. Bouvier and J. Kreisel from LMGP (Grenoble). The wavelength used is 0.3738 Åand is selected by a iodine K-edge filter and focused to a beam size of about 3 μm. The powder sample was loaded in a diamond-anvil cell (DAV) with diamond tips of diameter 250 μm and helium is used as pressure transmitting medium. The two dimension diffraction images were analyzed using the ESRF Fit2D software yielding intensity versus 2θ diffraction patterns.

After a careful inspection of the diffraction patterns looking for superstructure reflections and splitting of main refection peaks, at least five different phases as a function of pressure can be evidenced at critical pressures: 4.56 GPa, 7.83 GPa, 19.81 GPa, 33.08 GPa and 55.87 GPa.

At ambient pressure and temperature, PZO has an orthorhombic AFE structure with *Pbam* space group. There is an obvious superstructure diffraction peak which is indexed as ($\frac{3}{4}$ $\frac{1}{4}$ 0) associated to the multiplicity of the unit cell (the unit cell is multiplied 4 times in a and b directions). This superstructure is then of interest to investigate the evolution of the ambient orthorhombic phase. This extra peak is fitted using a Pseudo-Voigt shape as a function of pressure. The pressure dependent parameters are plotted in fig. 3.31.

Comparing the interplanar distance of superstructure distance, there are obvious jumps of the superstructure interplane distance at 4.56 GPa, 7.83 GPa and 33.08 GPa. Comparing the FWHM of the superstructure, it starts broad at 55.87 GPa. We also calculated the integral area of superstructure diffraction, the minimum occurs at 31.3 GPa where no superstructure diffraction was found (see fig. 3.35(a)).

We first checked that after pressure releasing the sample recovers its orthorhombic structure. While back to ambient pressure the structure indeed recovers its orthorhombic phase (same peaks and same peak positions and widths) the intensity changes (see fig. 3.31(c)) and thus reflects the domain configuration changes rather than a new symmetry phase. Therefore the investigation is done carefully by comparing all the structural features (peak position, width, intensity) to avoid any misinterpretation.

Looking at the superstructure peak position (fig.3.31(a)), three anomalies can be evidenced. The first one occurs between 0.87 GPa and 4.56GPa. Unfortunately we do not have enough data to conclude on the exact value of the first critical pressure that we fixed to 4.56GPa. Note that a change of the peak width reflects alos this change (fig. 3.31(b)). Another anomaly is clearly seen at 7.83 GPa on all the parameters (fig. 3.31). The most obvious changes occurs at 33.08 GPa with a strong decrease of the interplane distance and an inversion in the intensity evolution. In addition, two other anomalies, more subtle, can be evidenced. The less obvious one appears at 19.81GPa and can be seen on the change of slope of the intensity (fig. 3.31(c)) and an other higher pressure one can be seen in the change of width occuring at 55.87GPa (fig. 3.31(b)). Both critical pressures are confirmed in the following.

In addition to the superstructure peak, the p.c. (110) peak is also considered to determine the critical pressures. The fitted parameters were plotted in fig. 3.32.

It is obvious that both interplanar distance and FWHM of p.c. (110) show changes at the critical pressures. The pressure dependent interplanar distance displays changes at 19.8 GPa, 33 GPa and 55 GPa while the pressure dependent width shows modifications at 6-7 GPa, 20 GPa, 33 GPa and 56 GPa. The pressure evolution of p.c. (110) gives the same phase transition information as superstructure diffraction. The change at 20GPa which was subtle considering the superstructure peak is now more obvious because of the splitting of main Bragg peak as illustrated in fig. 3.33(a). The same situation occurs also for the high 56GPa pressure phase transition (see fig. 3.33(b)).

To summarize six different stable phases are found in PZO under high pressure. The typical diffraction patterns are plotted in fig. 3.34.

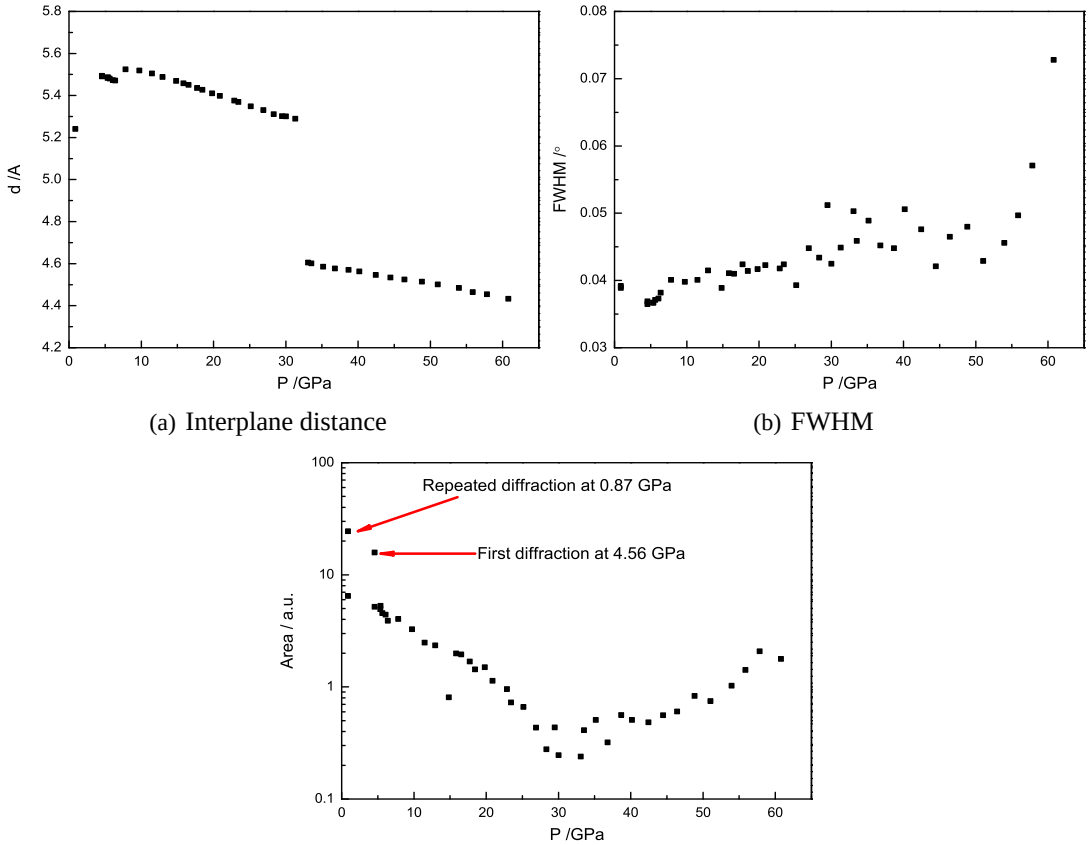

(a) Interplane distance (b) FWHM

(c) Integral area

Figure 3.31 *Pressure dependent fitted parameters of superstructure diffraction*

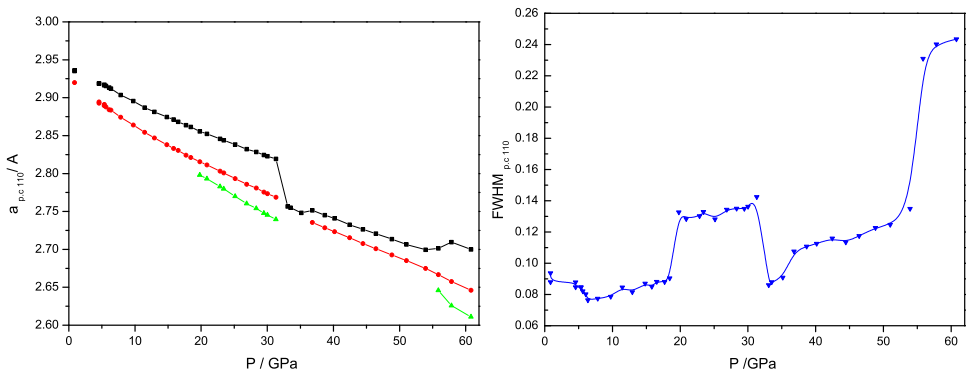

(a) $d_{p.c.(110)}$ (b) FWHM

Figure 3.32 *Pressure dependence of interplane distance and FWHM*

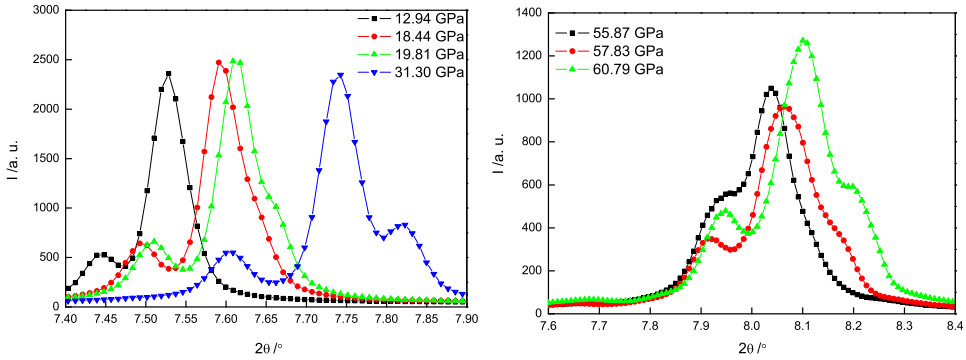

(a) Phase transition around 20GPa (b) Phase VI

Figure 3.33 *P.c. Bragg peak (110) at selected pressures*

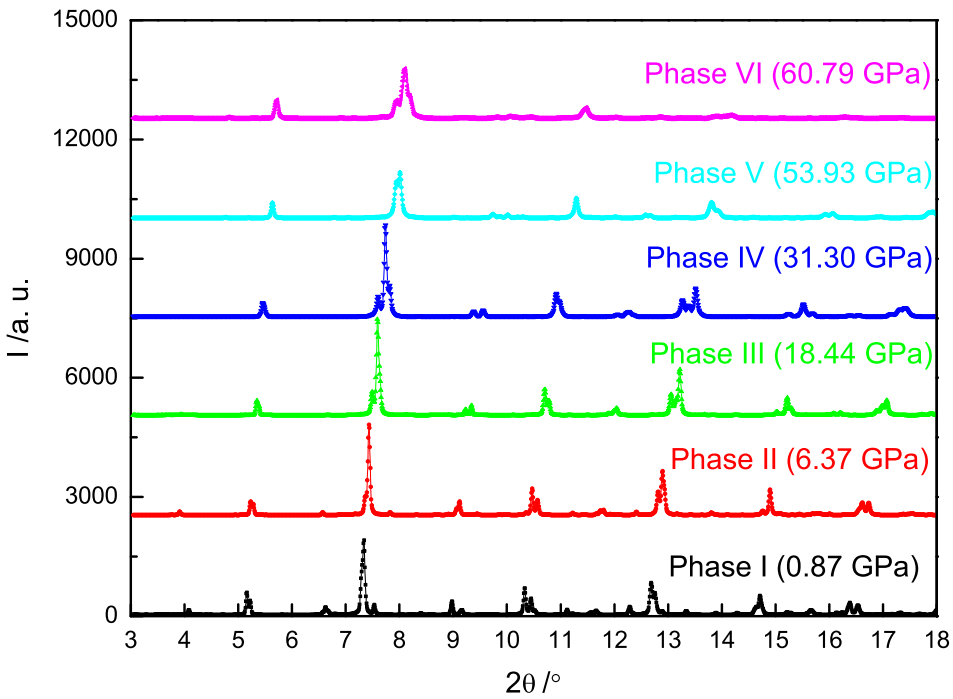

Figure 3.34 *X-ray diffraction patterns at selected pressures*

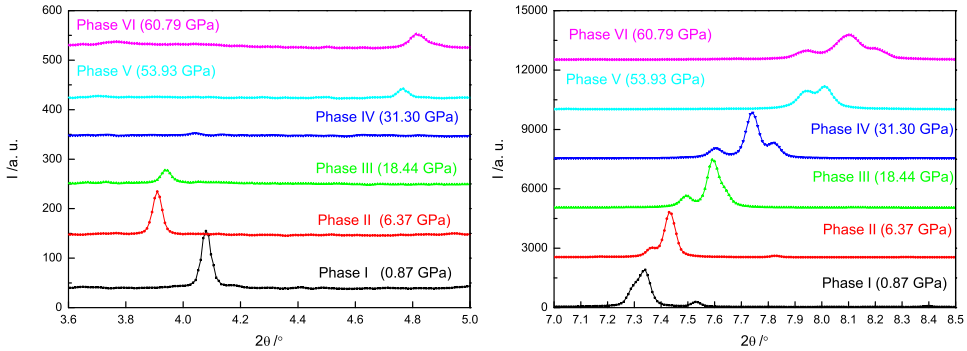

(a) Superstructure (b) Main Bragg p.c. (110)

Figure 3.35 *Superstructure and main Bragg p.c. (110) peak in different phases*

The six high pressure phases of PZO are named phase I to VI on increasing pressure up to 60.79 GPa. Besides, in order to illustrate the main changes between the different phases, fig. 3.35(a) and fig 3.35(b) are a focus of 2θ region associated to the superstructure peak and the main (110) Bragg peak.

Fig. 3.35(b) shows clear splitting associated to each phase and fig. 3.35(a) shows clear changes of the shape and position of the superstructure. Note that for 31.30 GPa, the superstructure peak is almost absent.

The phase transition between phase I and phase II occurs between 0.87 GPa and 4.56 GPa, this is consistence with the phase transition evidenced by Raman spectroscopy near 2.3 GPa [165] [166], the broad dielectric peak at ∼3 GPa [164] and the 4 GPa phase transition found by ab initio calculations [168].

The phase transition between phase II and phase III occurs at 7.83 GPa (or 6.37 GPa) and was not reported before. The phase transition between phase III and phase IV occurs at 19.8 GPa and is in agreement with the color change, the sharp dielectric peak at 19 GPa [164] and Raman data suggesting a phase transition at 17.5 GPa [165] [166].

The phase transitions between phase IV and phase V occuring at 33.08 GPa and that between phase V and VI occurring at 55.87 GPa could be related to the two high pressure monoclinic phases found by X-ray diffraction at 39.9 GPa and 75.9 GPa [164].

Using Crysfire software [88] the unit cell parameters are determined for pressure below 30GPa considering an orthorhombic-like phase. It is worth mentioning that above 30GPa, the same treatment is not possible because it was not possible to extract a satisfying structure. Depending on the FOM (Figure of Merit) of different unit cells and the results of profile using Jana2006 software, the lattice parameters are obtained. The result is presented in table 3.5.

The phase I is similar with the RT structure of PZO, a = $\sqrt{2}a_{p.c.}$, b = $2\sqrt{2}a_{p.c.}$, c = $2a_{p.c.}$ having a multiplicity of 8 (8 formula unit).

In the phase II the b axis increases and the unit cell is well described with a = $\sqrt{2}a_{p.c.}$, b = $3\sqrt{2}a_{p.c.}$, c = $a_{p.c.}$ having a multiplicity of 12. Note that the c parameter could be also multiplied by two as in the ambient condition. To extract properly the lattice parameters, for both I and II phases, we used a Rietveld refinement assuming a Pbam space group. Note that the agreement factor is not good and thus Pbam model does not reproduce the measured diffraction patterns above 4.56GPa. Indeed while the position are well reproduced there are some discrepancies in the intensity.

For the phase III and phase IV, we did Rietveld refinement using the another space group for all the pressure values. We first started the refinement with the data at 31.30GPa because the superstructure intensity is not detectable. At 31.30 GPa, the best refinement is obtained using a Cmmm space group. Fig.3.36 shows a very good matching between experiment and calculated pattern.

In this Cmmm orthorhombic structure having two formula unit, the lattice parameters are a = $\sqrt{2}a_{p.c.}$, b = $\sqrt{2}a_{p.c.}$, c = $a_{p.c.}$. The data of the Rietveld refinement at 31.30 GPa are listed in table 3.6. The refinement is improved using anisotropic thermal factors as reported in table 3.7.

Table 3.5 *The effect of pressure on the lattice parameters of PZO*

P /GPa	a/Å	b/Å	c/Å	$a_{p.c.}$/Å	$b_{p.c.}$/Å	$c_{p.c.}$/Å	$V_{p.c.}$/Å^3
			Phase I				
0.87	5.866	11.754	8.212	4.148	4.156	4.106	70.776
0.87	5.864	11.751	8.209	4.146	4.155	4.104	70.708
			Phase II				
4.56	5.791	17.506	4.072	4.095	4.126	4.072	68.801
4.56	5.790	17.508	4.071	4.094	4.127	4.071	68.780
5.37	5.786	17.496	4.068	4.091	4.124	4.068	68.635
5.35	5.782	17.488	4.066	4.088	4.122	4.066	68.523
5.62	5.779	17.483	4.064	4.086	4.121	4.064	68.434
6.08	5.771	17.472	4.060	4.081	4.118	4.060	68.229
6.37	5.767	17.459	4.057	4.078	4.115	4.057	68.080
			Phase III				
7.83	5.803	5.742	4.048	4.103	4.060	4.048	67.441
9.74	5.788	5.721	4.037	4.093	4.045	4.037	66.839
11.47	5.771	5.697	4.024	4.081	4.028	4.024	66.149
12.94	5.760	5.680	4.014	4.073	4.016	4.014	65.663
14.81	5.747	5.659	4.002	4.064	4.002	4.002	65.077
15.82	5.740	5.647	3.996	4.059	3.993	3.996	64.763
16.53	5.733	5.638	3.991	4.054	3.987	3.991	64.500
17.71	5.725	5.623	3.982	4.048	3.976	3.982	64.094
18.44	5.720	5.615	3.978	4.045	3.970	3.978	63.882
			Phase IV				
19.81	5.711	5.600	3.970	4.038	3.960	3.970	63.483
20.88	5.704	5.588	3.963	4.033	3.951	3.963	63.158
22.86	5.689	5.565	3.951	4.023	3.935	3.951	62.543
23.42	5.686	5.559	3.948	4.021	3.931	3.948	62.395
25.15	5.675	5.541	3.937	4.013	3.918	3.937	61.900
26.88	5.663	5.521	3.926	4.004	3.904	3.926	61.374
28.33	5.655	5.509	3.920	3.999	3.895	3.920	61.061
29.48	5.647	5.496	3.912	3.993	3.886	3.912	60.706
30.02	5.644	5.491	3.910	3.991	3.883	3.910	60.588
31.30	5.635	5.478	3.902	3.984	3.874	3.902	60.224

Table 3.6 *Refined structural parameters and agreement factors for PZO at 31.3 GPa*

a = 5.636Å b = 5.478Å c = 3.902Å				
	x	y	z	U
Pb	0	0	0.5	0.0071
Zr	0.5	0	0	0.0018
O1	0.25	0.25	0	0.0906
O2	0.5	0	0.5	0.2062
R = 5.44%, R_w = 7.39%				
R_F = 4.08%, $R_F w$ = 4.48%				

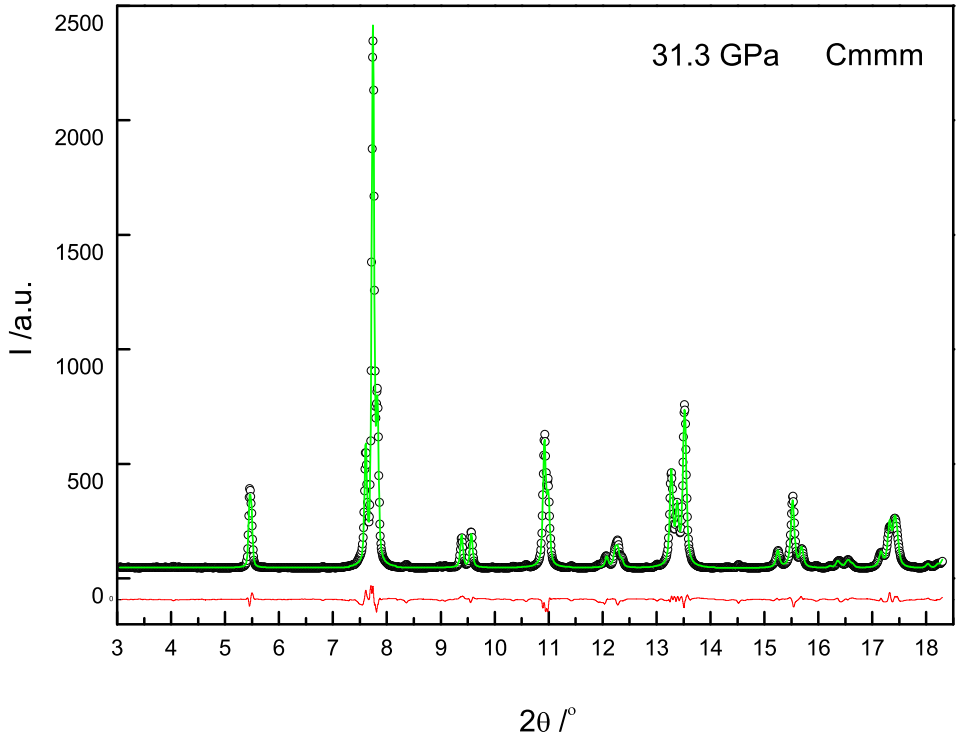

Figure 3.36 *Diffractogram of PZO with Rietveld refinement at 31.3 GPa*

Table 3.7 *Refined anisotropic thermal parameters for PZO at 31.3 GPa*

a = 5.635Å b = 5.478Å c = 3.902Å						
	U_{11}	U_{22}	U_{33}	U_{12}	U_{13}	U_{23}
Pb	0.0201	0.0043	-0.0010	0.0000	0.0000	0.0000
Zr	0.0089	-0.0141	0.0070	0.0000	0.0000	0.0000
O1	-0.0184	0.2277	0.4747	-0.1229	0.0000	0.0000
O2	0.4789	-0.0029	-0.0932	0.0000	0.0000	0.0000
R = 4.01%, R_w = 5.40%						
R_F = 2.21%, $R_F w$ = 2.59%						

In Cmmm group, the Pb^{2+}, Zr^{4+} and O^{2-} are fixed by symmetry and there are no oxygen octahedral tilting. It is interesting to remark that Cmmm is a supergroup of Pbam (No. 55) which is the ambient pressure structure of PZO and a supergroup of Cm2m (No. 123)which is the electric field induced FE structure in PZO. No improvement is obtained using this last ferroelectric group and thus we can not conclude on the polar character of the real structure. Note that the change of unit cell can be looked as an extending or a shrinking of the b axis with the anti-parallel shifts of Pb^{2+} decreasing continuously until becoming zero at 31.3 GPa.

Concerning the pressure between 7.83GPa and 31.30GPa, we used Cmmm space group to determine properly the unit cell parameters with Jana2006 through Rietveld refinements. Note nevertheless that Cmmm is not the true space group as there is superstructure peaks for all the pressure values (fig. 3.37 and fig. 3.38).

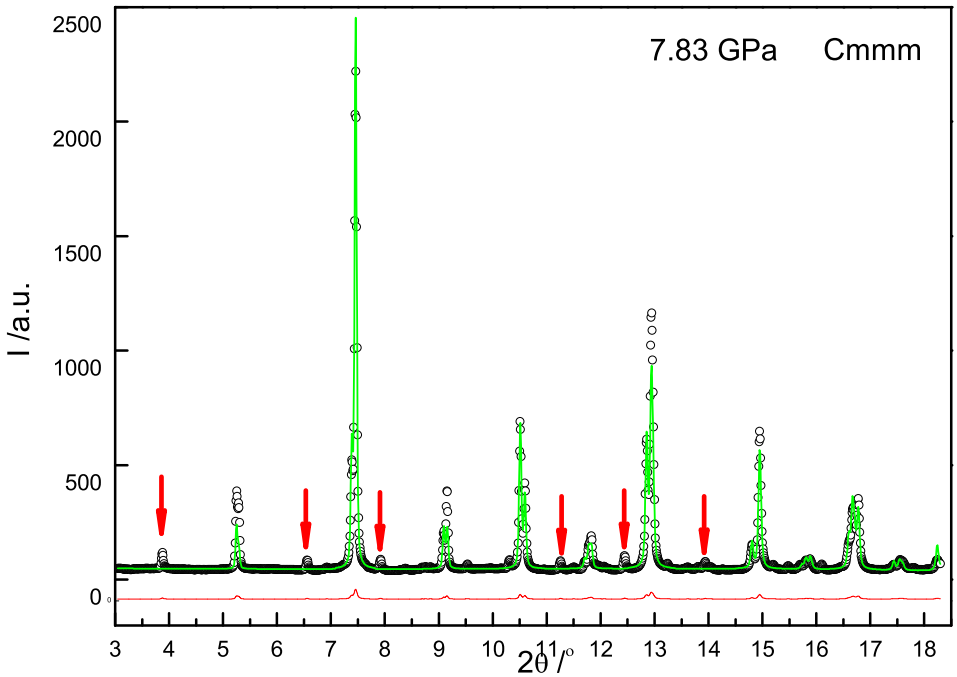

Figure 3.37 *Diffractogram of PZO with Rietveld refinement at 7.83 GPa (arrows indicates superstructure peaks)*

Note that the only pressure where the superstructure is not seen is 31.30GPa but below and above this pressure we still continue to observe it. Indeed fig. 3.39(a) shows a selected region of the diffraction pattern for a couple of pressure showing obvious change of the structure and at the same time fig 3.39(b) shows clear superstructure peaks in this new phase.

The p.c. cell volume is fitted by a third-order Birch-Murnaghan EoS by EOS-FIT (V5.2) [169] from 0.87 GPa to 31.3 GPa. There is a good fit agreement as shown in fig. 3.40.
V_0 is found to be equal to 70. 99 Å, very close to ambient p.c. volume of PZO which is 71.11 Å. K_0 is 146.12 GPa a value between 104 for $PbMg_{1/3}Nb_{2/3}O_3$ [170] and 238 for $BiFeO_3$ [160], K_P is 3.34 between 2.2 of $BiFeO_3$ [160] and 4.7 of $PbMg_{1/3}Nb_{2/3}O_3$ [170].

More complex phase transitions occur above 31.30 GPa (see fig.3.35(a) and fig. 3.35(b)). Phases IV, V and VI show clear splittings but unfortunately no satisfying space group to describe the structure was found. Note nevertheless that the cubic phase is never reached even at the highest pressure value as observed in other systems like in normal ferroelectric $PbTiO_3$ [171], relaxor ferroelectric $PbZn_{1/3}Nb_{2/3}O_3$ [172] or multiferroic $BiFeO_3$ [160] [161].

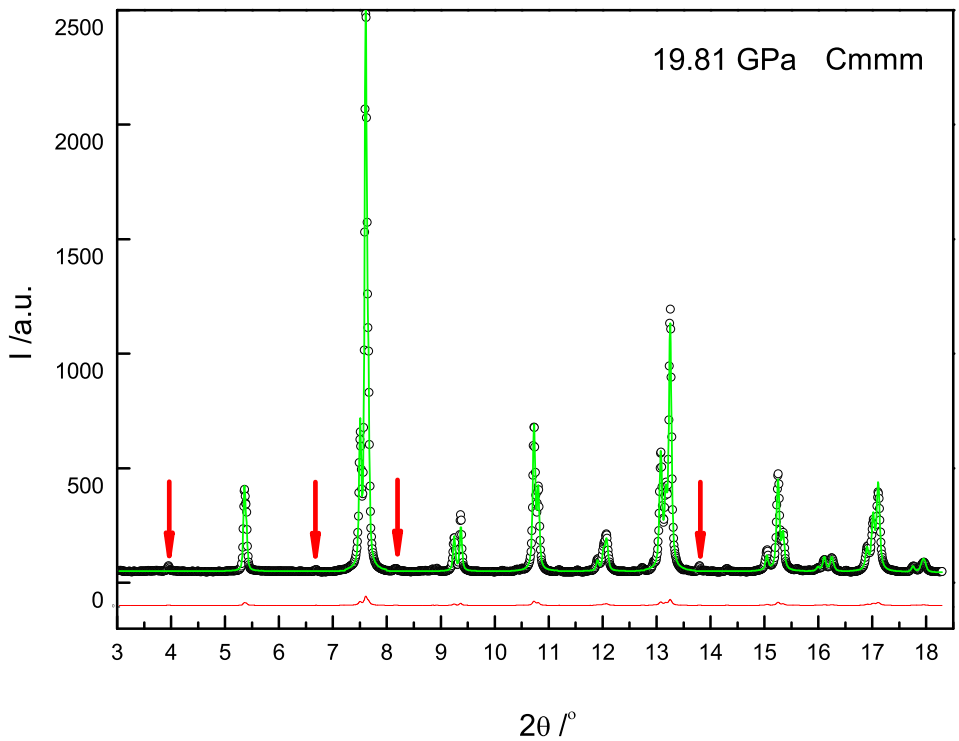

Figure 3.38 *Diffractogram of PZO with Rietveld refinement at 19.81 GPa (arrows indicates superstructure peaks)*

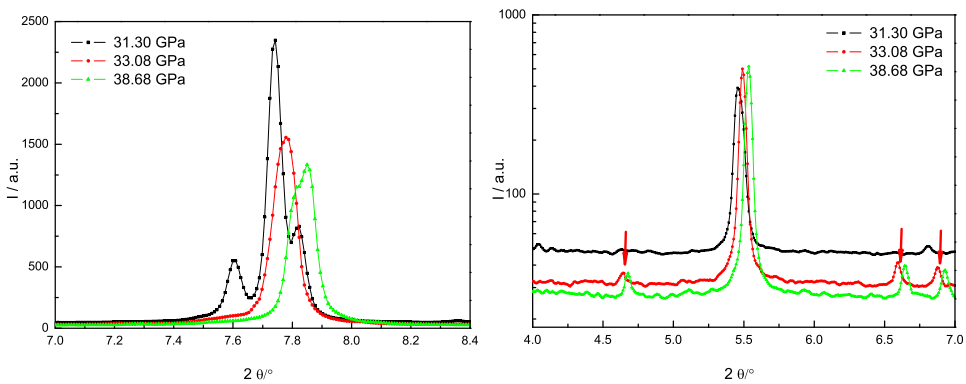

(a) Main Bragg p.c. (b) Superstructure

Figure 3.39 *Diffraction patterns for selected 2θ regions at 31.30, 33.08, 38.68 GPa*

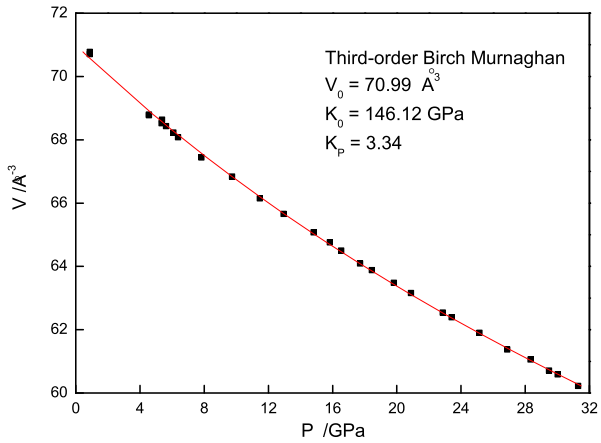

Figure 3.40 *Pressure-dependent evolution of unit-cell volume of PZO*

3.5 Conclusion

In this chapter, we investigate in details the different properties of both PFW and PZO. In case of PFW, there exists a long-range and short-range both polar and magnetic orders. This situation is explained through several instabilities which are in competition. Several peculiar temperatures have been evidenced including the freezing temperature (150K), the temperature associated to macroscopic polarization (170K), the local Curie temperature (240K) at which a phase transition can be induced using an external electric field, the Néel temperature (358K) and the spin-glass one (5K). All these physical properties can be related to the structure. Indeed while the structure remains cubic on average, several structural changes in the volume can be evidenced. The key entities behind both polar and magnetic properties are directly related to the local Pb disorder and to chemical inhomogeneities through random distribution of Fe and W ions and some local chemically ordered regions.

PZO is antiferroelectric with an orthorhombic structure having oxygen octahedra tilts. There exist also some instabilities especially in the region approaching the cubic phase with competition with a FE intermediate phase. The stability of the AFE phase can be also affected using external pressure. Indeed, five presure-induced phase transitions have been found.

It is then of interest to combine both compounds in order to get a solid solution having several kinds of instabilities. This is the goal of the next chapter.

Chapter 4

Lead Iron Tungsten - Lead Zirconate Solid Solution System

Preparing solid solution system is a common strategy for adjusting critical temperatures and bringing new and (or) unexpected properties. In fact, there are already many tentative strategies using PFW as a end member for either fabricating room temperature FE or studying interesting multiferroic behaviors. In this chapter, following a short literature on PFW based solid solution systems, the interesting and rich properties of PFW-PZO will be introduced.

4.1 Literature review on lead iron tungsten based solid solution systems

4.1.1 PFW-PTO

$PbTiO_3$ (PTO) is a well-studied displacive type of ferroelectic material. It has tertagonal symmetry (space group P4mm) with the spontaneous polarization vector parallel to the c-axis. and undergoes a cubic-to-tetragonal first-order phase transformation upon cooling at 763K [173] [174].

In order to modify polar orders [119] [175] [178] [110] [179] [182] [41] [115] [120] or fabricate novel multiferroic materials [180] [181] [115] [184], PFW-PZO solid solution was considered recently. A complete solid solution between PFW and PTO can be gotten by solid reaction method.

Fig.4.1(a) shows the polar diagram of PFW-PZO by combing various dielectric, different scanning calorimetry (DSC) and X-ray diffraction methods. A slight rhombohedral distortion was found for small PTO content solid solution; large PTO content solid solution crystallize in a PTO like P4mm structure. A morphotropic phase boundary (MBP) was found between $\sim$ 20% PTO and $\sim$ 40% PTO where both rhombohedral and tetragonal coexist.

Different with polar phase diagram, many confused conclusions were obtained for magnetic phase transition. Magnetic phase diagram of PFW-PTO shows in fig. 4.1(b) which was plotted by combining the experiments of SQUID [180] [115] and acoustic emission (AE) [184]. Firstly, a low temperature phase transition (T_{N1} in the figure) was found, in addition to the antiferromagnetic phase transition (T_{N2} in the figure). In our opinion, T_{N1} is spin glass phase transition as in pure PFW. Second, the tendency of T_{N2} with the content of PTO is not clear. People even proposed a core-shell model to explain the confusion [184] [183].

4.1.2 PFW-PZT

After starting the work of PFW-PZO, we noticed a encouraging result which are published in 2009. Magnetic control polarization is possible in $PbFe_{2/3}W_{1/3}O_3$-$PbZr_{0.53}Ti_{0.47}O_3$ (PFW-PZT) [185] [186] [187].

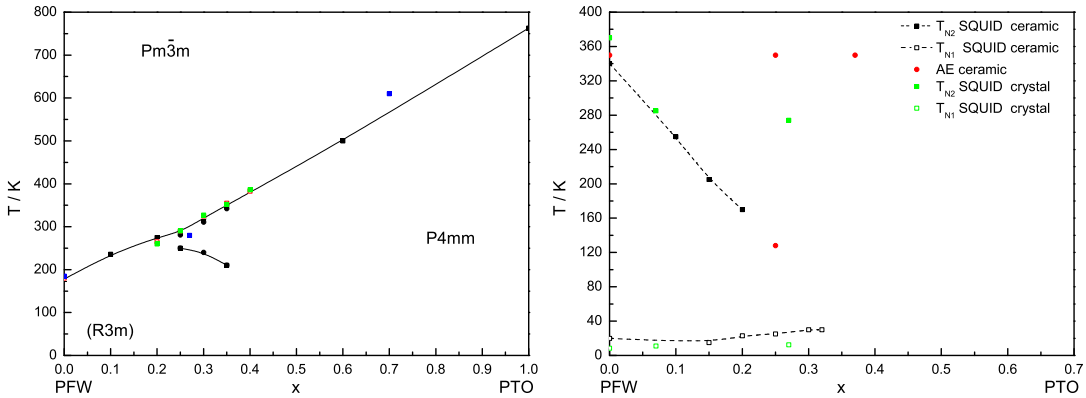

(a) Polar phase diagram (b) Magnetic phase diagram

Figure 4.1 *Phase and magnetic diagrams of PFW-PT. x represents the quantity of PTO in the solid solution. In fig (a), square points are experimental data of dielectric; Circle points are experiments of DSC; data from different authors are separated by color of points. In fig (b), two magnetic phase transitions were marked by T_{N1} and T_{N2} which is related to antiferromagnetic phase transition; black points are the experimental data of SQUID; red points are the experimental data of AE; green point are the single crystal data.*

Fig. 4.2 shows magnetic field control of polarization; magnetic field switches polarization to zero at 0.5 T. The result suggests the strong magnetoelectric coupling in PFW-PZT which is look as a birelaxor, consistence with strong magnetoelectric coupling in magnetoelectric relaxor and magnetoelectric multiglass [188] [189]. However, magnetic field switched-off polarization in PFW-PZT was not observed by other authors [190] [191].

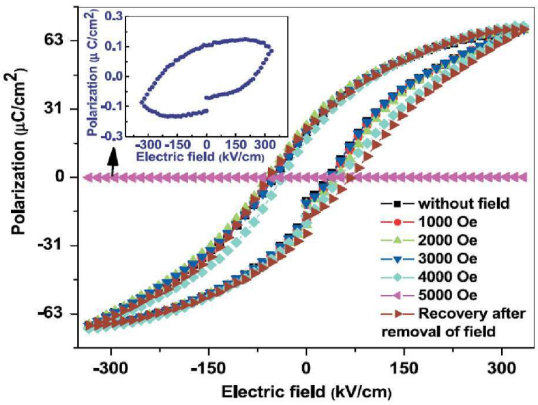

Figure 4.2 *P-E hysteresis under the application of external magnetic field from 0 to 0.5 T changes polarization to zero. The inset is the P = 0 relaxor state on expanded scale, showing a linear lossy dielectric [185].*

4.1.3 Antiferromagnetic phase transition

Considering our aim of fabricating novel multiferroic by combining PFW and PZO, it is emergent to get a clear information that how is antiferroelectric magnetic phase transition influenced by solid solution. Unfortunately, we did not find obvious conclusion in PFW-PTO. Here, the phase transition is consider by combining the results of PFW-PTO with other PFW based solid solutions, $PbFe_{2/3}W_{1/3}O_3$-$PbFe_{1/2}Nb_{1/2}O_3$(PFW-PFN) [192], $PbFe_{2/3}W_{1/3}O_3$-$PbSc_{2/3}W_{1/3}O_3$(PFW-PSW) [193], $PbFe_{2/3}W_{1/3}O_3$-$PbSc_{2/3}W_{1/3}O_3$-$PbTiO_3$(PFW-PSW-PTO) and $PbFe_{2/3}W_{1/3}O_3$-$PbSc_{2/3}W_{1/3}O_3$-$BiFeO_3$(PFW-PSW-BFO) [194].

We plotted the relationship between antiferromagnetic phase transition T_N and content of Fe^{3+} in related solid solution which is shown in fig. 4.3. T_N is localed between 160K and 360K but there is not a clear regulation between T_N and content of Fe^{3+}. After careful checked all the original literature, we find that antiferromagnetic phase transition is weak peak on magnetic susceptibility. Also, magnetic field dependent spin glass phase transition is not noticed by many authors. The misnamed T_N may be published.

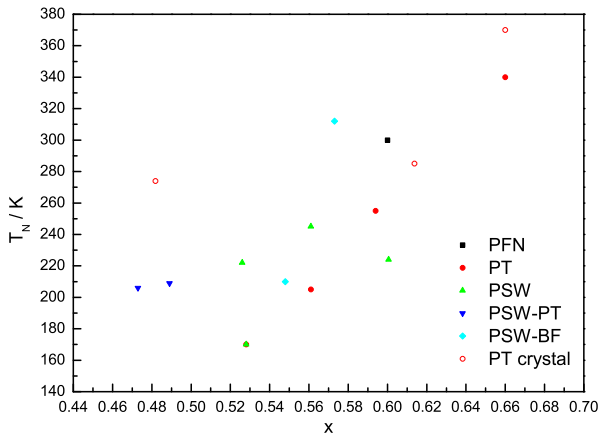

Figure 4.3 *T_N versus content of Fe^{3+} for PFW based solid solution. Black point represents datum of PFW-PFN; the red, green, blue and cyan points represent data of PFW-PT, PFW-PSW, PFW-PSW-PT, PFW-PSW-BF respectively, soft red points represent data of PFW-PT single crystal.*

4.2 PFW-PZO solid solution

PFW-PZO is a good candidate to study. We already demonstrated that many degrees of freedom exist in both PFW and PZO. PFW is a so-called relaxor ferroelectric with a T_C near to 180K and exhibits an antiferromagnetic phase transition below T_N near 358K and a spin glass phase transition near 5K. It is already a multiferroic and possesses for both ferroic parameters, short- and long-range orders and thus strong instability with respect to external stress. $PbZrO_3$ (PZO) is an antiferroelectric with high T_C near to 500K and exhibits a ferroelectric phase which is sensitive to temperature, sample... . Moreover, PZO alsp displays oxygen octahedra tilts (or antiferrodistorsive) in addition to antipolar structural shifts. In tilted structure, A-ions off-centering on adjacent ions are not equivalent, which may favor AFE state rather a FE one in the non-tilted structure [14]. In short, antiferrodistorsive is needed for antiferroelectic. Very often magnetic compounds crystallize in tilted phase (e.g. Pnma), (La, Sr)MnO3. Thus, antipolar and/or AFE with magnetism should coexist interestingly. Also, complete solid solution is possible [195] and critical temperature must approach room temperature.

After many tentative experiments, we successful fabricated complete (100-x)$PbFe_{2/3}W_{1/3}O_3$-x$PbZrO_3$ (xPZO, x varies from 0 to 100)solid solution without any parasitic phase. Instead of describing specific preparing processing, we will directly discuss the interesting properties of the solid solution.

4.3 Crystal structures of PFW-PZO

The crystal structures of PFW-PZO were firstly investigated at room temperature by X-ray diffraction which is produced by Cu target including both $k_{\alpha 1}$, $k_{\alpha 2}$ beams. After directly checking diffraction patterns, we found that a PFW similar structure keeps up to 40PZO. Then, a new type diffraction pattern was observed from 50PZO to 90PZO; at last, a PZO like structure appeared for 95PZO. Non super-

structure diffraction was found in all the diffraction patterns, it suggests that all compounds crystallize in a perovskite structure which is also expected because both PFW and PZO are perovskites.

Rietveld refinement was used to investigate precise structural informations for PFW-PZO. The homogeneous powder samples were used for data collection. The data were collected from 5° to 147° which is the maximum of our diffractometer by a step 0.02 5°, at every points stay 10s.

It is very surprising PFW-like cubic even exist for 40PZO because PFW already becomes instable after % PTO for solid solution PFW-PTO. Therefor, both cubic Pm$\bar{3}$m and a polar R3m space groups which is the most possible model were considered during Rietveld refinement. However, R3m does not show any advantagies because there is non obvious shifts of cantions and larger R factors were gotten comparing with cubic Pm$\bar{3}$m space group. In this average cubic structure, a parameter of unit cell increases by a step of 0.2 Åfor every 10% PZO. Because Zr^{4+} has larger ionic radius comparing with W^{6+} or Fe^{3+} [196], the evolution of lattice parameter suggests the B site replaced by Zr^{4+}.

The splitting regulations of Bragg peaks satisfy rhombohedral symmetry when the content of PZO changes from 50% to 90%. All the compounds were successful refined by a rhombohedral R3m space group. The simulation and experimental data match very well, i.e. shown in fig.4.4, fig.4.5 and 4.6.

The cubic Pm$\bar{3}$m space group was also built for comparing. The p.c. Bragg (200) and (222) peaks are plotted in fig. 4.7 including the simulated peaks. Rhombohedral model gives much better matching profile for both (200) and (222) peaks than cubic. In fact, cubic give R_F 5.33 and R_{FW} 5.47 which are significantly larger comparing with R_F 2.27% and R_{FW} 2.96% by rhombohedral structure. Also, abnormal u factors were found during simulation by cubic structure. We will see the dielectric properties also imply intrisic different between 40PZO and 50PZO.

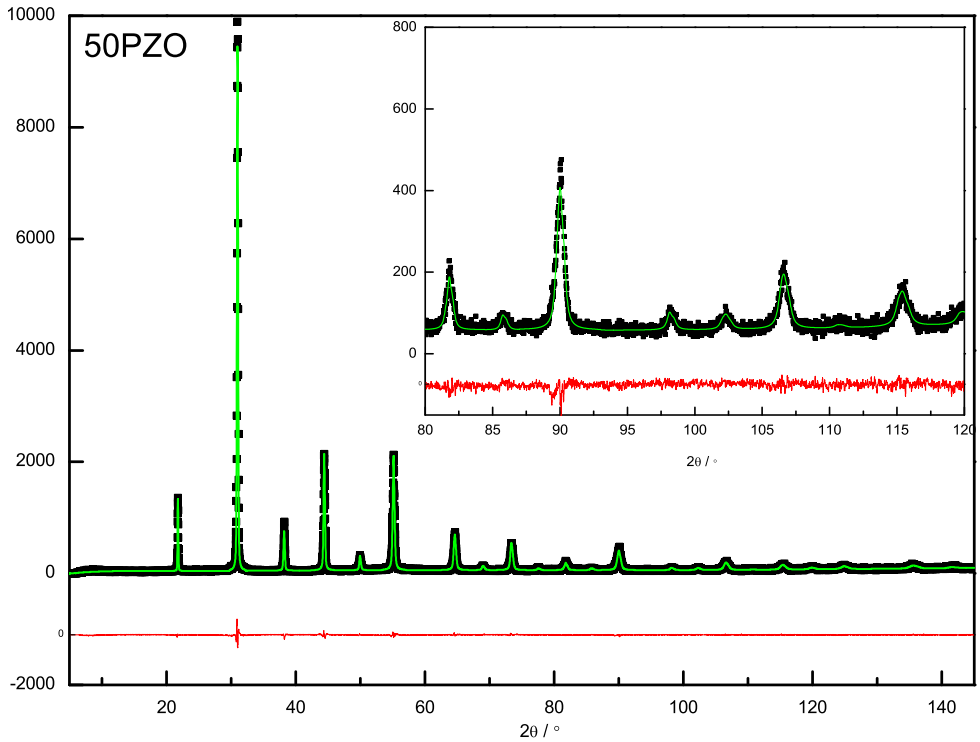

Figure 4.4 *Rietveld refinement plots for 50PZO. Points are experimental data; green lines are simulated diffraction peaks; red lines are the differences between two.*

The hexagonal triple obverse cell was used during refinement. There are three formula units for every cell. The Pb^{2+} coordinates was firstly directly decided by change flipping method and then refined. Rietveld refinement gives us the crystallographic data of the solid solution, i.e. table4.1, 70pzo-

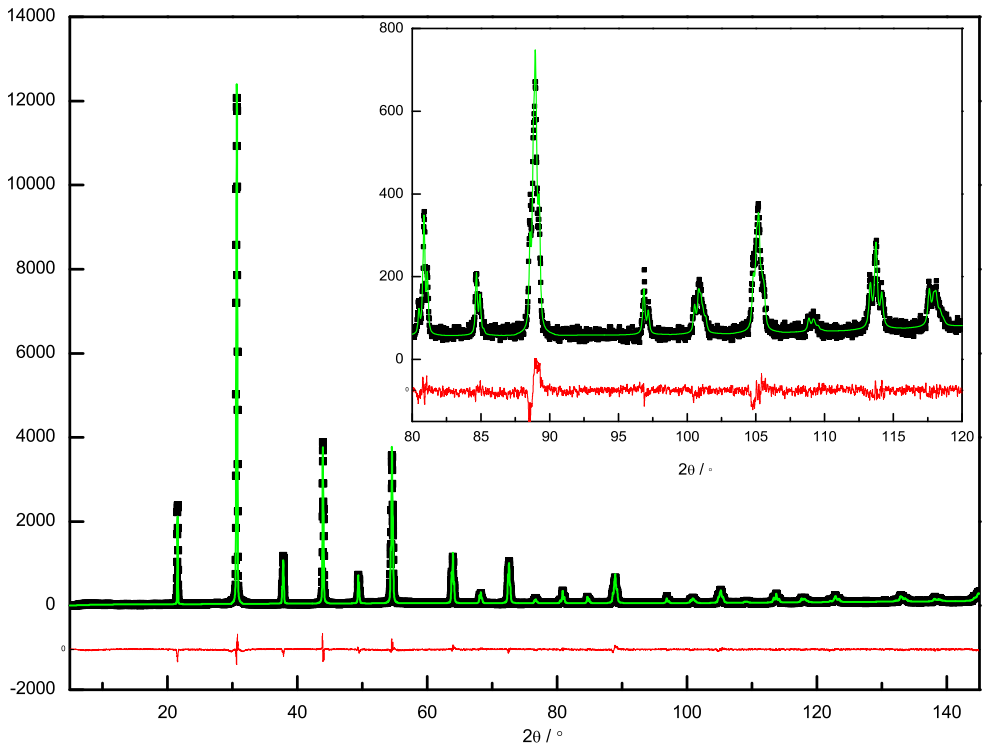

Figure 4.5 *Rietveld refinement plots for 70PZO. Points are experimental data; green lines are simulated diffraction peaks; red lines are the differences between two.*

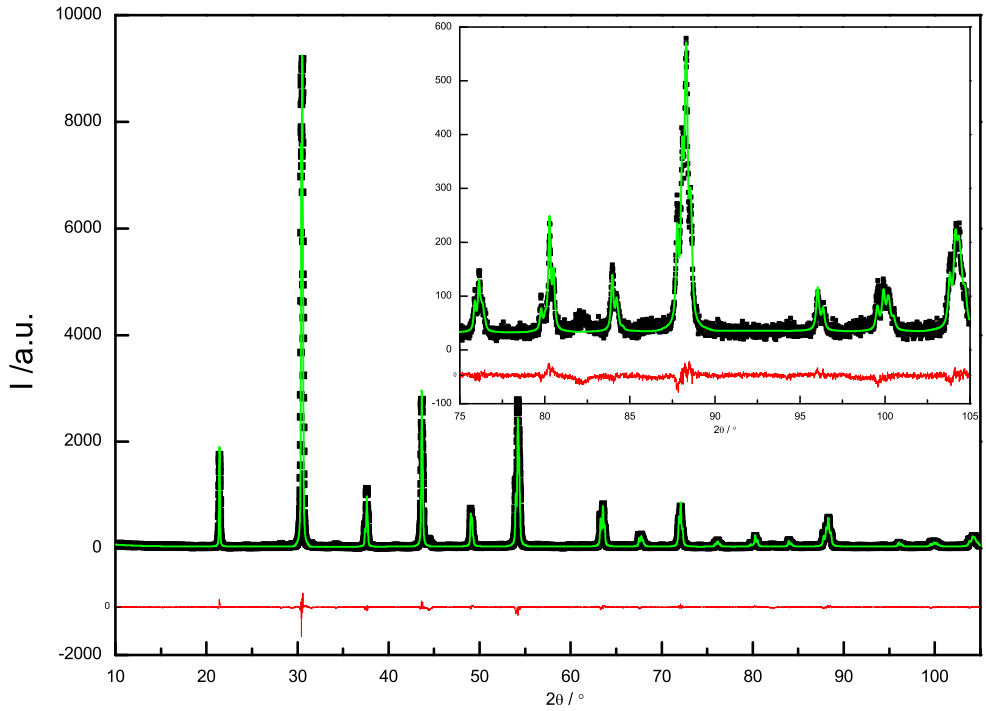

Figure 4.6 *Rietveld refinement plots for 50PZO. Points are experimental data; green lines are simulated diffraction peaks; red lines are the differences between two.*

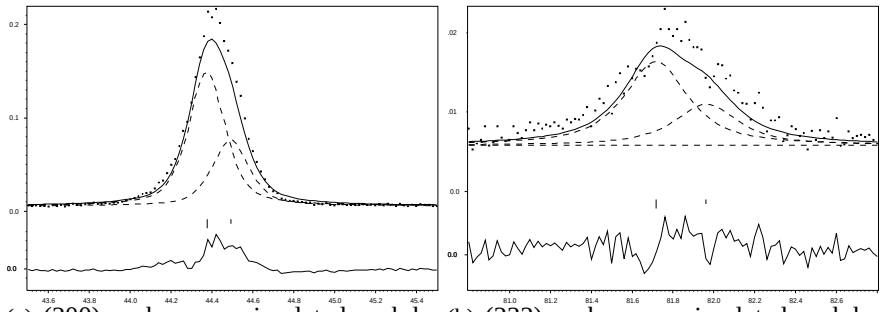

(a) (200) peak versus simulated peak by cubic model

(b) (222) peak versus simulated peak by cubic model

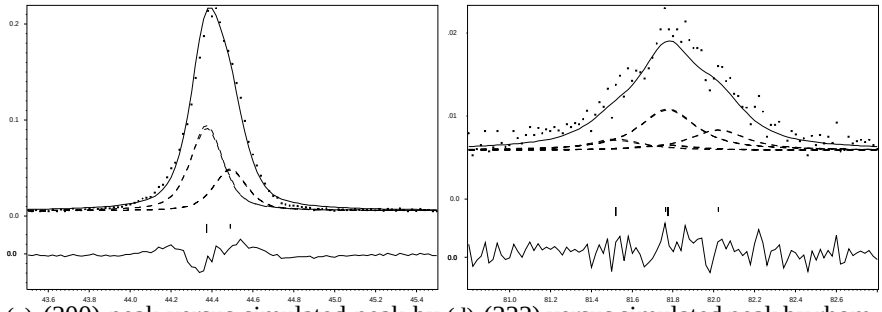

(c) (200) peak versus simulated peak by rhombohedral model

(d) (222) versus simulated peak by rhombohedral model

Figure 4.7 *P.c. Bragg (200) and (222) peaks (points) versus simulated diffraction peaks (lines) for 50PZO at 300K*

refinement and 4.3 show the data of 50PZO, 70PZO and 90PZO.

Table 4.1 *Refined structural parameters and agreement factors for 50PZO at room temperature*

a = 5.763Å c = 7.074Å				
	Coordinates			
Atom	x	y	z	U
Pb1	0	0	0.500	0.0619
Zr1	0	0	-0.030	0.0044
Fe1	0	0	-0.030	0.0044
W1	0	0	-0.030	0.0044
O1	0.3910	0.1955	0.1399	0.0030
R = 9.24%, R_w = 12.34%				
R_F = 2.27%, $R_F w$ = 2.96%				

Ferroelectric spontaneous polarization origins from the the shits of ions in a unit cell, i.e. , the Ti^+ shift in a BTO unit cell. Therefore, polarization can be directly calculated according to atomic coordinate and unit cell parameters by formula:

$$P_C = \frac{1}{V}\sum_i Q_i \vec{r}_i \tag{4.1}$$

Here, V is the unit cell volume, Q is the charge of i ion, $\vec{r}_i$ is the shit of i ion. The formula give a direct method to calculate polarization, in deed, we did calculate for PFW-PZO. We find that the major contributor to polarization is Pb^{2+} (fig.4.8). The results, once again, prove that lone pair Pb^{2+} is the origin of lead based ferroelectric.

X-ray diffraction pattern of 95PZO is similar with PZO, suggesting orthorhombic antiferroelectric

Table 4.2 *Refined structural parameters and agreement factors for 70PZO at room temperature*

a = 5.816Å c = 7.154Å				
	Coordinates			
Atom	x	y	z	U
Pb1	0	0	0.637	0.0529
Zr1	0	0	0.101	0.0013
Fe1	0	0	0.101	0.0013
W1	0	0	0.101	0.0013
O1	0.380	0.190	0.249	0.0188
R = 9.61%, R_w = 13.57%				
R_F = 2.52%, $R_F w$ = 3.34%				

Table 4.3 *Refined structural parameters and agreement factors for 90PZO at room temperature*

a = 5.850Å c = 7.206Å				
	Coordinates			
Atom	x	y	z	U
Pb1	0	0	0.724	0.0334
Zr1	0	0	0.189	0.0069
Fe1	0	0	0.189	0.0069
W1	0	0	0.189	0.0069
O1	0.332	0.166	0.328	0.0365
R = 10.96%, R_w = 15.41%				
R_F = 3.72%, $R_F w$ = 4.29%				

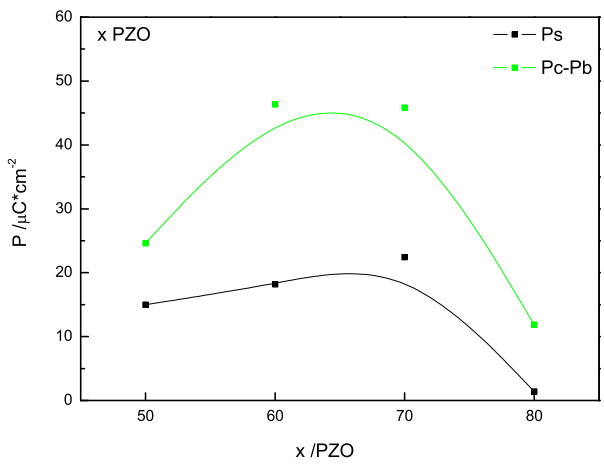

Figure 4.8 *Polarization versus compositions. Black points are experimental data; green points are calculated by Pb^{2+} shifts.*

structure. For illustration, we show the Room Temperature (RT) Rietveld refinement results. The experimental diffraction pattern and the calculated one are plotted in fig. 4.9 and the refined parameters are listed in table 4.4. During refining, the ADP of oxygens are rational fixed. The anti-parallel displacements of Pb^{2+} along p.c. [110]-direction are 0.25Åand 0.19Å. The values are slight smaller than the anti-parallel displacements of Pb^{2+} in PZO which are 0.26Åand 0.23Å.

Table 4.4 *Refined structural parameters and agreement factors for 95PZO at room temperature*

a = 5.86Å	b = 11.75Å	c = 8.21Å		
	Coordinates			
Atom	x	y	z	U
Pb1	0.793	0.131	0	0.021
Pb2	0.783	0.122	0.5	0.011
Zr1	0.257	0.119	0.251	0.0047
Fe1	0.257	0.119	0.251	0.0047
W1	0.257	0.119	0.251	0.0047
O1	0.229	0.119	0	0.001
O2	0.215	0.120	0.500	0.001
O3	0.998	0.261	0.273	0.001
O4	0	0.500	0.243	0.001
O5	0	0	0.245	0.001
R = 13.04%,		R_w = 16.80%		
R_F = 7.27%,		$R_F w$ = 8.08%		

The structural study of PFW-PZO reveals three structures, cubic, rhombohedral and orthorhombic depending on the content of PZO (fig. 4.10). Interestingly even unexpected, cubic is quite stable up to 40PZO. However, a local polar order and oxygen octahedra distortion is strongly expected because of PNRs in PFW and antiferrodistortive in PZO. The continuing deformation of rohombohedral was found after 40PZO by composition adjusting effect (fig.4.10(a)). The unit cell volume linear enlarges up to 90PZO, accompanying a reducing which marks the appearing of orthorhombic structure. Rhombohedra is a classic ferroelectric structure, thus room temperature ferroelectric is possible in PFW-PZO as we already described by polarization calculation.

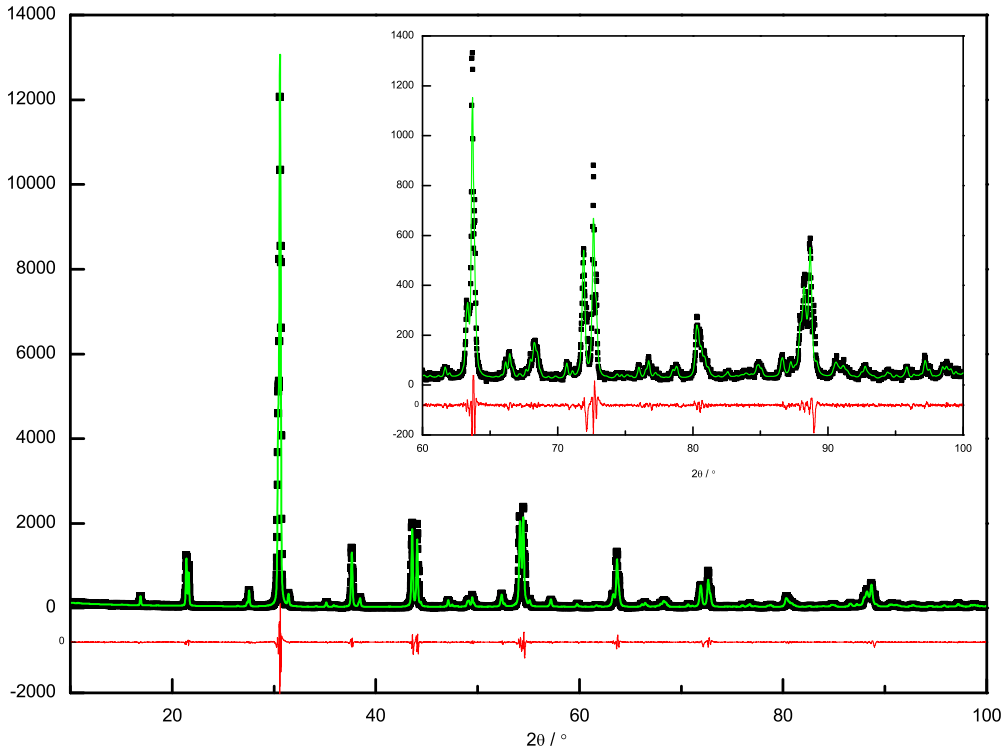

Figure 4.9 *Rietveld refinement plots for 95PZO. Points are experimental data; green lines are simulated diffraction peaks; red lines are the differences between two.*

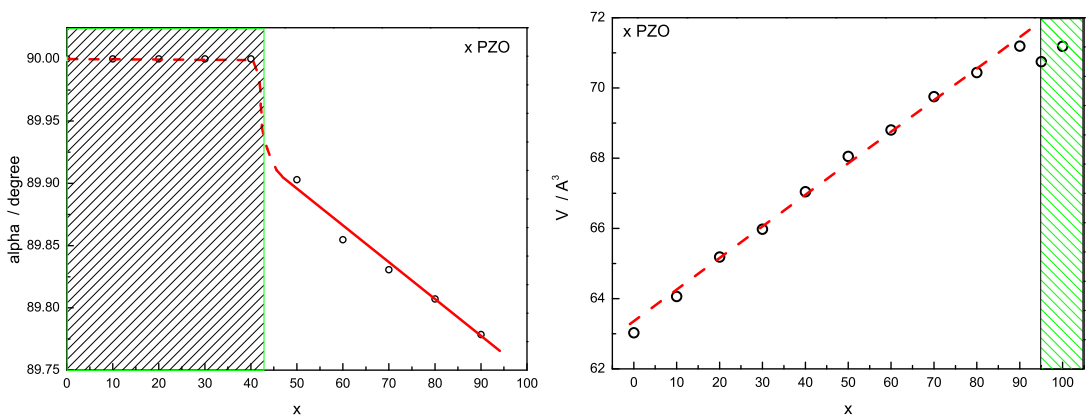

(a) α (b) V

Figure 4.10 *Rhombohedral deformation angle (α) and unit cell volume (V) as a function of content of PZO (x)*

4.4 Phase transitions and polar properties of PFW-PZO

4.4.1 (100-x) PFW - x PZO: 0 < x $\leq$ 40

Phase transitions

It is interesting to investigate the stability of cubic solid solution because the rich local phase transitions were found even in pure PFW. The Bragg (200), (220) and (222) peaks were recorded from 80K to 450K, i.e., Bragg peaks of 40PZO are plotted in fig.4.11. All peaks keep single whatever temperatures but the intensity at low temperature is significantly small. As we already discussed, the behavior suggest the presence of polar shift in a short range.

The short range order is difficult to be observed by direct splitting of Bragg peak but may sensitive with the size of unit cell [32]. This is the case for pure PFW. Thus we first checked the evolution of FWHM, unfortunately, the results are quite confused. Instead, the evolution of lattice parameters give rich informations. Fig. 4.12 shows lattice parameters versus temperature for three different relaxor solid solution, 20PZO, 30PZO and 40PZO.

On cooling, a linear shrinking of the lattice parameters is firstly obeyed, it is denoted as phase I. A anomaly occur at 320K, 380K and 390K for 20PZO, 30PZO and 40PZO respectively. Then, 20PZO keeps almost constant lattice parameter but a slow shrinking is observed for 30PZO and 40PZO, this is denoted as phase II. Another linear shrinking of the lattice parameters reflects phase III which is stable between 260K-180K, 260K-210K and 300K - 200K for 20PZO, 30PZO and 40PZO respectively. Phase IV exists between 180K - 130K, 210K - 160K and 200K-160K for 20PZO, 30PZO and 40PZO and there is a sharp decreasing the lattice parameter for 20PZO. A plateau is evidenced at last which is phase V, similar with other relaxor PFW, PMN... .

The common character is that five phases are separated by four phase transitions which are noticed by anomalies of lattice parameter versus temperature. The phase at here may slight different with the common concept. It should be a local polar shift because the structure of the solid solution is still cubic. But, it is quite surprising that there are so many 'phase' transition.

Dielectric properties

We also did dielectric measurement from 1kHz to 1MHz to study the polar behavior. Fig.4.13 shows the dielectric response for every composition. The dielectric relaxation is observed for all four compounds. Temperature of the dielectric maximum (T_m) increases with the content of PZO in the solid solution. It is 220K, 254K, 282K and 314K at 1kHz; 232K, 264K, 296K and 324K at 1MHz; for for 10PZO, 20PZO, 30PZO and 40PZO respectively. Thus, 40PZO is a room temperature relaxor. The results consist with the X-ray diffraction that the average cubic but local shifts of polar.

Large dielectric permittivities is noticed especially at high temperature and low frequency (fig. 4.13(a)) which is not a intrinsic behavior because it is strong dependent on samples. In fact, this relaxation is losses related which can be clearly noticed by dielectric loss tangent versus temperature (fig. 4.14). The relaxation satisfies Arrhenius relationship and gives a thermal activation energy around 0.5 eV for 10PZO and 20PZO which implies the defects related relaxation as in PFW.

Relaxor show interesting Vogel-Fulcher freezing, i.e.. PFW, PMN. According the experiments, the behavior was fitted by least-square method and fitted parameters are listed in table 4.5. The validation of the fitting is shown in fig. 4.15 where black points are experiments but the lines are fitted Vogel-Fulcher relationship. The relaxor solid solution obeys Vogel-Fulcher freezing, in addition, freezing temperature increases with the content of PZO. It suggests that the relaxation is enhanced by B site Zr^{4+} replacement. One of critical ingredient of relaxor is the quenched random electric and strain fields. It is obvious that B site Zr^{4+} replacement will enhance the fields. The relaxation activation energy is almost the same for all relaxor solid solution and comparable with PFW. Importantly, the freezing temperature is also

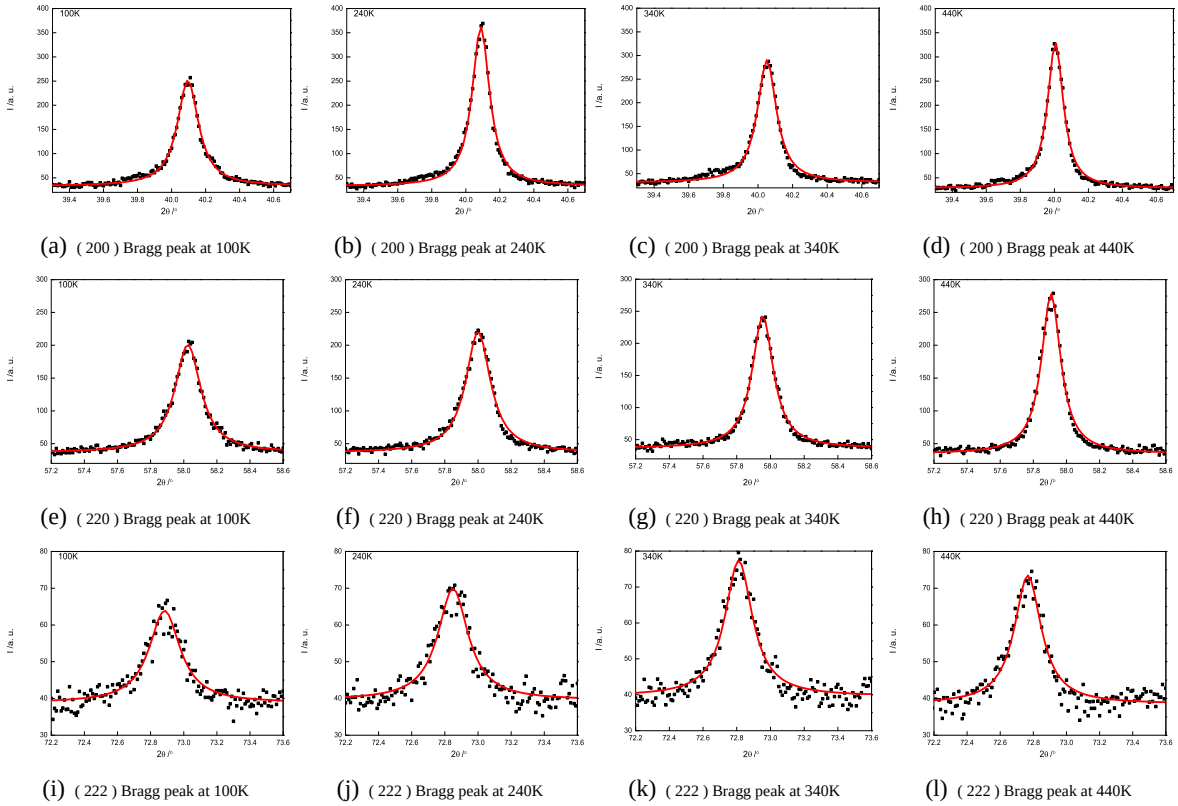

(a) (200) Bragg peak at 100K (b) (200) Bragg peak at 240K (c) (200) Bragg peak at 340K (d) (200) Bragg peak at 440K

(e) (220) Bragg peak at 100K (f) (220) Bragg peak at 240K (g) (220) Bragg peak at 340K (h) (220) Bragg peak at 440K

(i) (222) Bragg peak at 100K (j) (222) Bragg peak at 240K (k) (222) Bragg peak at 340K (l) (222) Bragg peak at 440K

Figure 4.11 *Main Bragg diffraction peaks (200), (220) and (222) of 40PZO at different temperatures*

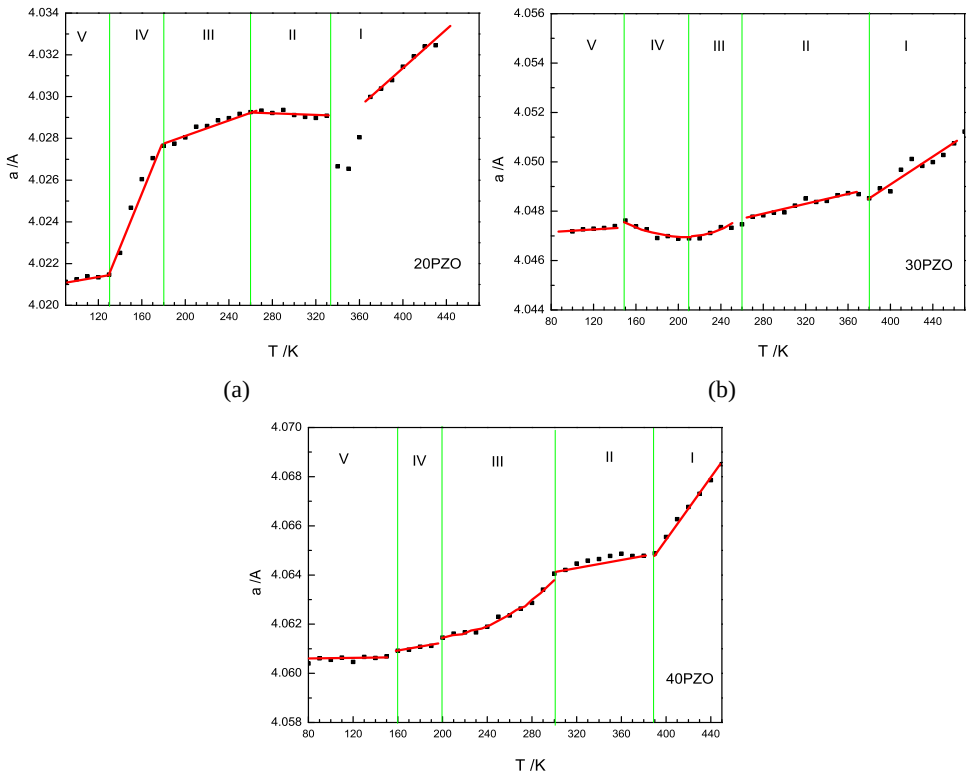

(a) (b)

(c)

Figure 4.12 *Lattice parameters versus temperature for : (a)20PZO (b)30PZO and (c)40PZO.*

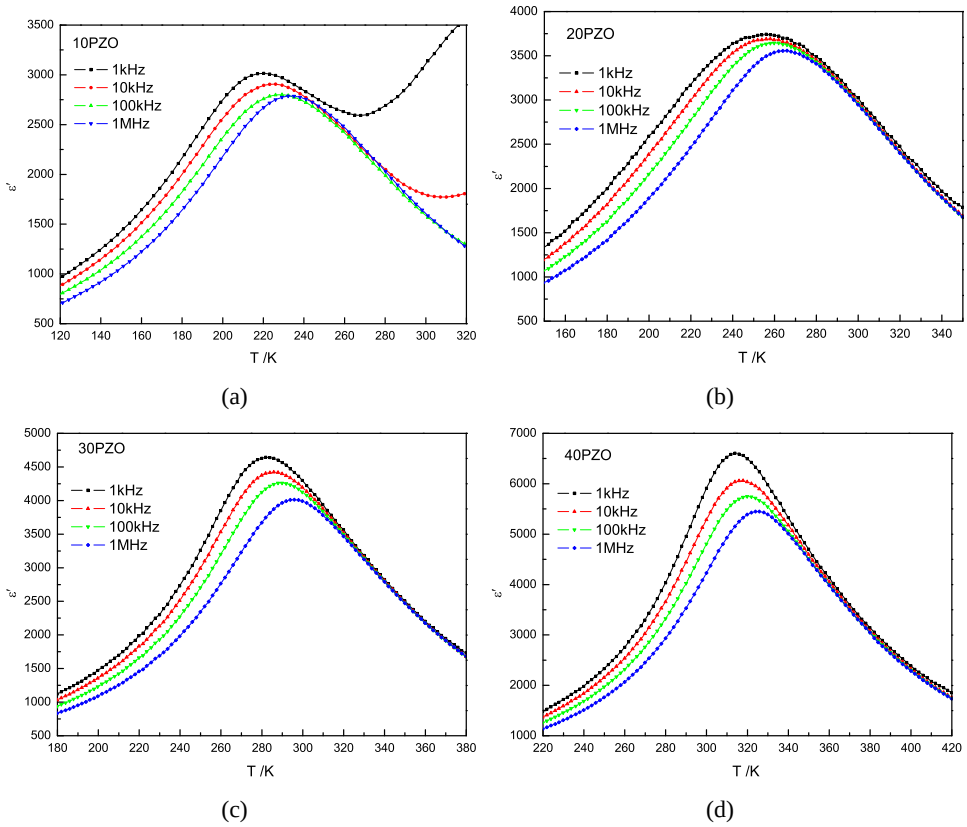

Figure 4.13 *Dielectric permittivity versus temperature for: (a)10PZO, (b)20PZO, (c)30PZO and (d)40PZO*

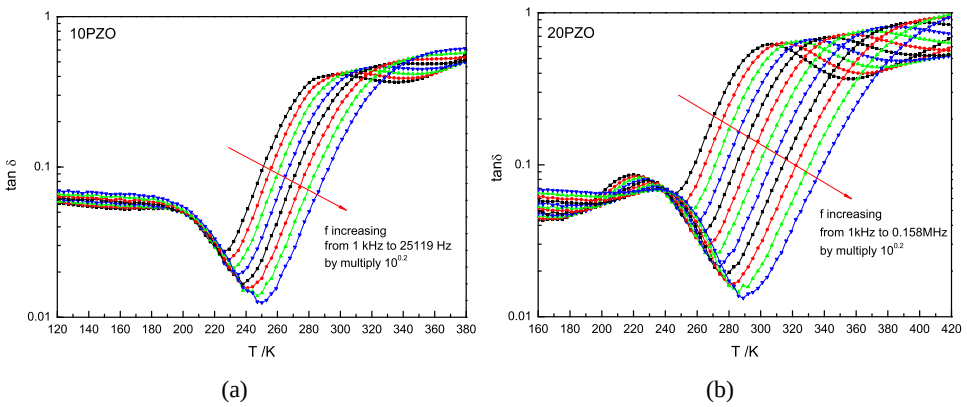

Figure 4.14 *Dielectric loss tangent versus temperature for 10PZO and 20PZO*

reflected by X-ray diffraction. It matches with the phase transition between Phase II to Phase III. Thus, different with PFW, there are other polar activities below freezing temperature for relaxor solid solution.

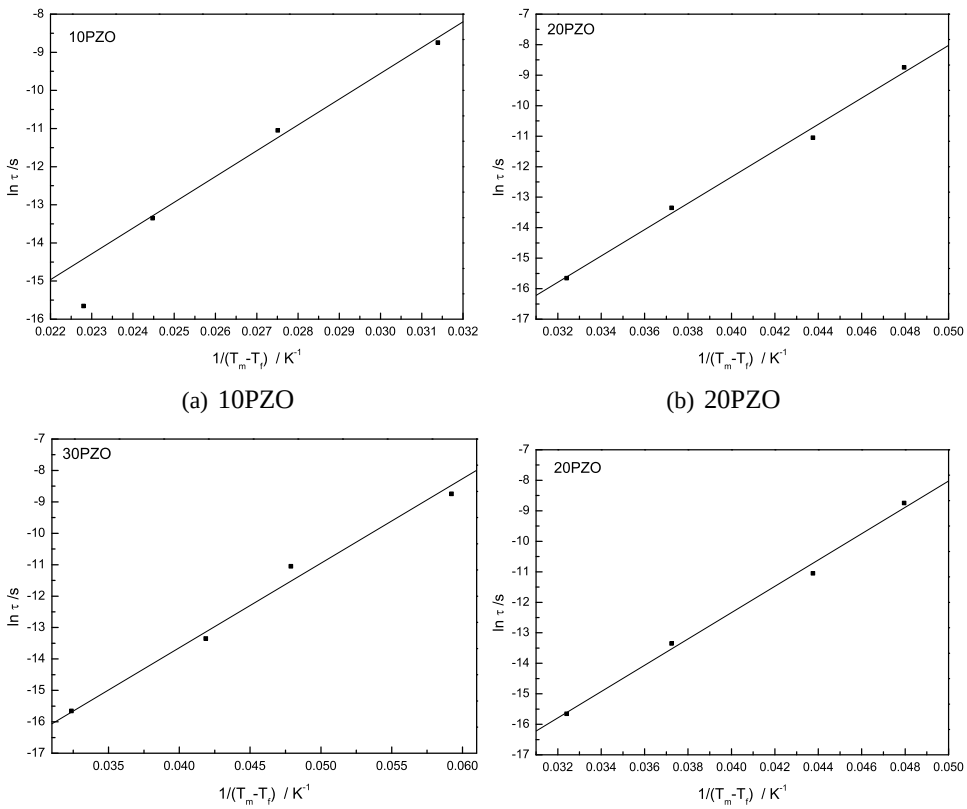

(a) 10PZO (b) 20PZO

(c) 30PZO (d) 40PZO

Figure 4.15 *lnτ versus 1/(T_m-T_f) for 10PZO, 20PZO, 30PZO and 40PZO. Points are the experimental data; lines are the fits with with parameters given in table 4.5*

Table 4.5 *Vogel-Fulcher freezing parameters for PFW, 10PZO, 20PZO, 30PZO and 40PZO*

x	T_f	f_0	E_a	$\Delta(T_m(1MHz)-T_f)$
PFW	150	5.30×10^{12}	0.067	34
10PZO	188	1.45×10^{12}	0.037	44
20PZO	233	1.14×10^{12}	0.037	31
30PZO	265	6.27×10^{9}	0.023	31
40PZO	293	1.15×10^{12}	0.037	31

Except polar freezing, relaxor also displays interesting diffuse phase transitions which is described by powder law. We also use least-square method to fit the diffuse phase transitions for relaxor solid solution. The fitted parameters are list in table 4.6 and the validation of fitting is shown in fig. 4.16). The relaxor solid solution obeys powder law. γ approaches complete relaxor which has a γ = 2. Increasing ε_m and T_m but decreasing δ_m may suggest that polar order is stabilized or/and enhanced by solid solution with PZO which brings long range polar order. In fact, we find the evolution of broadening parameter δ_m obeys mean field theory. In fig.4.17, black point are experiments and red line is the fitting curve by mean field theory based formula $\delta_m \propto (x_c - x)^{\alpha}$. The fitting gives a x_c which equals to 43. It suggests 43PZO is a critical composition. In fact, room temperature structural study already shows that that PFW-PZO shows a cubic structure for 40PZO but a rhombohedral structure for 50PZO.

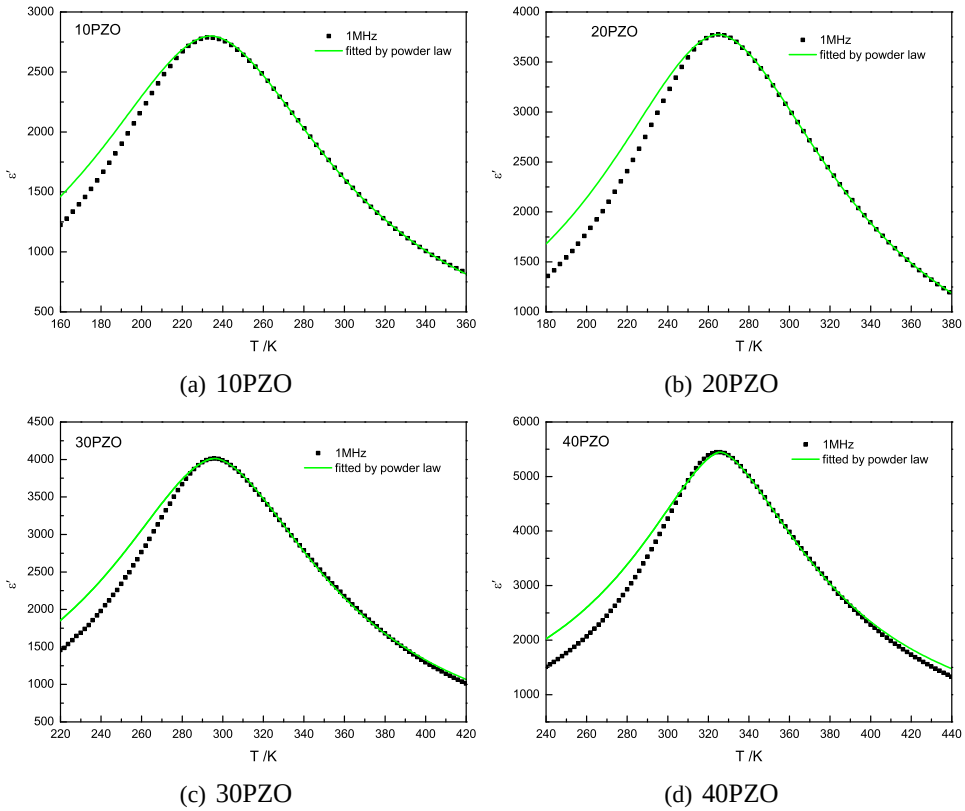

(a) 10PZO (b) 20PZO

(c) 30PZO (d) 40PZO

Figure 4.16 *ε' versus T for 10PZO, 20PZO, 30PZO and 40PZO. Points are the experimental data; lines are the fits with parameters given in table 4.6.*

Table 4.6 *Powder law parameters for x PZO (x=10, 20, 30 and 40)*

x	ε_m	T_m	γ	δ_m
10	2800	234	1.84	38.69
20	3775	265	1.83	36.74
30	4014	296	1.76	29.61
40	5448	326	1.62	20.49

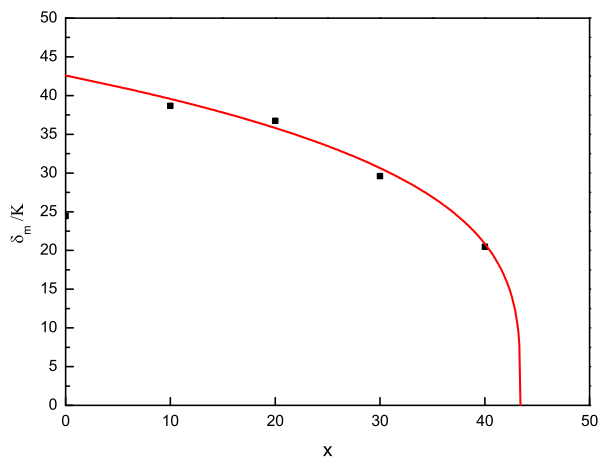

Figure 4.17 *The broadening parameter as a funtion of x*

Curie-Weiss law also was observed for relaxor, i.e., PMN. The line decreasing of lattice parameter at phase I is similar with the behavior of ferroelectric at paraelectic phase. Therefor, we study the dielectric behavior at high temperature far from conventional relaxation region. Fig. 4.18) shows the Curie-Weiss behavior for relaxor solids solution. After careful examining the dielectric permittivity and Curie-Weiss law, we find that the deviation temperature between two is the phase transition point between phase I and phase II. The deviation temperatures are also around 400K which is not so far from T* [32]. Both disturbing lattice parameter and Curie-Weiss law deviation suggest PNRs starts static behavior on cooling around 400K.

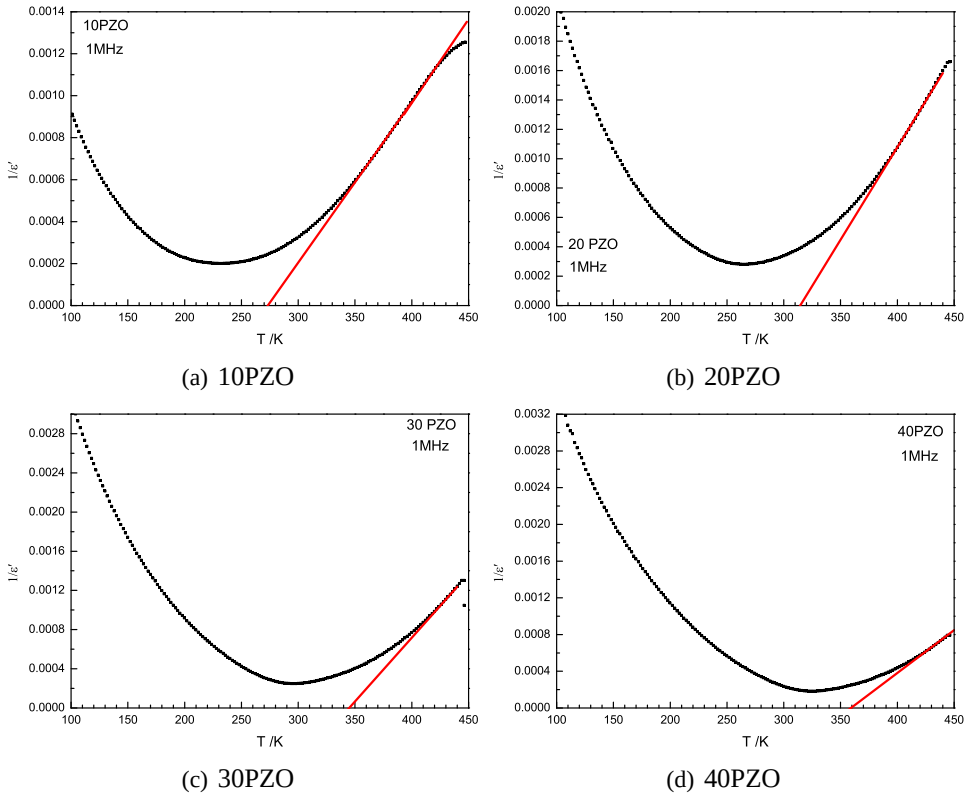

(a) 10PZO (b) 20PZO

(c) 30PZO (d) 40PZO

Figure 4.18 *1/ε′ versus T for 10PZO, 20PZO, 30PZO and 40PZO. Points are the experimental data; lines are the fits by Curie-Weiss law*

Ferroelectric properties

We already clear the phase transition from phase I to phase II is because starting of static polar and the phase transition from phase II to phase III is because polar freezing. However, there are more two phase transitions waiting to study. We did ferroelectric hysteresis loop experiment for relaxor solid solution over large temperature. Fig. 4.19 shows P-E relationship of 20PZO and 40PZO at three selected temperatures. Between high temperature paraelectric state and low temperature less or no ferroelectric state, a ferroelectric hysteresis loop is observed. 20PZO has a 'S' type loop which is similar with PFW but 40PZO shows a rectangular one which is similar with normal ferroelectric.

The temperature dependent P-E loops are summarized in fig. 4.20 where both polarization and coercive field are plotted as a function of temperature.

On cooling, the polarization appear at a temperature which match the phase transition from phase II to phase III; then, it stays stable with a plateau; after two different polarization decreasing states were observed. The two less ferroelectric states correspond to the phase transition from phase III to phase IV and the phase transition from phase IV to phase V. The maximum polarization is $3.6\mu C \bullet cm^{-2}$,

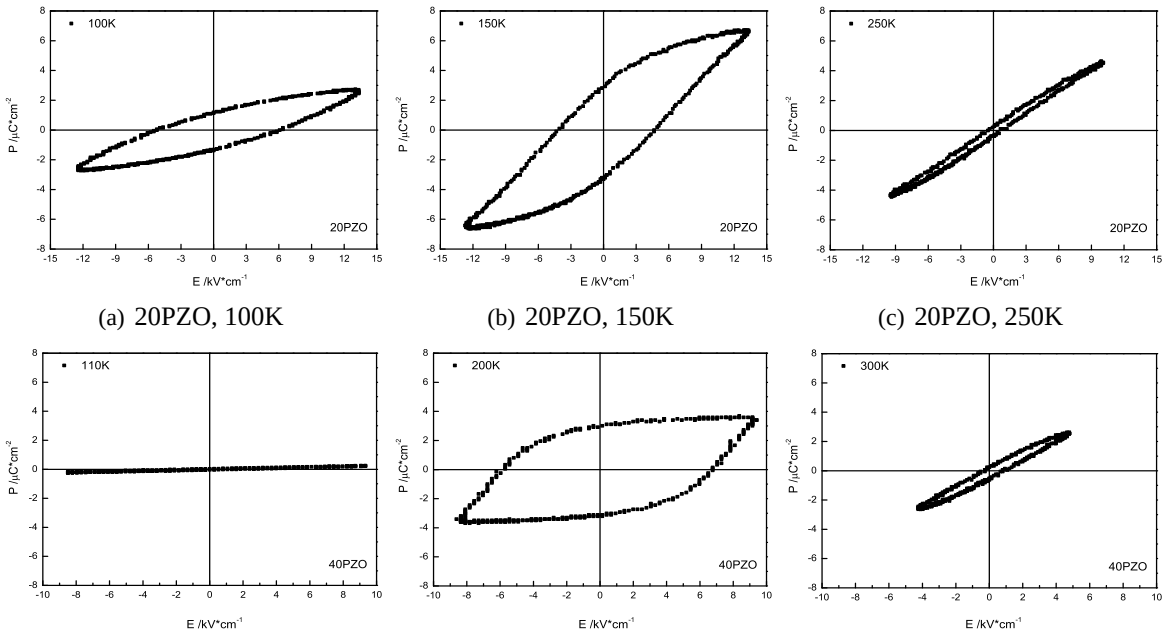

(a) 20PZO, 100K (b) 20PZO, 150K (c) 20PZO, 250K

(d) 110K (e) 200K (f) 300K

Figure 4.19 *P-E relationship of 40PZO at different temperatures*

$6.8\mu C \bullet cm^{-2}$, $2.65\mu C/cm^{-1}$ and 6.8 $\mu C/cm^{-1}$ for 10PZO, 20PZO, 30PZO and 40PZO. The values are smaller than the polarization of PFW or PZO and there is no obvious regulation between the polarization and the content of PZO. In fact, PZO shows both antiferrodistorsive and antipolar structural shifts which favor a less or antiferroelectic state. In a average cubic, the strong competitions between the short range polar and antiferrodistorsive (or / and antipolar) gives the true evolution of polarization. At last, a no ferroelectric or antiferroelectric is produced.

4.4.2 (100-x)PFW - x PZO: 50 $\leq$ x $\leq$ 80

Phase transitions

We already demonstrated PFW-PZO crystallines in a rhombohedra structure from 50PZO to 80PZO which is a classic ferroelectric structure. The rhombohedra is instable at low temperature accompanying tilts of octahedral for PZT. We also investigated the stability of rhombohedra for PFW-PZO by X-ray diffraction.

Fig.4.21 and fig. 4.22 show some diffraction peaks of 50PZO and 80PZO at selected temperatures. All diffraction peaks are single at high temperature; then, p.c. Bragg (200) keeps single on cooling but p.c. Bragg (220) and (222) peaks split in two. It should be noticed that the intensities of Bragg peaks decrease with temperature decreasing is a abnormal behavior as we already described, especially for Bragg (222) peak. The (222) peak is strongly related to oxygen octahedra. The decreasing of intensity suggests new or difference tilts occur at low temperature for rhombohedra solid solution.

The lattice parameters and unit cell volumes of rhombohedral solid solution were calculated by fitting Bragg peak using P-V function. Fig. 4.23 shows the unit cell volumes and FWHM as a function of temperature.

On cooling, the unit cell volume of 50PZO firstly decreases, then slowly increases below 360K, reaches a maximum at 260K, then decreases again below 260K with another slope. The unit cell volume evolution shows two anomalies at 360K and 260K. The similar behaviors are also found for 60PZO, 70PZO and 80PZO. Three different phases which are marked as Phase I, Phase II and Phase III in fig. 4.23 exist for rhombohedra PFW-PZO solid solution. The phase transitions occur at 400K and

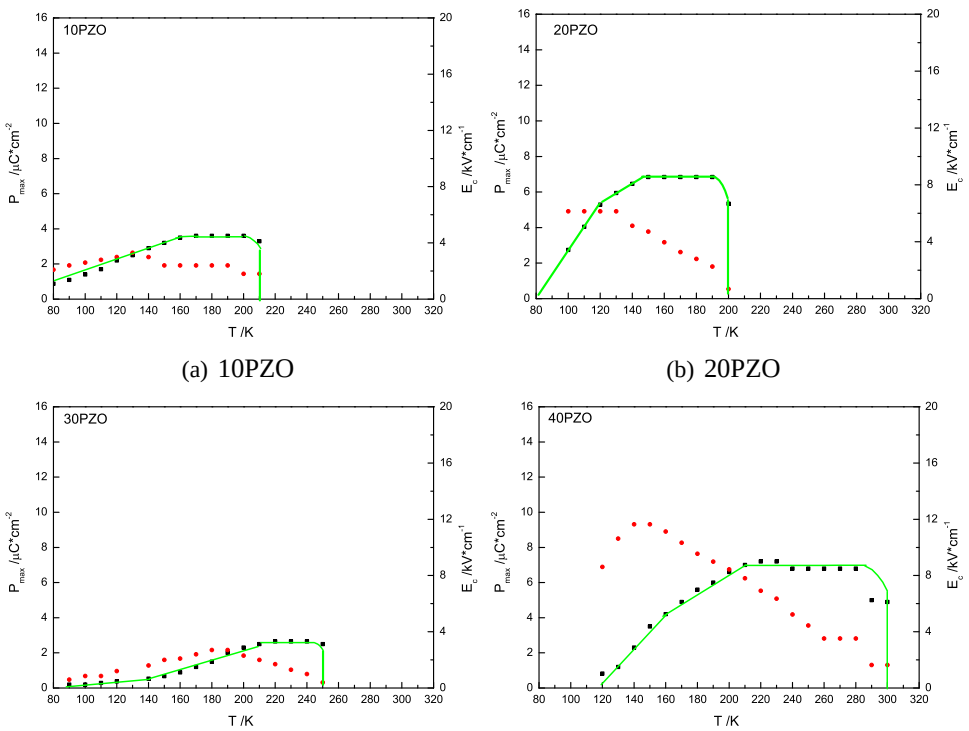

(a) 10PZO (b) 20PZO

(c) 30PZO (d) 40PZO

Figure 4.20 *Polarization versus temperature for PFW, PZO, 10PZO, 20PZO, 30PZO and 40PZO.*

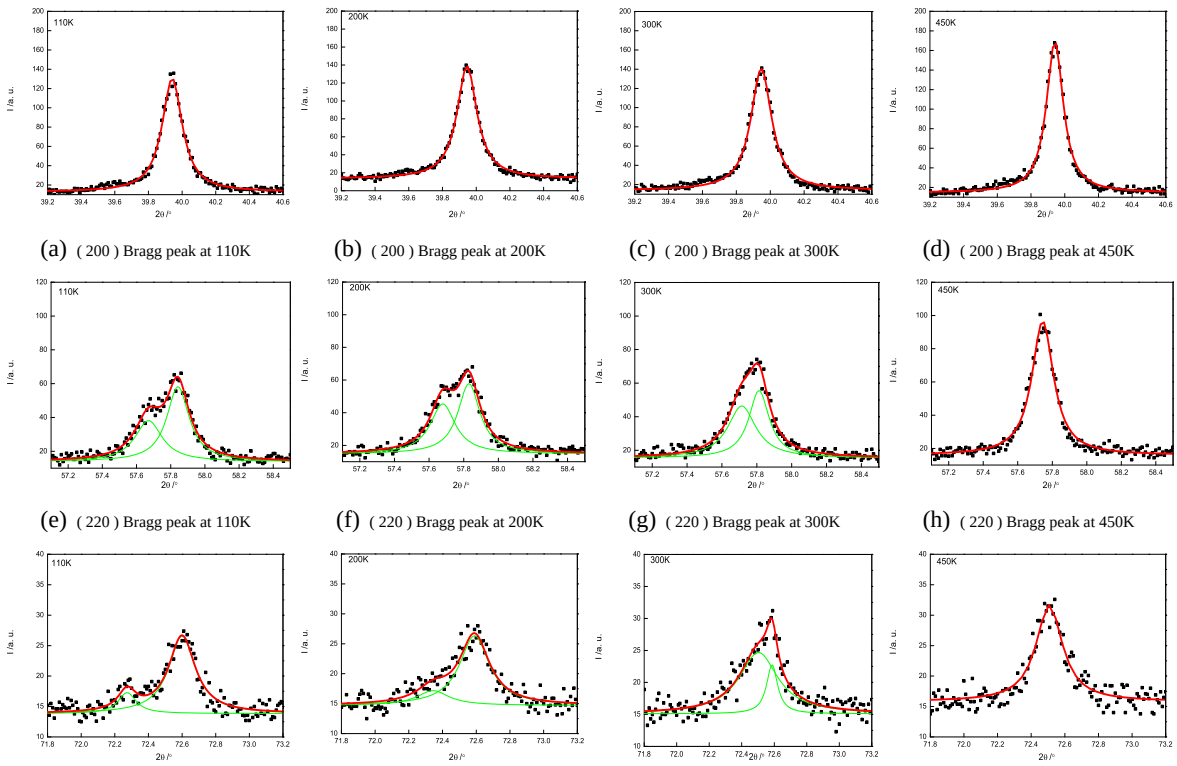

(a) (200) Bragg peak at 110K (b) (200) Bragg peak at 200K (c) (200) Bragg peak at 300K (d) (200) Bragg peak at 450K

(e) (220) Bragg peak at 110K (f) (220) Bragg peak at 200K (g) (220) Bragg peak at 300K (h) (220) Bragg peak at 450K

(i) (222) Bragg peak at 110K (j) (222) Bragg peak at 200K (k) (222) Bragg peak at 300K (l) (222) Bragg peak at 450K

Figure 4.21 *P.c. Bragg diffraction peaks (200), (220) and (222) of 50PZO at different temperatures*

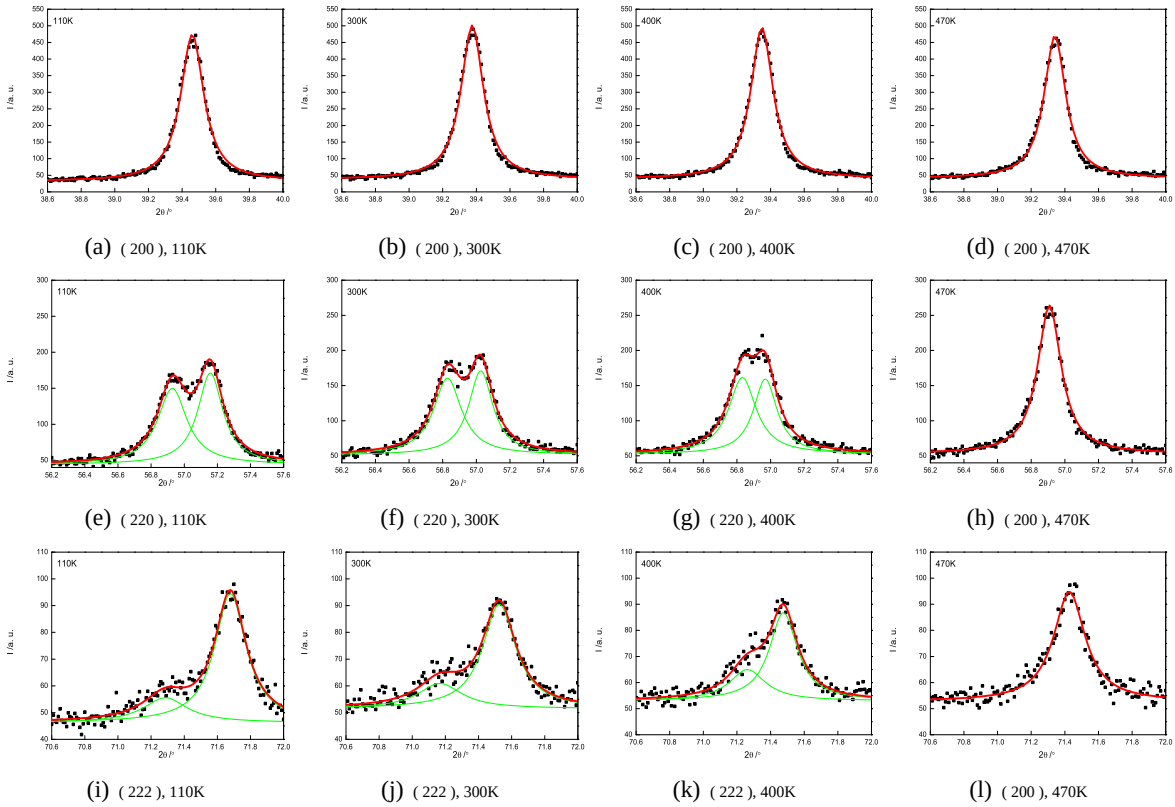

(a) (200), 110K (b) (200), 300K (c) (200), 400K (d) (200), 470K

(e) (220), 110K (f) (220), 300K (g) (220), 400K (h) (200), 470K

(i) (222), 110K (j) (222), 300K (k) (222), 400K (l) (200), 470K

Figure 4.22 *P.c. Bragg diffraction peaks (200), (220) and (222) of 80PZO at different temperatures*

340K for 60PZO; they are 420K and 270K for 70PZO; 450K and 390 for 80PZO. The phase transitions are also proved by the variation of FWHM.

Phase I is a cubic structure and Phase II is a rhombohedral R3m structure; but the structure of phase III is not clear. R3c is expected for Phase III because there is no obvious splitting of Bragg peaks and it is a tilts structure 'fighting' polarization.

Dielectric properties

The dielectric permittivity of rhomboheda solid solution was measured from 1kHz to 1MHz over large temperature range. Fig. 4.24 shows the dielectric permittivity at 1kH, 10kHz, 100kHz and 1MHz for 50PZO, 60PZO, 70PZO and 80PZO. One of common character is T_m independent of frequency as expected for a normal ferroelectric phase transition. In addition, T_m proves the phase transition between phase I to phase II by the evolution of unit cell volume. However, dielectric peak shows a flat or diffused shape, especial for 50PZO and 60PZO, instead of a sharp peak for classic ferroelectric. The peak of 80PZO is similar with classic ferroelectric.

In fact, the character of diffused dielectric peak is also reflected by Curie-Weiss law fitting dielectric permittivity.

Fig. 4.25 shows the reciprocal of dielectric permittivity (the black points) as a function of temperature. The red lines in the figure is the fitted Curie-Weiss. According landau phase transition theory, in FE phase, Curie-Weiss is expressed by:

$$\varepsilon' = \frac{C}{2(T_0 - T)} = \frac{C'}{(T_0 - T)} \tag{4.2}$$

Thus, we fitted both paraelectric and ferroelectric phases. The fitted parameters are listed in table 4.7. Typical, the dielectric permittivity deviates from Curie-Weiss law about 50K higher than T_0. For 50PZO, 60PZO and 70PZO, $T_0^{'} < T_0$, for 80PZO, $T_0^{'}$ is slight larger than T_0 which is similar with classic

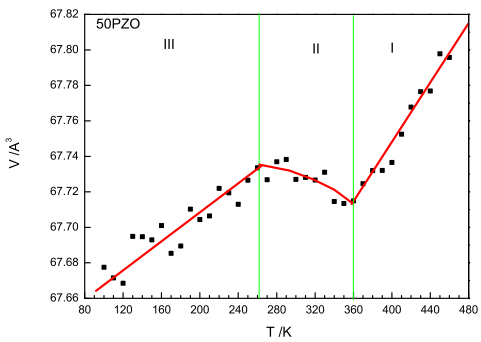

(a) Unit cell volum of 50PZO

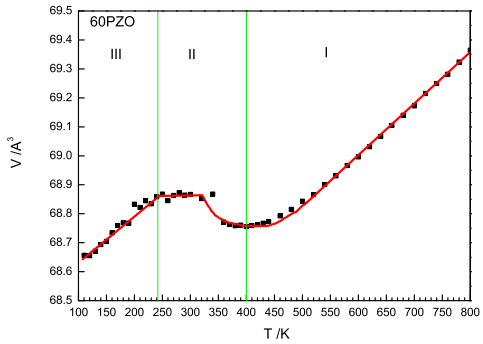

(b) Unit cell volum of 60PZO

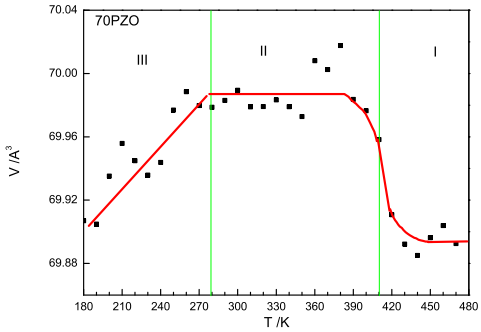

(c) Unit cell volum of 70PZO

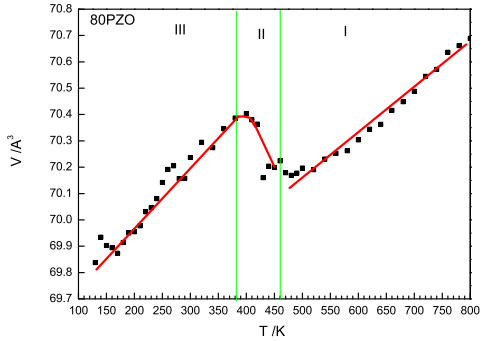

(d) Unit cell volum of 80PZO

Figure 4.23 *Temperature dependences of unit cell volume*

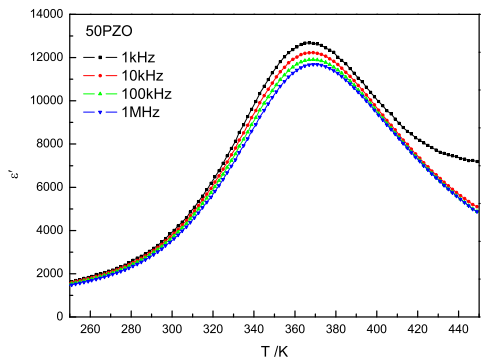

(a) 50PZO

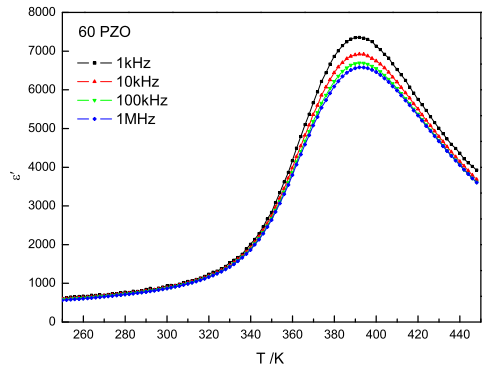

(b) 60PZO

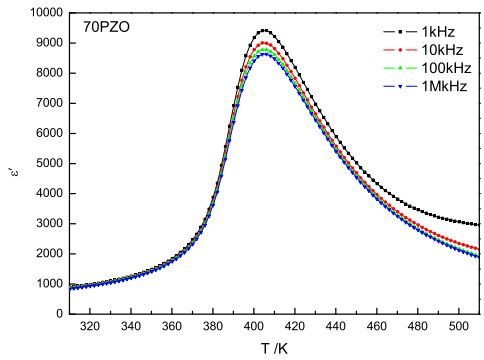

(c) 70PZO

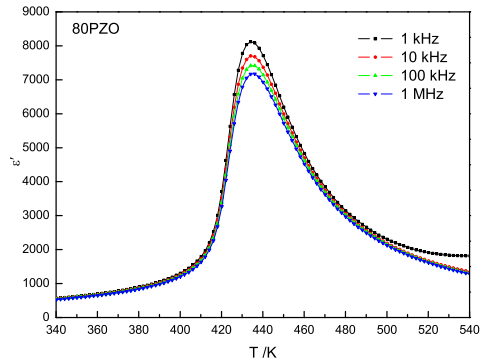

(d) 80PZO

Figure 4.24 *Dielectric permittivity versus temperature for 50PZO, 60PZO, 70PZO and 80PZO.*

ferroelectric. For all the compounds, the C' almost equals to half of C as expected by Landau phase transition theory.

Table 4.7 *Curie-Weiss parameters and T_m for rhombohedra solid solution*

x	C	T_0	C'	T'_0	T_m
50	3.72×10^5	372	1.20×10^5	332	369
60	1.20×10^5	409	5.77×10^4	365	392
70	1.46×10^5	432	8.27×10^4	409	406
80	1.30×10^5	440	5.70×10^4	448	435

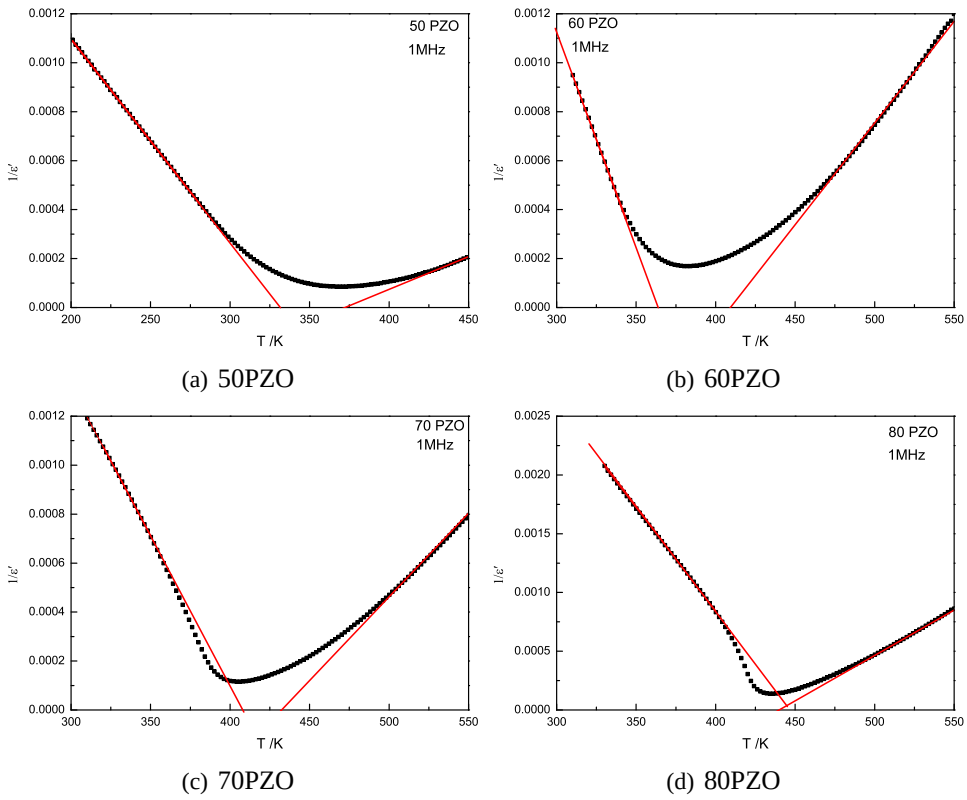

(a) 50PZO (b) 60PZO

(c) 70PZO (d) 80PZO

Figure 4.25 *$1/\varepsilon'$ versus T for 50PZO, 60PZO, 70PZO and 80PZO. Points are the experimental data; lines are the fits with parameters given in table 4.7*

Ferroelectric properties

We show in fig. 4.26 P-E at selected temperature for rhombohedra solid solution. P-E shows three different behaviors depending on temperature. Because the thermal active related defects conductivity, we observe a 'banana' P-E loop [107] at high temperature which is at phase ; a ferroelectric hysteresis loop is observed on cooling at phase II; interestingly, P-E shows shows a linear behavior at phase III. The dependences of polarization and coercive field as a function of temperature are plotted in fig. 4.27. There are three well-defined polarization regions. Polarization appears below T_C and is stabilized over large temperature range; then, it linear decreases on cooling. The two polarization transition temperatures match well with the anomalies of unit cell volume by X-ray diffraction. Large polarization is found in rhombohedra solid solution and all of them are room temperature ferroelectric. 70PZO even has a polarization $15.0\mu C/cm^{-2}$ which is larger than both PFW or PZO. Beyond finding the

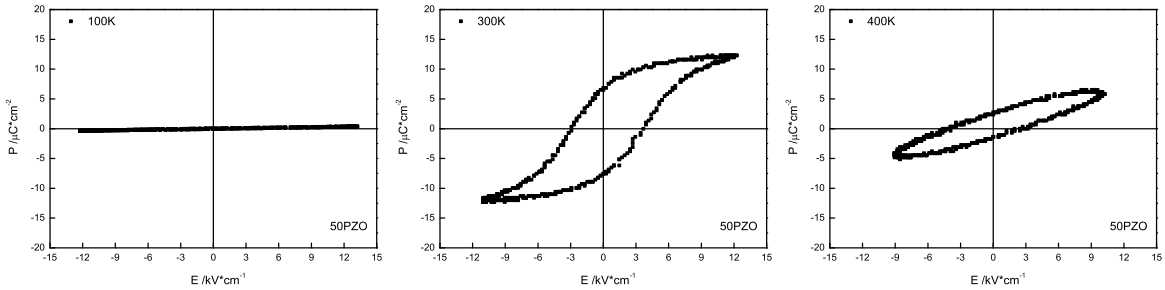

(a) 50PZO, 100K

(b) 50PZO, 300K

(c) 50PZO, 400K

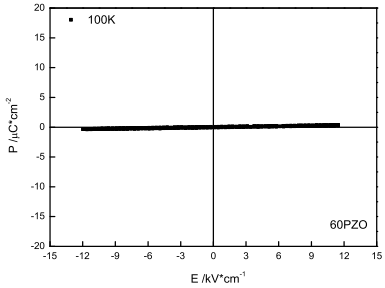

(d) 60PZO, 100K

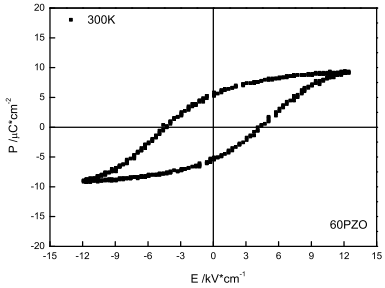

(e) 60PZO, 300K

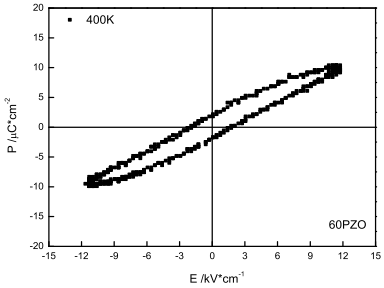

(f) 60PZO, 400K

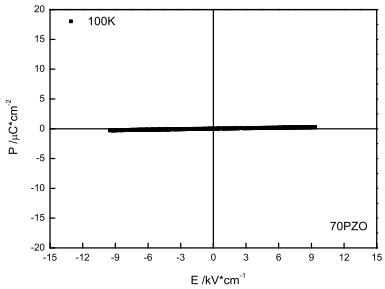

(g) 70PZO, 100K

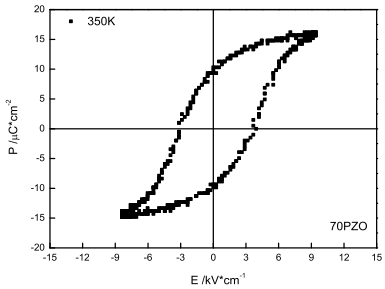

(h) 70PZO, 350K

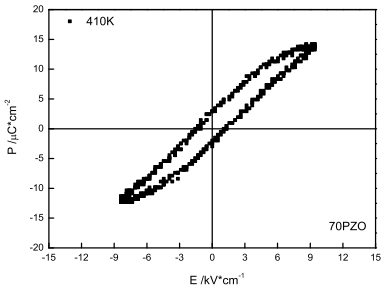

(i) 70PZO, 410K

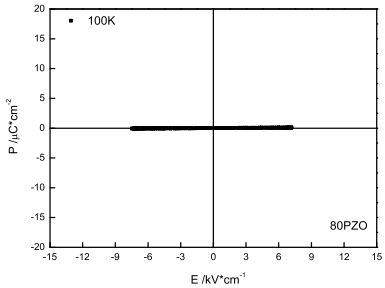

(j) 80PZO, 100K

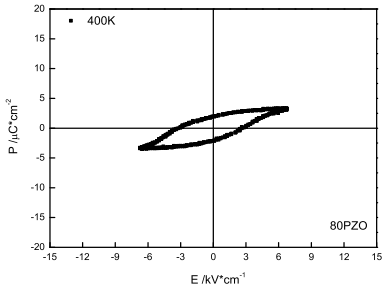

(k) 80PZO, 400K

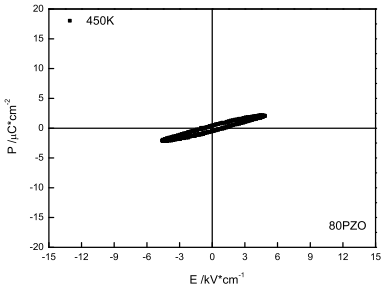

(l) 80PZO, 450K

Figure 4.26 *Some character FE hysteresis loops for 50PZO, 60PZO, 70PZO and 80PZO*

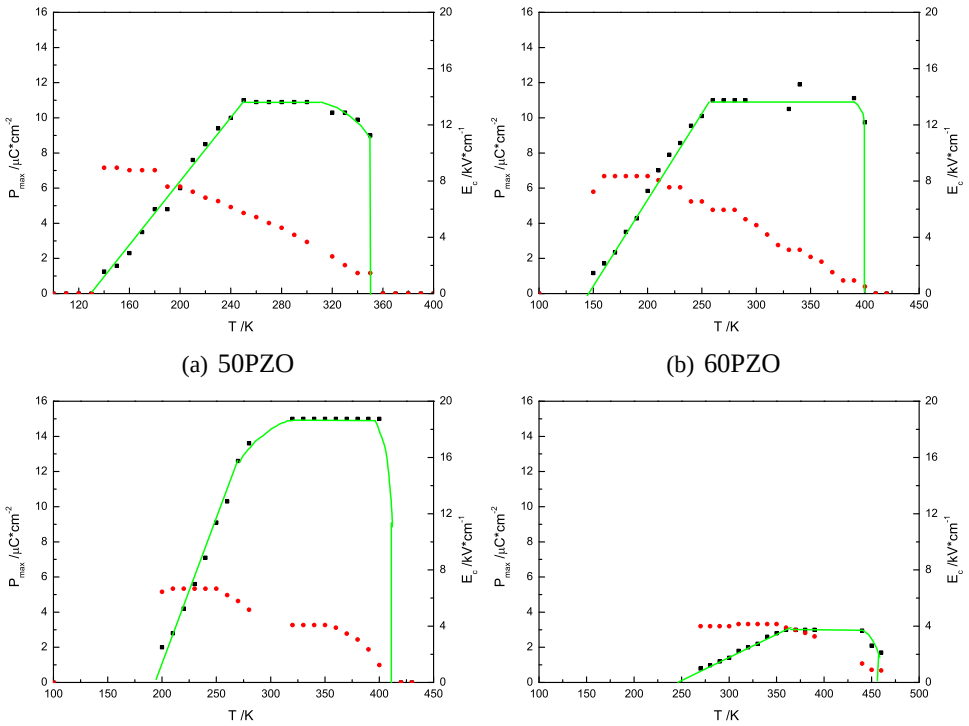

(a) 50PZO (b) 60PZO

(c) 70PZO (d) 80PZO

Figure 4.27 *Polarization, coercive field versus temperature for 50PZO, 60PZO, 70PZO and 80PZO*

ferroelectric of phase II, we find a interesting no ferroelectric phase III. Interestingly, polarization does not display a sharp change between phase II and phase III; it slowly decreases on cooling sample. The behavior shows a second order phase transition character. Nevertheless, we still expect the tilts of oxygen octahedra related phase transition is related to the no ferroelectric phase III. Logical, anti-polar as happening in PZO is also expected. Perhaps, both tilts and anti-polar give a real polar state for rhombohedra solid solution at low temperature.

4.4.3 90PZO

Phase transitions

Bragg peaks splitting of 90PZO (fig.4.28) also suggests rhombohedra symmetry at low temperature. Different with other rbombohedra solid solution, Bragg (222) peaks at low temperature has large intensity and the splitting is well separated.

Dependences of unit cell volume and FWHM of Bragg peaks are plotted in fig. 4.29(a). The FWHM of (200) peak remains constant whatever temperature as one would expect for a cubic phase. A large enhancement of width of (220) and (222) below 460K is obvious. It seems the rhomboheda is stable at low temperature. However, after calculating the unit cell volume which is shown in in fig. 4.29(b), we find two new anomalies except the phase transition at 460K: there is a obvious jump of unit cell volume at 390K and constant unit cell volume evolution is disturbed at 250K following another linear shrink on cooling.

A complete diffractogram was recorded at 100K for investigation the structural symmetry at low temperature. Surprisingly, the data still can be refined by R3m space group which is a room temperature structure of 90PZO.

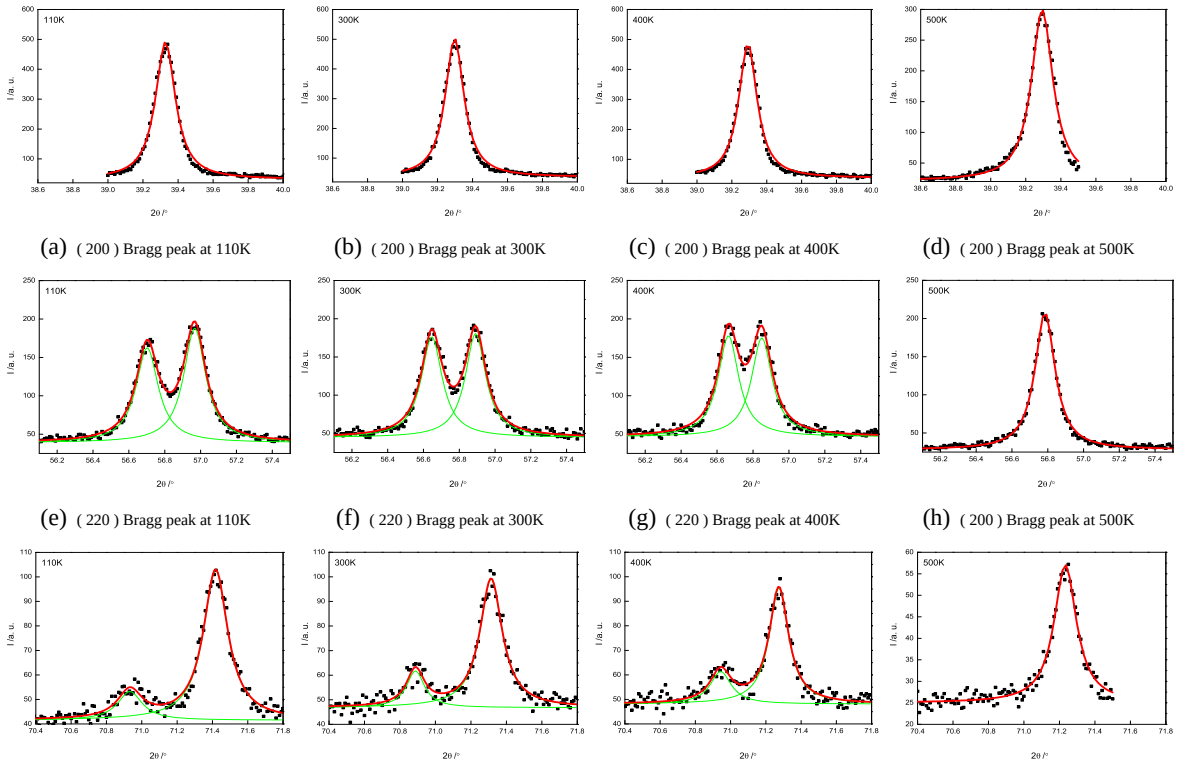

(a) (200) Bragg peak at 110K (b) (200) Bragg peak at 300K (c) (200) Bragg peak at 400K (d) (200) Bragg peak at 500K

(e) (220) Bragg peak at 110K (f) (220) Bragg peak at 300K (g) (220) Bragg peak at 400K (h) (200) Bragg peak at 500K

(i) (222) Bragg peak at 110K (j) (222) Bragg peak at 300K (k) (222) Bragg peak at 400K (l) (222) Bragg peak at 500K

Figure 4.28 *P.c. Bragg diffraction peaks (200), (220) and (222) of 90PZO at different temperatures*

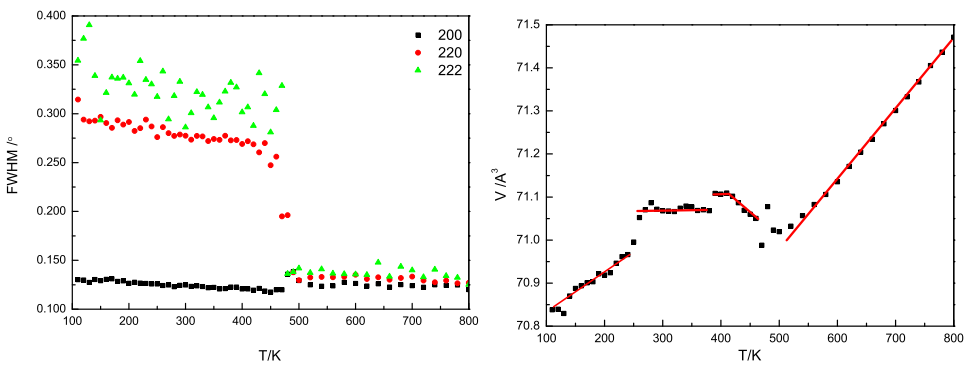

(a) FWHM (b) Unit cell volume

Figure 4.29 *Temperature dependence of FWHM and unit cell volume for 90PZO*

Dielectric and ferroelectric properties

The dielectric permittivity of 90PZO is plotted in fig.4.30(a). A sharp dielectric peak, at 463K, is observed at 463K. The dielectric permittivity obeys Curie-Weiss law, the fitted T_0 is 439.7K and T_0' is 487K. 90PZO exhibits a classic ferroelectric behavior.

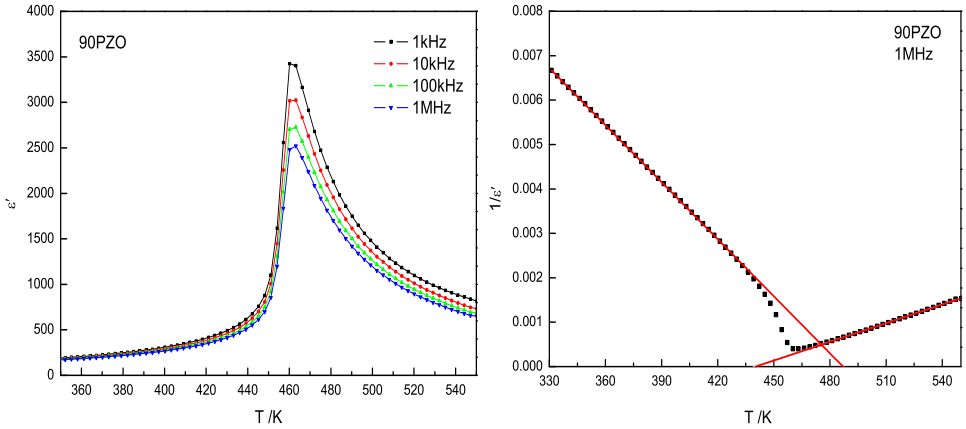

(a) ε' versus T

(b) $1/\varepsilon$ versus T. Points are experimental data, lines are the fits by Curie-Weiss law

Figure 4.30 *Dielectric permittivity and reciprocal dielectric permittivity of 90PZO. Lines is fitted Curie-Weiss Law*

The polar order of 90PZO is studied by P-E loop. Fig.4.31(a) shows the FE hysteresis loops of 90PZO at 300K. The polarization and coercive field are depicted in fig. 4.31(b). The polarization appears below 460K which is the evidenced T_C by X-ray diffraction, keeps a large polarization 19 μ C/cm^2. On cooling, polarization starts decreasing below 390K and shows another anomaly at 260K. In fact, these transitions are expected because we find the anomalies of unit cell volume evolution.

We did not find dielectric abnormal behavior around 390K. However, the phase transition at 260K is noticed by both dielectric permittivity (fig. 4.32(a)) and pyroelectric current (fig. 4.32(b)). The hysteresis behavior of pyroelectric current implies a first order phase transition switching occurs at 260K. Pyroelectric current also suggests the polar switching around 260K.

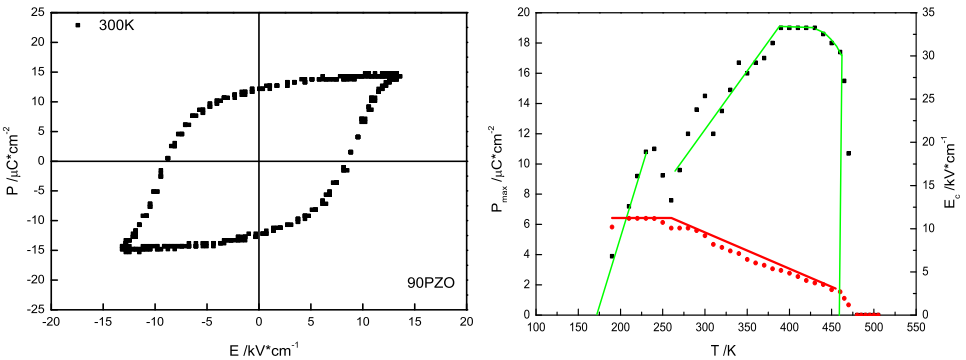

(a) P-E loop at 300K

(b) P, E versus T

Figure 4.31 *Ferroelectric hysteresis loop and temperature dependences of polarization and coercive field of 90PZO*

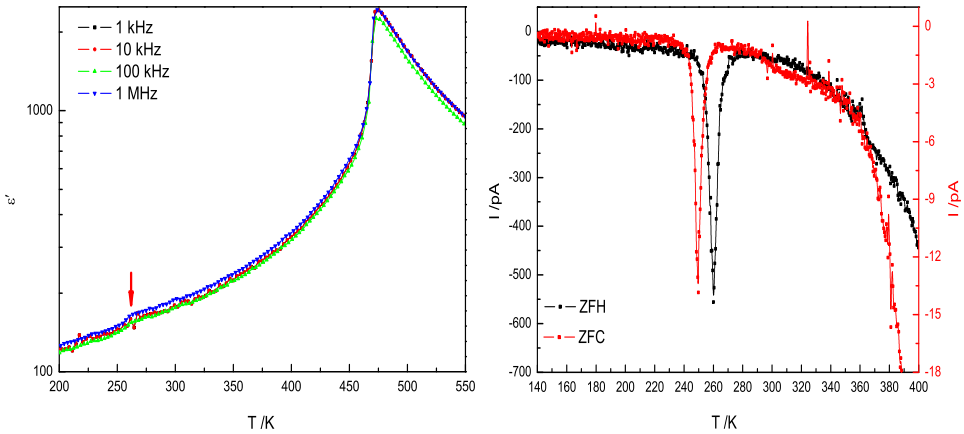

(a) Log ε' versus T (b) Pyroelectric current

Figure 4.32 *Evidences of phase transition around 250K*

4.4.4 95PZO

95PZO crystallines in a orthorhombic structure which is similar with PZO. The phase transition was studies between 300K to 600K. Some Bragg peaks at different temperatures are plotted in fig.4.33 for illustration. At 500K, all the Bragg peaks are single implying the ideal cubic structure. The splitting of Bragg peaks at 350K satisfies orthorhombic symmetry. Between two, at 450K, a different splittings occur where p.c. (200) Bragg peak keeps single but p.c. (220) and (222) Bragg peaks become double; it similar with 90PZO on cooling.

The unit cell volumes extracted from Bragg peak positions is depicted in fig. 4.34(a). According to the jumps of the unit cell volume at 480K and 390K, a intermediate phase between 390K and 480K is expected and the phase transitions is of first order. The FWHM give the same conclusion (fig 4.34(b)).

The real part of the dielectric permittivity of 95PZO shows in fig. 4.35(a) between 300K to 650K for a frequency ranging from 1kHz to 1MHz. Except a sharp peak at 482K, another peak at 380K is also noticeable which is also reflected by the imaginary part of dielectric permittivity and the dielectric loss tangent. Two phase transitions is clearly depicted by reciprocal dielectric permittivity at 1MHz in fig.4.35(b). The red line in the figure is the fitting of the Curie-Weiss law which gives T_0 = 450K and C = 0.93×10^5. The green line in the figure is the fitting of the Curie-Weiss similar relationship at intermediate phase, giving T'_C = 516 and C' = 0.38×10^5. Below 380K, dielectric permittivity does not obey Curie-Weiss law.

Let us now go to the ferroelectric aspects of 95PZO. In this goal, the polarization of 95PZO was measured directly through FE hysteresis loop as a function of temperature (fig. 4.36) obtained using Sawer-Tower electrical circuit. A rectangular ferroelectric hysteresis loop was seen at 400K between paraelectric state at 500K and antiferroelectric state at 310K. The ferroelectric property of 95PZO is stable from 370K to 480K (fig.4.37) with a large polarization about 25 μ C/cm^2. This is also the largest polarization in the solid solution. As we already introduced in last chapter, PZO shows interesting ferroelectric and antiferroelectric instabilities. The results suggest even 5 percent B site replacement can stabilize a ferroelectric intermediate phase over 100K.

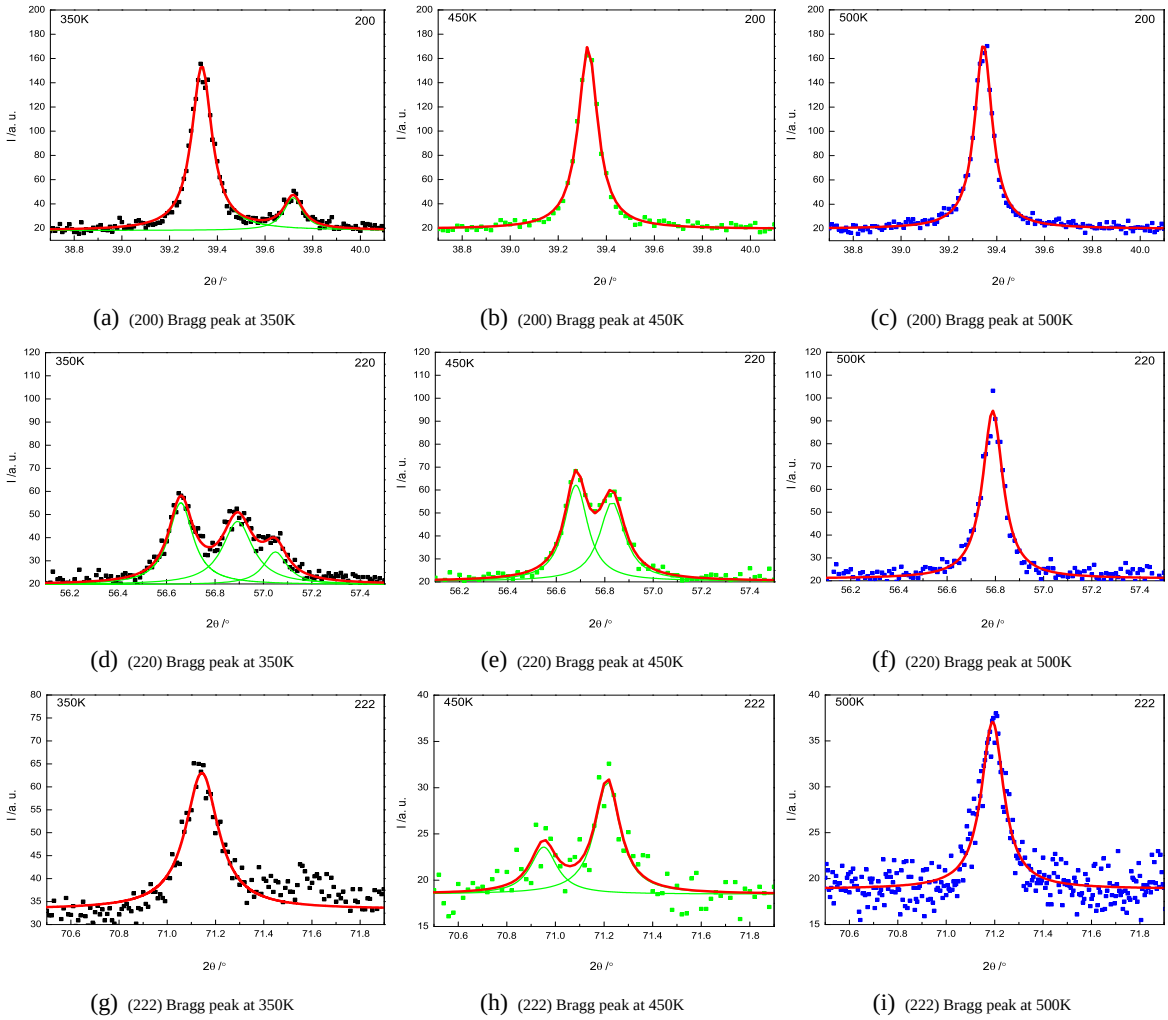

(a) (200) Bragg peak at 350K (b) (200) Bragg peak at 450K (c) (200) Bragg peak at 500K

(d) (220) Bragg peak at 350K (e) (220) Bragg peak at 450K (f) (220) Bragg peak at 500K

(g) (222) Bragg peak at 350K (h) (222) Bragg peak at 450K (i) (222) Bragg peak at 500K

Figure 4.33 *P.c. Bragg diffraction peaks (200), (220) and (222) of 95PZO at different temperatures*

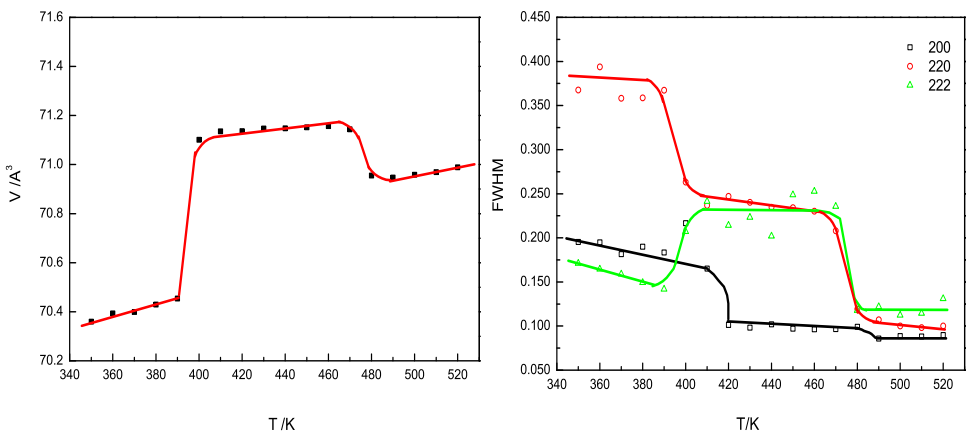

(a) Unit cell volume (b) FWHM

Figure 4.34 *Temperature dependences of unit cell volume and FWHM for 95PZO*

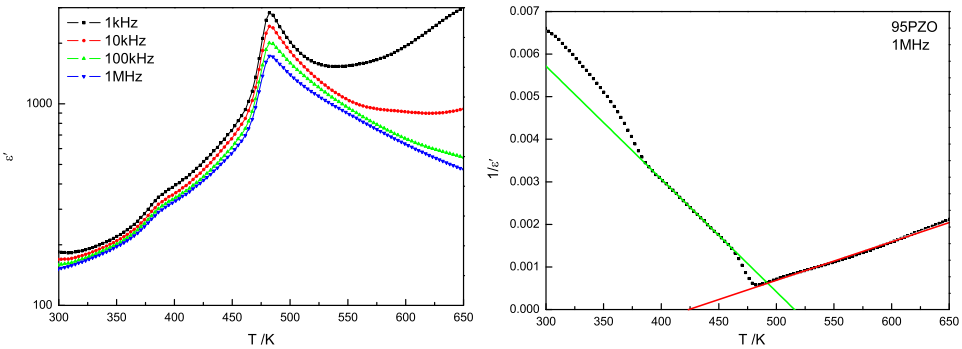

(a) Log ε' versus T

(b) $1/\varepsilon'$ versus T. Points are experiment data; lines are the fits by Curie-Weiss Law

Figure 4.35 *Dielectric properties of 95PZO*

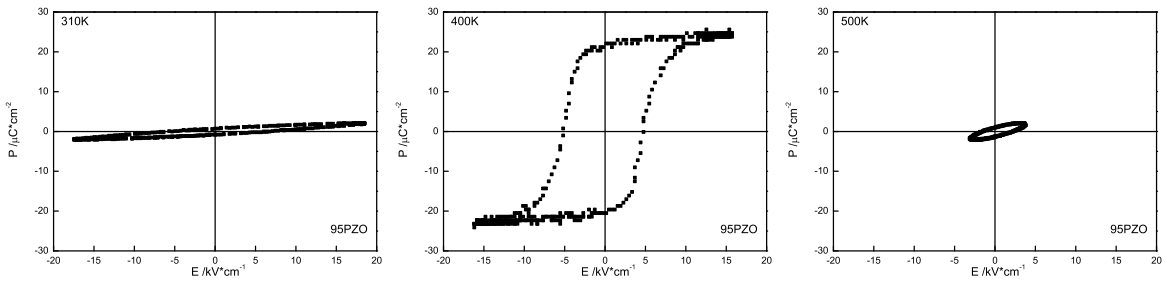

(a) 310K (b) 400K (c) 500K

Figure 4.36 *FE hysteresis loops of 95PZO at selected temperatures*

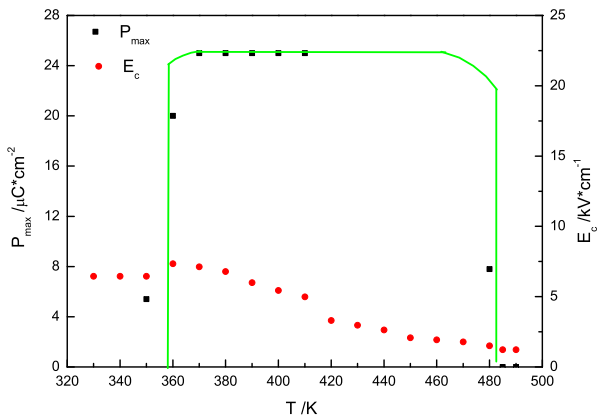

Figure 4.37 *Temperature dependences of Polarization and coercive field for 95PZO*

4.5 PFW-PZO under electric field

Obviously, both short-range and long-range polar orders can be influenced by an external DC electric field. It is interesting to investigate how the polar state can be affected in solid solution. Figure 4.38 shows the dielectric permittivity of 50PZO with a bias field between 1kV/cm to 6kV/cm on cooling at a frequency of 1MHz. The behaviors of PFW and PZO which already discussed in last chapter are also included for comparing. Obviously, solid solution manifests a dramatic effect by electric field especially, in relaxation region.

Electric field adjustable property is tunability of materials. Recently, people look for high tunability materials for tunable filters, phase shifters, antennas and else. The tunability of materials is calculated by:

$$t = \frac{\varepsilon(E_0) - \varepsilon(E)}{\varepsilon(E_0)} \tag{4.3}$$

We calculated t of PFW and 50PZO around dielectric maximum at 1MHz, the results are plotted in fig.4.39. The dash lines in the figure reflect the linear relationship between electric field and tunability: t = k*E, for pure PFW, k = 0.033 cm/kV, for 50PZO, k = 0.074 cm/kV. If $\varepsilon(E)$ is replaced by the dielectric permittivity of ZFHaFC, the recoverability of the dielectric permittivity after switching off electric field can be characterized:

$$t' = \frac{\varepsilon(E_0) - \varepsilon(ZFHaFC)}{\varepsilon(E_0)} \tag{4.4}$$

t' of PFW and 50PZO are also included in fig. 4.39 by soft points. Both of PFW and 50PZO perform a good recoverability. In 50PZO, after 3 kV/cm, the dielectric permittivity even is enhanced after electric field.

Comparing with high tunability $BaZr_{0.50}Ti_{0.50}O_3$ (t = 0. 37 at 144 K under 30 kV/cm bias) [197], under 5kV/cm bias, 50PZO can get $BaZr_{0.50}Ti_{0.50}O_3$ similar tunability at 371K which is not far from room temperature. The solid solution opens a door of a new tunability system.

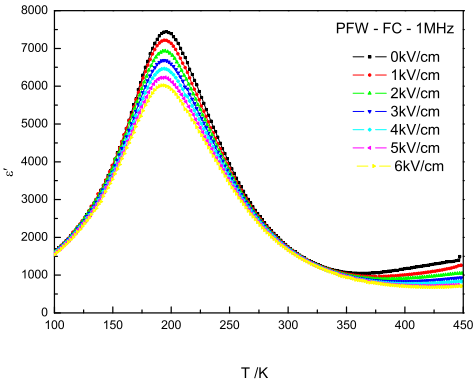

(a) PFW fields

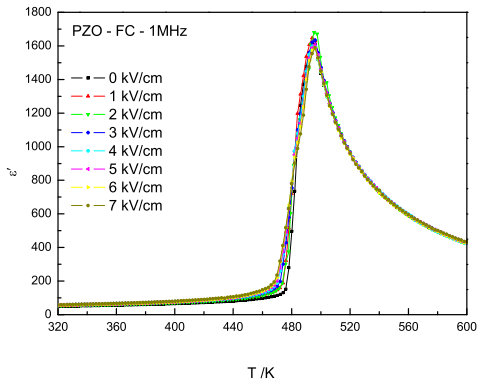

(b) PZO

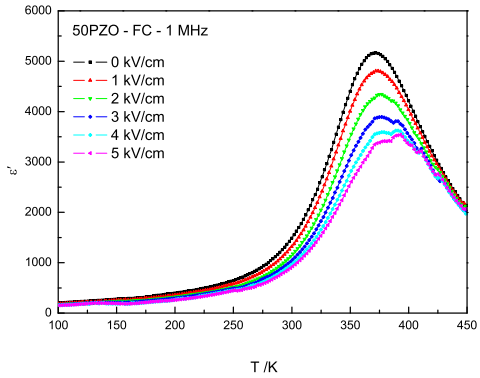

(c) 50PZO fields

Figure 4.38 *Dielectric permittivity and dielectric loss tangent after different DC bias fields for PFW, 50PZO and PZO*

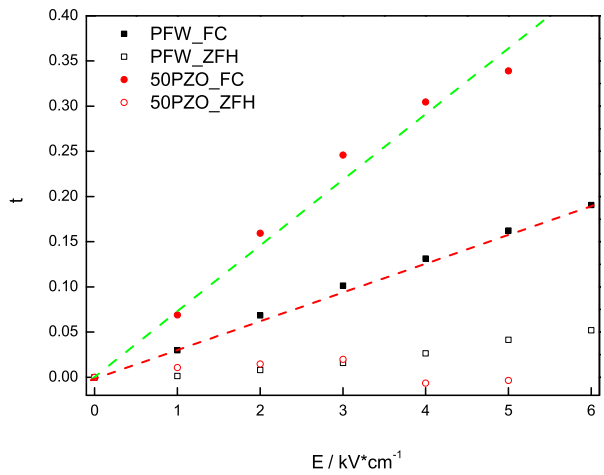

Figure 4.39 *t versus E*

4.6 Polar phase diagram of PFW-PZO

Depending on X-ray diffraction, various electric measurements (dielectric, pyroelectric, hysteresis loop), a complete and tentative polar phase diagram of PFW-PZO solid solution is gotten (see. 4.40). PE is the paraelectric phase of the solid solution which crystallizes a cubic Pm$\bar{3}$m structure. The phase diagram is characterized by a ferroelectric (FE) phase separating a relaxor phase (PFW side) and antiferroelectric (AFE) phase (PZO side). The most important feature of the PFW-PZO, being different from other solid solutions, is the existence of a no ferroelectric phase at low temperature. We already explained that no symmetry broken is found for this phase. The FE phase crystallizes a rhomboheral R3m structure and AFE phase crystallizes a orthorhombic Pbam structure which is the same as PZO.

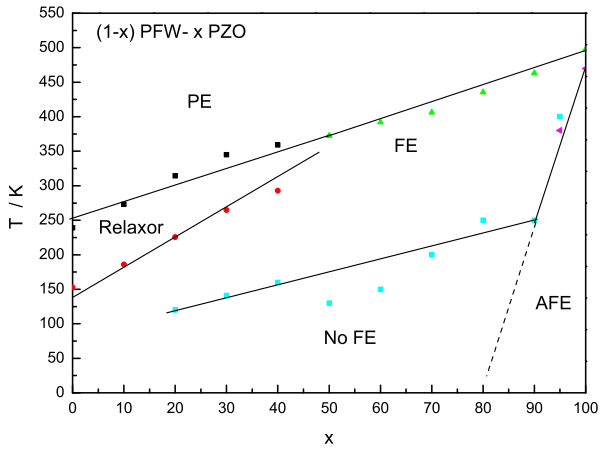

Figure 4.40 *Polar phase diagram of PFW-PZO*

It is become even more important to consider the polarization as our aim is to fabricate a room temperature multiferroic material. In this goal, the maximum polarization and coercive field as a function a character temperature which is the central of FE phase zone are plotted in fig.4.41). For all compositions, the coercive field are about 5 kV/cm. The maximum of polarization is about $25\mu C/cm^{-2}$ which is larger than pure PFW or pure PZO. At RT, a well defined FE material with polarization about $10\mu C/cm^{-2}$ can be found from 50PZO to 60PZO. Obviously, this region is very important to consider potential multiferroic property.

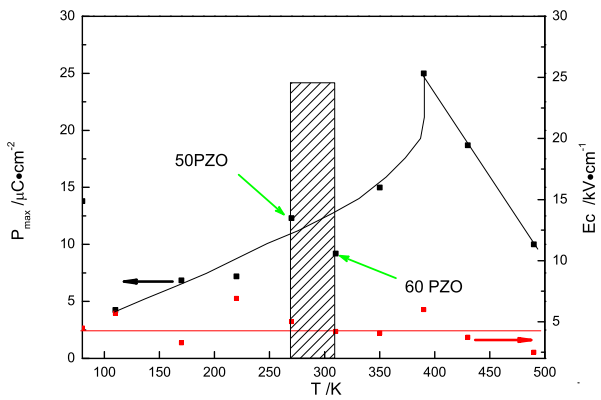

Figure 4.41 *Polarization, coercive field are plotted as a function of a character temperature. Because we find a platform in P versus T relationship, the center temperature of the platform is chosen as the character temperature*

4.7 Magnetic properties of PFW-PZO

4.7.1 Magnetic susceptibility

We investigated the magnetic susceptibility vs temperature in two different magnetic field regimes i.e. Zero-Field-Cooling (ZFC) and Field-Cooling (FC). In ZFC, the sample was measured by heating accompanying magnetic field after a first cooling without magnetic field. In FC, the sample was measured by cooling accompanying magnetic field. A small magnetic field, 100 Oe, was used during experiment.

The magnetic susceptibility of PFW-PZO as a function of temperature is plotted in fig. 4.42. From 30PZO to 50PZO, an obvious difference between ZFC and FC is clearly revealed. A tiny difference at very low temperature is found for 60PZO. There is no obvious difference for 70PZO and 90PZO which display a typical paramagnetic material behavior. In fact, for 90PZO, if assuming the magnetic moment of Fe^{3+} is 5 μ_B, the magnetic moment of 90PZO is 0.33μ_B per molecular. At 5K, the experimental magnetic moment is 0.00039 μ_B per f.u. which is 0.11% comparing with magnetic moment of a single 90PZO molecule. It implys that a long range magnetic order is not expected for 90PZO.

Careful checking the magnetic susceptibility versus temperature, a critical temperature which is marked by $T_{S.G.}$ with a green arrow in figure 4.42) is found. At $T_{S.G.}$, magnetic susceptibility displays a cusp on ZFC, a different tendency on FC, and a large splitting between ZFC and FC. It is the spin glass phase transition. Interestingly, we observed spin glass phase transition in pure PFW and. $T_{S.G.}$ is 13.21K, 25.17K, 13.3K and 7K for 30PZO, 40PZO, 50PZO and 60PZO respectively, higher than 5K of PFW. Figure 4.43 reveals the relationship between composition and $T_{S.G.}$. From PFW to 40PZO, $T_{S.G.}$ increases, from 50PZO to 60PZO, $T_{S.G.}$ decreases, a divergence occurs between 40PZO and 50PZO which is also the same region separating relaxor and ferroelectric phase.

The increasing of $T_{S.G.}$ means that the spin glass state is stabilized by B site Zr^{4+} replacement. PFW displays both long-range and short-range magnetic orders. Typically, the AFM order can be related to Fe^{3+}-O- Fe^{3+} superexchange mechanism through Fe/W disordered regions and the weak FM may come from Fe^{3+}-O-W-O-Fe^{3+} superexchange through Fe/W chemically ordered regions [63]. The competitions between weak FM clusters within an AFM matrix can give rise to a spin glass (or frustrated) behavior at low temperature. Obviously, non-magnetic-ion Zr^{4+} replacement enhances FM order but it disturbs AFM order. This is why we find increasing of $T_{S.G.}$ by increasing content of PZO. Also, disturbing AFM order make the AFM phase transition difficult to detect. In fact, it is already proved by many PFW based solid solution systems. Importantly, B site should still keep a average disorder after replacement because the spin glass is a frustrated structure. In fact, this is the case for solid solution because no superstructure diffraction was found in solid solution by X-ray.

4.7.2 Magnetic hysteresis loop

As PFW-PZO already shows interesting competitions between weak FM clusters within an AFM matrix. The magnetization at room temperature is strongly desired for the aim of fabricating novel multiferroic materials. We investigated the magnetization by hysteresis loop under 0.5T magnetic field. The results are plotted in fig. 4.44. It is very encouraging that the ferromagnetic like hysteresis loop is observed until 60PZO. The remnant magnetizations are 0.0153 μ_B per f. u. , 0.01299 μ_B per f. u. , 0.00846 μ_B per f. u. and 0.00303 μ_B per f. u., 0.00298 μ_B per f.u., and 0.00115 μ_B per f.u. for 10PZO, 20PZO, 30PZO, 40PZO, 50PZO and 60PZO respectively. For 70PZO, only a very tiny magnetization can be seen. 90PZO almost displays a linear M-H relationship. Even the experiments of magnetization are very small, considering the linear M-H relationship of PFW and no magnetic PZO, the result suggests the powerful of solid solution. According to magnetic susceptibility and magnetic hysteresis loop experiments, 60PZO is the last composition bring magnetic order with increasing PZO in solid solution.

For clearing the weak ferromagnetic behavior at room temperature, We consider three type magnetic orders which are possible and/or already found in perovskite:

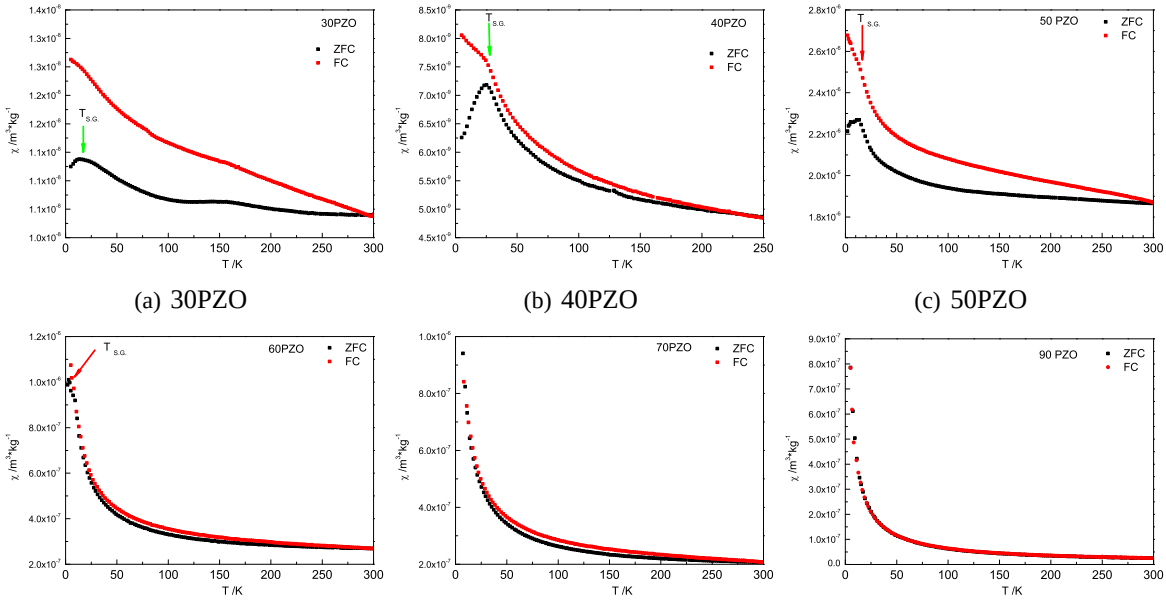

(a) 30PZO (b) 40PZO (c) 50PZO

(d) 60PZO (e) 70PZO (f) 90PZO

Figure 4.42 *Temperature dependence of magnetic susceptibility for 30PZO, 40PZO, 50PZO, 60PZO, 70PZO and 90PZO.*

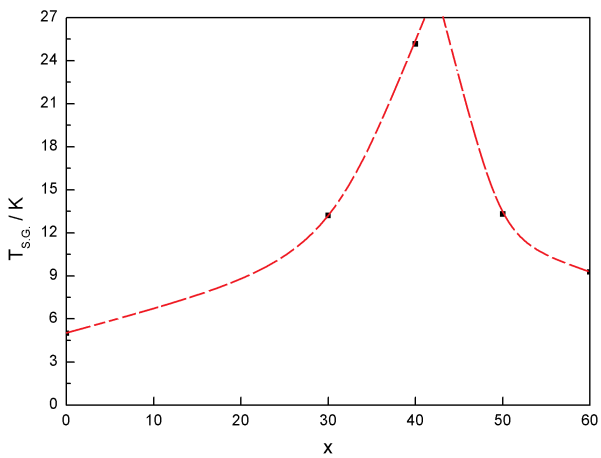

Figure 4.43 *$T_{S.G.}$ as a function of composition.*

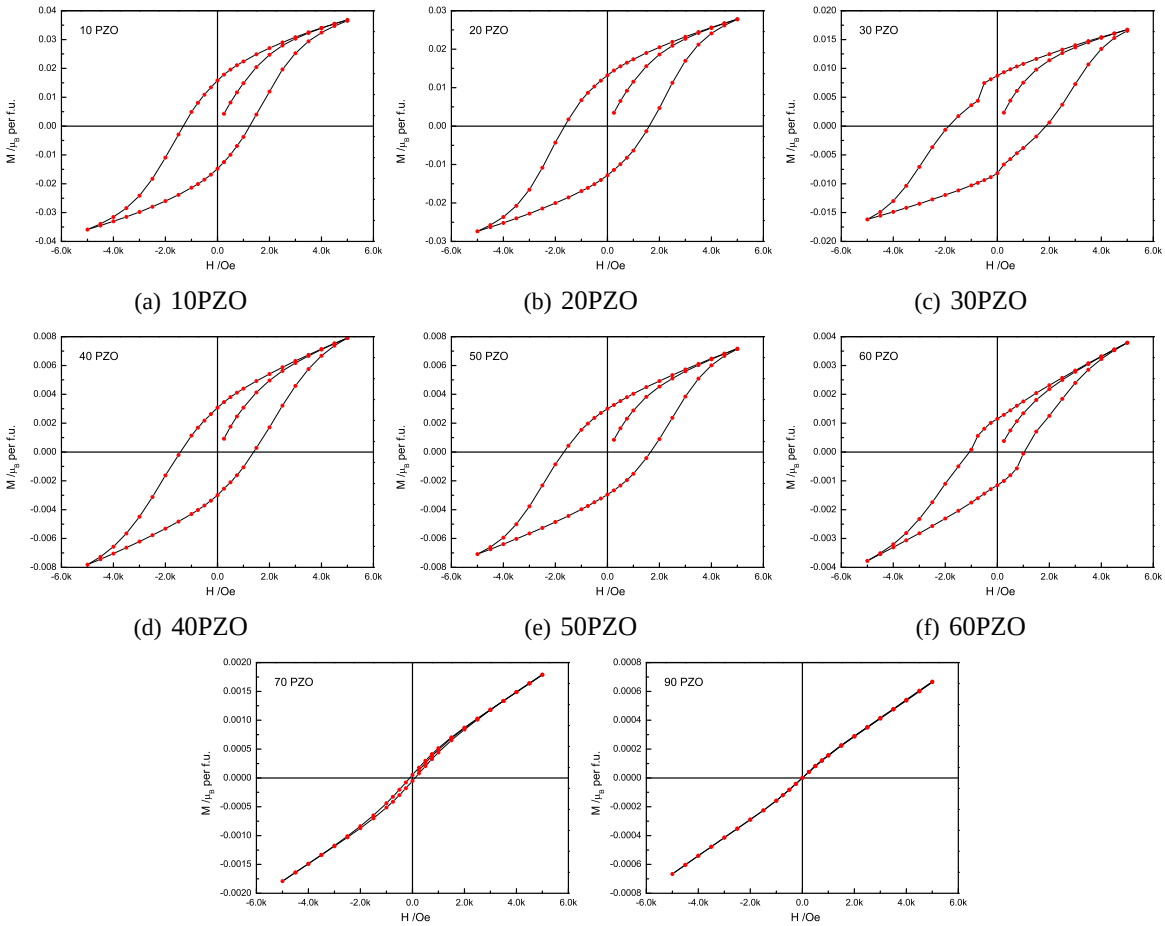

(a) 10PZO (b) 20PZO (c) 30PZO

(d) 40PZO (e) 50PZO (f) 60PZO

(g) 70PZO (h) 90PZO

Figure 4.44 *Magnetization hysteresis loops of PFW-PZO at 300K*

1. ferromagnetic order: all the magnetic moments which come from the spin of Fe^{3+} align each other.

2. ferrimagnetic order: it is a B site ordered system. If $Fe^{3+} \geq 0.5$, one of B site is unique occupies by Fe^{3+}, another B site is occupies by rest of Fe^{3+}, W^{6+} and Zr^{3+} ions, two type occupations alternate each other. For the situation of $Fe^{3+} \leq 0.5$, one of B site has Fe^{3+} but the other B site does not have Fe^{3+}. Obviously, this is a B site partly ordered structure.

3. spin canting order: the magnetic moment of PFW-PZO has 1° canting as BFO [129].

Our strategy is to calculate magnetization using assumed magnetic orders, then comparing with the experiments. The experimental, and calculated magnetizations are compared in fig.4.45. Ferromagnetic and ferrimagnetic orders are directly excluded; the experiments are comparable with 1° spin canting which is suggested for model multiferroic BFO. The magnetization as a function of composition is plotted in fig.4.45(d), the solid line in the figure is the magnetization of PFW under 0.5T, it is interesting that enhanced magnetization only exists in relaxor compounds. We already described that spin glass favor a cubic structure, thus, both long range (intrinsic existence or induced by magnetic field) and short range magnetic orders are easily stabilized in a cubic structure than a rhombohedral one.

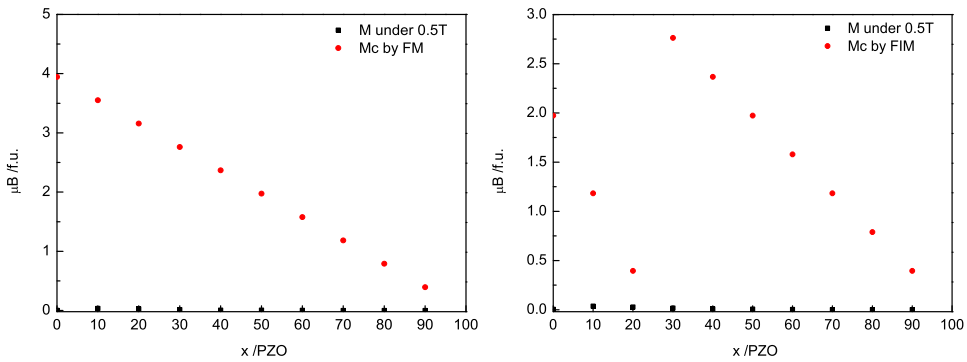

(a) Comparing with ferromagnetic order

(b) Comparing with ferrimagnetic order

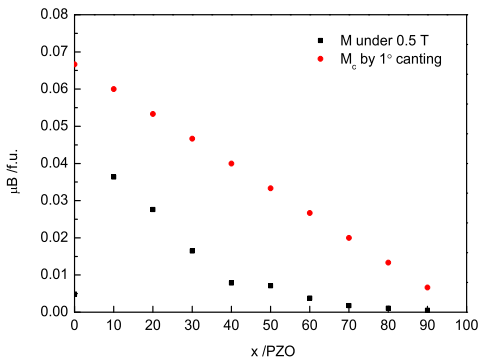

(c) Comparing with 1° as BFO

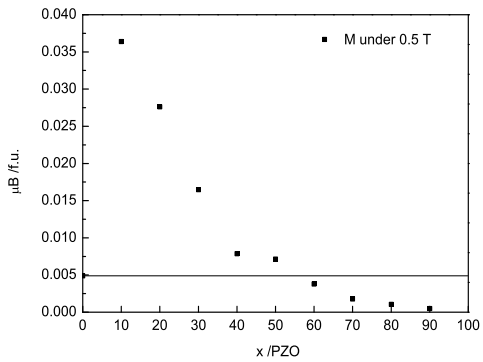

(d) Magnetization

Figure 4.45 *Magnetization as a function of composition. Black point are experimental data; red points are calculated data by different models.*

BFO is a G-type AFM and well studied because of its multiferroic properties. The magnetization is strongly related to samples [78] [198] [199]. The observed ferromagnetic behavior is because of the reduction of Fe^{3+} to Fe^{2+} [200] [202] or increase canting angle [201] [129]. The long range antiferromagnetic order is necessary for BFO spin canting model. In order to check the existence of long range antiferromagnetic order, we performed neutron diffraction which was done by D2B at ILL with a wavelength 1.594Å. The magnetic structure of PFW is G-type AFM which multiplies the crystal structure

two times in 3D, giving magnetic Bragg diffraction peaks. Fig 4.46 shows the neutron diffraction patterns of pure PFW, 30PZO and 50PZO. The blue arrow in the figure marks the magnetic Bragg peak of PFW. Unfortunately, we did observed the same type peak for 30PZO and 50PZO. It suggests that long range antiferromagnetic order is broken by solid solution. Thus, spin canting is not enough to explain the room temperature behavior of PFW-PZO.

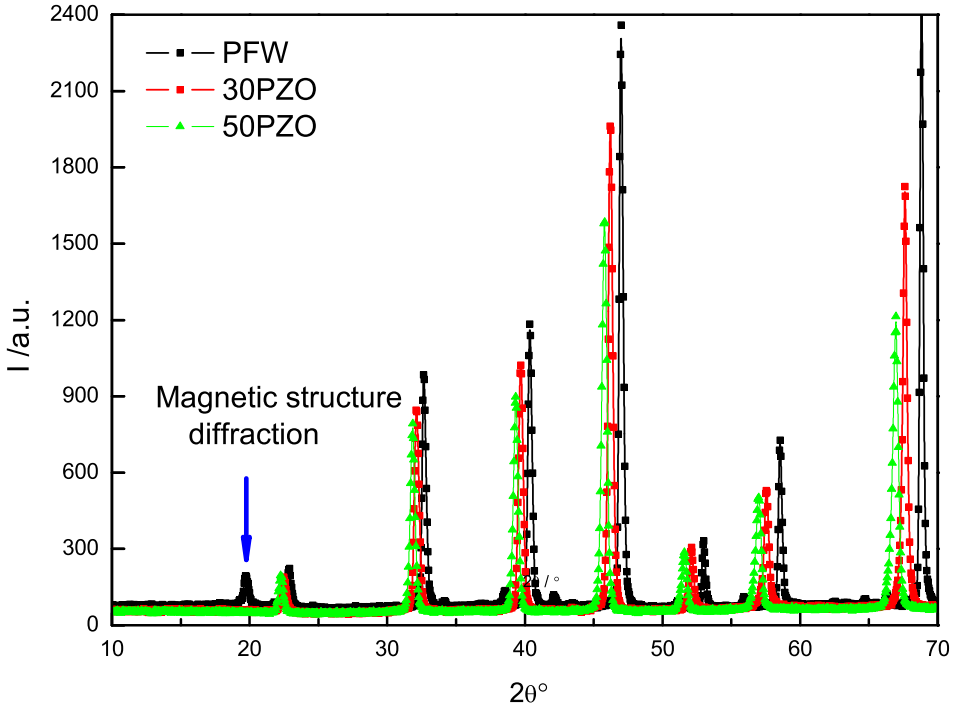

Figure 4.46 *Neutron diffraction patterns of PFW, 30PZO and 50PZO*

Does the observed magnetic behavior coming from any parasitic phase? The conventional iron oxides are wüstite (FeO), hematite (α-Fe_2O_3), maghemite (γ-Fe_2O_3), magnetite (Fe_3O_4).

Wüstite is a antiferromagnetic below ∼200K [203] [204]. It is immediately excluded as the origin of ferromagnetic behavior of PFW-PZO. Hematite has a weak ferromagnetic order which comes from the canting of spins and keeps up to about 950K [205] [206] [207] [208] [209]. The spontaneous magnetization is 0.0083 per f.u. [210]. Magnetite is a ferrimagnetic with T_C about 850K [211] [212] [213]. It changes from ferrimagnetic semiconductor to ferrimagnetic insulator at Verwey temperature about 123.7K accompanying a jump of magnetization 0.25 μ_B [214] or not [215]. For 5nm particles, super spin-glass phase occurs below 30K [216]. The saturated magnetization of bulk magnetite is 3.83μ_B [217]. The magnetic moment of single crystal is 4.05 3.83μ_B [218]. The theory magnetic moment could be 4.90 or 4 μ_B. Maghemite can be looked as a Fe_3O_4 empty $\frac{1}{6}$ Fe^{3+} from B site, it is a ferrimagnetic with T_C about 948K, it begins to transform to α-Fe_2O_3 at about 673K [219] [220] [221] [222] [223] [224] [225]. The magnetic moment is 2.36 μ_B at 4.2K [219], for 5nm particles it is 1.98 μ_B [226]. The theory magnetic moment of maghemite is 2.5 or 2.96 μ_B.

Assuming the magnetization comes from one iron oxide, we can obtain the quantity of the iron oxide in solid solution. The calculated quantities of of hematite, magnetite and maghemite are plotted in fig.4.47(a), fig.4.47(b) and fig.4.47(c). Obviously, hematite is impossible but around 1 % parsitic phase of magnetite or maghemite can induce related magnetization.

Except the iron oxides, there are also other possibilities, i.e., M-type hexaferrite, magnetoplumbite ($PbFe_{12}O_{19}$) which appears in PZT ceramic [227]. The magnetic moment of $PbFe_{12}O_{19}$ is 11.8 μ_B per f.u. [228] or 10 μ_B per f.u. [229]. If the magnetization of PFW-PZO comes from $PbFe_{12}O_{19}$, the maximum mass percent of $PbFe_{12}O_{19}$ in PFW-PZO is 1.22% (see fig.4.47(d)).

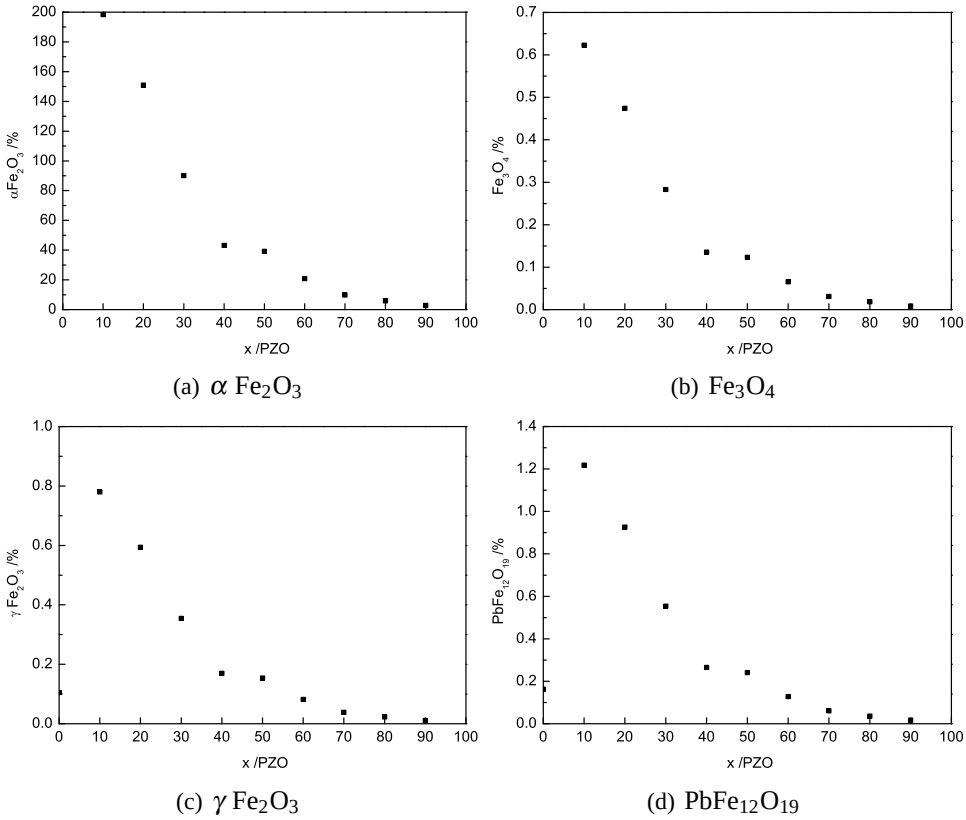

(a) α Fe_2O_3 (b) Fe_3O_4

(c) γ Fe_2O_3 (d) $PbFe_{12}O_{19}$

Figure 4.47 *Calculated quantity of parasitic phase versus composition. Four parasitic phases, α Fe_2O_3, Fe_3O_4, γ Fe_2O_3 and $PbFe_{12}O_{19}$ are considered.*

We did not find any parasitic phase in PFW-PZO by X-ray diffraction. For continuing study the possibility of parasitic phases, scanning electron microscope with energy-dispersive X-ray spectroscopy was used to study the solid solution samples. Two pieces of samples of PFW were examined, Fe rich zone was found in one of them (fig.4.48(b)). Zr rich zone was found in PZO (fig.4.48(d)). However, we did not observe any parasitic phase in 30PZO (fig. 4.48(c)). After many experiments, we found that Zr rich is quite normal after 70PZO but Fe rich is only found in PFW.

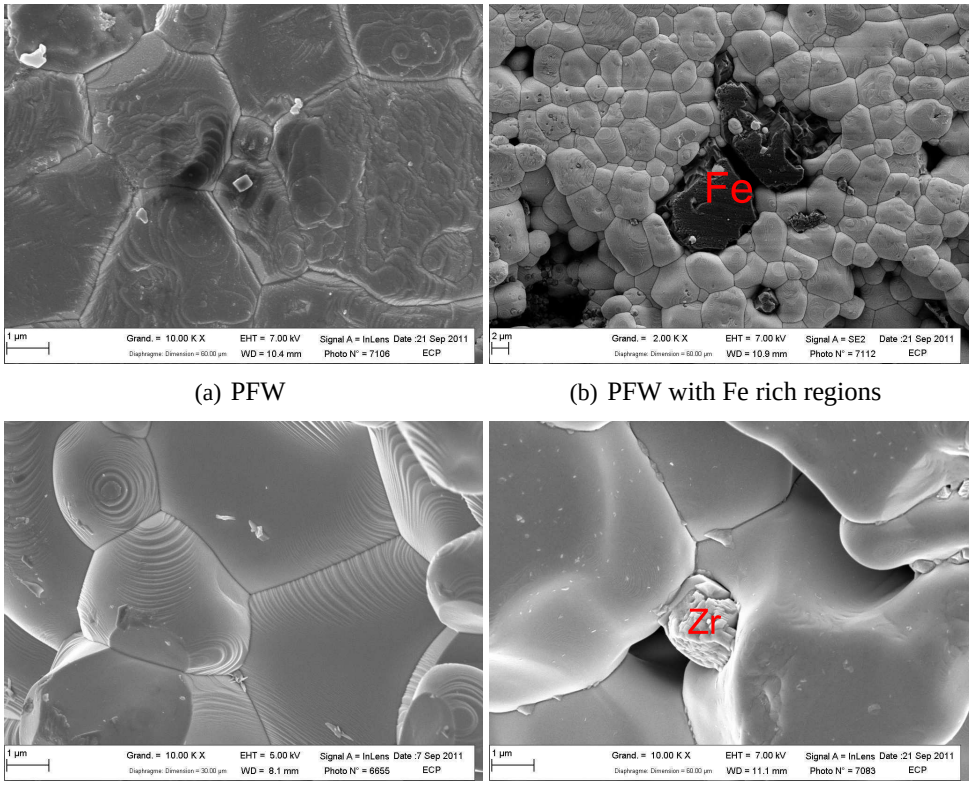

(a) PFW (b) PFW with Fe rich regions

(c) 30PZO (d) PZO

Figure 4.48 *Microstructures of PFW, 30PZO and PZO*

4.8 Conclusion

In summary, we investigate in details the structural, electric and magnetic properties of PFW-PZO. The solid solution transitions from a cubic to a rhombohedral, at last a orthorhombic by increasing the content of PZO. All the polar orders (PNRs, FE, FE with AFE/NON-FE, AFE) are formed in the solid solution. The solid solution can be separated into three regions, a cubic relaxor, a rhobohedral FE and a orthorhombic AFE. The rhombohedal FE is quite instable at low temperature. Rich phase transitions occur at low temperature for both relaxor and rhombohedral FE. In addition, room temperature magnetization, low temperature spin glass state were found in the solid solution.

The all set of data allows us to construct a complete multi-degrees-of-freedom phase diagram. From 40PZO to 50PZO, the solid solution transform from cubic to rhombohedral accompanying relaxor extinction. Interesting, the spin glass phase transition also displays a divergence between 40PZO and 50PZO. Therefore, beyond finding a room temperature multiferroic around 50PZO, the strong magnetoelectric coupling also is expected.

Chapter 5

Magnetic Ions Doped Lead Zirconate

Except study PFW-PZO solid solution, we also fabricated magnetic ions doped $PbZrO_3$ (PZMs). In fact, in order to look for novel multiferroic, $PbVO_3$, $PbFeO_3$ and $PbCrO_3$ were synthesized at high pressure high temperature [230], [231], [232] [233]. Generally, this type compounds should have both polar and magnetic properties because A site brings ferroelectric active ions but B site brings magnetically active transition metal. Unfortunately, in these compounds, the oxygen deficient structure which is related to the valences of A and B cations worsens the polar behavior [234].

We prepared several magnetic-like ions manganese ($Mn^{3+/4+}$), iron ($Fe^{2+/3+}$) and cobalt ($Co^{3+/4+}$) doped PZO at ambient environment by solid state reaction method.

Goldshmidt t factor which varies from 0.91 to 1.06 depending on charge and spin state of $Mn^{3+/4+}$, $Fe^{2+/3+}$ and $Co^{3+/4+}$ suggests that a stable perovskite is possble for all these doping. For convenient discussion the properties of doped PZO, the doped PZO is represented by PZM*x*, M is the doping ion ($Mn^{3+/4+}$, $Fe^{2+/3+}$ or $Co^{3+/4+}$), *x* is the atom percent of doped ion in the compound.

5.1 Limitation of doping

Doping is powerful for adjusting the performances of materials. But, doping also can induce parasitic phases. Before specifically discussing the doping effects, we first propose the limitation of doping which can be reflected by dielectric measurement, microstructure and X-ray diffraction.

Fig. 5.1 shows the dielectric permittivity versus temperature of PZM at 1MHz. The dielectric peak decreases from 498K to 472 K whatever the composition. This is a abnormal behavior for doping because a continuing sifting of critical temperature is expected generally.

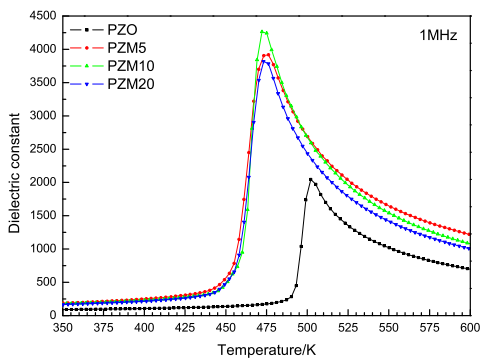

Figure 5.1 *Dielectric permittivity versus temperature of PZM. The data of PZO are also included for comparing.*

In fact, slight extra Bragg peaks which can be indexed as Mn_3O_4 and PbO_2 are found in PZM20

by X-ray diffraction. After multi-phases Rietveld refinement, there are 0.8% (vol) Mn_3O_4 and 0.1% (vol) PbO_2 0.8% (vol) in PZM20. This consists with the experiment of microscope by EDX (Energy-dispersive X-ray spectroscopy) embedded XL30 SEM (scanning electrode microscope). The microscope structures of PZM are shown in fig. 5.2. Comparing with PZM5, PZM20 has rich Mn zones (the dark zones in the figure).

All these results describe a doping evolution: with increasing doping quantity, doped $Mn^{4+/3+}$ firstly replace B site of crystal structure, then go to grain boundary, at last a Mn rich parasitic phase appears.

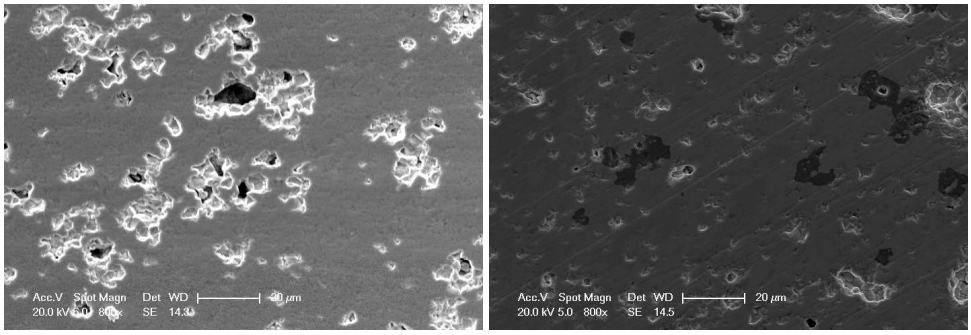

(a) PZM5 (b) PZM20

Figure 5.2 *Scanning electron microscopy of PZM*

The similar situation occurs in Fe and Co doped PZO (fig. 5.3). Obvious parasitic phase Bragg peak is observed in X-ray diffraction pattern of PZF20, a smaller shift of T_C is observed for PZC10 comparing to PZC5 by dielectric measurement.

We can careful conclude that 10% is a limitation for $Mn^{3+/4+}$, $Fe^{2+/3+}$ and $Co^{3+/4+}$ doped PZO by solid reaction method at ambient condition.

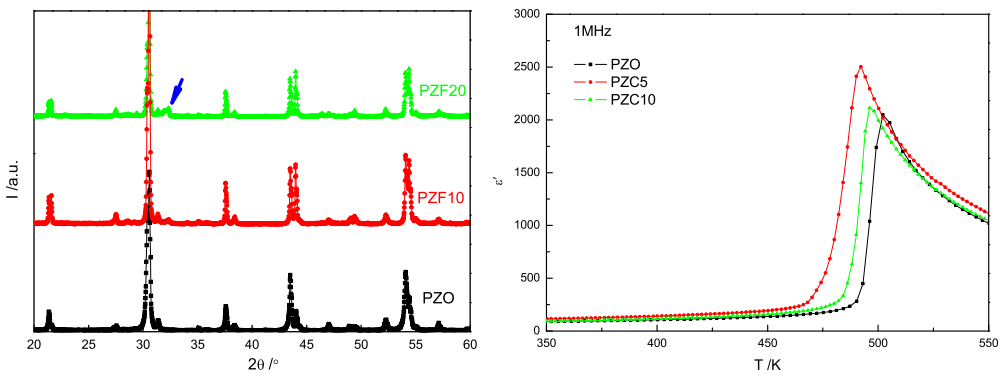

(a) (b)

Figure 5.3 *Evidences of doping limitation: (a) X-ray diffraction patterns of PZF, (b) temperature dependence of dielectric permittivity for PZC*

5.2 Doping effects

5.2.1 Stability of AFE

PZO crystallizes in a orthorhombic structure bring the anti-parallel displacements of Pb^{2+} along p.c. (110)-direction which are associated to the AFE state. It is interesting to investigate the influences of doping on antiferroelectric state. The AFE configuration of PZM, PZF and PZC is first studied by

Rietveld refinement. 2θ changes from 5° to 120° or 130 °. The high angle diffraction with Rietveld refinement are plotted in fig. 5.4 as we know that the high angle diffraction is important for deciding atomic positions and ADP. The experimental data (black points) and simulated peaks (green line) match very well and the differences between two are very small (red line). The refined lattice parameters are listed in table 5.1. There is no dramatic change of lattice parameters. Doping does not change the matrix of PZO. The anti-parallel displacements of Pb^{2+} along p.c. (110)-direction are calculated according refined Pb^{2+} coordinates and listed in table. 5.2. Pb^{2+} performs PZO similar shifts. Thus, AFE is stable by magnetic ion doping.

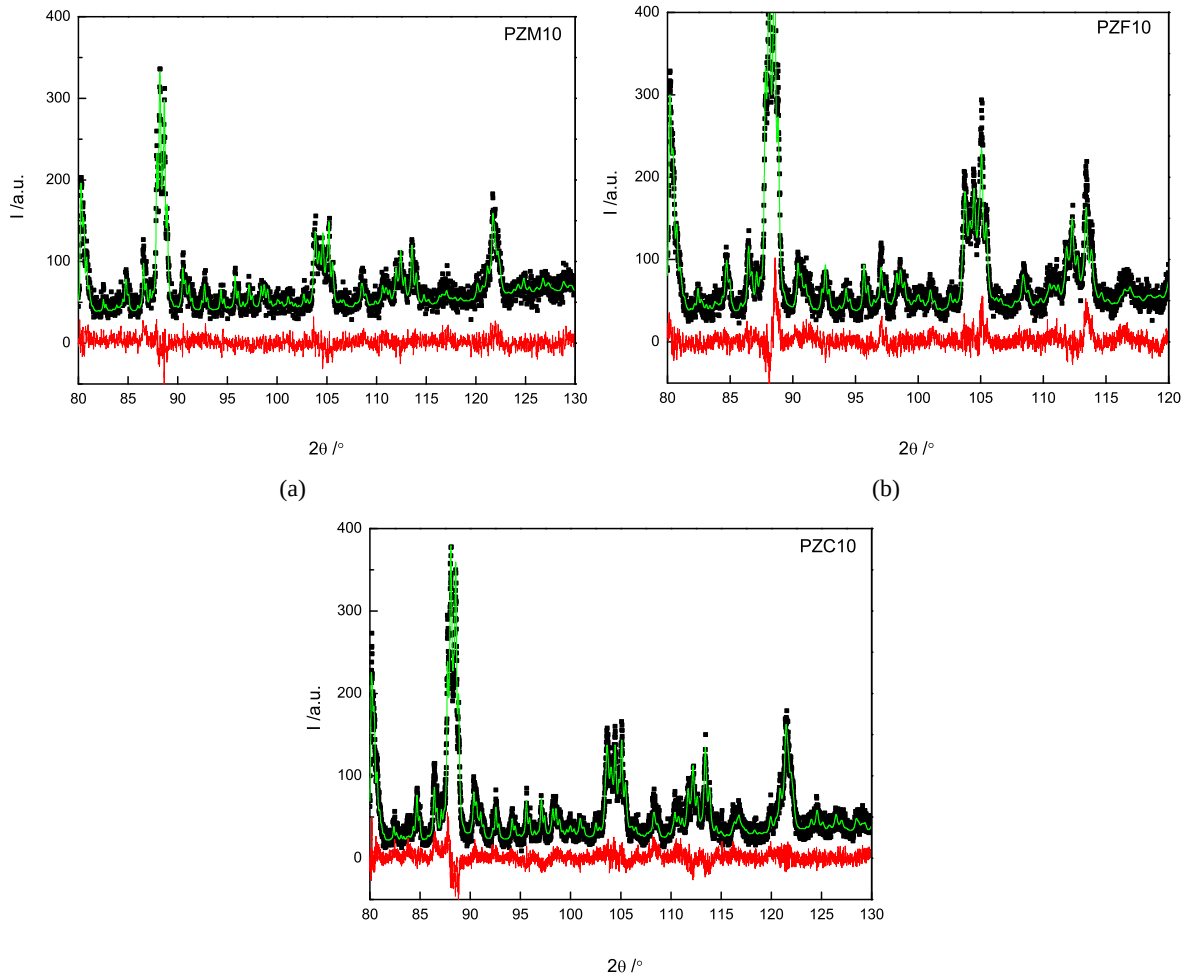

(a) (b) (c)

Figure 5.4 *Part of Rietveld refinement plots for (a)PZM10, (b)PZF10 and (c)PZC10. Points are experimental data; green lines are simulated diffraction peaks; red lines are the differences between two.*

5.2.2 Instability of octahedron

Except the anti-parallel displacements of Pb^{2+}, octahedron tilts ($a^-a^-c^0$ type) are also present in PZO. It is interesting to consider the situation of octahedron by doping because we know that magnetic perovskite has the famous Jahn-Teller distortion.

Projection of octahedron along p.c. (001) direction is shown in fig. 5.5. PZM5 has PZO similar deformation but PZM10 shows a some new characters. The similar behavior was also found in PZF and

Table 5.1 *Lattice parameters of doped PZM. Data of PZO is also included.*

	PZO	PZM5	PZM10	PZM20	PZF10	PZF20	PZC5	PZC10
a	5.879	5.869	5.869	5.869	5.873	5.873	5.877	5.878
b	11.776	11.757	11.756	11.757	11.763	11.766	11.772	11.777
c	8.226	8.216	8.216	8.217	8.224	8.223	8.224	8.224

Table 5.2 *Pb^{2+} antipolar structural shifts for PZM*

	PZO	PZM5	PZM10	PZM20	PZF10	PZF20	PZC5	PZC10
$Pb^{2+}1$	0.259	0.258	0.246	0.246	0.270	0.299	0.270	0.232
$Pb^{2+}2$	0.229	0.235	0.211	0.264	0.194	0.194	0.213	0.236

PZC.

Specifically, the B-O distances of doped PZO were calculated and listed in table 5.3 including the data of PZO. In the figure, all the abnormal distances are given a red color for highlight. In all the doped compounds, the distance of Zr-O3 is abnormal large in PZM10 and PZC10 but small Zr-O3 in PZF10.

In PZO type orthorhombic structure, the Jahn-Teller distortion axises are along [$\bar{2}$10], [210] and [001] directions. We now discuss the distortion of oxygen octahedron. Our strategy is to consider the possibility of two Jahn-Teller modes with the symmetry restriction of Pbam space group which is the structure of PZO. If assuming z axis along [001] direction, Q3 mode is impossible because O1 and O2 are fixed along c direction; Q2 mode is impossible because O4 and O5 are fixed in a-b plane. If z axis along [$\bar{2}$10], Q3 mode is impossible because O4 is fixed in a-b plane; Q2 mode is also impossible because O1, O2 are fixed along c axis and O5 is fixed along a-b plane. If z axis along [210], O3 mode is impossible because O5 is fixed in a-b plane; Q2 mode is impossible because O1 and O2 are fixed along z direction and O4 is fixed in a-b plane. Therefor, if Jahn-Teller distortion occurs, the Pbam symmetry will be broken. Thus, both Jahn-Teller driving octahedral distortion and structural symmetry of PZO give a octahedron distortion in doped PZO.

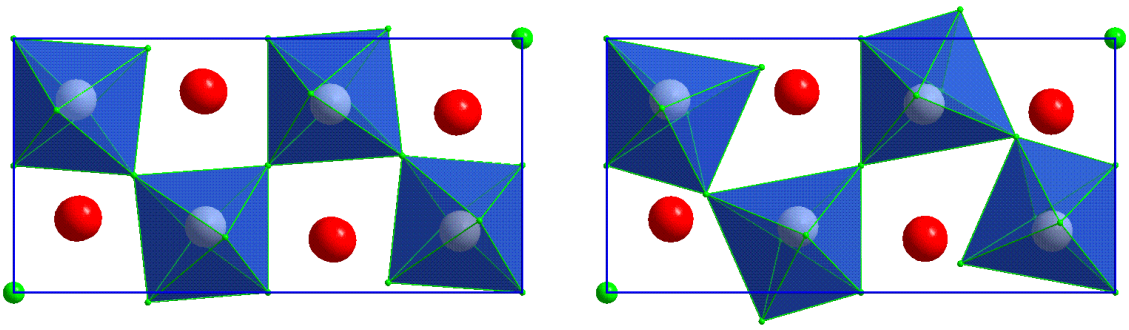

(a) PZM5 (b) PZM10

Figure 5.5 *Projection of the Octahedral deformation onto the c plane for PZM5 (a) and PZM10 (b)*

5.2.3 Existence of a ferroelectric intermediate phase

Fig. 5.6 shows the dielectric responses of doped PZO. PZM10 has a sharp dielectric peak at 474K accompanying another abnormal around 450K. For PZF10 and PZC10, except the sharp dielectric peak at 484K and 490K, the abnormal peak is also found at 460K and 464K respectively. Therefor, we can define a stable intermediate phase which is about 24K for PZM10 and PZF10, 30K for PZC10. Such a intermediate phase is also found in pure PZO strongly depending on sample type.

Table 5.3 *B-O distances of PZO, PZM10, PZF10 and PZC10*

Composition	PZO	PZM10	PZF10	PZC10
Zr-O1	2.098	1.997	2.148	2.021
Zr-O2	2.102	2.188	2.071	2.155
Zr-O3	2.041	2.288	1.849	2.463
Zr-O4	2.154	2.134	2.081	2.042
Zr-O5	2.050	2.048	2.004	2.126

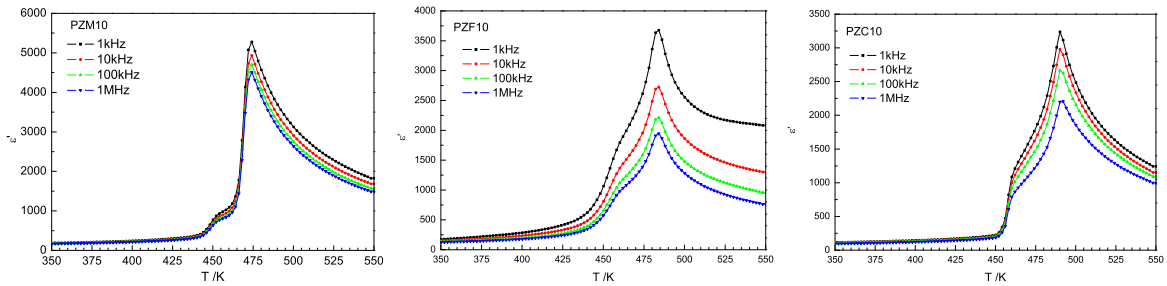

(a) (b) (c)

Figure 5.6 *Temperature dependence of dielectric permittivity for: (a) PZM10, (b)PZF10 and (c)PZC10*

For clearing the structural information of the intermediate phase. The p.c. Bragg (110), (111) and (200) peaks of PZM5 was studied by X-ray diffraction at different temperatures. The Bragg peaks at 300K, 470K and 500K are plotted in fig.5.7. On cooling, the Bragg (110) peak firstly broadens at 470K, then splits at 300K. The Bragg (111) peak splits at 470K and becomes single at 300K. For Bragg (200) peak, a tiny new peak is noticed at 470K and two well defined peaks at 300K. The splitting regulations at 470K suggest a rhombohedral structure. The tiny peak of Bragg (200) peak at 470 implies a small quantity of orthorhombic phase existence.

We did the same experiment for PZC10 but(110) peak was replaced by (220) for a better resolution. Some typical diffraction peaks is shown in fig.5.8. Here, the p.c. Bragg (220) peak become triple at 470K. The behavior strongly suggests a mixture of rhombohedral and orthorhombic.

The unit cell volume and FWHM are plotted as a function of temperature in fig. 5.9. The FWHM of Bragg (111) peak which broadens around 470K also suggests a rhombohedral intermediate phase. Beyond, the jumping of unit cell volume suggests a first order phase transition. We know that the hysteresis behavior exits for first order phase transition. Therefor, it is reasonable to explain the X-ray diffraction peaks by a mixture of two phases.

The FE property of doped PZO is directly charactered by a Sawyer-Tower electric circuit. Part of results are plotted in fig. 5.10. The well defined ferroelectric hysteresis loop is found in PZM10, PZM20, PZC5 and PZC10. The situation of PZF10 is not clear but the ferroelectric property is still expected. Two experimental results may propose this conclusion. Firstly, we find Curie-Weiss law at high temperature. Secondly and importantly, there is a obvious increasing of polarization at 460K comparing with 450K. The artificial polarization normally is because of conductivity [107] but a obviously increasing of conductivity is not expected from 450K to 460K. PZM10 gives a polarization of 20 $\mu C \bullet cm^{-1}$ which is about two times of PZO. Basically, the ferroelectric is induced by magnetic ion doping or the intrinsic ferroelectric mode in PZO is enhanced by magnetic ion doping.

5.2.4 Magnetic properties

We now discuss the magnetic behaviors of doped PZO. The M-H loops at room temperature are measured by SQUID magnetometer. The results are shown in fig. 5.11. PZM20 has a a linear M-H relationship until 1T magnetic field which gives a magnetic susceptibility of 2.104 $\times 10^{-6}$ emu $\cdot$ g $\cdot$

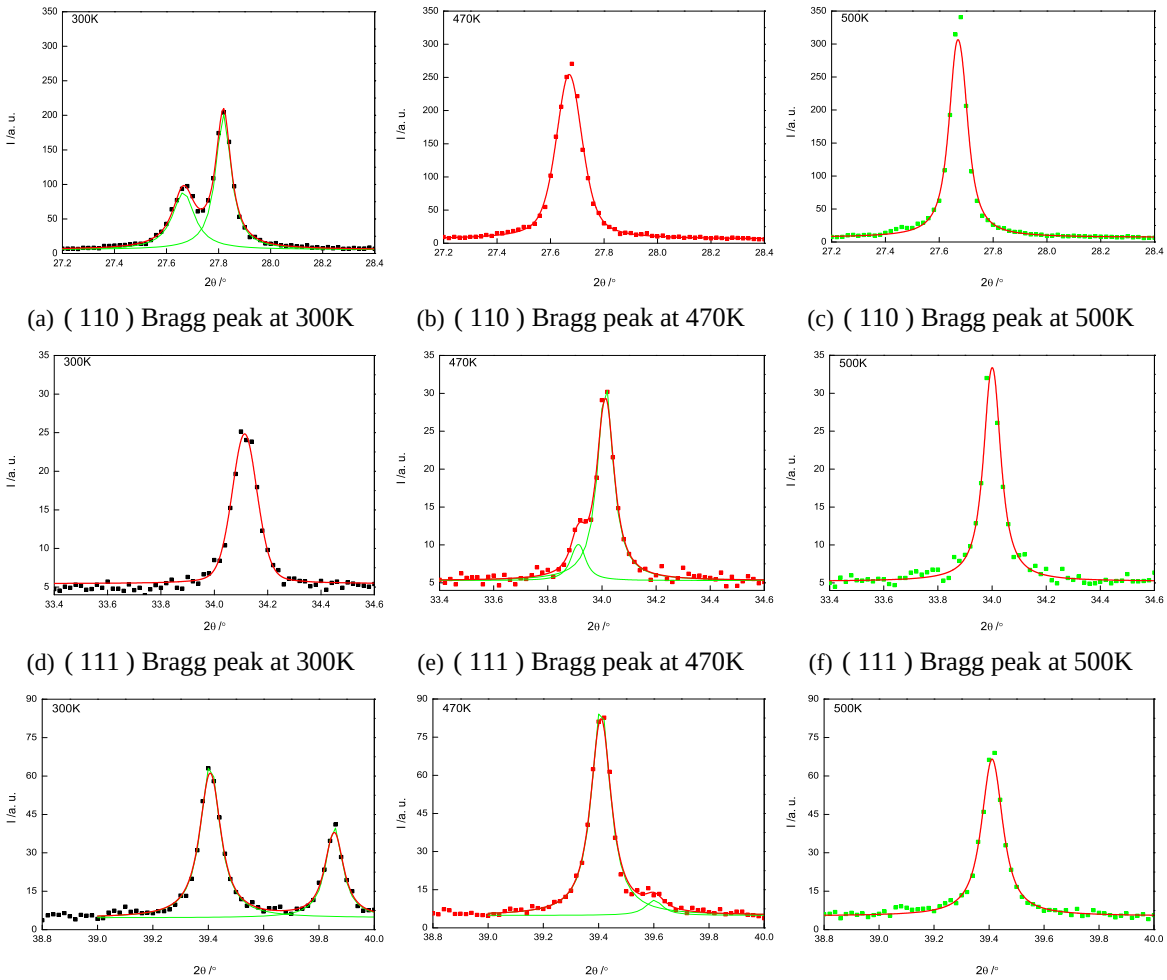

(a) (110) Bragg peak at 300K (b) (110) Bragg peak at 470K (c) (110) Bragg peak at 500K

(d) (111) Bragg peak at 300K (e) (111) Bragg peak at 470K (f) (111) Bragg peak at 500K

(g) (200) Bragg peak at 300K (h) (200) Bragg peak at 470K (i) (200) Bragg peak at 500K

Figure 5.7 *P.c. Bragg diffraction peaks (110), (111) and (200) of PZM5 at different temperatures*

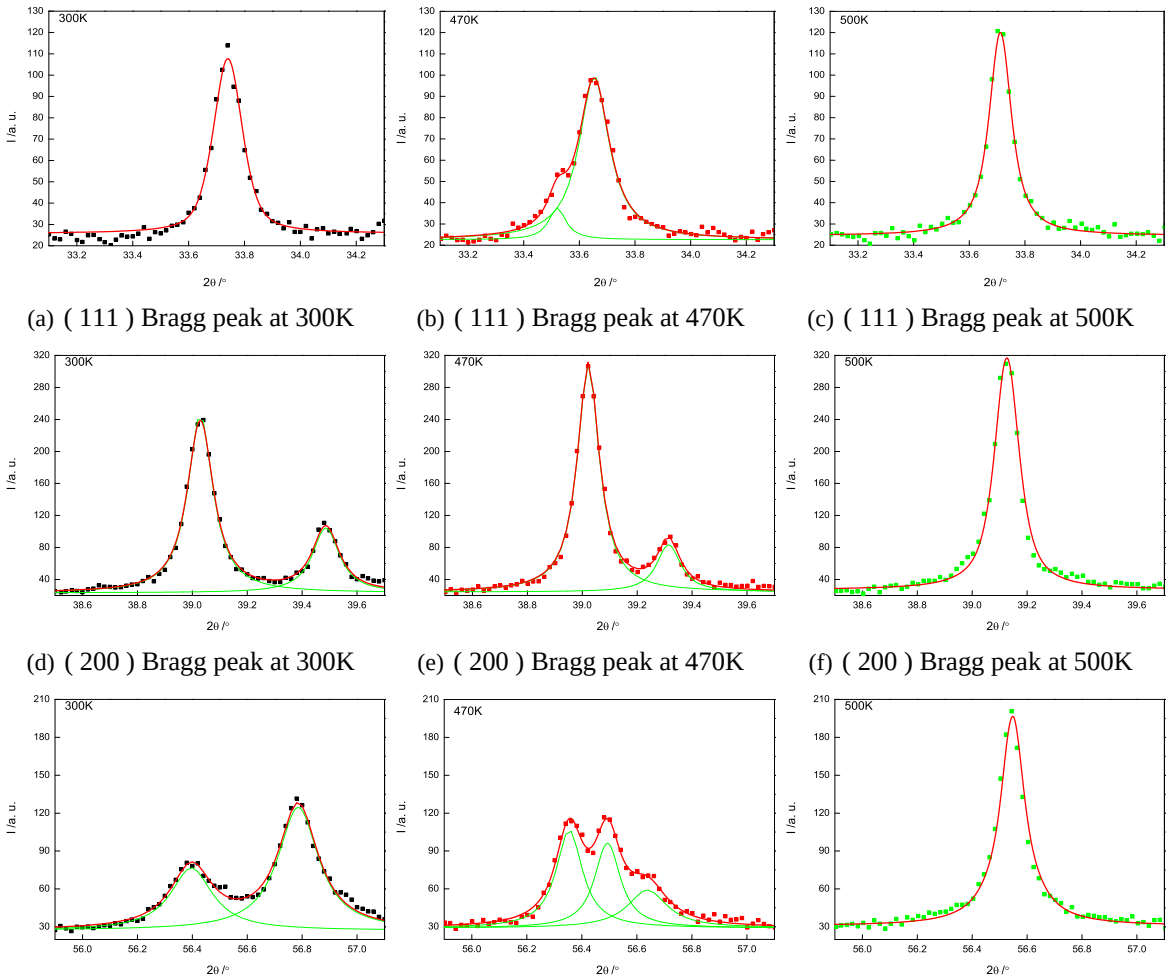

(a) (111) Bragg peak at 300K (b) (111) Bragg peak at 470K (c) (111) Bragg peak at 500K

(d) (200) Bragg peak at 300K (e) (200) Bragg peak at 470K (f) (200) Bragg peak at 500K

(g) (220) Bragg peak at 300K (h) (220) Bragg peak at 470K (i) (220) Bragg peak at 500K

Figure 5.8 *P. c. Bragg diffraction peaks (110), (111) and (200) of PZC10 at different temperatures*

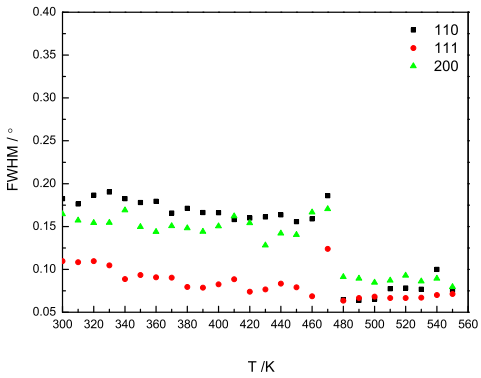

(a) Temperature dependence of FWHM for PZM5

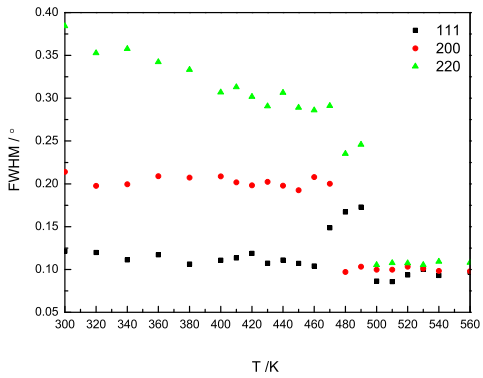

(b) Temperature dependence of FWHM for PZC10

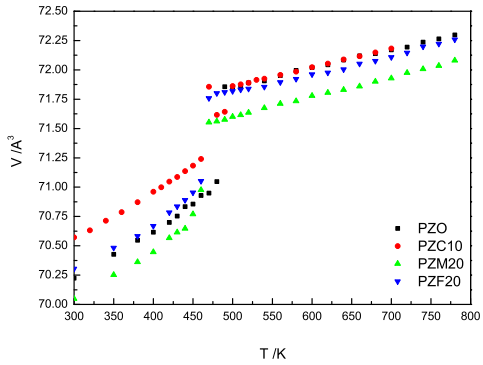

(c) Temperature dependence of V

Figure 5.9 *FWHM and unit cell versus temperature*

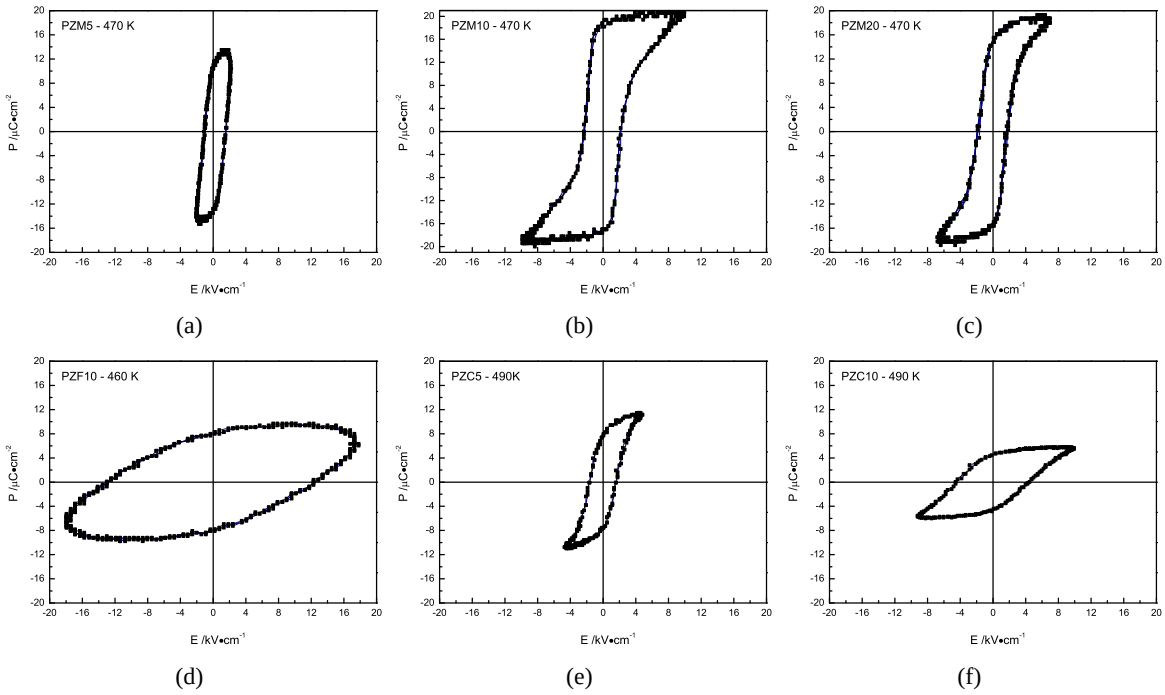

Figure 5.10 *Ferroelectric hysteresis loops for: (a)PZM5, (b)PZM10, (c)PZM20, (d)PZF10, (e)PZC5 and (f)PZC10*

Oe^{-1}. In the first section of this chapter, we described a parasitic Mn_3O_4 phase in PZM20. Mn_3O_4 is a paramagnetic material at room temperature bringing a magnetic susceptibility of 5 $\times 10^{-5}$ emu · g · Oe^{-1} [235]. 4.2% (mass) Mn_3O_4 in PZM20 can induce observed magnetic susceptibility in PZM20. In fact, ferromagnetic order is not expected at room temperature because pure $PbMnO_3$ exhibits magnetic order below 155K [233].

The behavior of PZC10 is similar with PZM20. The magnetic susceptibility is 1.218 $\times 10^{-6}$ emu · g · Oe^{-1}. Under 1T, the magnetic moment is 41.8 emu/Cr which is very large value comparing to 0.00303 emu/Cr [236] of Co_3O_4. In Co_3O_4 spinel structure, the octahedral B-site which is occupied by Co^{3+} LS does not bring magnetic moment, the tetrahedral A-site occupied by Co^{2+} HS brings 3/2 μ_B magnetic moment. Perhaps, in PZC10, Cobalt is Co^{4+} HS which brings 5/2 μ_B magnetic moment. This should be the true situation in PZC10 because no any information suggests a deficient structure.

Interestingly, ferromagnetic hysteresis loop is observed in PZF10 at room temperature. However, one should be careful because of the possibility of appearing iron oxides in the compound. Hematite (α-Fe_2O_3), maghemite (γ-Fe_2O_3), magnetite (Fe_3O_4) and magnetoplumbite ($PbFe_{12}O_{19}$) as the possible parasitic phases is considered. The magnetizations of all these oxides at room temperature are listed in table 5.4. The percents (mass) of relative oxides which can induce a experimental magnetizations in PZF10 are calculated and listed in the same table. Except α-Fe_2O_3, all the others are possible.

Table 5.4 *Magnetization of iron oxides at room temperature*

Compound	M / emu·g^{-1}	% (mass)
α-Fe_2O_3	0.29 [210]	269
γ-Fe_2O_3	82.53 [219]	0.95
Fe_3O_4	92.39 [217]	0.84
$PbFe_{12}O_{19}$	47.28 [229]	1.65

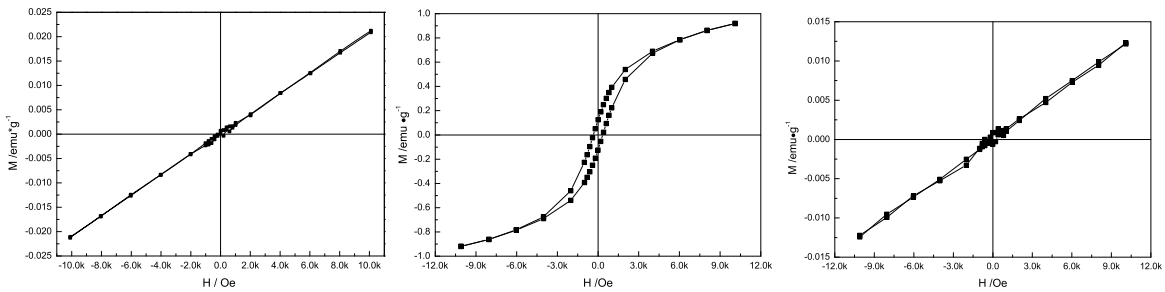

(a) PZM20 (b) PZF10 (c) PZC10

Figure 5.11 *Magnetization curves versus applied magnetic field for : (a) PZM20, (b) PZF10, and (c) PZC10*

Although ferromagnetic order is not confirmed for doped PZO, the results are also encourage, i.e. the large magnetization of PZC10 and ferromagnetic like behavior of PZF10.

5.3 Dielectric relaxation

In the dielectric permittivity of PZM5 and PZF20, we observed huge dielectric permittivity at high temperature low frequency (fig. 5.12).

Obviously, there is no direct connection between this dielectric dispersion and polar. After tentative electric parameters normalizations, we find that both PZM5 and PZF20 display a electric modulus relaxation. Fig.5.13 shows this type relaxation at some character temperatures by a Cole-Cole plots. In fact, we find that PZO also has the electric modulus relaxation (fig. 5.14).

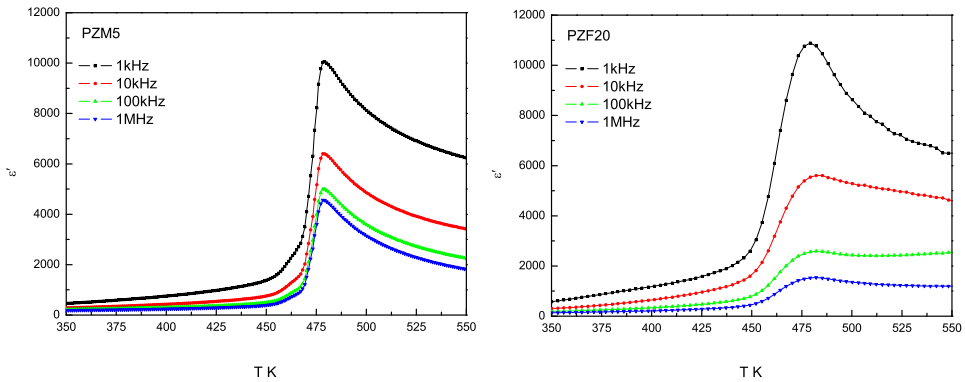

(a) PZM5 (b) PZF20

Figure 5.12 *Temperature dependence of ε′ for: (a) PZM5, (b) PZF20*

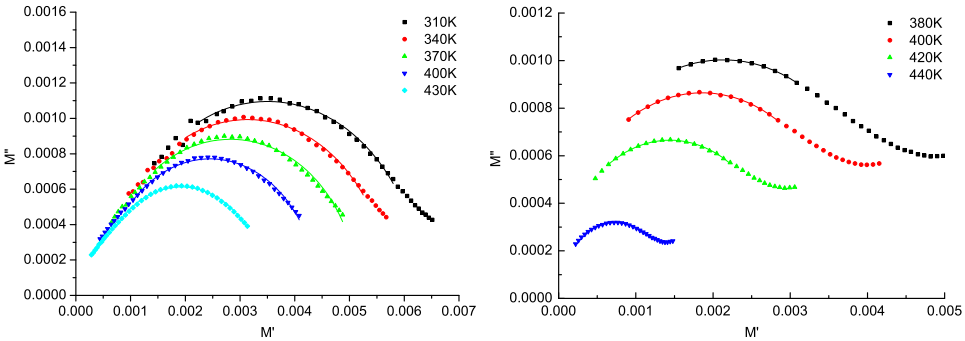

(a) (b)

Figure 5.13 *Cole-Cole plots of the imaginary part electric modulus versus the real part electric modulus for: (a) PZM5, (b) PZF20.*

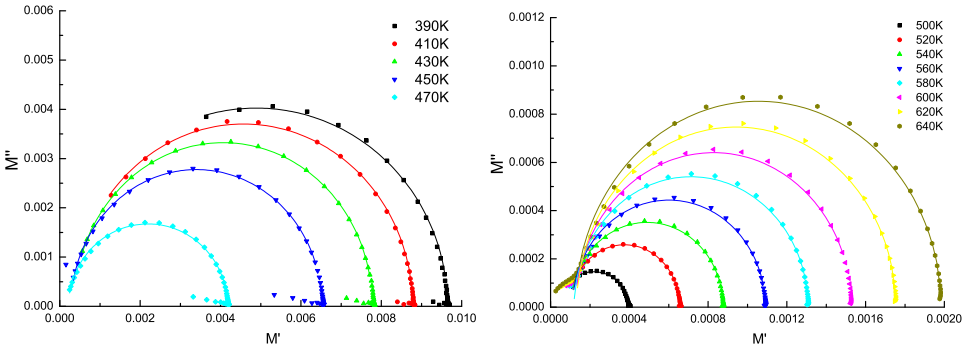

(a) (b)

Figure 5.14 *Cole-Cole plot of the imaginary part electric modulus versus the real part electric modulus for PZO: (a) in orthorhombic phase, (b) in cubic phase.*

Electric modulus relaxation is more sensitive to conductivity [99]. The ac conductivity of PZO and PZM5 is shown in fig.5.15. The ac conductivity of PZO is frequency independent. However, the ac conductivity of PZM5 satisfies a formula $\sigma_{AC} = A * f^n + B * f$), n is 0.59. This is typical universal dielectric relaxation. The ac conductivity of PZF is also controlled by universal dielectric relaxation and n varies from 0.3 to 0.74. So far, it seems dielectric dispersion accompanying both electric modulus relaxation and universal dielectric relaxation. But, what is the origin of both relaxation?

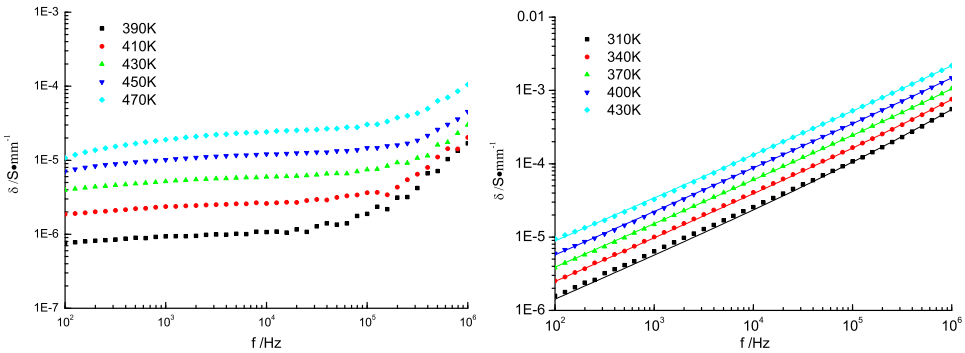

(a) (b)

Figure 5.15 *Double logarithmic plots of the variation of ac conductivity with frequency for: (a) PZO and (b)PZM5. Points are the measurements at various temperatures; lines are the fits with universal dielectric relaxation*

We did many experiments to study the electric modulus and ac conductivity in doped PZO. Both of the electric modulus and ac conductivity are sensitive to phase transition and independent to electrode in orthorhombic phase. We also find the electric modulus relaxation satisfying Arrhenius thermal active relationship(fig. 5.16). In orthorhombic phase, the thermal activation energy is ∼0.5 eV for PZO, ∼0.25 eV for PZM5 and ∼0.45 for PZF20. In cubic phase, it is ∼1 eV for PZO, ∼0.5 eV for PZM5 and ∼0.95 eV for PZF20. Generally, three type relaxations are well studies in perovskite: high temperature space charge relaxation has a ∼1eV activity energy [122] [125]; low temperature (< 120K) electron, polaronic or local polar cluster relaxation has a small than 0.1eV activity energy [121] [123] [237]; between two, the couping between conduction electrons and the motion of the off-centered B ions has a 0.2eV ∼ 0.4eV activity energy [238] [125]. Oxygen defects pay a important effect on relaxation [121] [122] [123] [124] [125] [126]. For Pb based ceramics, a thermal activated energy about 0.42 eV-0.78 eV was found over large temperature range (200K - 600K) [116] [117], [118], [119] [120] [117], [120] which is because of V''_{Pb} and electron hole. This is quite normal as Pb volatilization during sintering. Obviously, defects pay a important role for dielectric relaxation.

For PZM, Mn replacing Zr position is expected because of similar chemical properties (The electronegativity of Mn, Zr, Pb and O are 1.55, 1.33, 2.33 and 3.44 in Pauling scale) and energy favorable [239]. If B site replaced by Mn^{4+}, no defect was produced. If B site replaced by Mn^{3+}, the defect equation can be written as:

$$2MnO_2 + 2PbO + = 2Mn'_{Zr} + 5O_O + 2Pb_{Pb} + V_O^{\bullet\bullet} + \frac{1}{2}O_2 \uparrow \tag{5.1}$$

The point defects, Mn'_{Zr} and $V_O^{\bullet\bullet}$ were produced. the assumption is reasonable as $PbMnO_3$ is a oxygen deficient structure [233]. Also, electric modulus relaxation energy of PZM5 at orthorhombic phase is similar with trivalent rare-earth ions doped $SrTiO_3$ [238].

The defect equation of PZF can be written depending on the valence states of iron in PZO:

$$Fe_2O_3 + 2PbO + = 2Fe'_{Zr} + 5O_O + 2Pb_{Pb} + V_O^{\bullet\bullet} \tag{5.2}$$

$$Fe_2O_3 + 2PbO = 2Fe''_{Zr} + 4O_O + 2Pb_{Pb} + 2V_O^{\bullet\bullet} + 1/2O_2 \uparrow \tag{5.3}$$

Both are oxygen deficient structure. In fact, (Fe'_{Zr}-$V_O^{\bullet\bullet}$)$^{\bullet}$ defect associate was found in small iron doped PZO [240].

Therefor, the electric modulus relaxation of PZO, PZM5 and PZF20 is because of V''_{Pb} and (or) $V_O^{\bullet\bullet}$.

Different with electric modulus relaxation, the universal dielectric relaxation is understood as ion hopping effect [101] [102]. In PZM5 and PZF20, because of B site replaced by heterovalent ions, the universal dielectric relaxation occurs. There is no universal dielectric relaxation in PZO because all B sites occupied by Zr^{4+}.

In conclusion, dielectric dispersion of PZM5 and PZF20 is related to both electric modulus relaxation and universal dielectric relaxation which origin from B site heterovalent replacement.

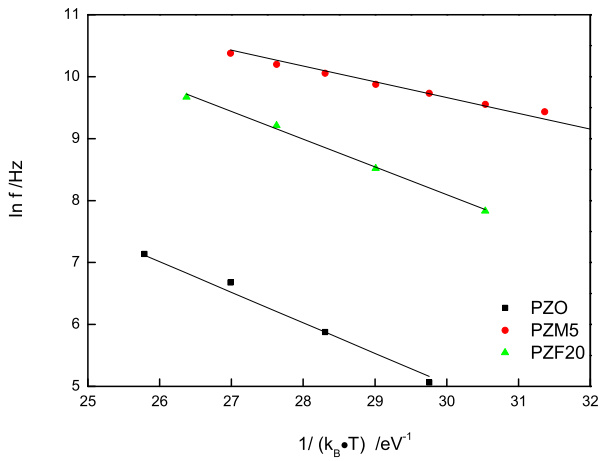

Figure 5.16 *Arrhenius plots of the electric modulus relaxation, as f vs. $1/k_BT$ for PZO, PZM5 and PZF20*

5.4 Conclusion

$Mn^{3+/4+}$, $Fe^{2+/3+}$ and $Co^{3+/4+}$ doped PZO was prepared by solid reaction method at ambient condition. The limitation of doping is about 10%. The antiferroelectric matix is kept by doping and the ferroelectric intermediate phase is even enhanced by doping. Ferroelectic is confirmed for PZM and PZC, is strongly expected for PZF.

There is a competition between orthorhombic PZO structure and Jahn-Teller distortion. Room temperature ferromagnetic is difficult to confirm but large magnetization is found in PZC and PZF shows interesting magnetic hysteresis loop.

PZF shows magnetic hysteresis loop but no ferroelectric hysteresis loop. On the contrary, PZM and PZC show well defined ferroelectric hysteresis loops but the M-H keeps a linear behavior. The results imply the very challenge of fabricating novel multiferroics.

At last, the dielectric dispersion of PZM5 and PZF20 are explained by combining electric modulus relaxation and universal dielectric relaxation which origin from B site heterovalent replacement.

Chapter 6

Conclusions and Perspectives

6.1 Conclusions

1. This study is the first time looking for new multiferroics using AntiFerroElectric (AFE) polar arrangements : it opens a new route to design multiferroics.

2. It allows to highlight the advantages to use AFE for multiferroic systems:
   AFE-FE Electric-field-induced phase transition accompanies polar arrangement which associates strain.
   AFE are always accompanied by oxygen tilted structures which are favorable for magnetism.

3. Two strategies were investigated : magnetic ion doping of PZO and solid solution with PFW.

4. Unfortunately the magnetic ion doping is restricted to 10%, but encouraging results are obtained like for instance Jahn-Teller distorsion in addition to AFE.

5. The solid solution PFW-PZO shows a rich multiferroic phase diagram including both short- and long-range orders

6. Room temperature coexistence of both polar and magnetic arrangement is evidenced : RT multiferroicity.

7. Polarization and magnetic moment values at RT for 50PZO are comparable to the only RT multiferroic namely BFO.

8. Magnetoelectricity is expected.

6.2 Perspectives

A lot of things remain to be done:

1. Better knowledge of the magnetic properties (vs temperature) is highly desired to get a complete picture of the ferroic phase diagram (SQUID, neutron, ..).

2. Neutron measurements are also required to investigate the existence of oxygen tilts.

3. Co-doping (two or more different magnetic ions) of PZO might enhance the limit of solubility and should decrease the leakage current.

4. Interesting to play with the degree of chemical order/disorder (through adequate thermal treatment) as it affects polar and magnetic properties.

5. Magnetoelectric measurements have to be performed.

Bibliography

[1] H. Megaw. Origin of ferroelectricity in barium titanate and other perovskite-type crystals. *Acta Crystallographica*, 5(6):739–749, 1952.

[2] H. D. Megaw and C. N. W. Darlington. Geometrical and structural relations in the rhombohedral perovskites. *Acta Crystallographica Section A*, 31(2):161–173, Mar 1975.

[3] A. Glazer. The classification of tilted octahedra in perovskites. *Acta Crystallographica Section B*, 28(11):3384–3392, 1972.

[4] A. Glazer. Simple ways of determining perovskite structures. *Acta Crystallographica Section A*, 31(6):756–762, 1975.

[5] Michael W Lufaso and Patrick M Woodward. Prediction of the crystal structures of perovskites using the software program SPuDS. *Acta Crystallographica Section B*, 57(6):725–738, 2001.

[6] V. M. Goldschmidt. Die gesetze der krystallochemie. *Naturwissenschaften*, 14(21):477–485, 1926.

[7] R. D. Shannon. Revised effective ionic radii and systematic studies of interatomic distances in halides and chalcogenides. *Acta Crystallographica Section A*, 32(5):751–767, Sep 1976.

[8] I. Orlov, K. Popov, and V. Urusov. Program for predicting interatomic distances in crystals by the bond valence method. *Journal of Structural Chemistry*, 39(4):575–579–579, July 1998.

[9] H. L. Yakel. On the structures of some compounds of the perovskite type. *Acta Crystallographica*, 8(7):394–398, Jul 1955.

[10] Y. Tokura and Y. Tomioka. Colossal magnetoresistive manganites. *Journal of Magnetism and Magnetic Materials*, 200(1-3):1 – 23, 1999.

[11] THEO HAHN, editor. *International tables for crystallography*, volume A space group symmetry. Springer, 5th edition, 2005.

[12] P. Woodward. Octahedral tilting in perovskites. II. structure stabilizing forces. *Acta Crystallographica Section B*, 53(1):44–66, 1997.

[13] M. E. Lines and A. M. Glass. *Principles and Applications of Ferroelectrics and Related Materials*. Clarendon Press, Oxford, 1977.

[14] Karin M. Rabe, Charles H. Ahn, and Jean-Marc Triscone, editors. *Physics of Ferroelectrics*, volume 105 of *Topics in Applied Physics*. Springer-Verlag Berlin Heidelberg, 2007.

[15] C. Kittel. Theory of antiferroelectric crystals. *Phys. Rev.*, 82(5):729–732, June 1951.

[16] Shepard Roberts. Dielectric and piezoelectric properties of barium titanate. *Phys. Rev.*, 71(12):890–895, Jun 1947.

[17] Walter J. Merz. The dielectric behavior of $BaTiO_3$ single-domain crystals. *Phys. Rev.*, 75(4):687, Feb 1949.

[18] P. W. Forsbergh. Domain structures and phase transitions in barium titanate. *Phys. Rev.*, 76(8):1187–1201, Oct 1949.

[19] A. von Hippel. Ferroelectricity, domain structure, and phase transitions of barium titanate. *Rev. Mod. Phys.*, 22(3):221–237, Jul 1950.

[20] Ronald E. Cohen. Origin of ferroelectricity in perovskite oxides. *Nature*, 358(6382):136–138, July 1992.

[21] P. Shiv Halasyamani and Kenneth R. Poeppelmeier. Noncentrosymmetric oxides. *Chemistry of Materials*, 10(10):2753–2769, 1998.

[22] C. Haas. Phase transitions in ferroelectric and antiferroelectric crystals. *Phys. Rev.*, 140(3A):A863–A868, Nov 1965.

[23] W. Cochran. Crystal stability and the theory of ferroelectricity. *Phys. Rev. Lett.*, 3(9):412–414, Nov 1959.

[24] W. Cochran. Crystal stability and the theory of ferroelectricity. *Advances in Physics*, 9(36):387–423, 1960.

[25] W. Cochran and A. Zia. Structure and dynamics of perovskite-type crystals. *physica status solidi (b)*, 25(1):273–283, 1968.

[26] R. A. Cowley. Lattice dynamics and phase transitions of strontium titanate. *Phys. Rev.*, 134(4A):A981–A997, May 1964.

[27] L. P. Bouckaert, R. Smoluchowski, and E. Wigner. Theory of brillouin zones and symmetry properties of wave functions in crystals. *Phys. Rev.*, 50(1):58–67, Jul 1936.

[28] J. F. Scott. Soft-mode spectroscopy: Experimental studies of structural phase transitions. *Rev. Mod. Phys.*, 46(1):83, Jan 1974.

[29] Ph. Ghosez, E. Cockayne, U. V. Waghmare, and K. M. Rabe. Lattice dynamics of $BaTiO_3$, $PbTiO_3$, and $PbZrO_3$: A comparative first-principles study. *Phys. Rev. B*, 60(2):836–843, Jul 1999.

[30] R. E. Cohen. Theory of ferroelectrics: a vision for the next decade and beyond. *Journal of Physics and Chemistry of Solids*, 61(2):139–146, February 2000.

[31] A. Bokov and Z.-G. Ye. Recent progress in relaxor ferroelectrics with perovskite structure. *Journal of Materials Science*, 41(1):31–52–52, January 2006.

[32] B. Dkhil, P. Gemeiner, A. Al-Barakaty, L. Bellaiche, E. Dul'kin, E. Mojaev, and M. Roth. Intermediate temperature scale T* in lead-based relaxor systems. *Phys. Rev. B*, 80(6):064103, 2009.

[33] V. Westphal, W. Kleemann, and M. D Glinchuk. Diffuse phase transitions and random-field-induced domain states of the "relaxor" ferroelectric $PbMg_{1/3}Nb_{2/3}O_3$. *Phys. Rev. Lett.*, 68(6):847–850, 1992.

[34] Gerald Burns and F. H Dacol. Crystalline ferroelectrics with glassy polarization behavior. *Phys. Rev. B*, 28(5):2527–2530, 1983.

[35] Dwight Viehland, S. J Jang, L. Eric Cross, and Manfred Wuttig. Deviation from Curie-Weiss behavior in relaxor ferroelectrics. *Phys. Rev. B*, 46(13):8003–8006, 1992.

[36] G. A. Smolenskii. Physical phenomena in ferroelectric with diffused phase transition. *J. Phy. Soc. Jpn*, 28(Suppl.):26–37, 1970.

[37] R. Clarke and J. C. Burfoot. The diffuse phase transition in potassium strontium niobate. *Ferroelectrics*, 8(1):505–506, 1974.

[38] Kenji Uchino and Shoichiro Nomura. Critical exponents of the dielectric constants in diffused-phase-transition crystals. *Ferroelectrics*, 44(1):55–61, 1982.

[39] D. U. Spínola, I. A. Santos, L. A. Bássora, J. A. Eiras, and D. Garcia. Dielectric properties of rare earth doped (Sr,Ba)Nb_2O_6 ceramics. *Journal of the European Ceramic Society*, 19(6-7):1111–1114, 1999.

[40] I A Santos and J A Eiras. Phenomenological description of the diffuse phase transition in ferroelectrics. *Journal of Physics: Condensed Matter*, 13(50):11733, 2001.

[41] Cheng-Shong Hong, Sheng-Yuan Chu, Wen-Chang Su, Ren-Chuan Chang, Hsiau-Hsian Nien, and Yung-Der Juang. Dielectric behaviors of $Pb(Fe_{2/3}W_{1/3})$-$PbTiO_3$ relaxors: Models comparison and numerical calculations. *Journal of Applied Physics*, 101(5):054120, 2007.

[42] Cheng-Shong Hong, Sheng-Yuan Chu, Wen-Chang Su, and Hsiau-Hsian Nien. Are the parameters of the empirical law dependent on the dielectric properties of the ferroelectric relaxors? *Ceramics International*, 36(3):1069–1074, 2010.

[43] Dwight Viehland, S. J. Jang, L. Eric Cross, and Manfred Wuttig. Freezing of the polarization fluctuations in lead magnesium niobate relaxors. *Journal of Applied Physics*, 68(6):2916–2921, 1990.

[44] Dwight Viehland, J. F Li, S. J Jang, L. Eric Cross, and Manfred Wuttig. Dipolar-glass model for lead magnesium niobate. *Phys. Rev. B*, 43(10):8316–8320, 1991.

[45] B. Dkhil, J. M Kiat, G. Calvarin, G. Baldinozzi, S. B Vakhrushev, and E. Suard. Local and long range polar order in the relaxor-ferroelectric compounds $PbMg_{1/3}Nb_{2/3}O_3$ and $PbMg_{0.3}Nb_{0.6}Ti_{0.1}O_3$. *Phys. Rev. B*, 65(2):024104, 2001.

[46] C. Zener. Interaction between the *d* shells in the transition metals. *Phys. Rev.*, 81(3):440¨C444, February 1951.

[47] Clarence Zener. Interaction between the *d*-Shells in the transition metals. II. ferromagnetic compounds of manganese with perovskite structure. *Phys. Rev.*, 82(3):403¨C405, May 1951.

[48] H. A. Kramers. L'interaction entre les atomes magnétogènes dans un cristal paramagnétique. *Physica*, 1(1-6):182–192, 1934.

[49] P. W Anderson. Antiferromagnetism. theory of superexchange interaction. *Phys. Rev.*, 79(2):350–356, July 1950.

[50] P. W Anderson. New approach to the theory of superexchange interactions. *Phys. Rev.*, 115(1):2, July 1959.

[51] John B Goodenough. Theory of the role of covalence in the Perovskite-Type manganites [La, M(II)]MnO_3. *Phys. Rev.*, 100(2):564–573, October 1955.

[52] Junjiro Kanamori. Crystal distortion in magnetic compounds. *Journal of Applied Physics*, 31(5):S14–S23, 1960.

[53] J. B Goodenough, A. Wold, R. J Arnott, and N. Menyuk. Relationship between crystal symmetry and magnetic properties of ionic compounds containing Mn^{3+}. *Phys. Rev.*, 124(2):373–384, October 1961.

[54] Nicolas GUIBLIN. *Synthèses, structures et mises en ordre électroniques d'ordre à valence mixte dans le système Pr-Ca-Mn-O*. PhD thesis, Universitè de Caen, 2002.

[55] E. O Wollan and W. C Koehler. Neutron diffraction study of the magnetic properties of the series of Perovskite-Type compounds [(1-x)La, xCa]MnO_3. *Phys. Rev.*, 100(2):545¨C563, October 1955.

[56] R. Przenioslo, A. Palewicz, M. Regulski, I. Sosnowska, R M Ibberson, and K S Knight. Does the modulated magnetic structure of $BiFeO_3$ change at low temperatures? *Journal of Physics: Condensed Matter*, 18(6):2069, 2006.

[57] A. Palewicz, I. Sosnowska, R. Przenioslo, and A. W. Hewat. $BiFeO_3$ crystal structure at low temperature. *ACTA PHYSICA POLONICA A*, 117(2):296, 2010.

[58] Sergey A Ivanov, Roland Tellgren, H*ä*kan Rundlof, Noel W Thomas, and Supon Ananta. Investigation of the structure of the relaxor ferroelectric $Pb(Fe_{1/2}Nb_{1/2})O_3$ by neutron powder diffraction. *Journal of Physics: Condensed Matter*, 12(11):2393, 2000.

[59] S A Ivanov, S. Eriksson, N W Thomas, R. Tellgren, and H. Rundlof. A neutron powder diffraction study of the ferroelectric relaxor $Pb(Fe_{1/2}Ta_{1/2})O_3$. *Journal of Physics: Condensed Matter*, 13(1):25, 2001.

[60] S.A. Ivanov, S.-G. Eriksson, R. Tellgren, and H. Rundlöof. Neutron powder diffraction study of the magnetoelectric relaxor $Pb(Fe_{2/3}W_{1/3})O_3$. *Materials Research Bulletin*, 39(14-15):2317–2328, December 2004.

[61] Y. Yang, J. -M Liu, H. B Huang, W. Q Zou, P. Bao, and Z. G Liu. Magnetoelectric coupling in ferroelectromagnet $Pb(Fe_{1/2}Nb_{1/2})O_3$ single crystals. *Phys. Rev. B*, 70(13):132101, 2004.

[62] Nathascia Lampis, Cesare Franchini, Guido Satta, Alessandra Geddo-Lehmann, and Sandro Massidda. Electronic structure of $PbFe_{1/2}Ta_{1/2}O_3$: crystallographic ordering and magnetic properties. *Phys. Rev. B*, 69(6):064412, 2004.

[63] Z.-G. Ye, K. Toda, M. Sato, E. Kita, and H. Shmid. Synthesis, structure and properties of the magnetic relaxor ferroelectric $Pb(Fe_{2/3}W_{1/3})O_3$ [PFW]. *J. Korean Phys.Soc.*, 32(93):S1028–S1031, 1998.

[64] I. P Raevski, S. P Kubrin, S. I Raevskaya, V. V Titov, D. A Sarychev, M. A Malitskaya, I. N Zakharchenko, and S. A Prosandeev. Experimental evidence of the crucial role of nonmagnetic Pb cations in the enhancement of the néel temperature in perovskite $Pb_{1-x}Ba_xFe_{1/2}$ $Nb_{1/2}O_3$. *Phys. Rev. B*, 80(2):024108, 2009.

[65] I. P. Raevski, S. P. Kubrin, S. I. Raevskaya, V. V. Titov, S. A. Prosandeev, D. A. Sarychev, M. A. Malitskaya, V. V. Stashenko, and I. N. Zakharchenko. Studies of ferroelectric and magnetic phase transitions in $Pb_{1-x}A_xFe_{1/2}Nb_{1/2}O_3$ (A-Ca, ba) solid solutions. *Ferroelectrics*, 398(1):16–25, 2010.

[66] H. A. Jahn and E. Teller. Stability of polyatomic molecules in degenerate electronic states. I. orbital degeneracy. *Proceedings of the Royal Society of London. Series A, Mathematical and Physical Sciences*, 161(905):220–235, 1937.

[67] Ashok Kumar, R. S. Katiyar, Carlos Rinaldi, Sergey G. Lushnikov, and Tatjana A. Shaplygina. Glasslike state in $PbFe_{1/2}Nb_{1/2}O_3$ single crystal. *Applied Physics Letters*, 93(23):232902, 2008.

[68] G. M Rotaru, B. Roessli, A. Amato, S. N Gvasaliya, C. Mudry, S. G Lushnikov, and T. A Shaplygina. Spin-glass state and long-range magnetic order in $PbFe_{1/2}Nb_{1/2}O_3$ seen via neutron scattering and muon spin rotation. *Phys. Rev. B*, 79(18):184430, 2009.

[69] R. Martinez, R. Palai, H. Huhtinen, J. Liu, J. F Scott, and R. S Katiyar. Nanoscale ordering and multiferroic behavior in $Pb(Fe_{1/2}Ta_{1/2})O_3$. *Phys. Rev. B*, 82(13):134104, 2010.

[70] Manoj K Singh, W. Prellier, M. P Singh, Ram S Katiyar, and J. F Scott. Spin-glass transition in single-crystal $BiFeo_3$. *Phys. Rev. B*, 77(14):144403, 2008.

[71] Manoj K Singh, Ram S Katiyar, W. Prellier, and J F Scott. The Almeida-Thouless line in $BiFeO_3$: is bismuth ferrite a mean field spin glass? *Journal of Physics: Condensed Matter*, 21(4):042202, 2009.

[72] Damir Pajié, Zvonko Jagličić, Marko Jagodič, Robert Blinc, Janez Hole, Marija Kosec, and Zvonko Trontelj. Low temperature magnetic behaviour of PZT-PFW bulk multiferroic ceramics. *Journal of Physics: Conference Series*, 303(1):012065, 2011.

[73] Hans Schmid. Multi-ferroic magnetoelectrics. *Ferroelectrics*, 162(1):317–338, 1994.

[74] Hans Schmid. Some symmetry aspects of ferroics and single phase multiferroics *. *Journal of Physics: Condensed Matter*, 20(43):434201, 2008.

[75] W. Eerenstein, N. D. Mathur, and J. F. Scott. Multiferroic and magnetoelectric materials. *Nature*, 442(7104):759–765, 2006.

[76] E. Ascher, H. Rieder, H. Schmid, and H. Stössel. Some properties of ferromagnetoelectric nickel-iodine boracite, $Ni_3B_7O_{13}I$. *Journal of Applied Physics*, 37(3):1404–1405, 1966.

[77] Nicola A. Hill. Why are there so few magnetic ferroelectrics? *The Journal of Physical Chemistry B*, 104(29):6694–6709, July 2000.

[78] J. Wang, J. B. Neaton, H. Zheng, V. Nagarajan, S. B. Ogale, B. Liu, D. Viehland, V. Vaithyanathan, D. G. Schlom, U. V. Waghmare, N. A. Spaldin, K. M. Rabe, M. Wuttig, and R. Ramesh. Epitaxial $BiFeO_3$ multiferroic thin film heterostructures. *Science*, 299(5613):1719 –1722, March 2003.

[79] T. Kimura, T. Goto, H. Shintani, K. Ishizaka, T. Arima, and Y. Tokura. Magnetic control of ferroelectric polarization. *Nature*, 426(6962):55–58, November 2003.

[80] N. Hur, S. Park, P. A. Sharma, J. S. Ahn, S. Guha, and S-W. Cheong. Electric polarization reversal and memory in a multiferroic material induced by magnetic fields. *Nature*, 429(6990):392–395, May 2004.

[81] Manfred Fiebig. Revival of the magnetoelectric effect. *Journal of Physics D: Applied Physics*, 38(8):R123, 2005.

[82] Sang-Wook Cheong and Maxim Mostovoy. Multiferroics: a magnetic twist for ferroelectricity. *Nat Mater*, 6(1):13–20, January 2007.

[83] Daniel Khomskii. Classifying multiferroics: Mechanisms and effects. *Physics*, 2:20, Mar 2009.

[84] K. F. Wang, J. -M. Liu, and Z. F. Ren. Multiferroicity: the coupling between magnetic and polarization orders. *Advances in Physics*, 58(4):321–448, 2009.

[85] W. F Brown, R. M Hornreich, and S. Shtrikman. Upper bound on the magnetoelectric susceptibility. *Phys. Rev.*, 168(2):574–577, April 1968.

[86] A. S. Wills. A new protocol for the determination of magnetic structures using simulated annealing and representational analysis (SARAh). *Physica B: Condensed Matter*, 276-278:680–681, March 2000.

[87] Wiesława Sikora, Franciszek Białas, and Lucjan Pytlik. *MODY*: a program for calculation of symmetry-adapted functions for ordered structures in crystals. *Journal of Applied Crystallography*, 37(6):1015–1019, Dec 2004.

[88] R. Shirley. Crysfire powder indexing system for dos/windows. CRYSFIRE Suite: The CRYSFIRE System for Automatic Powder Indexing, 2006.

[89] Armel Le Bail. Whole powder pattern decomposition methods and applications: A retrospection. *Powder Diffraction*, 20(4):316–326, 2005.

[90] Lukáš Palatinus and Gervais Chapuis. SUPERFLIP - a computer program for the solution of crystal structures by charge flipping in arbitrary dimensions. *Journal of Applied Crystallography*, 40(4):786–790, August 2007.

[91] H. M Rietveld. A profile refinement method for nuclear and magnetic structures. *Journal of Applied Crystallography*, 2(2):65–71, June 1969.

[92] J. F. Bérar. In *IUCr. Sat. Meeting on Powder Diffractometry*, Toulouse, 1990.

[93] Juan Rodríguez-Carvajal. Recent advances in magnetic structure determination by neutron powder diffraction. *Physica B: Condensed Matter*, 192(1-2):55–69, October 1993. http://www.ill.eu/sites/fullprof/.

[94] V. Petricek, M. Dusek, and L Palatinus. Jana2006. the crystallographic computing system. http://jana.fzu.cz/, 2006.

[95] L. B McCusker, R. B Von Dreele, D. E Cox, D. Louër, and P. Scardi. Rietveld refinement guidelines. *Journal of Applied Crystallography*, 32(1):36–50, February 1999.

[96] Juan Rodríguez-Carvajal. An introduction to the program fullprof 2000. Saclay, 2001.

[97] R. A. Young and D. B. Wiles. Profile shape functions in Rietveld refinements. *Journal of Applied Crystallography*, 15(4):430–438, Aug 1982.

[98] C. B Sawyer and C. H Tower. Rochelle salt as a dielectric. *Phys. Rev.*, 35(3):269–273, February 1930.

[99] I.M. Hodge, K.L. Ngai, and C.T. Moynihan. Comments on the electric modulus function. *Journal of Non-Crystalline Solids*, 351(2):104–115, 2005.

[100] A K Jonscher. *universal relaxation law*. Chelsea Dielectrics Press, London, 1996.

[101] C. León, A. Rivera, A. Várez, J. Sanz, J. Santamaria, and K. L. Ngai. Origin of constant loss in ionic conductors. *Phys. Rev. Lett.*, 86(7):1279–1282, Feb 2001.

[102] A. S. Nowick and B. S. Lim. Electrical relaxations: Simple versus complex ionic systems. *Phys. Rev. B*, 63(18):184115, Apr 2001.

[103] C. R. Bowen and D. P. Almond. Modelling the 'universal' dielectric response in heterogeneous materials using microstructural electrical networks. *Materials Science and Technology*, 22(6):719, 2006.

[104] Karl Willy Wagner. Zur theorie der vollkommenen dielektrika. *Annalen Der Physik*, 40(5):53, 1913.

[105] Karl Willy Wagner. Erkl1ärung der dielektrischen nachwirkungsvorgänge auf grund maxwellscher vorstellungen. *Archiv für Elektrotechnik*, 2(9):371, 1914.

[106] NICOLA A. SPALDIN. *MAGNETIC MATERIALS Fundamentals and Applications*. CAMBRIDGE UNIVERSITY PRESS, 2011.

[107] J F Scott. Ferroelectrics go bananas. *Journal of Physics: Condensed Matter*, 20(2):021001, 2008.

[108] A. Loidl, S. Krohns, J. Hemberger, and P. Lunkenheimer. Bananas go paraelectric. *Journal of Physics: Condensed Matter*, 20(19):191001, 2008.

[109] G. A. Smolenskii and V. A. Bokov. Coexistence of magnetic and electric ordering in crystals. *Journal of Applied Physics*, 35(3):915–918, 1964.

[110] Liliana Mitoseriu, Maria M. Carnasciali, Paolo Piaggio, and Paolo Nanni. Evidence of the relaxor-paraelectric phase transition in $Pb(Fe_{2/3}W_{2/3})O_3$ ceramics. *Applied Physics Letters*, 81(26):5006–5008, 2002.

[111] Z. -G. Ye and H. Schmid. Electric field induced effect on the optical, dielectric and ferroelectric properties of $Pb(Fe_{2/3}W_{1/3})O_3$ single crystals. *Ferroelectrics*, 162(1):119–133, 1994.

[112] Zuo-Guang Ye and Hans Schmid. Growth from high temperature solution and characterization of $Pb(Fe_{2/3}W_{1/3})O_3$ single crystals. *Journal of Crystal Growth*, 167(3-4):628–637, October 1996.

[113] R. -Y. Yang, M. -H. Lin, and H. -Y. Lu. Core-shell structures in pressureless-sintered undoped $Pb(Fe_{2/3}W_{1/3})O_3$ ceramics. *Acta Materialia*, 49(13):2597–2607, 2001.

[114] I. Raevskii, D. Sarychev, S. Bryugeman, L. Reznichenko, L. Shilkina, O. Razumovskaya, V. Nikolaev, N. Vyshatko, and A. Salak. Study of cation ordering and magnetic phase transitions in ternary Fe-containing perovskite oxides by mössbauer spectroscopy. *Crystallography Reports*, 47(6):1012–1015, November 2002.

[115] Li Feng, Haiyan Guo, and Zuo-Guang Ye. Magnetic ordering in relaxor ferroelectric (1-x)$PbFe_{2/3}W_{1/3}O_3$ - x$PbTiO_3$ single crystals. *Journal of Materials Research*, 22:2116–2124, 2006.

[116] Liqin Zhou, P. M. Vilarinho, and J. L. Baptista. The characteristics of the diffuse phase transition in mn doped $Pb(Fe_{2/3}W_1/3)O_3$ relaxor ceramics. *Journal of Applied Physics*, 85(4):2312–2317, 1999.

[117] D. Szwagierczak and J. Kulawik. Influence of MnO_2 and Co_3O_4 dopants on dielectric properties of $Pb(Fe_{2/3}W_{1/3})O_3$ ceramics. *Journal of the European Ceramic Society*, 25(9):1657–1662, 2005.

[118] Liqin Zhou, P. M. Vilarinho, P. Q. Mantas, J. L. Baptista, and E. Fortunato. The effects of la on the dielectric properties of lead iron tungstate $Pb(Fe_{2/3}W_{1/3})O_3$ relaxor ceramics. *Journal of the European Ceramic Society*, 20(8):1035–1041, 2000.

[119] Paula M. Vilarinho, Liqin Zhou, Manfred Pöckl, Nelson Marques, and Jo ao L. Baptista. Dielectric properties of $Pb(Fe_{2/3}W_{1/3})O_3$–$PbTiO_3$ Solid-Solution ceramics. *Journal of the American Ceramic Society*, 83(5):1149–1152, 2000.

[120] Cheng-Shong Hong, Sheng-Yuan Chu, Cheng-Che Tsai, and Chi-Cheng Hsu. Lanthanum dopant induced transition from the ferroelectric to the relaxor state in 0.7PFW-0.3PT ceramics. *Ceramics International*, 37(6):1911–1918, 2011.

[121] M. Maglione and M. Belkaoumi. Electron–relaxation-mode interaction in $BaTiO_3$:Nb. *Phys. Rev. B*, 45(5):2029–2034, 1992.

[122] O. Bidault, P. Goux, M. Kchikech, M. Belkaoumi, and M. Maglione. Space-charge relaxation in perovskites. *Phys. Rev. B*, 49(12):7868–7873, 1994.

[123] O. Bidault, M. Maglione, M. Actis, M. Kchikech, and B. Salce. Polaronic relaxation in perovskites. *Phys. Rev. B*, 52(6):4191–4197, 1995.

[124] Zhi Yu, Chen Ang, and L. E. Cross. Oxygen-vacancy-related dielectric anomalies in La:$SrTiO_3$. *Applied Physics Letters*, 74(20):3044–3046, 1999.

[125] Chen Ang, Zhi Yu, and L. E Cross. Oxygen-vacancy-related low-frequency dielectric relaxation and electrical conduction in Bi:$SrTiO_3$. *Phys. Rev. B*, 62(1):228–236, 2000.

[126] Jianjun Liu, Chun-Gang Duan, Wei-Guo Yin, W. N. Mei, R. W. Smith, and J. R. Hardy. Dielectric permittivity and electric modulus in $Bi_2Ti_4O_{11}$. *The Journal of Chemical Physics*, 119(5):2812–2819, 2003.

[127] A. P. Levanyuk et al. *Soviet Physics JETP*, 49:176, 1979.

[128] C. Gilles, P. Bonville, H. Rakoto, J. M. Broto, K. K. W. Wong, and S. Mann. Magnetic hysteresis and superantiferromagnetism in ferritin nanoparticles. *Journal of Magnetism and Magnetic Materials*, 241(2-3):430–440, 2002.

[129] Claude Ederer and Nicola A Spaldin. Weak ferromagnetism and magnetoelectric coupling in bismuth ferrite. *Phys. Rev. B*, 71(6):060401, February 2005.

[130] Michiyoshi Tanaka, Ryuichi Saito, and Kaoru Tsuzuki. Electron microscopic studies on domain structure of $PbZrO_3$. *Japanese Journal of Applied Physics*, 21(Part 1, No. 2):291–299, 1982.

[131] G. Shen, C. Lu, H. Shen, and Y. Wang. Transmission electron microscopy study of 180° domain structure in $PbZrO_3$. *Journal of Materials Science Letters*, 16(11):880–882–882, June 1997.

[132] G. J. Shen and K. Shen. Electron microscope study of domains in $PbZrO_3$. *Journal of Materials Science*, 34(20):5153–5156–5156, October 1999.

[133] SMEPARD ROBERTS. Dielectric properties of lead zirconate and Barium-Lead zirconate. *Journal of the American Ceramic Society*, 33(2):63–66, 1950.

[134] Gen Shirane, Sadao Hoshino, and Kazuo Suzuki. X-Ray study of the phase transition in lead titanate. *Phys. Rev.*, 80(6):1105¨C1106, 1950.

[135] E. Sawaguchi, H. Maniwa, and S. Hoshino. Antiferroelectric structure of lead zirconate. *Phys. Rev.*, 83(5):1078, September 1951.

[136] Xunhu Dai, Jie-Fang Li, and Dwight Viehland. Weak ferroelectricity in antiferroelectric lead zirconate. *Phys. Rev. B*, 51(5):2651–2655, February 1995.

[137] F. Jona, G. Shirane, and R. Pepinsky. Optical study of $PbZrO_3$ and $NaNbO_3$ single crystals. *Phys. Rev.*, 97(6):1584¨C1590, March 1955.

[138] A. E. PASTO and R. A. CONDRATE. Raman spectrum of $PbZrO_3$. *Journal of the American Ceramic Society*, 56(8):436–438, 1973.

[139] A. Leyderman, I. Leont'ev, O. Fesenko, and N. Leon'tev. Dipole order and stability of the ferroelectric and antiferroelectric states in lead zirconate. *Physics of the Solid State*, 40(7):1204–1207–1207, July 1998.

[140] A. M Glazer, K. Roleder, and J. Dec. Structure and disorder in single-crystal lead zirconate, $PbZrO_3$. *Acta Crystallographica Section B*, 49(5):846–852, October 1993.

[141] Hideshi Fujishita, Yōchi Shiozaki, Norio Achiwa, and Etsuro Sawaguchi. Crystal structure determination of antiferroelectric $PbZrO_3$ –application of profile analysis method to powder method of x-ray and neutron diffraction–*. *Journal of the Physical Society of Japan*, 51(11):3583–3591, 1982.

[142] Hideshi Fujishita and Sadao Hoshino. A study of structural phase transitions in antiferroelectric $PbZrO_3$ by neutron diffraction. *Journal of the Physical Society of Japan*, 53(1):226–234, 1984.

[143] G. Kugel, I. Jankowska-Sumara, K. Roleder, and J. Dec. High temperature raman light scattering in $PbZrO_3$ single crystals. *Journal of the Korean Physical Society*, 32(92):S581–S583, 1998.

[144] K. Roleder, G E Kugel, M D Fontana, J. Handerek, S. Lahlou, and C. Carabatos-Nedelec. Raman scattering in $PbZr_{1-x}Ti_xO_3$ single crystals with low ti content and a study of the ti influence. *Journal of Physics: Condensed Matter*, 1(12):2257, 1989.

[145] G. Shirane, E. Sawaguchi, and Y. Takagi. Dielectric properties of lead zirconate. *Phys. Rev.*, 84(3):476–481, Nov 1951.

[146] T. Ostapchuk, J. Petzelt, V. Zelezny, S. Kamba, V. Bovtun, V. Porokhonskyy, A. Pashkin, P. Kuzel, M D Glinchuk, I P Bykov, B. Gorshunov, and M. Dressel. Polar phonons and central mode in antiferroelectric $PbZrO_3$ ceramics. *Journal of Physics: Condensed Matter*, 13(11):2677, 2001.

[147] R W Whatmore and A M Glazer. Structural phase transitions in lead zirconate. *Journal of Physics C: Solid State Physics*, 12(8):1505, 1979.

[148] H. Fujishita and S. Katano. Re-examination of crystal structure of $PbZrO_3$ by neurton diffraction. *Journal of the Korean Physical Society*, 32(91):S202–S205, 1998.

[149] Zhengkui Xu, Xunhu Dai, Dwight Viehland, David A. Payne, Zhuang Li, and Yendao Jiang. Ferroelectric domains and incommensuration in the intermediate phase region of lead zirconate. *Journal of the American Ceramic Society*, 78(8):2220–2224, 1995.

[150] Dwight Viehland. Transmission electron microscopy study of high-Zr-content lead zirconate titanate. *Phys. Rev. B*, 52(2):778–791, Jul 1995.

[151] J. Handerek. Electric conductivity and dielectric absorption phenomena in lead zirconate ceramics. *Phys. Stat. sol.*, 21:323–329, 1967.

[152] K. Roleder and J. Dee. The defect-induced ferroelectric phase in thin $PbZrO_3$ single crystals. *Journal of Physics: Condensed Matter*, 1(8):1503, 1989.

[153] David J Singh. Structure and energetics of antiferroelectric $PbZrO_3$. *Phys. Rev. B*, 52(17):12559–12563, 1995.

[154] R. Kagimura and D. J Singh. First-principles investigations of elastic properties and energetics of antiferroelectric and ferroelectric phases of $PbZrO_3$. *Phys. Rev. B*, 77(10):104113, 2008.

[155] B. A. SCOTT and GERALD BURNS. Crystal growth and observation of the ferroelectric phase of $PbZrO_3$. *Journal of the American Ceramic Society*, 55(7):331–333, 1972.

[156] J. Dec and J. Kwapulinski. Crystallogeometry of phase transitions in $PbZrO_3$ single crystals. *Journal of Physics: Condensed Matter*, 1(22):3389, 1989.

[157] V A Shuvaeva, M Yu Antipin, O E Fesenko, V G Smotrakov, and Yu T Struchkov. X-ray diffraction investigation of the ferroelectric phase $PbZrO_3$, induced by a strong electric field. *Soviet physics. Crystallography*, 37(4):551–552, 1992.

[158] V A Shuvaeva, M Yu Antipin, O E Fesenko, and Yu T Struchkov. An x-ray diffraction and EXAFS study of the electric-field-induced $PbZrO_3$ ferroelectric phase. *Journal of Physics: Condensed Matter*, 8(11):1615–1620, 1996.

[159] G. A Samara, T. Sakudo, and K. Yoshimitsu. Important generalization concerning the role of competing forces in displacive phase transitions. *Phys. Rev. Lett.*, 35(26):1767–1769, 1975.

[160] R. Haumont, P. Bouvier, A. Pashkin, K. Rabia, S. Frank, B. Dkhil, W. A Crichton, C. A Kuntscher, and J. Kreisel. Effect of high pressure on multiferroic $BiFeO_3$. *Phys. Rev. B*, 79(18):184110, 2009.

[161] M. Guennou, P. Bouvier, G. S. Chen, B. Dkhil, R. Haumont, G. Garbarino, and J. Kreisel. Multiple high-pressure phase transitions in BiFeO3. *ArXiv e-prints*, August 2011.

[162] Eliezer Rapoport. Pressure dependence of the Orthorhombic-Cubic transformation in lead zirconate. *Phys. Rev. Lett.*, 17(21):1097–1099, 1966.

[163] G. A Samara. Pressure and temperature dependence of the dielectric properties and phase transitions of the antiferroelectric perovskites: $PbZrO_3$ and $PbHfO_3$. *Phys. Rev. B*, 1(9):3777–3786, 1970.

[164] Y. Kobayashi, S. Endo, L.C. Ming, K. Deguchi, T. Ashida, and H. Fujishita. X-ray diffraction and dielectric measurements on $PbZrO_3$ at high pressure: a phase transformation study. *Journal of Physics and Chemistry of Solids*, 60(1):57–64, 1999.

[165] H. Furuta, S. Endo, L. C. Ming, and M. Kobayashi. Raman scattering study of $PbZrO_3$ under high pressure. *Physica B: Condensed Matter*, 263-264:816–818, 1999.

[166] H. Furuta, S. Endo, L.C. Ming, and H. Fujishita. Phase transitions in $PbZrO_3$ under high pressure studied by raman scattering. *Journal of Physics and Chemistry of Solids*, 60(1):65–67, 1999.

[167] E. Cockayne and K. M. Rabe. Pressure dependence of instabilities in perovskite $PbZrO_3$. *Journal of Physics and Chemistry of Solids*, 61(2):305–308, 2000.

[168] K. Leunga and A. F. Wrighta. Lead zirconate at ambient and high pressure. *Ferroelectrics*, 281(2):171–186, 2002.

[169] Ross J. Angel. Equations of state. In Robert M. Hazen and Robert T. Downs, editors, *High-temperature and high-pressure crystal chemistry*, volume 41, chapter 2, pages 35–60. Mineralogical Society of America Geochemical Society, robert m. hazen and robert t. downs edition, December 2000.

[170] B. Chaabane, J. Kreisel, B. Dkhil, P. Bouvier, and M. Mezouar. Pressure-Induced suppression of the diffuse scattering in the model relaxor ferroelectric $PbMg_{1/3}Nb_{2/3}O_3$. *Phys. Rev. Lett.*, 90(25):257601, 2003.

[171] P. -E Janolin, P. Bouvier, J. Kreisel, P. A Thomas, I. A Kornev, L. Bellaiche, W. Crichton, M. Hanfland, and B. Dkhil. High-Pressure effect on $PbTiO_3$: An investigation by raman and X-Ray scattering up to 63 GPa. *Phys. Rev. Lett.*, 101(23):237601, 2008.

[172] P. -E Janolin, B. Dkhil, P. Bouvier, J. Kreisel, and P. A Thomas. Pressure instabilities up to 46 gpa in the relaxor ferroelectric $PbZn_{1/3}Nb_{2/3}O_3$. *Phys. Rev. B*, 73(9):094128, 2006.

[173] Gen Shirane, Etsuro Sawaguchi, and Akitsu Takeda. On the phase transition in lead zirconate. *Phys. Rev.*, 80(3):485, November 1950.

[174] G. Shirane, J. D Axe, J. Harada, and J. P Remeika. Soft ferroelectric modes in lead titanate. *Phys. Rev. B*, 2(1):155¨C159, 1970.

[175] L. Feng and Z. -G. Ye. Phase diagram and phase transitions in the relaxor ferroelectric $Pb(Fe_{2/3}W_{1/3})O_3$-PbTiO3 system. *Journal of Solid State Chemistry*, 163(2):484–490, 2002.

[176] Liliana Mitoseriu, Paula M. Vilarinho, and Joao L. Baptista. Phase coexistence in $Pb(Fe_{2/3}W_{1/3})O_3$-$PbTiO_3$ solid solutions. *Applied Physics Letters*, 80(23):4422–4424, 2002.

[177] P. M. Vilarinho, L. Zhou, L. Mitoseriu, E. Finocchio, M. R. Soares, and J. L. Baptista. Morphotropic phase boundary in $PbFe_{2/3}W_{1/3}O_3$ - $PbTiO_3$ system. *Ferroelectrics*, 270(1):253–258, 2002.

[178] Liliana Mitoseriu, Paula M. Vilarinho, Massimo Viviani, and João L. Baptista. Structural study of $Pb(Fe_{2/3}W_{1/3})O_3$-PbTiO3 system. *Materials Letters*, 57(3):609–614, 2002.

[179] Liliana Mitoseriu, Alexandru Stancu, Cristina Fedor, and Paula M. Vilarinho. Analysis of the composition-induced transition from relaxor to ferroelectric state in $Pb(Fe_{2/3}W_{1/3})O_3$-PbTiO3 solid solutions. *Journal of Applied Physics*, 94(3):1918–1925, 2003.

[180] Liliana Mitoseriu, Daniele Marre, Antonio Sergio Siri, and Paolo Nanni. Magnetic properties of $Pb(Fe_{2/3}W_{1/3})O_3$-PbTiO3 solid solutions. *Applied Physics Letters*, 83(26):5509–5511, 2003.

[181] L. Mitoseriu, D. Marré, A. S. Siri, A. Stancu, C. E. Fedora, and P. Nanni. Magnetoelectric coupling in the multiferroic $PbFe_{2/3}W_{1/3}O_3$-$PbTiO_3$ system. *Journal of optoelectronics and adavnced materials*, 6(2):723–728, June 2004.

[182] L Mitoseriu, C. E. Ciomaga, and A Stancu. Evolution of the nanopolar order in (1-x)$pbfe_{2/3}w_{1/3}o_3$-$xpbtio_3$ relaxor investigated by raman and dielectric study. *Journal of Optoelectronics and Advanced Materials*, 6(3):1085–1088, 2004.

[183] Zhenrong Li, Aiying Wu, P M Vilarinho, and Ian M Reaney. Core-shell microstructures in0.68$Pb(Fe_{2/3}W_{1/3})O_3$- 0.32$PbTiO_3$ at the morphotropic phase boundary. *Journal of Physics: Condensed Matter*, 17(13):2167, 2005.

[184] E. Dul'kin, E. Mojaev, M. Roth, S. Kamba, and P. M. Vilarinho. Burns, néel, and structural phase transitions in multiferoic $Pb(Fe_{2/3}W_{1/3})O_3$–$PbTiO_3$ detected by an acoustic emission. *Journal of Applied Physics*, 103(8):083542, 2008.

[185] Ashok Kumar, G L Sharma, R S Katiyar, R. Pirc, R. Blinc, and J F Scott. Magnetic control of large room-temperature polarization. *Journal of Physics: Condensed Matter*, 21(38):382204, 2009.

[186] Ashok Kumar, R. S. Katiyar, and J. F. Scott. Fabrication and characterization of the multiferroic birelaxor lead¨ciron¨ctungstate/lead¨czirconate¨ctitanate. *Journal of Applied Physics*, 108(6):064105, 2010.

[187] R. Pirc, R. Blinc, and J. F. Scott. Mesoscopic model of a system possessing both relaxor ferroelectric and relaxor ferromagnetic properties. *Phys. Rev. B*, 79(21):214114, Jun 2009.

[188] A. Levstik, V. Bobnar, C. Filipič, J. Holc, M. Kosec, R. Blinc, Z. Trontelj, and Z. Jagličić. Magnetoelectric relaxor. *Applied Physics Letters*, 91(1):012905, 2007.

[189] V. V Shvartsman, S. Bedanta, P. Borisov, W. Kleemann, A. Tkach, and P. M Vilarinho. $(Sr,Mn)TiO_3$: a magnetoelectric multiglass. *Phys. Rev. Lett.*, 101(16):165704, October 2008.

[190] D. Lee, Y-A Park, S M Yang, T K Song, Y. Jo, N. Hur, J H Jung, and T W Noh. Suppressed magnetoelectric effect in epitaxially grown multiferroic $Pb(Zr_{0.57}Ti_{0.43})O_3$-$Pb(Fe_{2/3}W_{1/3}O_3$ solid-solution thin films. *Journal of Physics D: Applied Physics*, 43(45):455403, 2010.

[191] M. Kempa, S. Kamba, M. Savinov, M. Maryško, Z. Frait, P. Vaněk, M. Tomczyk, and P M Vilarinho. Bulk dielectric and magnetic properties of PFW-PZT ceramics: absence of magnetically switched-off polarization. *Journal of Physics: Condensed Matter*, 22(44):445902, 2010.

[192] S.A. Ivanov, P. Nordblad, R. Tellgren, T. Ericsson, and H. Rundlof. Structural, magnetic and mössbauer spectroscopic investigations of the magnetoelectric relaxor $Pb(Fe_{0.6}W_{0.2}Nb_{0.2})O_3$. *Solid State Sciences*, 9(5):440–450, May 2007.

[193] R. Wongmaneerung, X. Tan, R. W. McCallum, S. Ananta, and R. Yimnirun. Cation, dipole, and spin order in $PbFe_{2/3}W_{1/3}O_3$-based magnetoelectric multiferroic compounds. *Applied Physics Letters*, 90(24):242905, 2007.

[194] X. Tan, R. Wongmaneerung, and R. W. McCallum. Ferroelectric and magnetic properties of $PbFe_{2/3}W_{1/3}O_3$-based multiferroic compounds with cation order. *Journal of Applied Physics*, 102(10):104114, 2007.

[195] Masaru Yokosuka and Hidehiko Kojima. Dielectric and piezoelectric properties of the solid solution system $Pb(Fe_{2/3}W_{1/3})O_3$–$PbZrO_3$. *Japanese Journal of Applied Physics*, 36(Part 1, No. 9B):6046–6050, 1997.

[196] R. D Shannon. Revised effective ionic radii and systematic studies of interatomic distances in halides and chalcogenides. *Acta Crystallographica Section A*, 32(5):751–767, 1976.

[197] Tanmoy Maiti, R. Guo, and A. S. Bhalla. Electric field dependent dielectric properties and high tunability of $bazr_xti_{1-x}o_3$ relaxor ferroelectrics. *Applied physics letters*, 89(12):122909, 2006.

[198] R. Mazumder, P. Sujatha Devi, Dipten Bhattacharya, P. Choudhury, A. Sen, and M. Raja. Ferromagnetism in nanoscale $BiFeO_3$. *Applied Physics Letters*, 91(6):062510, 2007.

[199] D. Lebeugle, D. Colson, A. Forget, M. Viret, P. Bonville, J. F Marucco, and S. Fusil. Room-temperature coexistence of large electric polarization and magnetic order in $BiFeO_3$single crystals. *Phys. Rev. B*, 76(2):024116, 2007.

[200] W. Eerenstein, F. D. Morrison, J. Dho, M. G. Blamire, J. F. Scott, and N. D. Mathur. Comment on "Epitaxial BiFeO3 multiferroic thin film heterostructures". *Science*, 307(5713):1203, 2005.

[201] J. Wang, A. Scholl, H. Zheng, S. B. Ogale, D. Viehland, D. G. Schlom, N. A. Spaldin, K. M. Rabe, M. Wuttig, L. Mohaddes, J. Neaton, U. Waghmare, T. Zhao, and R. Ramesh. Response to comment on "Epitaxial BiFeO3 multiferroic thin film heterostructures". *Science*, 307(5713):1203, 2005.

[202] Hélène Béa, Manuel Bibes, Stéphane Fusil, Karim Bouzehouane, Eric Jacquet, Karsten Rode, Peter Bencok, and Agnès Barthélémy. Investigation on the origin of the magnetic moment of $BiFeO_3$ thin films by advanced x-ray characterizations. *Phys. Rev. B*, 74(2):020101, 2006.

[203] F. B. Koch and M. E. Fine. Magnetic properties of Fe_xO as related to the defect structure. *Journal of Applied Physics*, 38(3):1470–1471, 1967.

[204] M. E. Fine and F. B. Koch. Néel transformation in Near-Stoichiometric Fe_xO. *Journal of Applied Physics*, 39(5):2478–2479, 1968.

[205] F. J Morin. Magnetic susceptibility of αFe_2O_3 and αFe_2O_3 with added titanium. *Phys. Rev.*, 78(6):819–820, 1950.

[206] C. G Shull, W. A Strauser, and E. O Wollan. Neutron diffraction by paramagnetic and antiferromagnetic substances. *Phys. Rev.*, 83(2):333–345, 1951.

[207] L. M. Corliss, J. M. Hastings, and J. E. Goldman. Neutron diffraction study of the anisotropy transition in α-Fe_2O_3. *Phys. Rev.*, 93(4):893–894, Feb 1954.

[208] Yin-Yuan Li. Domain walls in antiferromagnets and the weak ferromagnetism of α-Fe_2O_3. *Phys. Rev.*, 101(5):1450–1454, 1956.

[209] A. Aharoni, E. H Frei, and M. Schieber. Curie point and origin of weak ferromagnetism in hematite. *Phys. Rev.*, 127(2):439–441, 1962.

[210] Franz Bødker, Mikkel F Hansen, Christian Bender Koch, Kim Lefmann, and Steen Mørup. Magnetic properties of hematite nanoparticles. *Phys. Rev. B*, 61(10):6826¨C6838, 2000.

[211] C. G Shull, E. O Wollan, and W. C Koehler. Neutron scattering and polarization by ferromagnetic materials. *Phys. Rev.*, 84(5):912¨C921, 1951.

[212] D. O Smith. Magnetization of a magnetite single crystal near the curie point. *Phys. Rev.*, 102(4):959¨C963, 1956.

[213] G. A Samara and A. A Giardini. Effect of pressure on the néel temperature of magnetite. *Phys. Rev.*, 186(2):577–580, 1969.

[214] Karen Paul. Magnetic and transport properties of monocrystalline Fe_3O_4. *Central European Journal of Physics*, 3(1):115–126, March 2005.

[215] J. A Duffy, J. W Taylor, S. B Dugdale, C. Shenton-Taylor, M. W Butchers, S. R Giblin, M. J Cooper, Y. Sakurai, and M. Itou. Spin and orbital moments in Fe_3O_4. *Phys. Rev. B*, 81(13):134424, 2010.

[216] Masatsugu Suzuki, Sharbani I Fullem, Itsuko S Suzuki, Lingyan Wang, and Chuan-Jian Zhong. Observation of superspin-glass behavior in Fe_3O_4 nanoparticles. *Phys. Rev. B*, 79(2):024418, 2009.

[217] D. T Margulies, F. T Parker, F. E Spada, R. S Goldman, J. Li, R. Sinclair, and A. E Berkowitz. Anomalous moment and anisotropy behavior in Fe_3O_4 films. *Phys. Rev. B*, 53(14):9175–9187, 1996.

[218] S. K Arora, Han-Chun Wu, R. J Choudhary, I. V Shvets, O. N Mryasov, Hongzhi Yao, and W. Y Ching. Giant magnetic moment in epitaxial Fe_3O_4 thin films on MgO(100). *Phys. Rev. B*, 77(13):134443, 2008.

[219] Warren E Henry and Mary Jo Boehm. Intradomain magnetic saturation and magnetic structure of γ-Fe_2O_3. *Phys. Rev.*, 101(4):1253–1254, 1956.

[220] R. Bauminger, S. G Cohen, A. Marinov, S. Ofer, and E. Segal. Study of the Low-Temperature transition in magnetite and the internal fields acting on iron nuclei in some spinel ferrites, using mössbauer absorption. *Phys. Rev.*, 122(5):1447–1450, 1961.

[221] W. H Kelly, V. J Folen, M. Hass, W. N Schreiner, and G. B Beard. Magnetic field at the nucleus in Spinel-Type crystals. *Phys. Rev.*, 124(1):80–84, 1961.

[222] Jr William Fuller Brown and Jr Clark E. Johnson. Temperature variation of saturation magnetization of Gamma-Ferric oxide. *Journal of Applied Physics*, 33(9):2752–2754, 1962.

[223] E. P Valstyn, J. P Hanton, and A. H Morrish. Ferromagnetic resonance of Single-Domain particles. *Phys. Rev.*, 128(5):2078–2087, 1962.

[224] W. O. Milligan, Y. Tamai, and J. T. Richardson. Magnetic properties of the dual oxide system CuO-Fe_2O_3. *Journal of Applied Physics*, 34(7):2093–2096, 1963.

[225] D. F. Eagle and J. C. Mallinson. On the coercivity of γFe_2O_3 particles. *Journal of Applied Physics*, 38(3):995–997, 1967.

[226] S. M Yusuf, J. M De Teresa, M. D Mukadam, J. Kohlbrecher, M. R Ibarra, J. Arbiol, P. Sharma, and S. K Kulshreshtha. Experimental study of the structural and magnetic properties of γ-Fe_2O_3 nanoparticles. *Phys. Rev. B*, 74(22):224428, 2006.

[227] Hans-Joachim Kleebe, Stefan Lauterbach, Laura Silvestroni, Hans Kungl, Michael J. Hoffmann, Emre Erdem, and Rudiger-A. Eichel. Formation of magnetic grains in ferroelectric $Pb[Zr_{0.6}Ti_{0.4}]O_3$ ceramics doped with fe^{3+} above the solubility limit. *Applied Physics Letters*, 94(14):142901, 2009.

[228] S. Díaz-Castañón, J. L. Sánchez Ll., E. Estevez-Rams, F. Leccabue, and B. E. Watts. Magneto-structural properties of $PbFe_12O_{19}$ hexaferrite powders prepared by decomposition of hydroxide-carbonate and metal-organic precipitates. *Journal of Magnetism and Magnetic Materials*, 185(2):194–198, 1998.

[229] G. -L Tan and M. Wang. Multiferroic $PbFe_12O_{19}$ ceramics. *ArXiv e-prints*, 2011.

[230] Roman V Shpanchenko, Viktoria V Chernaya, Alexander A Tsirlin, Pavel S Chizhov, Dmitry E Sklovsky, Evgeny V Antipov, Evgeny P Khlybov, Vladimir Pomjakushin, Anatoly M Balagurov, Julia E Medvedeva, Enrique E Kaul, and Christoph Geibel. Synthesis, structure, and properties of new perovskite $PbVO_3$. *Chemistry of Materials*, 16(17):3267–3273, 2004.

[231] J.E. Greedan, T. Katsumata, T. Tsuchiya, Y. Inaguma, , and S. Derakhshan. Crystal and magnetic structure of potentially multi-ferroic $PbFeO_3$. Annual Report 80, NRC-CNBC, 2007.

[232] Ángel M. Arévalo-López and MiguelÁ. Alario-Franco. On the structure and microstructure of "PbCrO3". *Journal of Solid State Chemistry*, 180(11):3271–3279, 2007.

[233] Kengo Oka, Masaki Azuma, Shigeto Hirai, Alexei A Belik, Hiroshi Kojitani, Masaki Akaogi, Mikio Takano, and Yuich Shimakawa. Pressure-Induced transformation of 6H hexagonal to 3C perovskite structure in $PbMnO_3$. *Inorganic Chemistry*, 48(5):2285–2288, 2009.

[234] Artem M. Abakumov, Joke Hadermann, Gustaaf Van Tendeloo, and Evgeny V. Antipov. Chemistry and structure of Anion-Deficient perovskites with translational interfaces. *Journal of the American Ceramic Society*, 91(6):1807–1813, 2008.

[235] T.I. Arbuzova, S.V. Naumov, B.A. Gizhevskii, V.L. Arbuzov, K.V. Shal‘nov, and E.A. Koslov. Short-range magnetic order in nanoceramic and bulk Mn_3O_4 irradiated electrons. In *Proceedings of the Third Moscow International Symposium on Magnetism*, 2005.

[236] Y. Ikedo, J. Sugiyama, H. Nozaki, H. Itahara, J. H Brewer, E. J Ansaldo, G. D Morris, D. Andreica, and A. Amato. Spatial inhomogeneity of magnetic moments in the cobalt oxide spinel Co_3O_4. *Phys. Rev. B*, 75(5):054424, 2007.

[237] Chen Ang, J. F Scott, Zhi Yu, H. Ledbetter, and J. L Baptista. Dielectric and ultrasonic anomalies at 16, 37, and 65 k in $SrTiO_3$. *Phys. Rev. B*, 59(10):6661–6664, 1999.

[238] D. W. Johnson, L. E. Cross, and F. A. Hummel. Dielectric relaxation in strontium titanates containing Rare-Earth ions. *Journal of Applied Physics*, 41(7):2828–2833, 1970.

[239] Adisak Boonchun, M. F. Smith, B. Cherdhirunkorn, and Sukit Limpijumnong. First principles study of Mn impurities in $PbTiO_3$ and $PbZrO_3$. *Journal of Applied Physics*, 101(4):043521, 2007.

[240] Hrvoje Meštric, Rüdiger-A Eichel, Klaus-Peter Dinse, Andrew Ozarowski, Johan van Tol, Louis Claude Brunel, Hans Kungl, Michael J Hoffmann, Kristin A Schönau, Michael Knapp, and Hartmut Fuess. Iron-oxygen vacancy defect association in polycrystalline iron-modified $PbZrO_3$ antiferroelectrics: Multifrequency electron paramagnetic resonance and newman superposition model analysis. *Phys. Rev. B*, 73(18):184105, 2006.

Acknowledge

This work has been done in laboratoire Structures, Propriétés et Modélisation des Solides (SPMS) of École Central Paris (ECP) and Centre National de la Recherche Scientifique (CNRS, UMR 8580) of France.

I would like to thank KREISEL Jens, Directeur de Recherche at CNRS-Grenoble INP, and DEFAY Emmanuel, Ingénieur at CEA-Grenoble for accepting to be the referees of my thesis. I would also like to thank KORNEV Igor, Professeur at l'École Centrale Paris, KIAT Jean-Michel, Directeur de Recherche at l'École Centrale Paris, LE MARREC, Françoise, Maître de Conférences at Université de Picardie Jules Verne as the committee members of thesis defense.

I would like to express my sincere gratitude to DKHIL Brahim for his supervision and guidance. Brahim is very experienced in guiding thesis and has profound knowledge in condensed matter physics. The same time, he has excellent personal character. All these give me a very good environment to finish my thesis.

I would like to thank GUIBLIN Nicolas for helping on diffraction experiments and explaining on crystallography and Rietveld Refinement. Also, He introduced many powerful softwares to me like Intensité which is complied by himself, Inkscape and Python are very useful for scientific work.

I would like to think GEMEINER Pascale. We together did many experiments during my first year in SPMS which were very helpful for later experiments.

I would like to show my gratitude to HAUMONT Raphaël, JARRIER Romain and WEI Jie did SQUID experiments in Institut de Chimie Moléculaire et des Matériaux d'Orsay (ICMMO). All these experiments are indispensable for my thesis.

Thanks to engineers and technicians in the laboratory, CHEVREUL Jacques, SOBOT Johan, GRAMOND Michel, MIVUMBI Obadias, BOEMARE Gilles, BOGICEVIC Christine, KAROLAK Fabienne, LUNEAU Christopher and XBR-MIEC Xavier who provided a excellent work station for us.

It is also important to mention that we do not only have study, We have café! MARTIN Thierry, BENARD Agnès, BOEMARE Gilles and ROUSSEL Claire are some early birds in SPMS. We had some memorable morning café.

I wish to express my gratitude to DEZANNEAU Guilhem, Giot Maud et al. who showed consideration about my thesis work, to BECKER Pierre, JOUAN Michel, GILLET Jean-Michel ( ), GEIGER Sandrine et al. who are very kind to me.

I would like to thank all Ph. D. candidates (some of them are already graduated) of the laboratory, WANG Yanzhong, BEVILLON emile, LIU Pufeng, DUPÉ Bertrand, BRAIDA Marc-David, HU Yang, ANOUFA Mickaël, THIERCELIN Mickaël, RABACHE Camille, NAHAS Yousra, ZHANG Yan et. al. and Ph. D. candidates of other laboratory, CHEN Si, GARNIER Carole...we had some memorable activities.

The thesis is supported by China State Scholarship Fund which is managed by China Scholarship Council (CSC). I would like to thank the people of Xi'an Jiaotong university (XJTU), École Centrale Paris (ECP), China Scholarship Council (CSC) and Service de l'Education Ambassade de la République Populaire de Chine en République Franccaise (SE) who did many works for the reality of finance support the thesis. The secretaries of École Doctorale (ED), LHOPITAL Catherine,

SBAIZERO Caroline, CARBONEL Géraldine and et al. are great acknowledgment. The secretaries of SPMS, SALVINI Pascale, VINEE-JACQUIN Christine also are also great acknowledgment for many practical works.

Thanks all the others who did contributions during the thesis work!